

Deciphering molecular spectra
of
syn- and *gauche*-propanal



Inaugural-Dissertation

zur

Erlangung des Doktorgrades

der Mathematisch-Naturwissenschaftlichen Fakultät

der Universität zu Köln

vorgelegt von

Oliver Zingsheim

aus Dormagen

2020

Berichterstatter:
(Gutachter)

Prof. Dr. Stephan Schlemmer
(Universität zu Köln)

Prof. Dr. Laurent Margulès
(Université de Lille)

Prof. Dr. Cristina Puzzarini
(Università di Bologna)

Tag der mündlichen Prüfung:

27.11.2020

Für mein Patenkind, Leonie.

*Die alle Ereignisse dieses Jahres,
diese Arbeit eingeschlossen,
so unbedeutend erscheinen lässt.*

List of Publications

All publications with contributions from the author of this thesis are listed below, ordered by publication date. One of these publications reports on the spectroscopy of propanal (title in bold), the molecule which is the subject and focus of this thesis.

M. Juanes, R. T. Saragi, Y. Jin, **O. Zingsheim**, S. Schlemmer, and A. Lesarri. Rotational spectrum and intramolecular hydrogen bonding in 1,2-butanedithiol. Journal of Molecular Structure, 1211:128080, 2020. doi:10.1016/j.molstruc.2020.128080

M. H. Ordu, **O. Zingsheim**, A. Belloche, F. Lewen, R. T. Garrod, K. M. Menten, S. Schlemmer, and H. S. P. Müller. Laboratory rotational spectroscopy of isotopic acetone, $\text{CH}_3^{13}\text{C}(\text{O})\text{CH}_3$ and $^{13}\text{CH}_3\text{C}(\text{O})\text{CH}_3$, and astronomical search in Sagittarius B2(N2). Astronomy & Astrophysics, 629:A72, 2019. doi:10.1051/0004-6361/201935887

M.-A. Martin-Drumel, K. L. K. Lee, A. Belloche, **O. Zingsheim**, S. Thorwirth, H. S. P. Müller, F. Lewen, R. T. Garrod, K. M. Menten, M. C. McCarthy, and S. Schlemmer. Submillimeter spectroscopy and astronomical searches of vinyl mercaptan, $\text{C}_2\text{H}_3\text{SH}$. Astronomy & Astrophysics, 623:A167, 2019. doi:10.1051/0004-6361/201935032

O. Zingsheim, M.-A. Martin-Drumel, S. Thorwirth, S. Schlemmer, C. A. Gottlieb, J. Gauss, and M. C. McCarthy. Germanium Dicarbide: Evidence for a T-Shaped Ground State Structure. The Journal of Physical Chemistry Letters, 8(16):3776–3781, 2017. doi:10.1021/acs.jpcllett.7b01544

O. Zingsheim, H. S. P. Müller, F. Lewen, J. K. Jørgensen, and S. Schlemmer. **Millimeter and submillimeter wave spectroscopy of propanal**. Journal of Molecular Spectroscopy, 342:125–131, 2017. doi:10.1016/j.jms.2017.07.008

H. S. P. Müller, **O. Zingsheim**, N. Wehres, J.-U. Grabow, F. Lewen, and S. Schlemmer. Rotational Spectroscopy of the Lowest Energy Conformer of 2- Cyanobutane. The Journal of Physical Chemistry A, 121(38):7121–7129, 2017. doi:10.1021/acs.jpca.7b06072

S. Thorwirth, M.-A. Martin-Drumel, C. P. Endres, T. Salomon, **O. Zingsheim**, J. van Wijngaarden, O. Pirali, S. Gruet, F. Lewen, S. Schlemmer, and M. C. McCarthy. An ASAP treatment of vibrationally excited S_2O : The ν_3 mode and the $\nu_3 + \nu_2 - \nu_2$ hot band. Journal of Molecular Spectroscopy, 319:47–49, 2016. doi:10.1016/j.jms.2015.12.009

M.-A. Martin-Drumel, C. P. Endres, **O. Zingsheim**, T. Salomon, J. van Wijngaarden, O. Pirali, S. Gruet, F. Lewen, S. Schlemmer, M. C. McCarthy, and S. Thorwirth. The SOLEIL view on sulfur rich oxides: The S_2O bending mode ν_2 at 380 cm^{-1} and its analysis using an Automated Spectral Assignment Procedure (ASAP). Journal of Molecular Spectroscopy, 315:72–79, 2015. doi:10.1016/j.jms.2015.02.014

M.-A. Martin-Drumel, J. van Wijngaarden, **O. Zingsheim**, F. Lewen, M. E. Harding, S. Schlemmer, and S. Thorwirth. Millimeter- and submillimeter-wave spectroscopy of disulfur dioxide, OSSO. Journal of Molecular Spectroscopy, 307:33–39, 2015. doi:10.1016/j.jms.2014.11.007

Note

A new manuscript has been published in the process of publishing this thesis, see below. It reports in detail on the newly developed double-modulation double-resonance (DM-DR) experimental technique, also presented within this thesis. In particular figures are identical and are subsequently referenced, also in order to fulfill publication rights. Publications which report on the rotational spectroscopy of *gauche*-propanal and the ro-vibrational spectroscopy of *syn*- and *gauche*-propanal, also (partly) presented in this thesis, are planned for the future as well.

O. Zingsheim, L. Bonah, F. Lewen, S. Thorwirth, H. S. P. Müller, and S. Schlemmer. Millimeter-millimeter-wave double-modulation double-resonance spectroscopy. Journal of Molecular Spectroscopy, 381:111519, 2021. doi:10.1016/j.jms.2021.111519

Abstract

The present work features the measurements and detailed analyses of the rotational and ro-vibrational spectra of propanal, or propionaldehyde ($\text{CH}_3\text{CH}_2\text{CHO}$). Broadband spectra were taken with (sub-)millimeter wavelength spectrometers in the frequency regions of 75–129 GHz and 170–500 GHz in Cologne. Additional far infrared spectra were recorded with a synchrotron-based Fourier-transform infrared spectrometer in the region of 80–700 cm^{-1} (SOLEIL synchrotron - AILES A beamline, Paris).

Propanal has two stable conformers, referred to as the *syn*- and *gauche*-forms. They differ mainly in the orientation of the aldehyde group (-CHO) with respect to the rigid carbon atom framework of the molecule. The rotational lines of *syn*-propanal show splittings due to internal rotation of the methyl group (-CH₃) and are fit with Groner's ERHAM program. The spectrum of *gauche*-propanal shows somewhat larger tunneling splittings originating from two stable energetically degenerate conformers and are analyzed with Pickett's SPFIT program. In summary, rotational spectra of $v = 0$, $v_{24} = 1$, $v_{23} = 1$, $v_{15} = 1$, $v_{24} = 2$, and $v_{24} = v_{23} = 1$ vibrational states of *syn*-propanal as well as $v = 0$ and $v_{24} = 1$ of *gauche*-propanal are studied. The fundamental vibrational frequency ν_{24} of *gauche*-propanal is redetermined to 68.75037(30) cm^{-1} on account of observed Coriolis interactions and Fermi resonances in the rotational analysis. Another main result is the reassignment of the fundamental band ν_{24} of *syn*-propanal in the far infrared spectrum at 133.9754525(39) cm^{-1} .

The millimeter- millimeter-wave double resonance experimental technique is established in Cologne using a newly assembled spectrometer allowing to unambiguously assign lines owing to the Autler-Townes effect. Furthermore, the implementation of a double modulation technique (modulation of both the pump and probe sources) allows for baseline- and confusion-free spectra containing only the line(s) of interest.

Kurzzusammenfassung

In dieser Arbeit werden molekulare Fingerabdrücke von Propanal, auch Propionaldehyd genannt ($\text{CH}_3\text{CH}_2\text{CHO}$), studiert. Dafür wurden breitbandige Rotationsspektren in den Frequenzbereichen von 75–129 GHz und 170–500 GHz mit konventionellen Absorptionsspektrometern in Köln gemessen. Für die Messung der Rotations-Vibrations Spektren wurde hingegen Strahlung des SOLEIL-Synchrotrons in Paris genutzt (AILES A beamline). Die Ferninfrarot Spektren wurden von 80–700 cm^{-1} gemessen.

Propanal kommt in der Natur in den zwei stabilen Konformationen *syn*- und *gauche*-Propanal vor. Die beiden unterscheiden sich im Wesentlichen in der Stellung ihrer Aldehyd-Gruppe (-CHO), während die Struktur des Kohlenstoff Gerüsts, inklusive gebundener Wasserstoffatome, nahezu identisch bleibt. Mit dem ERHAM-Programm konnten die beobachteten Torsionsaufspaltungen in *syn*-Propanal beschrieben werden, welche aus der internen Rotation der Methylgruppe (- CH_3) resultieren. Dabei wurden die Fingerabdrücke der Rotationsspektren in den Schwingungszuständen $v = 0$, $v_{24} = 1$, $v_{23} = 1$, $v_{15} = 1$, $v_{24} = 2$, und $v_{24} = v_{23} = 1$ analysiert. Die Bestimmung der fundamentalen Schwingungsfrequenz $\nu_{24} = 133.9754525(39) \text{ cm}^{-1}$ von *syn*-Propanal ist das Ergebnis der Auswertung der Ferninfrarot Spektren. Bei Drehung der Aldehydgruppe (-CHO) aus der Symmetrieebene, welche durch die Kohlenstoffatome aufgespannt ist, entstehen zwei energetisch entartete Konfigurationen: links- und rechts-händisches *gauche*-Propanal. Hier resultiert durch Tunneln der Aldehydgruppe zwischen diesen beiden Konfigurationen ebenfalls eine Aufspaltung der Rotationslinien. Im Vergleich zu den Aufspaltungen in *syn*-Propanal sind die Aufspaltungen etwas größer. Die resultierenden Fingerabdrücke wurden mit dem SPFIT-Programm beschrieben. Bei der Analyse der Zustände $v = 0$ und $v_{24} = 1$ von *gauche*-Propanal dienen die beobachteten Coriolis-Wechselwirkungen und Fermi-Resonanzen der Bestimmung der Frequenz der Fundamental-Schwingung $\nu_{24} = 68.75037(30) \text{ cm}^{-1}$.

Das im Rahmen der vorliegenden Arbeit neu aufgebaute Millimeter-Millimeterwellen Doppelresonanz-Experiment erlaubt die eindeutige Zuordnung von Moleküllinien aufgrund des Autler-Townes Effektes. Weiterhin wurde ein zweites Modulationsschema etabliert, hierbei wird neben der Proben- auch die Pumpfrequenz moduliert. Das führt zu stark vereinfachten Spektren ohne Stehwellencharakteristik, die nur die gesuchte(n) Linie(n) enthalten.

Contents

1	Laboratory Astrophysics	1
1.1	Rotational Fingerprints in Space	3
1.2	Double Resonance Spectroscopy	6
1.3	Molecule of Interest: Propanal	7
2	Theory of Molecular Spectroscopy	12
2.1	Pure Rotational Hamiltonians	13
2.1.1	Linear Molecules	16
2.1.2	Symmetric-Top Molecules	16
2.1.3	Asymmetric-Top Molecules	17
2.1.3.a	Watson's A Reduction	19
2.1.3.b	S Reduction	20
2.1.3.c	Selection Rules	21
2.1.3.d	Parity Selection Rules	24
2.1.3.e	Line Intensities	25
2.1.3.f	Line Shapes	26
2.2	Rotation-Vibration Hamiltonians	27
2.3	Treatments of Perturbations in Molecular Spectroscopy	28
2.3.1	Two-Level Systems	28
2.3.2	Rabi Cycle	29
2.3.3	Autler-Townes Effect	30
2.3.4	Fermi Resonance	33
2.3.5	Coriolis Interaction	34
2.4	Large Amplitude Motions - Internal Rotation	35
3	Absorption Spectrometers	41
3.1	(Sub-)Millimeter Wave Spectrometers	41
3.1.1	Conventional Measurements - Measuring Rotational Fingerprints	41
3.1.2	Double Resonance Measurements - Identifying Linkages	44
3.1.3	Double Modulation Measurements - Clearing up Molecular Spectra	46
3.2	Synchrotron based Fourier-Transform Infrared Spectrometer	49
4	Analysis Procedure and Analytical Tools	51
4.1	General Assignment, Fitting, and Predicting Procedure	51
4.2	Deciphering hidden Fingerprints - A specific Assignment Strategy	52
4.3	Analysis Software	55
4.3.1	SPFIT/SPCAT Suite of Programs	55
4.3.2	ERHAM Program	57

5	Molecular Fingerprints of Propanal	59
5.1	<i>Syn</i> -Propanal	59
5.1.1	Vibrational Ground State $v = 0$	62
5.1.2	Aldehyde Torsion ν_{24}	65
5.1.2.a	Aldehyde Torsion $\nu_{24} = 1$	65
5.1.2.b	Fundamental Band $\nu_{24} = 1 \leftarrow 0$	67
5.1.3	Methyl Torsion $\nu_{23} = 1$	70
5.1.4	Vibrationally Excited States $\nu_{24} = 2$, $\nu_{15} = 1$, and $\nu_{24} = \nu_{23} = 1$	72
5.2	<i>Gauche</i> -Propanal	78
5.2.1	Single State Analysis of $v = 0$	79
5.2.2	Single State Analysis of $\nu_{24} = 1$	86
5.2.3	Global Analysis of $v = 0$ and $\nu_{24} = 1$	92
6	Summary, Discussion, and Conclusions	102
6.1	<i>Syn</i> -Propanal	102
6.2	<i>Gauche</i> -Propanal	105
6.3	Millimeter-Millimeter Wave Double Resonance Spectroscopy	108
7	Prospects	110
7.1	<i>Syn</i> -Propanal	110
7.2	<i>Gauche</i> -Propanal	112
7.3	Future Experimental Ideas	113
7.3.1	Baseline-free Spectroscopy	113
7.3.2	Automated Deciphering of Molecular Fingerprints	113
	Appendix	116
	Data Storage and Used Programs	116
	Abbreviations	116
	Equations	118
	Group Theory of <i>Syn</i> -Propanal	122
	Tables	127
	Detailed Iterative Fitting Procedure	129
	Assignment Software	132
	Figures	134
	Figures: <i>Syn</i> -Propanal	142
	Figures: <i>Gauche</i> -Propanal	148
	References	161
	List of Figures	173

CONTENTS

List of Tables	176
Acknowledgments	177
Eigenständigkeitserklärung	180

1 Laboratory Astrophysics

”Whoever needs a motivation is lost.”

- Stephan Schlemmer -

Molecular spectroscopic fingerprints are covering a large range of the electromagnetic spectrum, see Fig. 1, spanning from the radio frequency (RF) region (rotational degrees of freedom), over the infrared (IR) region (vibrational degrees of freedom) up to the optical regime and beyond (electronic excitation). Rotational fingerprints can be found typically from a few gigahertz up to the terahertz region, covering the microwave (MW), millimeter-wave (MMW) as well as the sub-millimeter-wave (sub-MMW) regions and are usually presented in units of frequency (s^{-1} , or Hz; typically in MHz). Bending and stretching vibrations are typically located in the IR region between some 100 cm^{-1} ($\approx 3 \text{ THz}$) to 4000 cm^{-1} ($\approx 120 \text{ THz}$), respectively. In the far-infrared (FIR) region, lower-lying vibrations such as torsional motions may be found. Electronic excitations, famously known from flame tests and fireworks, are located in the optical regime from $400\text{--}700 \text{ nm}$ (or $3.1\text{--}1.8 \text{ eV}$) well into the ultraviolet (UV) region.

The aforementioned spectroscopic molecular fingerprints are the same all over the universe. Describing a fingerprint in the laboratory allows thus to search for the same fingerprint in astronomical observations and therefore in far distant galaxies, molecular clouds, star-forming regions, or any other astronomical object. In fact, various physical properties of distant objects, such as temperatures, column densities and oth-

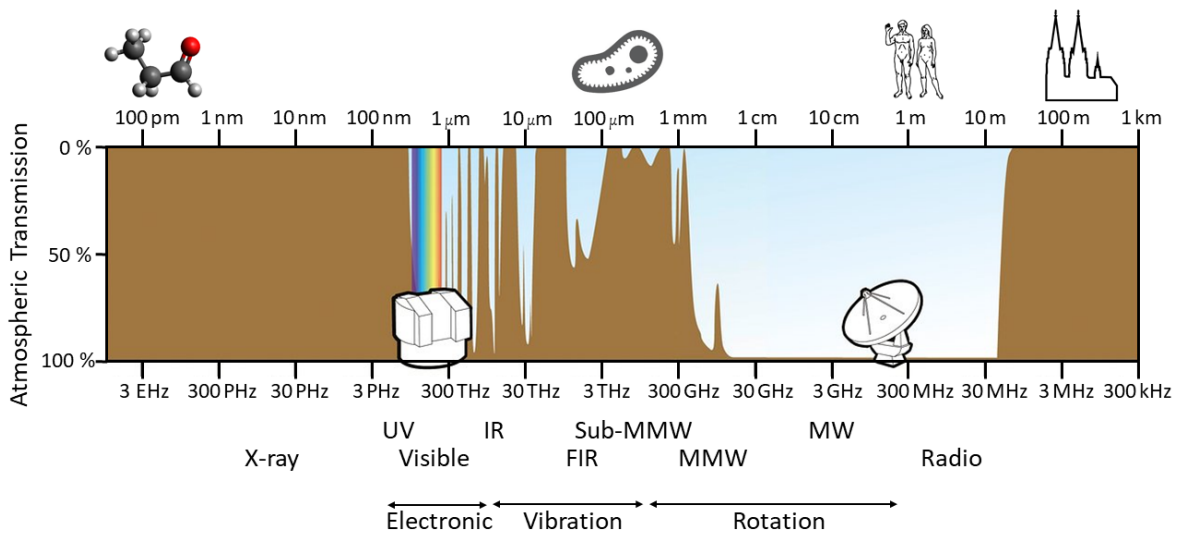


Figure 1: Schematic of the electromagnetic spectrum highlighting various wavelength regions, see text. The respective wavelengths are depicted by the size of propanal, a human cell, humans and the Cologne cathedral. The brown area shows the opacity of the earth atmosphere, highlighting ground-based observations in the visible and radio windows. The figure is partly adapted from ESA/Hubble (F. Granato) [1].

ers, can be derived with a proper knowledge of the molecular fingerprints. Nearly all our knowledge from space is derived by studying electromagnetic radiation (cf. Fig. 1) emitted from distant objects in the universe with the exception of *in situ* measurements of some solar system objects and the recent emergence of direct detection of gravitational waves [2]. Temperatures prevalent in different astronomical sources range, for example, from a few Kelvin in cold molecular clouds up to thousands of Kelvin in outer layers of stars. However, molecular fingerprints are not found at very high temperatures as molecules will eventually dissociate ($T \sim 5000$ K). Nevertheless, the large temperature range expose the need for proper quantum mechanical descriptions of molecules which are able to predict their spectra at any temperature. In fact, the molecular fingerprint for any temperature may be predicted by analyzing the spectrum at only a single temperature if a proper model Hamiltonian is available.

Detecting weak signals of molecules in space is very challenging and comparable to looking for a needle in a haystack. Therefore, accurate predictions of molecular spectra are indispensable for a clear detection of molecules in space. Complex organic molecules (COMs) play a central role in laboratory astrophysics. COMs contain carbon-hydrogen bonds and are composed of six or more atoms. **One of the key aspects is to reveal the level of complexity of COMs in space.** Associated with that is the fundamental question whether precursor molecules of life will be found in the interstellar medium (ISM) and, if so, at which quantity, see Sec. 1.1. There is a chance that these precursors already formed in the ISM and not only, for example, on earth under special conditions. If these precursors are found, they may be spread throughout the universe, which would probably favor the formation of extraterrestrial life. This scenario is however highly speculative.

As will be shown in the present thesis, absorption spectroscopy is a versatile tool to study spectroscopic molecular fingerprints (cf. also Refs. [3–8], and references therein). The double resonance (DR) technique simplifies the analysis of complex molecular systems and is frequently used in several frequency regions (cf. Refs. [9–17], and references therein). In addition, the development of new or the extension of well established experimental techniques facilitate the understanding of complex molecular fingerprints, which are challenging to analyze otherwise. **The DR technique is not commonly used in the MMW region**, see Sec. 1.2, but the Autler-Townes effect (Refs. [18, 19]; cf. Sec. 2.3.3) allows for an extension of a conventional absorption spectrometer for establishing a MMW-MMW DR scheme within this work. Initially, **the work on propanal was motivated by deviations between observed astronomical spectra and their predictions**, besides the fundamental interest of its potential energy surface, see Sec. 1.3. Propanal is the main focus of this thesis which is conducted in the framework of the Collaborative Research Center (CRC) 956 "Conditions and impact of star formation" and is part of subproject B3, with a focus on tracing complex

molecules in space.

1.1 Rotational Fingerprints in Space

”Before you start this, is it really necessary?”

- Sven Thorwirth -

For a long time it had been commonly assumed that molecules in the ISM were only simple diatomic or small-sized molecules due to the harsh interstellar environment, such as UV starlight and fast protons from supernovae events, which would prevent the formation of more complex species. Nowadays it is known, that even COMs are present in the ISM. The detection of new species, combined with the understanding of their formation route, is one of the quests of modern astrochemistry. Therefore, molecules driving the ongoing chemistry in space need to be known to derive accurate chemical networks which explain the formation route and the presence of COMs in space.

To circumvent opacity issues of the earth atmosphere (cf. Fig. 1), high altitudes as well as a dry atmosphere are beneficial for astronomical observations in the MW and (sub-)MMW regions where rotational fingerprints of molecules are found. An ideal location for earthbound observations satisfying these requirements is the Chajnantor-Plateaus at an altitude of around 5000 m in the Atacama desert. Here, the Atacama Large Millimeter Array (ALMA) is located.¹ ALMA operates, for example, in the frequency region of 84–116 GHz (W-band region; ALMA Band 3), where many polar molecules have their typical rotational fingerprints. The high sensitivity of ALMA allows to search for the weak radio signals of COMs in space. One promising object for a search in space is the molecular cloud Sagittarius (Sgr) B2(N2). Acetone ($\text{CH}_3\text{C}(\text{O})\text{CH}_3$), an isomer of propanal, is detected towards this source [8], among other molecules, see Fig. 2. Detection of rare isotopologues of acetone was possible because of the availability of proper quantum mechanical models [20], which were refined in the framework of this thesis. The final models are not presented in this thesis but are published in Ref. [8]. Interestingly, not only the ground vibrational state of the main isotopologue was detected in space, but also vibrational satellites from energetically low-lying vibrationally excited states. This demonstrates the necessity of studying more than just the ground vibrational state of a molecule. First of all, the detection of vibrational satellites helps to disentangle the dense astronomical spectra, but more importantly, their presence influences the ongoing chemistry, as excited molecules carry more energy which may allow them to overcome reaction barriers more easily.

The molecular complexity in space can be seen by the detection of many molecules with straight chains of carbon atoms in the ISM, e.g. propanal [23], ethyl cyanide

¹<https://www.almaobservatory.org/en/home/> [Online; accessed 08-August-2020].

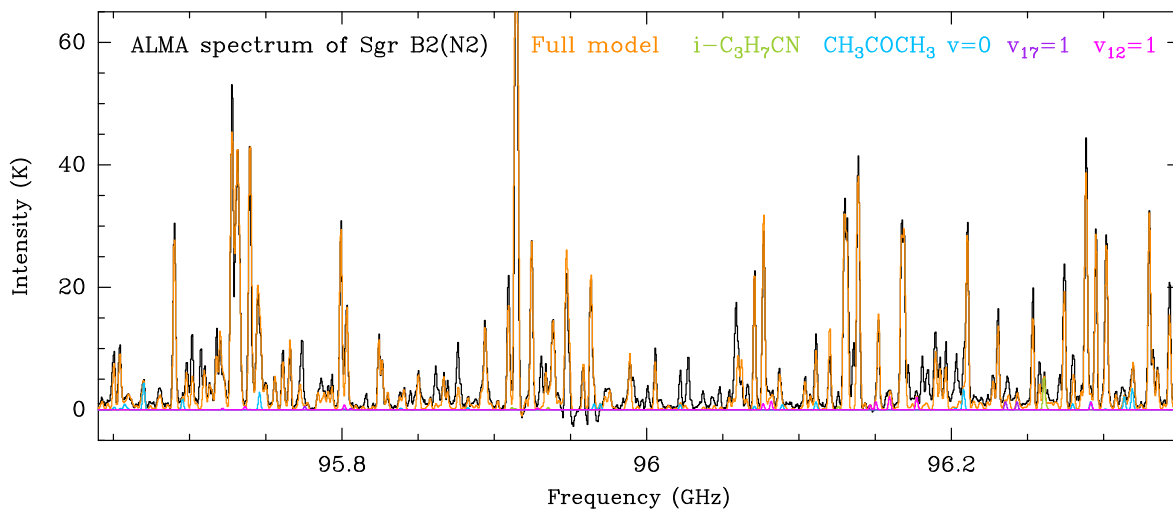


Figure 2: Exploring Molecular Complexity with ALMA (EMoCA) survey in the region of 95.64–96.34 GHz [21]. The black line is the emission spectrum of Sagittarius (Sgr) B2(N2). The strongest line at 95.92 GHz is cut off. The spectrum shows quite some line confusion, seen by the density of lines which are frequently blended, making accurate predictions indispensable for a clear detection. Furthermore, some unidentified lines are visible, for example around 96.025 GHz, showing the need for more laboratory studies of new molecules as well as of isotopologues and vibrationally excited states of already detected molecules, to be able to assign these lines. A full model of all identified molecular species is shown in orange. Other colored lines show the rotational fingerprints of acetone ($\text{CH}_3\text{C}(\text{O})\text{CH}_3$) in different vibrational states as well as the branched molecule *iso*-propyl cyanide ($i\text{-C}_3\text{H}_7\text{CN}$). Figure credits: A. Belloche [22].

[24], and *n*-propyl cyanide [25]. On the other hand, for precursor of life also the branched configurations of molecules play an important role. The detection of the first branched molecule in space, *iso*-propyl cyanide ($i\text{-C}_3\text{H}_7\text{CN}$), was reported in 2014 [26]. The detection of this molecule is also highlighted in Fig. 2. Furthermore, even a chiral molecule, propylene oxide ($\text{CH}_3\text{CHCH}_2\text{O}$), which is, like acetone, an isomer of propanal, was found in 2016 toward the galactic center [27]. The life on earth is strongly influenced by an observed homochirality and detection of these molecules in space may give further hints concerning this field of research, even though the chirality of molecules can not be determined directly by astronomical observations.

The (surprising) richness of chemistry in space can be seen by the detection of more than 200 molecules in the ISM or circumstellar shells (the reader is also referred to the "molecules in space" section of the Cologne Database for Molecular Spectroscopy, CDMS² [28–30]). Multi-national collaborations equip new-era observatories, such as ALMA, with manpower and cutting-edge technologies which are critical to detect the

²<https://cdms.astro.uni-koeln.de/classic/molecules> [Online; accessed 21-July-2020].

weak signals of molecules in space. In regard of the effort, the number of molecules found in space seems to be quite limited at first glance. As already mentioned, detecting new species in space is comparable to looking for a needle in a haystack. Therefore, it is advisable that observers make educated guesses for possible candidate molecules in space. Following the quotation of this section by S. Thorwirth, a crucial step in laboratory astrophysics is to filter out promising candidate molecules for a possible detection in space. This is important as measuring molecular fingerprints in the laboratory and especially their interpretation and modeling can be very time consuming. Promising candidates are usually missing molecules in chemical networks, which are most likely formed in space provided the model is adequate. Here, even a non-detection can lead to some further important insights into the ongoing chemistry. Also molecules where one atom is exchanged by the next higher group element from the periodic table are promising candidates to search for, if the lighter isovalent variant was already found in space. As an example for exchanging oxygen by sulfur, the laboratory fingerprints of vinyl mercaptan (CH_2CHSH) were studied in more detail [33], partly in the framework of this thesis, as vinyl alcohol (CH_2CHOH), the isovalent counterpart, was already found in space [34]. Another starting point for a search of a new molecule in space may be the higher member of a homologous series. In case the small members are quite abundant in space, higher members may also be detectable. As an example, in 1969 methanal, or formaldehyde (H_2CO), was found in space [31], followed by ethanal, or acetaldehyde (CH_3CHO), 14 years later [32]. Finally, propanal, or propionaldehyde ($\text{CH}_3\text{CH}_2\text{CHO}$), was found in space in 2004 [23]. These aforementioned molecules are the first members of the homologous series of alkanales, an alkyl group attached to an aldehyde group (R-CHO), and are depicted in Fig. 3. It is for sure a matter of speculation if butanal, or butyraldehyde ($\text{CH}_3\text{CH}_2\text{CH}_2\text{CHO}$), will be found in space, too. On the other hand, as already pointed out, it is important to study also vibrationally excited states of molecules which have been detected already in space. In this respect, it is also worth to study laboratory fingerprints of energetically low-lying vibrationally

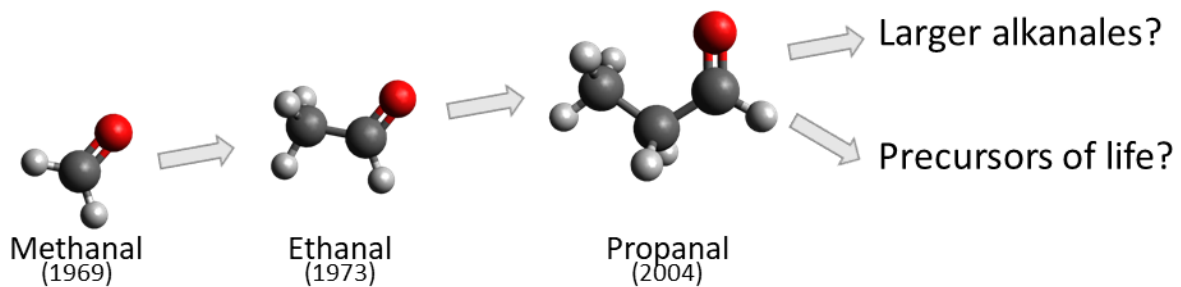


Figure 3: The homologous series of alkanales (aldehydes). The smallest three members are given with the year of their first detection in space [23, 31, 32]. This series shows the evolution of detection of growing complexity of molecules in space.

excited states of propanal in quite some detail.

1.2 Double Resonance Spectroscopy

As complex molecules frequently occur in the form of several conformers, each of them with naturally abundant isotopologues and all of them with a number of vibrationally excited states populated, the room temperature spectra of molecules can be quite dense. Thousands of lines can appear in comparably small frequency windows of a molecular spectrum. Observations close to the confusion limit are hampering the understanding, in particular the unambiguous assignment, of molecular transitions. Possible interactions between vibrational states, which lead to perturbed energy levels, may aggravate the assignment even further. This may result in more than just one possibility for a line assignment. DR spectroscopy facilitates spectroscopic assignments in these cases. Two independent light sources manipulate the molecular sample (nearly) simultaneously in DR experiments. Thereby, the probe radiation is conventionally measuring the spectrum. The second radiation, referred to as the pump radiation, is perturbing a two-level system. The effect of the perturbation may be noticed in the resulting spectrum if probe and pump frequencies are resonant to two transitions which share one energy level. In this way, spectroscopic linkages can be identified which simplify the analyses dramatically, especially those of perturbed systems.

The DR experimental technique is not commonly used in the MMW region which is surrounded by MW and IR regions, where DR is a well established experimental technique. For example in the MW region, in chirped pulse (CP) Fourier transform (FT) MW experiments [35, 36], the phase coherence of the molecular free induction decay (FID) signal can be lifted by the pump radiation and allows in best cases for complete depletion of the signal [12]. On the other hand, huge population differences of two-level systems make the DR a versatile tool in the IR region as the population difference can be manipulated by the pump radiation. As mentioned before, bending and stretching vibrations are typically located in the region between some 100 cm^{-1} to 4000 cm^{-1} , respectively. In thermal equilibrium and at room temperature (300 K) the relative population N_f/N_i of a first excited to the ground state is calculated with the help of the Boltzmann factor

$$\frac{N_f}{N_i} = e^{-\Delta E/(k_B T)} \quad (1.1)$$

to be around 62 % and $5 \cdot 10^{-7}$ %, respectively (1000 cm^{-1} correspond to approximately 0.8 %). In contrast, destroying the phase coherence and induced population changes can not straightforwardly be extended to the MMW region. Indeed, CP-FT experiments were recently extended to the W-band region [37, 38], but cannot compete with the signal-to-noise ratios (SNRs) of conventional measurement setups up to now. On

the other hand, the relative population of a simple two-level system, separated by 100 GHz, or 3.34 cm^{-1} , is $\frac{N_f}{N_i} \approx 0.984$.³ This elucidates the small effect of changes of the population differences to be expected here. Nevertheless, the Autler-Townes effect (Refs. [18,19]; cf. Sec. 2.3.3) allows for establishing a MMW-MMW DR scheme within the framework of this thesis, see Sec. 3.1, which allows to unravel weak molecular fingerprints of propanal as well as to derive accurate models of interacting states. The extended experimental setup developed here is expected to help to decipher many more complex molecular fingerprints in the future.

1.3 Molecule of Interest: Propanal

”Propanal is a nice introductory project.

This project will be finished within a year.”

- Holger S. P. Müller -

The pioneering work on propanal and some of its low-lying vibrational states as well as deuterated isotopic species was performed in 1964 by measuring rotational spectra up to 38 GHz with a conventional Hughes-Wilson type microwave spectrometer [39]. Therein, Butcher and Wilson established the existence of two stable conformers, so-called *syn*- and *gauche*-propanal [39]. Accurate structures of both conformers were determined by measuring a total of twelve and six isotopic species of *syn*- and *gauche*-propanal in the MW region, respectively [40]. The conformers can be converted to each other by an internal rotation of the aldehyde group (-CHO) with respect to a rigid rest framework of the molecule, see Fig. 4. The most stable configuration, the global minimum of the potential energy surface, has a planar configuration of all four heavy nuclei (CCCO) with a dihedral angle of zero degrees. This conformer is called *syn*-propanal, sometimes also referred to as *cis*-propanal. A sketch is shown on the right hand side of Fig. 4. *Syn*-propanal has a symmetry plane which coincides with the heavy nuclei plane (C_s symmetry, see Table A9). Rotation of the aldehyde group by 180° leads to an *anti* conformer which is a transition state as the potential energy function has a local maximum at this rotation angle, see Fig. 4. The resulting barrier is separating two equivalent local potential minima. These give rise to the equivalent left and right handed configurations of *gauche*-propanal (C_1 symmetry, see Table A10), where the aldehyde group is rotated by $\pm 128.2^\circ$ in comparison to *syn*-propanal [41]. The low barrier height facilitates tunneling between the two minima (C_s symmetry with allowed tunneling). As a consequence, a splitting of each vibrational state is observed. The resulting symmetric (+) and antisymmetric (-) tunneling states of each vibrational state are labeled with X^+ and X^- , see Sec. 2.4. The existence of the doubly-degenerate *gauche* conformer

³For asymmetric rotor molecules different degeneracies of the two-level system, spin statistics, and more effects need to be considered for a proper calculation of the population change.

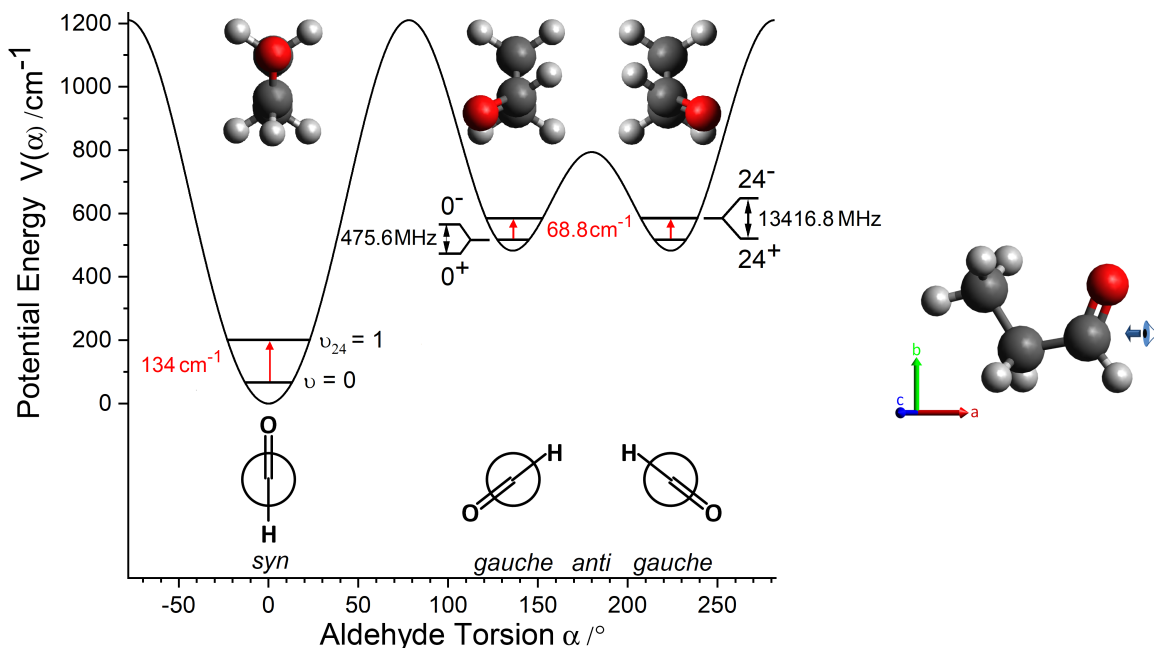


Figure 4: Calculated potential energy function of propanal with respect to the aldehyde group (-CHO) rotation [41]. On the right hand side *syn*-propanal is shown as face-on view. The white, black, and red spheres in propanal sketches designate hydrogen, carbon, and oxygen atoms, respectively. Simplified Newman projections are highlighting the orientation of the aldehyde group in *syn*- and *gauche*-propanal. The low barrier of the double-well potential between the two *gauche* configurations leads to observable tunneling splittings. The resulting substates are labeled with X^+ and X^- . Given energy differences are key results of this work.

was also shown by Butcher and Wilson [39]. In fact, the authors showed that tunneling splitting arising from the low barrier between the two *gauche* configurations is observable. Butcher and Wilson excluded the internal rotation of the methyl group as a possibility of the observed splitting of transitions of *gauche*-propanal as comparable splittings were observed for *gauche*- $\text{CD}_3\text{CH}_2\text{CHO}$ and for *gauche*- $\text{CH}_3\text{CH}_2\text{CHO}$ [39]. A deuterated methyl group ($-\text{CD}_3$) would result in much smaller internal rotation splittings than a CH_3 one, as higher (reduced) masses make tunneling less probable. On the other hand, *syn*-propanal shows a clearer splitting caused by the internal rotation of the methyl group for a fair fraction of the rotational transitions [39]. The barrier height V_3 of the methyl group internal rotation was determined for the ground vibrational state of *syn*-propanal in a microwave study to $793.7(25)\text{ cm}^{-1}$ [42] and with measurements up to the MMW region to $784.2(90)\text{ cm}^{-1}$ [43]. The barrier height V_3 of the methyl group internal rotation of *gauche*-propanal was determined later to be $886(10)\text{ cm}^{-1}$, which is only slightly higher than for *syn*-propanal [44]. This was achieved by measuring transitions which showed additional splittings due to the internal rotation of the

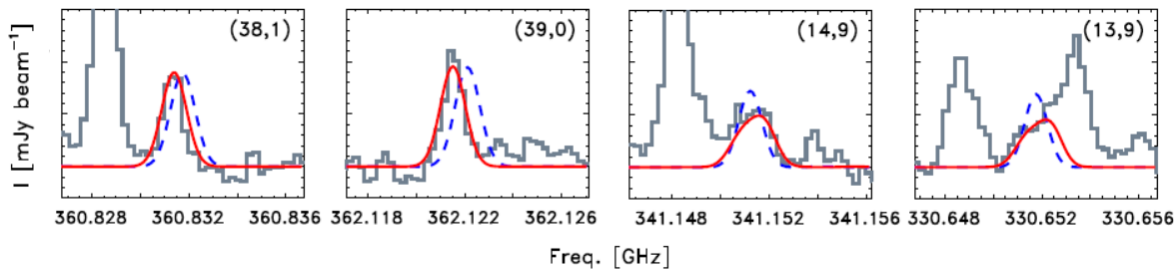


Figure 5: Selected emission features of *syn*-propanal towards a protostellar binary in the ALMA-PILS survey (see Refs. [48] and [49] for details). Astronomical observations are shown in grey and predictions of an initial model are shown by the blue dashed lines. New predictions, based on the model derived in this work, are shown in red. Quantum numbers (J, K_a) are given for the upper energy level of a depicted transition and will be introduced later. The newly derived model predicts the center frequencies for transitions with high J more accurately, see the two plots on the left hand side. Furthermore the methyl group internal rotation splittings are treated more satisfactorily, see the two plots on the right hand side. Broadened line profiles are observed because two torsional components are partly blended. The figure is an extraction from Fig. 5 of Ref. [50] to which the reader is referred to for more information.

methyl group.⁴

In addition, vibrational modes of both conformers were studied by low-resolution FIR [45] as well as by mid-IR spectroscopy [46]. In particular, also the hot bands of the aldehyde vibration were assigned [45]. From a chemical point of view, a main interest is in understanding the potential energy function of the aldehyde group rotation of the molecule, which is shown in Fig. 4. It was studied in more detail by different groups [41,45,47]. Furthermore, the enthalpy difference of the two conformers is derived in several studies but shows scatter in the determined values of $315 \pm 35 \text{ cm}^{-1}$ [39], $420 \pm 27 \text{ cm}^{-1}$ [41], $241 \pm 10 \text{ cm}^{-1}$ [45], and $370 \pm 21 \text{ cm}^{-1}$ [46]. The interplay of the two large amplitude motions, the internal rotations of the aldehyde and of the methyl group, may be of even greater significance for quantum chemists as benchmark tests of their calculations.

Alkanales, R-CHO, are of interest for astrochemistry as is demonstrated by the detection of the three smallest members in space [23, 31, 32], cf. Fig. 3. Initially, the work on propanal was motivated by deviations between observed astronomical spectra and their predictions, see Fig. 5. This is one of the reasons why propanal is the main focus of this work, even though it was already studied spectroscopically quite exten-

⁴Additional transitions which showed splittings were so-called *b*- and *c*-type transitions, which will be introduced later on. Initially observed transitions are expected to be only marginally split and are therefore observed as blended transitions, which is usually the case for *a*-type transitions in *gauche*-propanal.

sively before [39–47], permitting its detection in space [23]. However, line intensities of propanal were partially overestimated and significant shifts in the frequency domain were observed also. The discrepancy of observed and predicted molecular fingerprints of the ground vibrational state of *syn*-propanal seen in Fig. 5 could be solved to a large extent within this work, see also Ref. [50]. Furthermore, the ground vibrational state of *gauche*-propanal and low-lying vibrationally excited states of both conformers are studied in detail to derive accurate quantum mechanical models.

In summary, not only the astronomical relevance, which is already of considerable importance itself, is a key motivation to study propanal, but also the fundamental interest of the potential energy surface, which is indirectly probed by measuring transitions between energy levels of the molecule. Throughout this work, the author tries to convince the reader why the extensive study of both conformers, *syn*-propanal and *gauche*-propanal, ended up to be the heart of this thesis, in contradiction to what might have been expected by looking at the quote of Holger S. P. Müller given at the beginning of this section.

The outline of the remainder of the present thesis is as follows: The unique fingerprints of molecules can be described by means of quantum mechanics. For that reason the theoretical aspects which are essential to understand and finally describe the observed spectra of propanal, or its spectroscopic molecular fingerprints, are presented in Ch. 2. Subsequently, the experimental setups for measuring rotational as well as ro-vibrational spectra are presented in Ch. 3. A focus is on the newly established MMW-MMW DR experimental setup. As will be shown in detail, the analysis can be simplified dramatically with this setup. Furthermore, weak as well as heavily blended transitions can be measured with the help of a second modulation scheme which allows to derive additional information of molecules which may have been hidden before. Afterwards, analytical tools and analyses routines, in particular the iterative fitting procedure, are presented in Ch. 4. The deciphered molecular fingerprints of *syn*- and *gauche*-propanal are presented in Ch. 5. This chapter is the central part of this thesis, containing detailed descriptions of the complex fingerprints of various vibrational states of propanal and their proper quantum mechanical descriptions. This allows to search for the spectroscopic molecular fingerprints in space. The measurements and the analyses are summarized and discussed in Ch. 6. From this, specific conclusions are drawn for the various analyzed vibrational states. Finally, based on these conclusions, possible next steps in studying propanal as well as further possibilities to facilitate the understanding of astrophysically and quantum chemically relevant molecules are pointed out in Ch. 7, in particular by making use of the DR technique to decipher hidden fingerprints.

All of this may be a small puzzle piece in a much larger picture which reveals the characteristic spectral features of molecules on earth as well as in space. This work can be seen as one very small but important step in deciphering astronomical spectra close to the confusion limit and therefore in understanding the complexity of molecules in the ISM. To express this in a provocative sentence: Ultimately, it might help to better understand the evolution of life, starting from the big bang to modern life as we know it.

2 Theory of Molecular Spectroscopy

”[...] auf dass du weiter gerne an Symmetrie denkst!”

- Hanno Schmiedt -

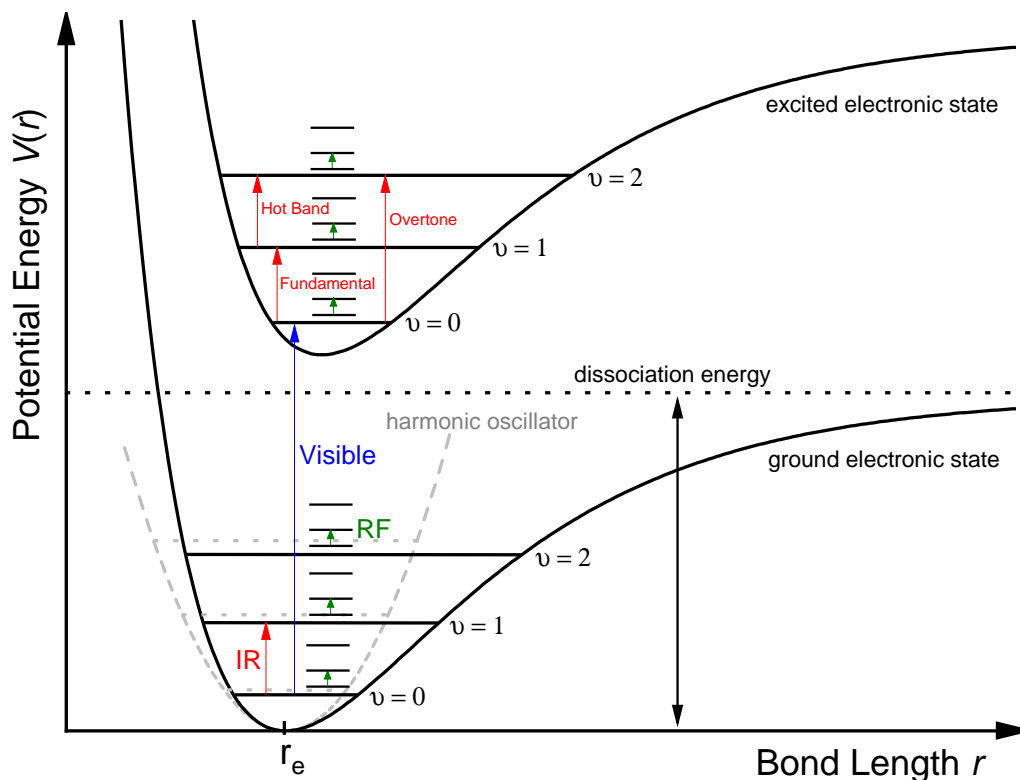


Figure 6: Schematic potential energy function of a diatomic molecule related to the bond length r . Selected electronic, vibrational, and rotational transitions between respective energy states are shown in blue, red, and green, respectively.

The theoretical description of molecules, in particular of their electronic, vibrational, or rotational configurations, are filling a multitude of books. A schematic overview of the resulting energy states of a diatomic molecule and their interplay is visualized in Fig. 6. In the harmonic approximation, the potential function is a parabola and the quantized energy levels E_v can be calculated by

$$E_v = \hbar\omega \left(v + \frac{1}{2} \right) \quad (2.1)$$

with their vibrational quantum number v and the fundamental vibrational frequency ω . The different length of the colored arrows can be translated to different wavelength regions, indicating the broad coverage of the electromagnetic spectrum for spectroscopic molecular fingerprints (cf. Fig. 1). This chapter concentrates on the phenomena and characteristics of rotationally resolved fingerprints of complex molecules, both in

rotational (RF) and ro-vibrational (IR) spectra. The basic description of molecules, why molecules form bonds and why they look the way they look, in particular a basic knowledge of the electronic and vibrational configuration of the molecule is assumed to be familiar to the reader. Important details and applications from theory, with an essential influence to observed phenomena in this work, are brought to the readers attention. Therefore, a detailed knowledge of the electronic and vibrational part is not crucial to understand phenomena explained in this thesis. This mainly results from the fact, that the electronic, vibrational, and rotational energies differ strongly in most molecules. Resulting from the Born–Oppenheimer approximation, based on the assumption that the motion of electrons and nuclei can be treated separately, the total wave function of the molecule can be written as a product

$$\Psi_{total} = \Psi_{el} \cdot \Psi_{vib} \cdot \Psi_{rot} \cdot \Psi_{ns} \quad (2.2)$$

of electronic, vibrational, rotational, and nuclear spin wave functions. This allows for solving the Schrödinger equation

$$\hat{\mathcal{H}}_i \Psi_i = E_i \Psi_i \quad (2.3)$$

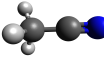
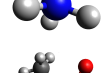
to a first approximation for each wave function separately. A direct consequence based on this assumption is, that the energy of a molecule is a simple sum of its different parts. For this reason, in a first step, the pure electronic and vibrational wave functions of the molecule are simply considered to be unimportant or known, simplifying the mathematical treatment to solve the problem of pure rotational wave functions (Sec. 2.1), as nuclear spin wave functions can be neglected. Followed by a rough overview of the treatment of vibrational wave functions (Sec. 2.2), necessary to interpret the FIR spectra. Indeed, some perturbative treatments for non negligible interactions between rotation and vibration as well as between light and matter need to be considered for a complete understanding of the observed spectra (Secs. 2.3 and 2.4). An informative overview, but often not exceeding a rather qualitative description, of the theory can be found in the book by P. Bernath [4]. Furthermore, the following theoretical discussions, derived equations, and formalisms, can be found to a large extend in several textbooks dealing with rotational spectroscopy [4, 5, 51, 52]. If not stated explicitly, the explanations given in this chapter can be found in the book by W. Gordy and R. L. Cook [51]. The reader is also referred to this work for a much more detailed mathematical derivation, as will be presented within the scope of this thesis.

2.1 Pure Rotational Hamiltonians

In this section, fundamental explanations of various pure rotational Hamiltonians are summarized. This is done in some detail, even though the whole theory is described

in much greater detail in Ref. [51] and not all presented Hamiltonians are needed to analyze molecular fingerprints of propanal. However, the origin of specific patterns, which play a key role in the analysis of molecular spectra of propanal, is clarified in detail. The reader, who is familiar with the concepts of rotational spectroscopy of different classes of molecules, may directly skip to Sec. 2.1.3.c on page 21, from there on explanations with special significance for deciphering molecular fingerprints of propanal are presented.

The unique rotational fingerprint of each molecule is a direct consequence of their different structural configurations, defined by their atomic masses, bond lengths and angles. The inertia tensor \mathbf{I} of a molecule is a 3×3 matrix, depending on the three space coordinates of each atom and their masses. The inertia tensor can always be diagonalized to a molecular-fixed principal axis system (x , y , and z), where all off-diagonal terms are zero. Typically, the z -axis denotes the axis having the highest order of rotational symmetry and the x -axis is defined for planar molecules as coinciding with the out-of-plane axis. Further on, the principal axes are labeled with a , b , and c , leading to six possible correlations between the axis systems, see Table A6. Based on a convention in spectroscopy, the three principle axes of inertia are ordered as $I_a \leq I_b \leq I_c$. In this way, molecules are separated in different classes based on their moments of inertia:

- Linear rotor: $I_a = 0, I_b = I_c$, e.g. carbonyl sulfide 
- Spherical symmetric-top rotor: $I_a = I_b = I_c$, e.g. methane 
- Prolate symmetric-top rotor: $I_a < I_b = I_c$, e.g. acetonitrile 
- Obate symmetric-top rotor: $I_a = I_b < I_c$, e.g. ammonia 
- Asymmetric-top rotor: $I_a < I_b < I_c$, e.g. propanal 

For solving Eq. (2.3), first the Hamiltonian of a molecule needs to be set up. The rotational energy of a molecule is classically given by

$$E_{rot} = \frac{1}{2}I_a\omega_a^2 + \frac{1}{2}I_b\omega_b^2 + \frac{1}{2}I_c\omega_c^2 \quad (2.4a)$$

$$= \frac{J_a^2}{2I_a} + \frac{J_b^2}{2I_b} + \frac{J_c^2}{2I_c} \quad (2.4b)$$

with ω_i being the angular frequency components and J_i being the components of the total angular momentum vector \vec{J} . By translating the classical angular momenta to the quantum mechanical angular momentum operator conjugates \hat{J}_i , the rigid rotor

Hamiltonian $\hat{\mathcal{H}}_{rr}$ is already set up. In general, the pure rotational Hamiltonian $\hat{\mathcal{H}}_{rot}$ is set up as the sum of a rigid rotor part and a perturbative treatment of the effects of centrifugal distortion $\hat{\mathcal{H}}_{cd}$, as the bond length and angles are changing when molecules rotate faster

$$\hat{\mathcal{H}}_{rot} = \hat{\mathcal{H}}_{rr} + \hat{\mathcal{H}}_{cd}. \quad (2.5)$$

The centrifugal distortion part of Eq. (2.5) can be expressed in a first order approximation as

$$\hat{\mathcal{H}}_{cd} = \frac{1}{4} \sum_{\alpha, \beta, \gamma, \delta} \tau_{\alpha\beta\gamma\delta} \hat{J}_\alpha \hat{J}_\beta \hat{J}_\gamma \hat{J}_\delta \quad (2.6)$$

where $\alpha, \beta, \gamma, \delta$ can take on the values x, y, z and the centrifugal distortion constants are given by

$$\tau_{\alpha\beta\gamma\delta} = -\frac{1}{2} \sum_{ij} \mu_{\alpha\beta}^{(i)} (f^{-1})_{ij} \mu_{\gamma\delta}^{(j)}. \quad (2.7)$$

The centrifugal distortion constants of a molecule are dependent on $3N - 6$ independent internal displacement coordinates i and j ($3N - 5$ for linear molecules), as the displacements are dependent on the potential energy surface. Thus the influence of all their contributions needs to be summed up. The centrifugal distortion constants are naturally depending on the inverse of the force constants matrix in regard to the displacement coordinates, its elements given by $(f^{-1})_{ij}$, and on the elements of the partial derivative of the reciprocal moment of inertia tensor, given by $\mu_{\alpha\beta}^{(i)}$. The inverse moment of inertia tensor $\mu_{\alpha\beta}$ is depending on the internal displacement coordinates as the molecule is no longer assumed to be rigid. Typically, it is approximated by a series expansion. Centrifugal distortion constants provide direct information on the shape of the potential energy surface itself.

The eigenvalues of the Hamiltonian in Eq. (2.5) represent the rotational energy levels of the molecule. Therefore, the influence of the Hamiltonian on the eigenfunctions of such a system needs to be analyzed. In fact, for this problem, the eigenfunctions do not have to be known explicitly, as the effect of the angular momentum operators can be directly, and more conveniently, derived from their commutation rules, see Eqs. (A1a)-(A1l) in the Appendix. The rotational constants are defined as $X_i = \hbar^2/2I_i$, with $i = x, y$, and z . Thereby, the rotational constants are typically presented as $X_i = A, B$, and C , by applying Table A6.⁵ A direct consequence of Heisenberg's uncertainty principle is that not all three components of the angular momentum can be determined at the same

⁵The SI unit of the rotational constants is Joule. In spectroscopy, the value is typically reported in MHz with $X_i[\text{MHz}] = 10^{-6}h/(8\pi^2I_i)$, via $E = h\nu$. In general, spectroscopic parameters are depending on the observed vibrational state v . A subscript v is omitted in the following for clarity.

time, excluding an analytical solution for asymmetric-top rotors. However, solving the pure rotational Hamiltonian for linear molecules (Sec. 2.1.1) is a backbone of the solutions for both symmetric-top rotors (Sec. 2.1.2). Here, analytical solutions of field-free, in particular no external electric nor magnetic fields are applied to the observed system, pure rotational Hamiltonians for these rotors are introduced. These are finally leading to an understanding of the complex rotational fingerprints of asymmetric rotor molecules (Sec. 2.1.3), like propanal.

2.1.1 Linear Molecules

The moment of inertia of the rotation around the molecular axis is zero, $I_a = 0$, for linear molecules. In addition, the rotation around the other two axes, perpendicular to the molecular axis, are identical $I_b = I_c = I$. The rigid rotor Hamiltonian simplifies to $H_{rr} = \hat{J}^2/2I$. The operator \hat{J}^2 only has diagonal elements as nonvanishing matrix elements in the basis of wave functions $|J, M\rangle$,⁶ see. Eq. (A1a). There is only one axis of distortion which leads to the simple energy expression of

$$E = BJ(J+1) - D_J J^2(J+1)^2 + \dots \quad (2.8)$$

with D_J being the quartic centrifugal distortion constant. J is called the rotational quantum number (with $J \in \mathbb{N}$). The quartic centrifugal distortion constant D_J is always positive for linear molecules, leading to an effective lowering of the energy levels in comparison to the rigid rotor assumption especially for higher J values.

2.1.2 Symmetric-Top Molecules

Expressions for the prolate and oblate symmetric-top molecules can be derived in the same way. The rigid rotor Hamiltonian can now be rewritten as

$$\hat{\mathcal{H}}_{rr}^{(prolate)} = \frac{1}{2I_b} \hat{j}^2 + \left(\frac{1}{2I_a} - \frac{1}{2I_b} \right) \hat{J}_a^2 \quad (2.9a)$$

$$\hat{\mathcal{H}}_{rr}^{(oblate)} = \frac{1}{2I_b} \hat{j}^2 + \left(\frac{1}{2I_c} - \frac{1}{2I_b} \right) \hat{J}_c^2 \quad (2.9b)$$

where the symmetry axis z is designated to the a - and c -axis for prolate and oblate rotors, respectively. The axis of rotation, or the orientation of \hat{J} , does not need to be perpendicular to the symmetry axis anymore, as it is the case for linear molecules, thus the effect of \hat{J}_z^2 has to be examined, see. Eq. (A1c). Given that \hat{J} commutes

⁶Thereby, M is the quantum number of the projection of \hat{J} onto the space-fixed axes system. As no external electric or magnetic fields are applied, it results in a $(2J+1)$ -degeneracy of energy levels and is not of further interest for deriving energy expressions.

with \hat{J}_z , the Hamiltonian is still diagonal, now in the basis of $|J, K, M\rangle$. For describing the energy levels of symmetric-top molecules, the additional quantum number K is describing the projection of \hat{J} onto the molecular-fixed symmetry axis.

The labeling K_a and K_c of the K quantum number is introduced to differentiate between the prolate and oblate case, respectively. This becomes particularly useful for labeling asymmetric rotor levels later on. The energy levels are given by

$$E = BJ(J + 1) + (A - B)K_a^2 - D_J J^2(J + 1)^2 - D_{JK} J(J + 1)K_a^2 - D_K K_a^4 + \dots \quad (2.10a)$$

$$E = BJ(J + 1) + (C - B)K_c^2 - D_J J^2(J + 1)^2 - D_{JK} J(J + 1)K_c^2 - D_K K_c^4 + \dots \quad (2.10b)$$

Note that, in the rigid rotor assumption, rotational levels with $K_a = 0$ and $K_c = 0$ have the same energies as for the linear molecule, assuming an identical rotational constant B for all three types of molecules, see Fig. 7.

2.1.3 Asymmetric-Top Molecules

The rotational Hamiltonian of asymmetric-top molecules needs to take into account three different nonzero moments of inertia, hindering a closed analytical solution. In particular, none of the projections onto the principal axes is conserved. Therefore K is not a good quantum number anymore. By creating the asymmetric-top wave functions as linear combinations of the limiting symmetric cases, 'quasi-good' pseudo quantum numbers K_a and K_c are introduced. Allowed combinations for energy levels are $K_a + K_c = J$ or $K_a + K_c = J + 1$. From here on, simply called the J and $J + 1$ asymmetry side, respectively. The splitting of energy levels with identical J and K_a is called the asymmetry splitting for prolate rotors. The correlation for labeling the energy levels is schematically shown in Fig. 7. A quantitative solution may be found, by starting to reformulate the rotational Hamiltonian to

$$\hat{\mathcal{H}}_{rr} = \frac{1}{2}(A + C)\hat{J}^2 + \frac{1}{2}(A - C)(\hat{J}_a^2 + \kappa\hat{J}_b^2 - \hat{J}_c^2) \quad (2.11)$$

where κ is Ray's asymmetry parameter, a measure for the asymmetry of molecules, defined as

$$\kappa = \frac{2B - A - C}{A - C}. \quad (2.12)$$

For the prolate symmetric-top limit it takes the value $\kappa = -1$ and for the oblate case it is $\kappa = +1$. The most asymmetric configuration of a rotor is determined by $\kappa = 0$.

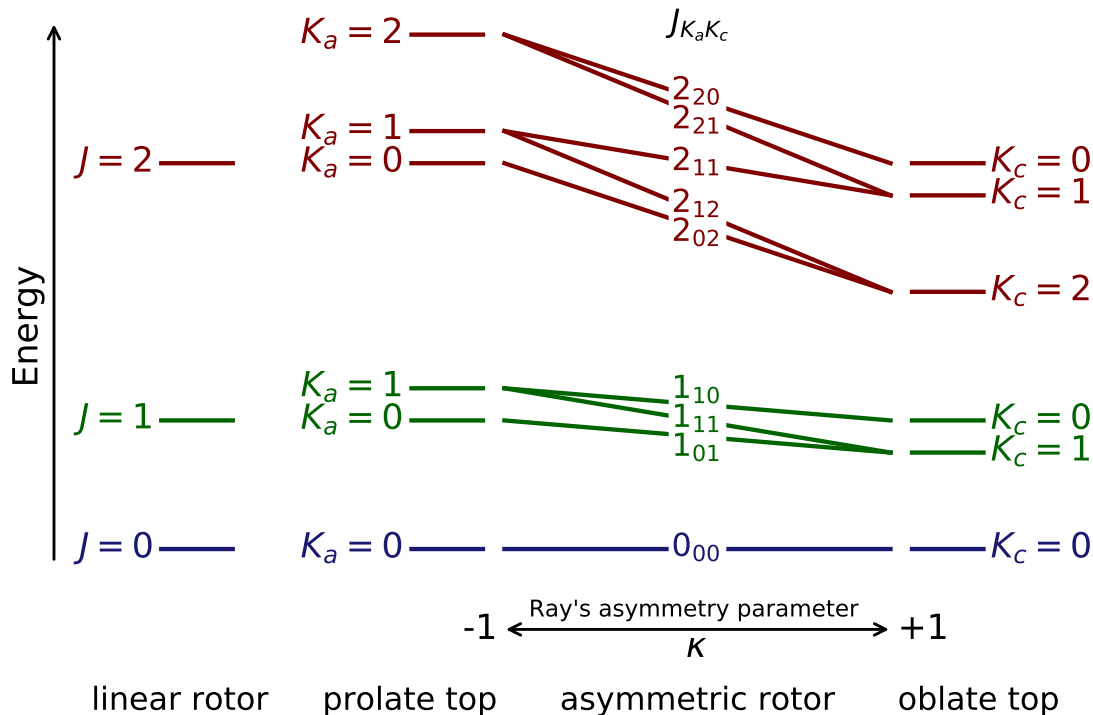


Figure 7: Schematic correlation diagram for labeling asymmetric rotor energy levels. Prolate and oblate symmetric rotors are limiting cases, as described by Ray's asymmetry parameter defined in Eq. (2.12). Energy levels with identical quantum number J are shown in the same color. Note that for rigid rotors and for same J quantum numbers, the energy levels of linear molecules are identical to prolate and oblate symmetric rotors, with $K_a = 0$ and $K_c = 0$, respectively.

Again, the angular momenta matrix elements need to be known, see Eqs. (A1a)-(A1l). This time, also resulting in off-diagonal entries. Finally, the energy levels are derived by solving the secular determinant ($|\hat{\mathcal{H}} - \mathbb{1}E| = 0$). For setting up the Hamiltonian a thoughtful choice of the representation is advisable, see Table A6. The best diagonalization routine is thereby also depending on the asymmetry of the molecule, compare to Eq. (2.12). In general, there are different ways to simplify or speed up this diagonalization process. As there are no off-diagonal terms with respect to J , for each value of J the secular determinant can be solved separately. For each J , the dimension of the secular determinant is a $2J + 1$ squared matrix. Further on, as the rigid rotor Hamiltonian is invariant under the operations of the Four group, see Table A7, it has its symmetry.⁷ Consequently, the secular determinant of each J can be factorized into four independent determinable subdeterminants, called the Wang-subblocks. The symmetry of an asymmetric rotor level is given by the evenness (e) or oddness (o) of

⁷The symmetric rotor wave functions do not belong to the Four-group, but linear combinations of symmetric rotor wave functions introduced by Wang belong to the Four-group [53].

K_a and K_c .

Unfortunately, a closed analytical form of the centrifugal distortion effects from Eq. (2.5) can not be derived either. However, the centrifugal distortion effects of a large number of molecules can be treated as first-order perturbations [54]. Later, Watson introduced a reduced Hamiltonian for fitting rotationally resolved spectra [55, 56]. In general, the Hamiltonian in Eq. (2.5) can be rewritten in the standard form [56] as

$$\hat{\mathcal{H}}_{st} = \sum_{p,q,r=0}^{\infty} h_{pqr} (\hat{J}_x^p \hat{J}_y^q \hat{J}_z^r + \hat{J}_z^r \hat{J}_y^q \hat{J}_x^p). \quad (2.13)$$

As the Hamiltonian is invariant to the operation of time reversal and to the Hermitian conjugation only even values of $n = p+q+r$, the degree of the total angular momentum, are allowed. Also following that, the coefficients h_{pqr} are real. For molecules with orthorhombic symmetry, and to a first approximation for all others, p , q , and r need to be even as well [56]. The standard Hamiltonian, Eq. (2.13), can be brought to a form

$$\hat{\mathcal{H}}_{rot} = \hat{\mathcal{H}}_{rr}^{(2)} + \sum_{n \geq 4} \hat{\mathcal{H}}_{cd}^{(n)} \quad (2.14)$$

which is comparable to Eq. (2.5), with n being even. For $n = 2$ and 4 this leads to 3 and 6 possible terms for the rotational constants and quartic centrifugal distortion constants, respectively. For the latter ones, it was observed that there is an indeterminacy in fitting uniquely all 6 constants to experimental data. A further linear relation of the commutation relation was found to solve this problem and reducing the quartic centrifugal distortion constants to 5 [55].

2.1.3.a Watson's A Reduction

For empirical fitting and ensuing simulation of rotational spectra, more precisely of rotational energy levels, Watson proposed a reduced Hamiltonian $\hat{\mathcal{H}}_{red}$ in 1966 [55], which was derived in more detail one year later [56] and has the form of Eq. (2.14). The centrifugal distortion terms consists of $(n + 1)$ determinable parameters. Here, basically the parameters of the ladder operators are set to zero. Pleasingly, all diagonal components in a symmetric-top basis fulfill $\Delta K = 0$ and all off-diagonal $\Delta K = \pm 2$. This trigonal form is comparable to the rigid rotor, compare to Eq. (2.11) with the use of Eq. (A1). The same methods for diagonalizing the secular determinant as explained before can be adopted. The lowest order terms with n up to 10 from Eq. (2.14) are of

the following explicit form

$$\hat{\mathcal{H}}_{rr}^{(2)} = \left(\frac{B_x + B_y}{2} \right) \hat{J}^2 + \left(B_z - \frac{B_x + B_y}{2} \right) \hat{J}_z^2 + \left(\frac{B_x - B_y}{2} \right) (\hat{J}_x^2 - \hat{J}_y^2) \quad (2.15a)$$

$$\begin{aligned} \hat{\mathcal{H}}_{cd}^{(4)} = & \Delta_J \hat{J}^4 - \Delta_{JK} \hat{J}^2 \hat{J}_z^2 - \Delta_K \hat{J}_z^4 \\ & - 2\delta_J \hat{J}^2 (\hat{J}_x^2 - \hat{J}_y^2) - \delta_K \left[\hat{J}_z^2 (\hat{J}_x^2 - \hat{J}_y^2) + (\hat{J}_x^2 - \hat{J}_y^2) \hat{J}_z^2 \right] \end{aligned} \quad (2.15b)$$

$$\begin{aligned} \hat{\mathcal{H}}_{cd}^{(6)} = & \Phi_J \hat{J}^6 + \Phi_{JK} \hat{J}^4 \hat{J}_z^2 + \Phi_{KJ} \hat{J}^2 \hat{J}_z^4 + \Phi_K \hat{J}_z^6 \\ & + 2\phi_J \hat{J}^4 (\hat{J}_x^2 - \hat{J}_y^2) + \phi_{JK} \hat{J}^2 [\hat{J}_z^2 (\hat{J}_x^2 - \hat{J}_y^2) + (\hat{J}_x^2 - \hat{J}_y^2) \hat{J}_z^2] \\ & + \phi_K [\hat{J}_z^4 (\hat{J}_x^2 - \hat{J}_y^2) + (\hat{J}_x^2 - \hat{J}_y^2) \hat{J}_z^4] \end{aligned} \quad (2.15c)$$

$$\begin{aligned} \hat{\mathcal{H}}_{cd}^{(8)} = & L_J \hat{J}^8 + L_{JJK} \hat{J}^6 \hat{J}_z^2 + L_{JK} \hat{J}^4 \hat{J}_z^4 + L_{KKJ} \hat{J}^2 \hat{J}_z^6 + L_K \hat{J}_z^8 \\ & + 2l_J \hat{J}^6 (\hat{J}_x^2 - \hat{J}_y^2) + l_{JK} \hat{J}^4 [\hat{J}_z^2 (\hat{J}_x^2 - \hat{J}_y^2) + (\hat{J}_x^2 - \hat{J}_y^2) \hat{J}_z^2] \\ & + l_{KJ} \hat{J}^2 [\hat{J}_z^4 (\hat{J}_x^2 - \hat{J}_y^2) + (\hat{J}_x^2 - \hat{J}_y^2) \hat{J}_z^4] + l_K [\hat{J}_z^6 (\hat{J}_x^2 - \hat{J}_y^2) + (\hat{J}_x^2 - \hat{J}_y^2) \hat{J}_z^6] \end{aligned} \quad (2.15d)$$

$$\begin{aligned} \hat{\mathcal{H}}_{cd}^{(10)} = & P_J \hat{J}^{10} + P_{JJK} \hat{J}^8 \hat{J}_z^2 + P_{JK} \hat{J}^6 \hat{J}_z^4 + P_{KJ} \hat{J}^4 \hat{J}_z^6 + P_{KKJ} \hat{J}^2 \hat{J}_z^8 + P_K \hat{J}_z^{10} \\ & + 2p_J \hat{J}^8 (\hat{J}_x^2 - \hat{J}_y^2) + p_{JJK} \hat{J}^6 [\hat{J}_z^2 (\hat{J}_x^2 - \hat{J}_y^2) + (\hat{J}_x^2 - \hat{J}_y^2) \hat{J}_z^2] \\ & + p_{JK} \hat{J}^4 [\hat{J}_z^4 (\hat{J}_x^2 - \hat{J}_y^2) + (\hat{J}_x^2 - \hat{J}_y^2) \hat{J}_z^4] + p_{KJ} \hat{J}^2 [\hat{J}_z^6 (\hat{J}_x^2 - \hat{J}_y^2) + (\hat{J}_x^2 - \hat{J}_y^2) \hat{J}_z^6] \\ & + p_K [\hat{J}_z^8 (\hat{J}_x^2 - \hat{J}_y^2) + (\hat{J}_x^2 - \hat{J}_y^2) \hat{J}_z^8] \end{aligned} \quad (2.15e)$$

and are presented as they are required to model the spectra of *syn*-propanal to experimental uncertainty within this work.

2.1.3.b S Reduction

Watson's A reduction has some limitations, especially when two rotational constants are almost equal, as was already stated in one of his research publications [56]. In other words, problems are occurring for slightly asymmetric molecules, which are close to the prolate or oblate limit. A new approach to describe the energy levels of a molecule extremely close to the symmetric-top limit has been utilized by Winnewisser in 1972 [57]. The splitting for energy levels with $K_a = 1, 2$ of the doubly deuterated species of hydrogen disulfide DSSD ($\kappa = -0.99999934$) was observed to be dominated by the centrifugal distortion splitting, in contrast to the asymmetry splitting. Nearly two years later van Eijck reformulated the reduced Hamiltonian [58]. This time, basically the parameters of the K -dependent operators are set to zero, in particular not the ladder ones as in Watson's A reduction. The so called S reduction is similar to Watson's A reduction of the form in Eq. (2.14), but with the lowest order terms up to $n = 10$

given by

$$\hat{\mathcal{H}}_{rr}^{(2)} = \left(\frac{B_x + B_y}{2} \right) \hat{J}^2 + \left(B_z - \frac{B_x + B_y}{2} \right) \hat{J}_z^2 + \left(\frac{B_x - B_y}{4} \right) (\hat{J}_+^2 + \hat{J}_-^2) \quad (2.16a)$$

$$\begin{aligned} \hat{\mathcal{H}}_{cd}^{(4)} = & -D_J \hat{J}^4 - D_{JK} \hat{J}^2 \hat{J}_z^2 - D_K \hat{J}_z^4 \\ & + d_1 \hat{J}^2 (\hat{J}_+^2 + \hat{J}_-^2) + d_2 (\hat{J}_+^4 + \hat{J}_-^4) \end{aligned} \quad (2.16b)$$

$$\begin{aligned} \hat{\mathcal{H}}_{cd}^{(6)} = & H_J \hat{J}^6 + H_{JK} \hat{J}^4 \hat{J}_z^2 + H_{KJ} \hat{J}^2 \hat{J}_z^4 + H_K \hat{J}_z^6 \\ & + h_1 \hat{J}^4 (\hat{J}_+^2 + \hat{J}_-^2) + h_2 \hat{J}^2 (\hat{J}_+^4 + \hat{J}_-^4) + h_3 (\hat{J}_+^6 + \hat{J}_-^6) \end{aligned} \quad (2.16c)$$

$$\begin{aligned} \hat{\mathcal{H}}_{cd}^{(8)} = & L_J \hat{J}^8 + L_{JJK} \hat{J}^6 \hat{J}_z^2 + L_{JK} \hat{J}^4 \hat{J}_z^4 + L_{KKJ} \hat{J}^2 \hat{J}_z^6 + L_K \hat{J}_z^8 \\ & + l_1 \hat{J}^6 (\hat{J}_+^2 + \hat{J}_-^2) + l_2 \hat{J}^4 (\hat{J}_+^4 + \hat{J}_-^4) + l_3 \hat{J}^2 (\hat{J}_+^6 + \hat{J}_-^6) + l_4 (\hat{J}_+^8 + \hat{J}_-^8) \end{aligned} \quad (2.16d)$$

$$\begin{aligned} \hat{\mathcal{H}}_{cd}^{(10)} = & P_J \hat{J}^{10} + P_{JJK} \hat{J}^8 \hat{J}_z^2 + P_{JK} \hat{J}^6 \hat{J}_z^4 + P_{KJ} \hat{J}^4 \hat{J}_z^6 + P_{KKJ} \hat{J}^2 \hat{J}_z^8 + P_K \hat{J}_z^{10} \\ & + p_1 \hat{J}^8 (\hat{J}_+^2 + \hat{J}_-^2) + p_2 \hat{J}^6 (\hat{J}_+^4 + \hat{J}_-^4) + p_3 \hat{J}^4 (\hat{J}_+^6 + \hat{J}_-^6) \\ & + p_4 \hat{J}^2 (\hat{J}_+^8 + \hat{J}_-^8) + p_5 (\hat{J}_+^{10} + \hat{J}_-^{10}) \end{aligned} \quad (2.16e)$$

which are presented as they are required to model the spectra of *gauche*-propanal to experimental uncertainty within this work. \hat{J}_+ and \hat{J}_- are lowering and raising operators defined by $\hat{J}_\pm = \hat{J}_x \pm i\hat{J}_y$, respectively.

2.1.3.c Selection Rules

The strongest rotational lines are arising from the coupling of the electric dipole moment components of most (polar) molecules with the radiation to induce transitions between two energy levels. However, not all transitions from an initial state Ψ_i to a final state Ψ_f are equally probable or even allowed. To derive selection rules, the dipole moment matrix elements

$$\langle f | \hat{\mu}_g | i \rangle = \int \Psi_f^* \hat{\mu}_g \Psi_i d\tau \quad (2.17)$$

need to be evaluated, for $g = a, b, c$. Naturally, the projections of the dipole moment components onto the molecule-fixed principal axes need to be nonvanishing. For this reason, **transitions are classified as a-, b-, or c-type transitions**. The selection rules for J and M for asymmetric-top rotors are given by

$$\Delta J = 0; \pm 1 \quad \Delta M = 0; \pm 1 \quad (2.18)$$

and those for the pseudo quantum numbers K_a and K_c are given in Table 1.

In spectroscopy, transitions of asymmetric rotor molecules are typically presented as $J_{K_a, K_c} = J'_{K'_a, K'_c} \leftarrow J''_{K''_a, K''_c}$ (absorption). Thereby, single primes relate to the quantum numbers of the upper energy levels, whereas double primes to the lower ones.

Table 1: Selection rules of asymmetric-top molecules for the quasi-good quantum numbers K_a and K_c . Transitions following selection rules in parentheses are increasingly less intense, in particular for nearly symmetric-top molecules.

name	dipole moment component	ΔK_a	ΔK_c	$K'_a K'_c \leftrightarrow K''_a K''_c$
<i>a</i> -type	μ_a	0 ($\pm 2, \pm 4, \dots$)	± 1 ($\pm 3, \pm 5, \dots$)	ee \leftrightarrow eo oo \leftrightarrow oe
<i>b</i> -type	μ_b	± 1 ($\pm 3, \pm 5, \dots$)	± 1 ($\pm 3, \pm 5, \dots$)	ee \leftrightarrow oo eo \leftrightarrow oe
<i>c</i> -type	μ_c	± 1 ($\pm 3, \pm 5, \dots$)	0 ($\pm 2, \pm 4, \dots$)	ee \leftrightarrow oe oo \leftrightarrow eo

Transitions obeying identical selection rules with sequential values in specific quantum numbers, while others might be fixed, are often referred to as series and play a very important role in unambiguously assigning rotational spectra, as is highlighted in Fig. 8 and demonstrated in Ch. 5. In the literature, series (also called branches) are often labeled as $^{\Delta K_a} \Delta J$, with the superscript letters p, q , and r for $\Delta K_a = -1, 0, +1$, respectively, as well as with P, Q , and R for $\Delta J = -1, 0$, and $+1$, respectively. In addition, the **two possible asymmetry sides**, $K_a + K_c = J$ or $K_a + K_c = J + 1$, are important to label certain series.

A variety of transitions obeying different selection rules is desirable for a proper description of the energy pattern, as from a single type of transitions, often, not all rotational constants can be determined to sufficient accuracy. For example, **${}^q R$ series** transitions (with $\Delta K_a = 0$ and $\Delta J = +1$) of nearly prolate rotors contain predominantly information of the B and C rotational constants. But the energy difference of different ${}^q R$ series is strongly dependent on the A rotational constant, see Fig. 8, which can only be poorly determined by measuring solely transitions of the ${}^q R$ series. For example, by measuring *c*-type transitions, which connect different ${}^q R$ series as is shown by the red lines in Fig. 8, this lack of information can be overcome and all constants can be determined. Typical **K_a structures**, made of *a*-type transitions of different ${}^q R$ series with identical J 's, of nearly prolate symmetric rotor molecules appear frequently in narrow frequency windows, see Fig. A6, as they are arising from the lifting of the $(2J + 1)$ K -degeneracy in asymmetric-top rotors, see the green transitions in Fig. 8.

Further obvious assignable patterns of series are originating in prolate and oblate paired energy levels. At low J values, energy levels of both asymmetry sides, in particular levels with the same K_a , may be blended. This is called **prolate pairing** (energies of J_{K_a, K_c+1} are equal to energies of J_{K_a, K_c}). A significant splitting of prolate pairs is observed if J increases until at even higher J **oblate pairing** of energy levels is observed. Here, energy levels with the same K_c are blended (energies of J_{K_a+1, K_c} are equal to energies of J_{K_a, K_c}). This is illustrated best in reduced energy diagrams, see Fig. 9. The reduced energy E_{red} of a rotational level with energy E is derived by

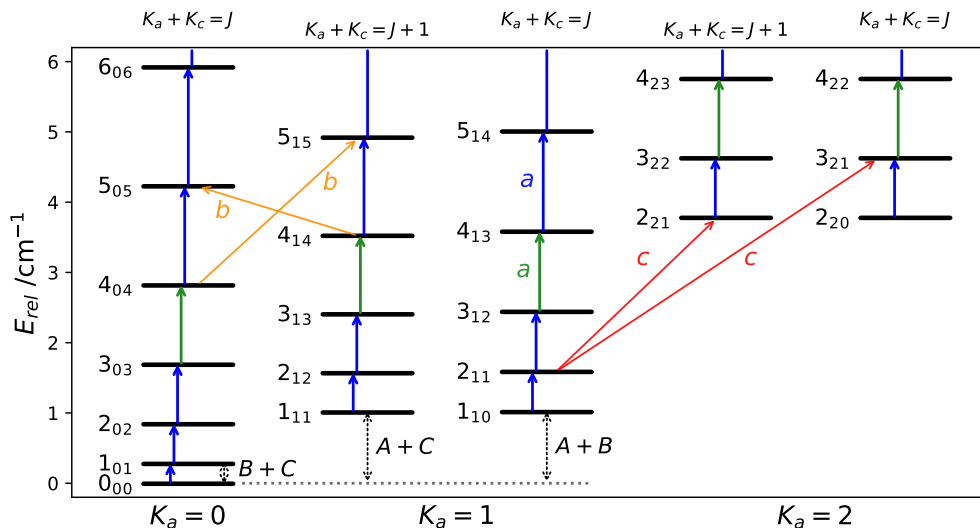


Figure 8: Schematic energy level diagram of a nearly prolate rotor molecule ($\kappa = -0.9849$). The energy levels are separated into different energy ladders in respect to their K_a quantum numbers and respective **asymmetry side** $K_a + K_c = J$ or $K_a + K_c = J + 1$. In this fashion, **qR series** are clearly seen by the **a-type transitions** within each ladder, indicated by the vertically adjacent blue and green arrows, see text for more information. Furthermore, the green arrows refer to a typical **K_a structure** with transitions $4_{K_a, K_c} \leftarrow 3_{K_a, K_c-1}$. K_a structures appear in small frequency windows for near prolate rotors. Two example **b- and c-type transitions** are shown in orange and red, respectively, to highlight the possibility of linking different energy ladders. Of course there are many more allowed transitions which are not shown here for the sake of clarity (cf. Table 1).

$$E_{red} = E - E_{vib} - J(J+1)(B+C)/2. \quad (2.19)$$

Usually the energy of the vibrational state is set to zero, simply by subtraction of its energy E_{vib} . The reduced energy E_{red} of tunneling states of *gauche*-propanal is derived by setting E_{vib} to the energy of the vibrational ground state energy of *gauche*-propanal E_g , i.e. $E_{vib} = E_g$, when the vibrational ground state energy of *syn*-propanal is set to zero, i.e. $E_s = 0 \text{ cm}^{-1}$. Notice that rigid rotor symmetric-top molecules would show parallel lines to the x -axis for energy levels with the same K_a in reduced energy diagrams, see Eqs. (2.10) and (2.19). In Fig. 8, an oblate pairing would occur between vertical energy level ladders directly next to each other and differing by one in K_a . For example, the two *b*-type transitions shown in orange and the two *a*-type transitions in blue, which form a **closed loop of transitions** in Fig. 8, would have all the same frequency if the energy levels $4_{0,4}$ and $4_{1,4}$ as well as $5_{0,5}$ and $5_{1,5}$ would be oblate paired. In this case the four transitions are blended in the spectrum and only a

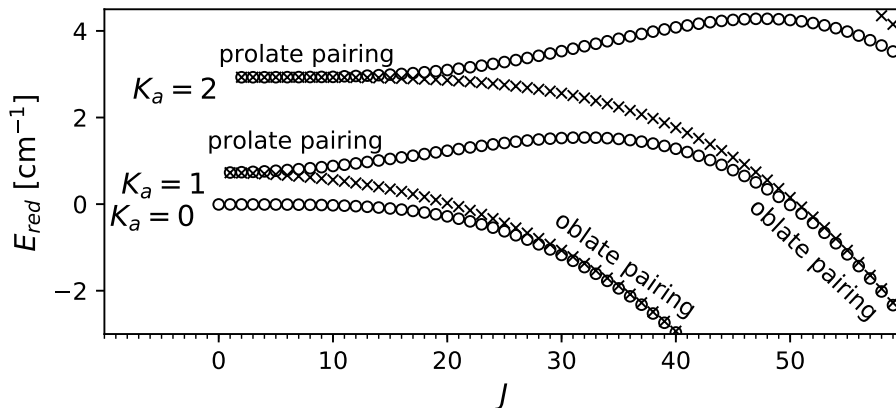


Figure 9: Reduced energy diagram of a nearly prolate rotor molecule ($\kappa = -0.9849$), see Eq. (2.19). The plotted energies are calculated from quantum mechanical models derived within this thesis and energy levels belonging to the **asymmetry side** $K_a + K_c = J$ are marked by a circle ('o'), whereas $K_a + K_c = J + 1$ levels are marked with a cross ('x') in all presented reduced energy diagrams. **Prolate or oblate pairing** is observed if the energy of J_{K_a, K_c} is equal to the one of J_{K_a, K_c+1} or J_{K_a+1, K_c} , respectively.

single line is observed. In general, the **quartet of lines**⁸ (b -, a -, a -, b -type pattern; i: $J_{K_a, J-K_a} \leftarrow (J-1)_{K_a+1, J-K_a-1}$; ii: $J_{K_a+1, J-K_a} \leftarrow (J-1)_{K_a+1, J-K_a-1}$; iii: $J_{K_a, J-K_a} \leftarrow (J-1)_{K_a, J-K_a-1}$; iv: $J_{K_a+1, J-K_a} \leftarrow (J-1)_{K_a, J-K_a-1}$) is a typical fingerprint for molecules with an a - and b -type spectrum, see Fig. A5, hence for all vibrational states of *syn*-propanal, due to its two rather strong dipole moment components $\mu_a = 1.71$ D and $\mu_b = 1.85$ D [39]. As an example, this rotational fingerprint was the first successful assignment of 2-cyanobutane, see Fig. 3 of Ref. [59].

2.1.3.d Parity Selection Rules

Parity selection rules are derived by identifying properties of symmetry operations onto the wave functions and their resulting effect on the dipole moment matrix elements, compare to Eq. (2.17). Every symmetry operation is either not changing the overall wave function at all or only its sign. In general, the integrals from Eq. (2.17) cannot change their sign, if they are nonzero, as they are definite integrals. If the sign of μ_i is unchanged (changed) by applying a symmetry operation, the eigenfunctions Φ_i and Φ_j need to have the same (different) parity.

These considerations play an important role when vibration-rotation interactions need to be taken into account. If a molecule, such as *gauche*-propanal, exists in a left- and

⁸The quartet of lines is labeled only with its K_a 's in the course of this thesis for simplicity:

i: b -type $K_a \leftarrow K_a + 1$; ii: a -type $K_a + 1 \leftarrow K_a + 1$; iii: a -type $K_a \leftarrow K_a$; iv: b -type $K_a + 1 \leftarrow K_a$

in a right-handed configuration, with a small potential barrier between the two configurations, inversion doublets appear, which originate in the X^+ and X^- substates introduced in Sec. 1.3 and explained in somewhat more detail in Sec. 2.4. Considering now a reflection plane, spanned by the a - and b -axis of *syn*-propanal, see Fig. 4, transposing the two possible *gauche* configurations into each other, the parity selection rules for the two substates of *gauche*-propanal can be derived with the help of the C_s character table (cf. Table A9). The signs of μ_a and μ_b are unchanged upon this symmetry operation, whereas μ_c changes its sign, see also Fig. 4. That is why a - and b -type transitions occur within X^+ and X^- substates ($X^+ \leftrightarrow X^+$ and $X^- \leftrightarrow X^-$), while c -type transitions occur between the two substates ($X^+ \leftrightarrow X^-$).

2.1.3.e Line Intensities

The probability of absorbing a photon is the product of the spectral energy density and the Einstein B coefficient. In turn, the Einstein B coefficient is proportional to the sum of the three squared matrix elements of the electric dipole moment component of the molecule, with the matrix elements given by Eq. (2.17). Naturally the line intensity is not only dependent on the probability of absorbing a photon, but also on the number of particles present in a state m . The fraction of particles in each state N_m in comparison to the total number of particles N per unit volume can be calculated with

$$F_m = \frac{N_m}{N} = \frac{g_m e^{-E_m/(k_B T)}}{\sum_i g_i e^{-E_i/(k_B T)}} = \frac{g_m e^{-E_m/(k_B T)}}{Q} \quad (2.20)$$

where Q is the partition function of a molecule. Obviously the fraction is dependent on all energy levels E_i of a molecule, based on Boltzmann's law in thermal equilibrium, and their degeneracies g_i .⁹ Determining the partition function Q is of fundamental importance for calculating absolute intensities and is, for example, inevitable for determining column densities of molecules in space.¹⁰ Finally, the absorption coefficient

⁹The degeneracy g_i of each level is a product of all underlying degeneracies.

¹⁰Note that for absolute line intensities the full partition function is a product of electronic, vibrational, rotational, and nuclear spin partition functions, see Eq. (2.2). Often closed shell molecules have a singlet Σ electronic ground state and can be considered to be solely populated in that ground state, thus $Q_{el} = 1$. The vibrational correction factor Q_{vib} is frequently, compare also to the CDMS [28–30], derived by an expansion of the fundamental modes to all their excited states in regard of the harmonic oscillator approximation, see Eq. (2.1). This can be approximated by using the geometric series to $Q_{vib} = \sum_i (1 - \exp(-h\omega_i/k_B T))^{-d_i}$, ω_i being the fundamental frequency and d_i being the degeneracy of the vibrational state. Q_{vib} can easily be larger than 10 for complex molecules with low-lying fundamental states and thus change absolute intensities by more than an order of magnitude. The rotational partition function of asymmetric rotor molecules can be approximated with $Q_{rot} = (5.34 \cdot 10^6 / \sigma) \sqrt{T^3 / (ABC)}$, where σ is a measure of the degree of symmetry and A , B , and C are in units of MHz and T is in units of K.

α_ν of a non-degenerate two-level system is given in thermal equilibrium by

$$\alpha_\nu = \frac{8\pi^3 N F_m \nu^2}{3ck_B T} \left(1 - \frac{h\nu}{2k_B T}\right) S(\nu, \nu_0) \sum_j |\langle f | \hat{\mu}_j | i \rangle|^2 \quad (2.21)$$

if spontaneous emission is neglected and $h\nu \ll k_B T$ is used for approximation of the Boltzmann factor. The resonance frequency of a photon is ν_0 . Line intensities calculated by the used analysis programs SPFIT/SPCAT and ERHAM, which will be introduced later, can be found in Eqs. (A4) and (A5). In fact, observed lines are broadened by different mechanisms, thus a normalized line shape function $S(\nu, \nu_0)$ needs to be considered as well to reproduce experimental spectra.

2.1.3.f Line Shapes

There are several mechanisms defining line shapes. Solely some of them are presented here, especially the most fundamental one and the ones essentially contributing to the line widths of observed transitions in this work.

The natural line width is arising from the possibility of spontaneous emission and is based on the uncertainty principle, $\Delta t \cdot \Delta E \geq \frac{\hbar}{2}$. As the lifetime of a molecule in a specific state is not infinite, the corresponding spread in the frequency domain leads to a broadening of the line which is described by a Lorentzian function. This fundamental effect can be neglected for the measurements conducted in this work.

Pressure Broadening is observed, as higher pressures in the cell lead to more frequent collisions of molecules, decreasing the aforementioned lifetime, resulting in a broader linewidth. Again, the line shape is described by a Lorentzian. This contributes only marginally to the observed line width for measurement pressures of some microbars at room temperature.

Doppler broadening is dominating the line width for observed transitions in this work. At room temperature, or generally speaking for all temperatures above 0 K, molecules have translational velocity components in all spatial directions following the Maxwell-Boltzmann distribution, in particular also parallel to the direction of propagation of the electromagnetic radiation. This leads, due to the Doppler effect, to the Doppler broadening. The resulting line shape is described by a Gaussian of the form

$$S_D(\nu, \nu_0) = A \cdot \exp \left\{ -\ln(2) \left(\frac{\nu - \nu_0}{\Delta\nu_D} \right)^2 \right\} \quad (2.22)$$

with normalization factor A (amplitude) and half width at half maximum (HWHM) $\Delta\nu_D$. In this work the linewidth is considered to be the full width at half maximum (FWHM) which is given by

$$2\Delta\nu_D = 2\nu_0 \sqrt{\frac{2Nk_B T \ln(2)}{Mc^2}} \approx 7.15 \cdot 10^{-7} \nu_0 \sqrt{\frac{T}{M}} \quad (2.23)$$

with absolute temperature T (in K) and the mass of the molecule M (in atomic mass units). The Doppler linewidth of propanal ($M = 58$ amu) at 300 GHz is predicted to be about 0.5 MHz.

A convolution of Lorentzian and Gaussian functions is called a Voigt profile and is observed if various broadening mechanisms are taken into account. Experimental techniques can also have a significant influence on the observed line shapes, see Sec. 3.1. Besides, there are more broadening mechanisms, which are all negligible for the experiments conducted in this work, such as power broadening, collisions of the molecules with the cell walls, and more.

2.2 Rotation-Vibration Hamiltonians

The theory for rotational spectroscopy can be simply transposed to a large extent to understand ro-vibrational fingerprints. It can be seen from Eq. (2.2) that in a first approximation the energies of vibrational and rotational degrees of freedom can simply be added. In particular, the energy levels can be found by solving the ro-vibrational Hamiltonian

$$\hat{\mathcal{H}}_{rovib} = \hat{\mathcal{H}}_{vib} + \hat{\mathcal{H}}_{rot} \quad (2.24)$$

which is the sum of vibrational and rotational Hamiltonians. In a first approximation the vibrational part simply adds an energy value for the vibrational state of interest (cf. Eq. (2.1)). The major difference is observed in deriving line intensities and consequently also selection rules for the vibrational degrees of freedom. In general, a N -atomic molecule has $3N - 6$ vibrational degrees of freedom ($3N - 5$ for linear molecules) each associated with a normal mode coordinate Q_i , as mentioned before. As the molecule is vibrating the structure is changed periodically and due to that the dipole moment as well. The dipole moment can be expressed by a Taylor series with

$$\mu = \mu_0 + \sum_{i=1}^{3N-6} \left(\frac{\partial \mu}{\partial Q_i} \right)_0 Q_i + \dots \quad (2.25)$$

Intensities can be derived with Eq. (2.17), but this time the integration is done over all normal modes. The initial and final wave functions of fundamental modes are orthogonal and therefore the integral with μ_0 is zero. First nonzero contributions are resulting from the dipole moment derivative. To a first approximation, fundamental vibrational transitions, transitions between the vibrational ground state ($v = 0$) and a first excited state ($v_i = 1$) are proportional to the square of the dipole moment derivative,

in contrast to the square of μ_0 itself in rotational spectroscopy (cf. Eq. (2.21)). Ro-vibrational transitions between similar vibrational states are called a band structure with P , Q , and R branches. For anharmonic potential surfaces and higher order terms of Eq. (2.25) the selection rules for the vibrational quantum number are $\Delta v = \pm 1$ (± 2 , ± 3 , ...). The numbers in parentheses are less likely. Selection rules of pure rotation are still valid (Sec. 2.1.3.c) and line shapes are again explained by the mechanisms introduced in Sec. 2.1.3.f. Ro-vibrational bands with transitions $v' \leftrightarrow v''$ are in addition to fundamental bands further categorized into hot bands ($\Delta v = \pm 1$ with $v' \neq 0$ and $v'' \neq 0$) and overtone bands ($|\Delta v| > 1$). Each of the aforementioned bands is represented for one selected transition in a diatomic molecule by the red arrows in Fig. 6.

Propanal consists of ten atoms leading to 24 different vibrational modes. The symmetry of a vibrationally excited state of *syn*-propanal is either A' for in-plane vibrations or A'' for out-of-plane vibrations, compare to the C_s point group in Table A9. The modes are labeled by v_i with $i = 1, 2, \dots, 24$. First numbers are reserved for vibrations with A' symmetry followed by A'' ones according to the Herzberg convention (*syn*-propanal: $\Gamma = 15A' \oplus 9A''$). Given that for in-plane vibrations of *syn*-propanal only μ_a and μ_b dipole moment components are changed, but not μ_c , an a/b -hybrid type spectrum is observed, whereas for out-of-plane vibrations a substantive c -type spectrum occurs. For both symmetries the highest mode number corresponds to the lowest energy. The CCC in-plane bending mode v_{15} is the energetically lowest A' vibration, whereas the aldehyde torsion v_{24} and the methyl torsion v_{23} are the two lowest out-of-plane vibrations. The labeling of vibrational states of *gauche*- is according to *syn*-propanal, but hybrid spectra arising from all dipole moment components may be considered as *gauche*-propanal has C_1 symmetry without tunneling.

2.3 Treatments of Perturbations in Molecular Spectroscopy

In Sec. 2.1 it was already shown that it can be reasonable to solve a quantum mechanical system by looking first at an unperturbed system with subsequent treatment of perturbations, see also Eq. (2.5). This procedure can be applied to several other effects, observable by means of rotational spectroscopy. For this reason a general treatment of a perturbed two-level system is introduced at first in Sec. 2.3.1. Subsequently different perturbations of rotational Hamiltonians, affecting the experimental data of this work, are presented in Secs. 2.3.2–2.3.5.

2.3.1 Two-Level Systems

Assuming that an unperturbed quantum mechanical two-level system is solved, described by its two eigenenergies E_1 and E_2 , the perturbed system is solved by writing

the full Hamiltonian of Eq. (2.3) as the sum of the unperturbed Hamiltonian $\hat{\mathcal{H}}^0$ and its perturbation $\hat{\mathcal{H}}^p$. Frequently, the basis functions are chosen to be the wave functions of the unperturbed system, $|\Phi_1\rangle$ and $|\Phi_2\rangle$, and linear combinations of them are describing the perturbed system. A solution of the perturbed system is regularly to be easier found by symmetrizing the problem with the help of $E = \frac{E_1+E_2}{2}$ and $\Delta = \frac{E_2-E_1}{2}$. By solving the perturbed Hamiltonian

$$\hat{\mathcal{H}} = \hat{\mathcal{H}}^0 + \hat{\mathcal{H}}^p = \begin{bmatrix} E_1 & 0 \\ 0 & E_2 \end{bmatrix} + \begin{bmatrix} 0 & V \\ V^* & 0 \end{bmatrix} = \begin{bmatrix} E_1 & V \\ V^* & E_2 \end{bmatrix} = \begin{bmatrix} E - \Delta & V \\ V^* & E + \Delta \end{bmatrix} \quad (2.26)$$

the eigenenergies

$$E^\pm = E \pm \sqrt{\Delta^2 + |V|^2} \quad (2.27)$$

and eigenstates

$$|\psi^-\rangle = \cos \Theta |\Phi_1\rangle + \sin \Theta |\Phi_2\rangle \quad (2.28a)$$

$$|\psi^+\rangle = -\sin \Theta |\Phi_1\rangle + \cos \Theta |\Phi_2\rangle \quad (2.28b)$$

with $\tan 2\Theta = \frac{-V}{\Delta}$ can be derived, with $0 \leq \Theta \leq \pi$. The perturbed Hamiltonian is diagonal in terms of this new basis set and the contributions are often referred as mixing coefficients, following $\sin^2 \Theta + \cos^2 \Theta = 1$. Another important quantity is derived by expanding and approximating the square root in Eq. (2.27) which leads to perturbed energies of

$$E^+ = E_2 + \frac{V^2}{2\Delta} \quad \text{and} \quad E^- = E_1 - \frac{V^2}{2\Delta}. \quad (2.29)$$

Thus it appears that the perturbation is getting larger, if the magnitude of interaction is increasing or the energy difference is getting smaller. Actually, the same result can be derived by second-order perturbation theory.

2.3.2 Rabi Cycle

The Rabi cycle reveals the nature of the population changes which makes the DR spectroscopy a versatile tool in the IR region and, more importantly, it is fundamental for deriving the Autler-Townes effect. For these reasons, basic ideas are shortly summarized here.

The Rabi cycle can be observed if an external electric field is applied to an initially unperturbed two-level system. Here, a time dependent perturbation $\hat{\mathcal{H}}^p = \mu_{21} E' \cos(\omega t)$

is originating from the coupling of the electric field E' of the polarized electromagnetic radiation with frequency ω to the transition dipole moment μ_{21} of the two-level system. The detuned Rabi frequency $\Omega = \sqrt{\omega_R^2 + \delta^2}$ is defined by the Rabi frequency $\omega_R = \frac{\mu_{21}E'}{\hbar}$ and by the detuning $\delta = \omega - \omega_{21}$ of the applied frequency ω in comparison to the resonance frequency of the unperturbed two-level system $\omega_{21} = \frac{E_2 - E_1}{\hbar}$. As the electric field of the radiation is coupling to the transition dipole moment, the populations of the two states are altered, which can be described by two coupled differential equations. Assuming the population to be initially fully in the lower state, $p_1(t=0) = 1$ and $p_2(t=0) = 0$, the time dependent population of the two-level system is given by

$$p_1(t) = 1 - \frac{\omega_R^2}{\Omega^2} \sin^2\left(\frac{\Omega t}{2}\right) \quad (2.30a)$$

$$p_2(t) = \frac{\omega_R^2}{\Omega^2} \sin^2\left(\frac{\Omega t}{2}\right) \quad (2.30b)$$

and is oscillating with time [4]. The prefactor is $0 \leq \frac{\omega_R^2}{\Omega^2} \leq 1$, implying that the population is not changed or completely inverted, i.e. for a π -pulse ($t = \frac{\pi}{\omega_R}$) with zero detuning ($\delta = 0 \Rightarrow \Omega = \omega_R$), as the respective limiting cases. A damping, e.g. due to collisions of the molecules (so called T_2 -processes, compare to nuclear magnetic resonance (NMR) phenomena) and spontaneous emission (T_1 -processes), is observed in real systems, which is not integrated in Eq. (2.30). This damping leads to an equally shared population for a saturated system with long exposing times and zero detuning. This implies that the population of the lower level is changed by 50% for long exposure times, if $p_1(t=0) = 1$. The relative change is decreasing if the two states are initially populated more equally. Neglecting degenerate states, the populations of the two states are approaching in thermal equilibrium if the energy difference of the two levels is getting smaller. This is not favorably for DR experiments in the MMW region.

2.3.3 Autler-Townes Effect

Rotational spectra can usually be explained by means of a semiclassical picture. The energy levels of an asymmetric-top molecule are derived by a quantum mechanical treatment (cf. Secs. 2.1 and 2.2), and the light field is treated in a classical manner. On the other hand, if an intense enough radiation is applied to a two level system, called **pump transition**, a **probe transition** from one of the two states to a third state is observed to be split into two components. This effect is called the Autler-Townes effect [18, 19]. Its explanation requires a full quantum mechanical picture of the 2-level pump system.¹¹

¹¹The probe power is considered to be sufficiently low, here the semiclassical picture is still valid.

Assuming the molecular part to be solved, the number of photons of the light field N have to be taken into account. The wave functions can be set up as $|JKM, N\rangle$, or for a two-level system simply shortened by $|1, N\rangle$ and $|2, N\rangle$. The energies of the unperturbed $|1, N+1\rangle$ and $|2, N\rangle$ states are identical if the photon energy $\hbar\omega$ is identical to the energy difference of the unperturbed two-level system $\hbar\omega_{21}$, i.e. $\hbar\omega = \hbar\omega_{21}$. Interactions between these two states need to be taken into account and the Hamiltonian can be set up identical to Eq. (2.26). The interaction Hamiltonian is expressing the absorption or emission of a photon by subsequent excitation or de-excitation of the molecule, respectively. In the rotating wave approximation, the coupling term can be approximated by $V = \langle 1, N+1 | \hat{\mathcal{H}}^p | 2, N \rangle = \hbar\omega_R/2$ [19]. The diagonal entries are simply the sum of the rotational energies and the photon energy. Setting the energy of the lower molecular state $|1, N\rangle$ to 0 and, again, symmetrizing the mathematical problem, the Hamiltonian can be written as

$$\hat{\mathcal{H}} = \hbar \begin{bmatrix} (N+1)\omega & \frac{\omega_R}{2} \\ \frac{\omega_R}{2} & N\omega + \omega_{21} \end{bmatrix} = \hbar \begin{bmatrix} (N + \frac{1}{2})\omega + \frac{\omega_{21}}{2} + \frac{\delta}{2} & \frac{\omega_R}{2} \\ \frac{\omega_R}{2} & (N + \frac{1}{2})\omega + \frac{\omega_{21}}{2} - \frac{\delta}{2} \end{bmatrix} \quad (2.31)$$

where the energy difference is described with the help of the detuning δ . By a direct comparison of the Hamiltonian in Eq. (2.31) to the one from Eq. (2.26), eigenenergies can directly be determined with the help of Eq. (2.27) to

$$E^\pm = \hbar \left[\left(N + \frac{1}{2} \right) \omega + \frac{\omega_{21}}{2} \pm \frac{1}{2} \sqrt{\omega_R^2 + \delta^2} \right] \quad (2.32)$$

by using the substitutions $E = \hbar (N + \frac{1}{2}) \omega + \hbar\omega_{21}/2$, $\Delta = -\hbar\delta/2$, and $V = \hbar\omega_R/2$. In this case, the average energy without a laser field (zero photons, $N = 0$), in particular the average energy of the two unperturbed energy levels, is $E = \hbar\omega_{21}/2$. The two dressed states $|+\rangle$ and $|-\rangle$ are separated by $\Delta E = E^+ - E^- = \hbar\Omega$, i.e. $\Delta E = \hbar\omega_R$ for zero detuning. The behavior of the dressed states is depicted in Fig. 10.

Assuming that a transition of the lower unperturbed state to a third unperturbed state is forbidden ($|3, N\rangle \leftarrow |1, N\rangle$), the intensities of the probe transitions $|3, N\rangle \leftarrow |\pm\rangle$ are dependent on the mixing coefficient of the unperturbed state $|2, N\rangle$ in $|+\rangle$ and $|-\rangle$. The intensities of the two probe components, depicted by the broadness of the curly black arrows in Fig. 10, are strongly dependent on the detuning as a consequence. The mixing coefficient can be calculated from expectation values out of Eq. (2.28). The intensities are equally strong for zero detuning $\delta = 0$, in particular case ii) for on-resonance pumping with $\omega = \omega_{21}$. For case i), off-resonant pumping with $\omega < \omega_{21}$ the red-shifted frequency component is more intense, whereas for case iii), off-resonant pumping with $\omega > \omega_{21}$ the blue-shifted frequency component is more intense. This holds for the depicted progressive energy level arrangement ($E_3 > E_2 > E_1$) in Fig. 10.

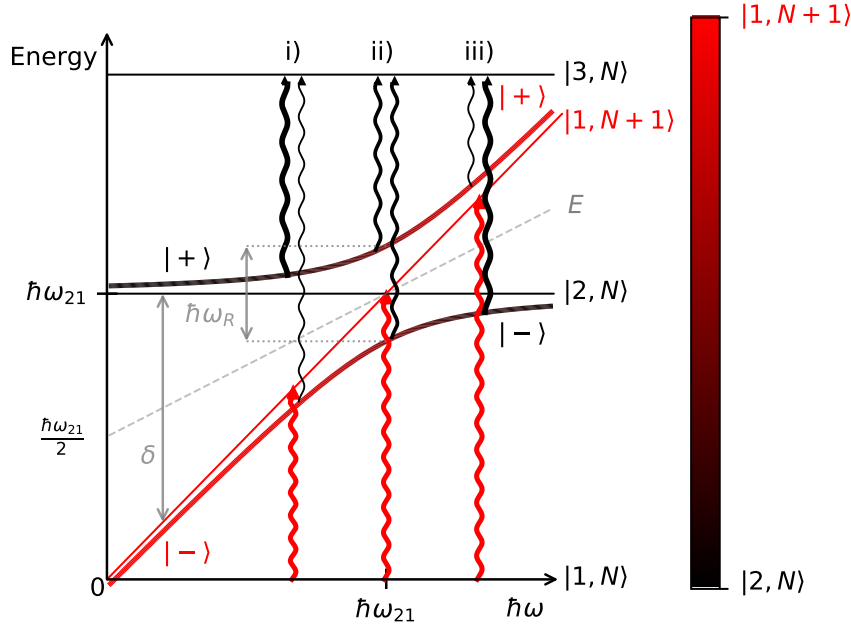


Figure 10: Simplified Autler-Townes effect of a 3-level system when a 2-level system is pumped. The **probe** transition is split into two components (black curved lines) when the **pump** radiation $\hbar\omega$ is intense enough (red curved lines) to split the dressed states $|+\rangle$ and $|-\rangle$ prominently. This splitting is highlighted for three different cases: i) Off-resonance pumping with $\omega < \omega_{21}$, ii) On-resonance pumping with $\omega = \omega_{21}$, iii) Off-resonance pumping with $\omega > \omega_{21}$. The intensity of the probe radiation is depicted by the broadness of the curved black lines and is proportional to the mixing coefficient of $|2, N\rangle$ for $|+\rangle$ and $|-\rangle$. The figure is adapted from Ref. [19].

So far it was neglected that the states $|1, N\rangle$ and $|2, N-1\rangle$ also have the same energy if $\omega = \omega_{21}$. Taking also interaction between these states into account, $|1, N\rangle$ will also split into two dressed states, see the left hand side of Fig. 11. There are four different energy level arrangements for a three-level system connected by two allowed transitions, see the right hand side of Fig. 11. The arrangements are separated into **regressive and progressive level arrangements**. Transitions start (V -type) or end (Λ -type) in the same level in regressive arrangements, for progressive ones they are connected in a ladder fashion. From the intensities of the two probe components a distinction between progressive and regressive level arrangements can be made, if off-resonant pumping is applied. For $\omega > \omega_{21}$ (case iii of Fig. 10), progressive pumping leads to more intense blue-shifted probe components, as was already mentioned before, whereas for regressive level arrangements the red-shifted probe components are more intense. Vice versa intensity ratios are observed for $\omega < \omega_{21}$, see Fig. 11.

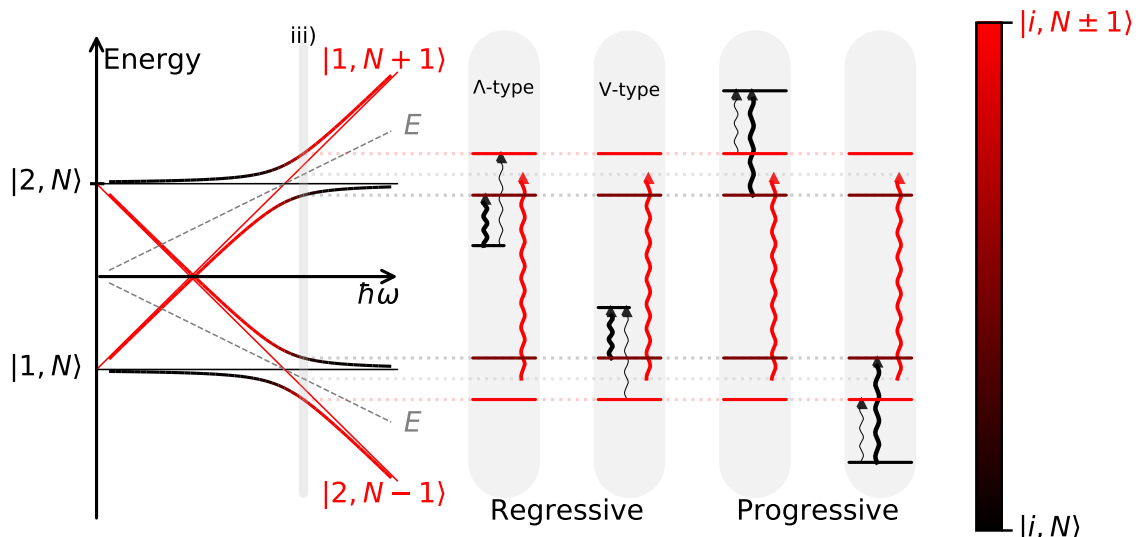


Figure 11: Autler-Townes effect for off-resonant pumping with $\omega > \omega_{21}$, see case iii) of Fig. 10. On the left hand side the pumped 2-level system with its dressed states is depicted. The respective dressed energy levels of the pumped system are plotted in black and red, depending on their mixing coefficients. On the right hand side the four possible energy level arrangements are shown. Transitions to (or from) a third energy level from (or to) a dressed energy level, are more intense for larger mixing coefficients of $|i, N\rangle$ of the dressed state. The red-shifted component of the probe transition is more intense for regressive energy level arrangements, whereas the blue-shifted for progressive ones.

In summary, based on the Autler-Townes effect, transitions which share an energy level can be identified if the pump radiation is intense enough to split the probe transition into two components. This is the basis for establishing a MMW-MMW DR experiment. Furthermore, regressive and progressive energy level arrangements can be distinguished in future experiments if needed, as was already demonstrated in the literature [13,14].

2.3.4 Fermi Resonance

Fermi resonances are, in the general sense, perturbations between two energetically nearly degenerate vibrational states of the same symmetry. In general, for a harmonic oscillator no interactions between different normal modes are to be expected. However, anharmonic terms can couple different vibrational modes. The Hamiltonian can again be set up in the form of Eq. (2.26). As the potential within the interaction term, $\hat{V} = \int \Psi_f^* V_{\text{Morse}} \Psi_i d\tau$, is not depending on the Euler angles, the wave functions need to have the same angular-momentum quantum numbers, if \hat{V} is nonvanishing [52]. Therefore, Fermi resonances occur only between states of the same symmetry. Again,

perturbed wave functions ψ_i^F are written as linear combinations of their unperturbed wave functions Φ_i^0 [52], compare to Eq. (2.28). Defining mixing coefficients with $a^2 + b^2 = 1$, the rotational constants are determined by [52]

$$X_1^F = a^2 \cdot X_1^0 + b^2 \cdot X_2^0 \quad (2.33a)$$

$$X_2^F = b^2 \cdot X_1^0 + a^2 \cdot X_2^0. \quad (2.33b)$$

The sums of the rotational constants, with $(X_1^F + X_2^F)$ and without $(X_1^0 + X_2^0)$ treatment of perturbations, are identical. This results in an observable Fermi shift, one rotational constant is effectively getting larger, while the one from the other vibrational state is reduced by the same magnitude.

Fermi parameters used in the analysis of *gauche*-propanal are of the form [60–62]¹²

$$\hat{\mathcal{H}}_{\nu'\nu''}^F = F_0 + F_J \hat{J}^2 + F_K \hat{J}_a^2 + 2F_2(\hat{J}_b^2 - \hat{J}_c^2) + \dots \quad (2.34)$$

2.3.5 Coriolis Interaction

If two vibrational states are nearly degenerate, not only Fermi resonances can occur, but also their vibration-rotation coupling needs to be considered. Naturally, this time the angular momentum quantum numbers are not the same for the initial and final states. Possible Coriolis interaction can be derived from the character table of the molecule by means of group theoretical considerations. If the species of rotation R_g is contained in the direct product of the symmetry species g (with $g = a, b, c$), Coriolis interactions can occur between two states [62].

The complete Hamiltonian, consisting of the two unperturbed rotational Hamiltonians of the two distinct vibrational states, $\hat{\mathcal{H}}_{\nu'}$ and $\hat{\mathcal{H}}_{\nu''}$, their energy difference ΔE and their interactions $\hat{\mathcal{H}}_{\nu'\nu''} = \hat{\mathcal{H}}_{\nu'\nu''}^F + \hat{\mathcal{H}}_{\nu'\nu''}^C$, by taking into account Fermi resonance $\hat{\mathcal{H}}_{\nu'\nu''}^F$ and Coriolis interaction $\hat{\mathcal{H}}_{\nu'\nu''}^C$, is set up as

$$\hat{\mathcal{H}} = \begin{bmatrix} \hat{\mathcal{H}}_{\nu''} & \hat{\mathcal{H}}_{\nu'\nu''} \\ \hat{\mathcal{H}}_{\nu'\nu''} & \hat{\mathcal{H}}_{\nu'} + \Delta E \end{bmatrix}. \quad (2.35)$$

This Hamiltonian is diagonal in J and has the dimension $2(2J+1) \times 2(2J+1)$. Coriolis interaction parameters of a -symmetry are of the form

$$\begin{aligned} \hat{\mathcal{H}}_{\nu'\nu''}^C = & + iG_a \hat{J}_a + F_{bc}(\hat{J}_b \hat{J}_c + \hat{J}_c \hat{J}_b) \\ & + F_{bc}^J \hat{J}^2(\hat{J}_b \hat{J}_c + \hat{J}_c \hat{J}_b) + F_{bc}^K \{(\hat{J}_b \hat{J}_c + \hat{J}_c \hat{J}_b), \hat{J}_a^2\} / 2 + \dots \end{aligned} \quad (2.36)$$

¹²The labeling of Fermi parameters differs frequently in the literature. F_2 [62] is also referred to as F_{\pm} [60] or W_{\pm} [61] (Refs. are examples). In the latter case, all Fermi parameters are labeled with W_i .

with $\{, \}$ being the anticommutator [60–64]. All Coriolis interaction parameters used in this work to reproduce the experimental spectrum and their operators can be found in Eq. (A2) in the Appendix. For example, possible Coriolis interactions of *syn*-propanal are derived from the C_s character table and *c*-type Coriolis interactions can occur between vibrational states with A' symmetry ($A' \leftrightarrow A'$), since $A' \otimes A' = A'$ (the direct product of symmetry species a and b contains R_c , cf. Table A9).

Even though the origin and the treatment of tunneling-rotation interaction e.g. in the ground vibrational state of *gauche*-propanal are different, see Sec. 2.4, it is appropriate to discuss this phenomenon here. Pickett proposed a **reduced axis system (RAS)** for the treatment of tunneling-rotation interactions [65]. Therein, the employed operators are Coriolis operators, however, in the RAS Hamiltonian only even order operators are used, whereas in the general Coriolis treatment operators of odd and even order occur (cf. Eqs. (2.36), (A2), and (A3)). The RAS can be considered as a rotation of the old axis system to reduce the effects of the tunneling-rotation interaction. For example, again, the C_s character table needs to be looked-up to determine the effects of Coriolis interaction parameters for *gauche*-propanal with allowed tunneling. Notably, F_{ab} (*c*-type) is acting within each tunneling state (see above: $A' \otimes A' = A'$), in contrast to F_{bc} and F_{ca} (*a*- and *b*-type Coriolis interactions are expected to occur between the two substates: $A' \otimes A'' = A''$). The difference of F_{ab} of X^+ and X^- can be considered as a rotation of two axes system against each other. F_{bc} and F_{ca} can be considered as identical rotations of both axes systems to derive the RAS.

2.4 Large Amplitude Motions - Internal Rotation

Vibrational motions can frequently be separated from the overall rotation as energy differences are large enough, see Eq. (2.2) and Sec. 2.2. Generally, this is not the case for vibrations displaying large amplitude motions (LAMs). The feasible internal rotation of the aldehyde group in *gauche*-propanal is one example of such a LAM, as is already mentioned in Sec. 1.3. The usually hindered internal rotation of a methyl group is another example. A very prominent example of a LAM is the inversion motion in ammonia [66]. Of course there are more examples of LAMs, not of further interest concerning this work. Fundamental descriptions of phenomena of internal rotation are given in the book of W. J. Orville-Thomas [67].

The energy levels of *gauche*-propanal are split into X^+ and X^- substates due to a LAM. The treatment of a double-well potential (cf. Fig. 4) is extensively studied and can be looked up in many textbooks dealing with quantum mechanics. An infinitely high barrier leads to a double degeneracy of the energy levels. On the other hand, a splitting of each energy level is observed for low enough barriers as wave functions from one minimum can tunnel to the other minimum. The resulting wave functions

can be symmetric or antisymmetric linear combinations of the original wave functions. Therefore, resulting tunneling states are often designated as (+) and (−) substates. As these splittings occur for several vibrational states of the ν_{24} mode, these tunneling states are labeled with X^+ and X^- within this work, in particular with 0^+ and 0^- for $\nu = 0$, 24^+ and 24^- for $\nu_{24} = 1$, and 24^{2+} and 24^{2-} for $\nu_{24} = 2$. Pickett’s RAS is used to describe the tunneling-rotation interaction originating in the symmetric double minimum potential of the two equivalent *gauche*-propanal configurations [65], see Sec. 2.3.5.

The rotational lines of medium sized molecules containing a methyl group are frequently split into doublets [68,69]. This splitting is also observed for *syn*-propanal and made an analysis considering internal rotation necessary. To a minor extend the splitting is also observed for some specific transitions of *gauche*-propanal, but a treatment of this splitting is not needed to reproduce the overwhelming majority of the observed fingerprint to experimental uncertainty and is therefore neglected here for time saving reasons.

General theoretical descriptions of internal rotation are frequently explained in several textbooks and overview articles by means of a methyl group internal rotation [51,67,68,70,71]. The same holds for the following theoretical overview. The formalism, derived equations and their discussions are still referred to explanations collected by W. Gordy and R. L. Cook [51], if not stated differently. The number of equivalent configurations n a molecule can adopt is the most fundamental property in describing the potential function of internal rotation. Essential for n is not only the functional group itself, but also the symmetry of the molecule. For example, in many cases, an internal rotation of a methyl group leads to a threefold degeneracy of the potential. CH_3NO_2 is an example for sixfold degeneracy. As *syn*-propanal has C_s point group symmetry, the rotation of the methyl group results in three equivalent configurations ($n = 3$). The potential function can be assumed to be periodically, with period $2\pi/n$, and to be an even function, as rotations clockwise and counterclockwise starting from the equilibrium configuration are indistinguishable. As a result, the potential function represented by a Fourier series expansion is described only by cosine contributions. As a reminder, the sine function is odd and therefore all its coefficients are zero. In general, a n -fold degenerate internal rotation potential may be expressed as

$$V(\alpha) = \sum_{k=0}^{\infty} \frac{V_{kn}}{2} [1 - \cos(kn\alpha)] \quad (2.37)$$

where α is the angle of the internal rotation, also referred to as torsional angle. For *syn*-propanal, the torsional angle describes the rotation of a plane spanned by the carbon skeleton of the molecule (C-C-C) with respect to a plane spanned by the methyl and methylene carbon atoms and one of the three hydrogen atoms of the methyl group (C-

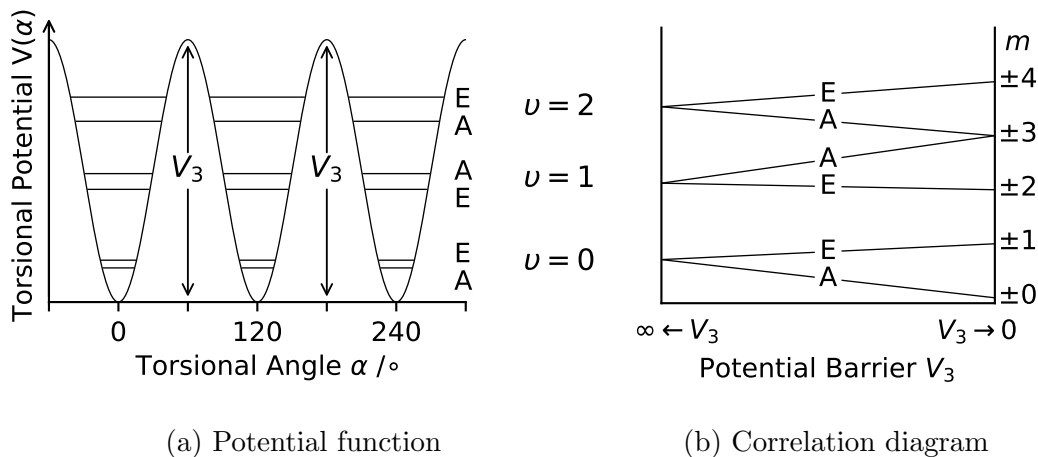


Figure 12: Threefold degenerate internal rotation potential and its energy level labeling. (a) The potential function for internal rotation is described by Eq. (2.38). Each vibrational state is labeled by the harmonic oscillator quantum number ν and its torsional sublevels A and E. (b) The schematic correlation diagram of the two limiting cases, solely harmonic oscillations ($V_3 \rightarrow \infty$, labeled with ν) and free rotation ($V_3 \rightarrow 0$, labeled by m), is clarifying the torsional sublevel labeling for a finite barrier. The figures are adapted from Ref. [51].

C-H). In a first approximation and using $V(\alpha_i = 2\pi i/n) = 0$ with $i \in \mathbb{Z}$ the threefold degenerate internal rotation potential is described by

$$V(\alpha) \approx \frac{V_3}{2} [1 - \cos(3\alpha)] \quad (2.38)$$

if higher order terms can be neglected. This potential function is illustrated in Fig. 12a. The maximum energy of this potential is called the barrier height V_3 . Using the one-dimensional time independent Schrödinger equation, the wave equation for internal rotation with a potential described by Eq. (2.38) is

$$-F \frac{d^2 U(\alpha)}{d\alpha^2} + \left(\frac{V_3}{2} [1 - \cos(3\alpha)] - E \right) U(\alpha) = 0 \quad (2.39)$$

with $F = \hbar^2/2I_\alpha$ being the internal rotation constant and I_α being the reduced moment of inertia for the relative motion of the functional group with respect to the framework of the molecule. Regarding a finite potential barrier, it is expedient to take a look at the two limiting cases for very small barriers, $V_3 \rightarrow 0$ (free rotation), and very high barriers, $V_3 \rightarrow \infty$ (harmonic oscillation), to elucidate the torsional eigenvalues E of Eq. (2.39).

Very small barriers, $V_3 \rightarrow 0$, lead to a (nearly) free internal rotation of the functional group. In this limit, the wave equation Eq. (2.39) simplifies to

$$\frac{d^2U(\alpha)}{d\alpha^2} + \left(\frac{E}{F}\right)U(\alpha) = 0 \quad (2.40)$$

having the form of a spatial free rotor with a fixed axis of rotation, which is comparable to the Schrödinger equation of a free-particle. Derived eigenfunctions are $U(\alpha) = Ae^{im\alpha}$, with a normalization factor A and the energy given by

$$E = Fm^2. \quad (2.41)$$

Angles larger or equal to 2π are not describing new configurations of the molecule. A consequence of this cyclic boundary condition, $U(\alpha) = U(\alpha + 2\pi)$, is that $m \in \mathbb{Z}$. The energy levels are doubly degenerate, except for $m = 0$. The positive and negative values of m may classically be interpreted as a clockwise and counter-clockwise internal rotation.

Very high barriers, $V_3 \rightarrow \infty$, solely allow for small harmonic oscillations. In particular, tunneling is not feasible. For very limited rotations (small α 's), the potential function in Eq. (2.38) can be approximated by $V(\alpha) = \frac{9}{4}V_3\alpha^2$ (with $\cos(3\alpha) \approx 1 - \frac{9}{2}\alpha^2$). This approximation translates Eq. (2.39) to

$$\frac{d^2U(\alpha)}{d\alpha^2} + \frac{1}{F} \left[E - \frac{1}{2} \left(\frac{9}{2}V_3 \right) \alpha^2 \right] U(\alpha) = 0 \quad (2.42)$$

which is comparable to a harmonic oscillator wave function. Thereof, the energies are given by

$$E = 3\sqrt{V_3F} \left(v + \frac{1}{2} \right) \quad (2.43)$$

with $v \in \mathbb{N}$. These energy levels are triply degenerate due to the three equivalent potential minima (cf. Fig. 12a and Eq. (2.38)), or quantum mechanically speaking, describing the torsional eigenfunction as linear combinations of three harmonic oscillator wave-functions, each centered in one of the three minima.

A finite potential barrier V_3 lifts the threefold degeneracy of energy levels of small harmonic oscillations, as tunneling is now feasible. The rate of this tunneling process depends on the width and the height of the barrier. For a quantitative analysis of finite potential barriers the differential wave equation for internal rotation in Eq. (2.39) is substituted to the form of Mathieu's equation

$$\frac{d^2M(x)}{dx^2} + (b - s \cos^2(x))M(x) = 0 \quad (2.44)$$

using $U(\alpha) = M(x)$, $3\alpha + \pi = 2x$, $E = \frac{9}{4}Fb$, and $V_3 = \frac{9}{4}Fs$, with the reduced barrier height s and eigenvalues b . By satisfying the cyclic boundary condition $U(\alpha) = U(\alpha + 2\pi)$, or $M(x) = M(x + 3\pi)$, eigenvalues can be looked up in existing tables of

this problem. As a result of two possible periods $\frac{2}{3}\pi$ and 2π in α , or π and 3π in x , the energy levels of each v , for $V_3 \rightarrow \infty$, are split into two sublevels. A periodic solution of the wave functions in Eqs. (2.39) and (2.44) can be expressed, by using a Fourier expansion, as

$$U_\sigma^{(v)}(\alpha) = \sum_{k=-\infty}^{\infty} A_k^{(v)} e^{i(3k+\sigma)\alpha}. \quad (2.45)$$

The symmetry of the sublevels, or generally speaking of the torsional wave function, is described by the symmetry label σ . The two sublevels are originating mathematically from the two periods and are a direct result of allowed tunneling. By determining the effect of the torsional wave functions, in Eq. (2.45), under the symmetry operations of the point group C_3 for each σ (cf. Table A8), the torsional sublevels are called A ($\sigma = 0$) and E ($\sigma = \pm 1$). The sublevel A is nondegenerate and the E sublevel is doubly degenerated.

Schematic connections of the limiting cases of free internal rotation and of solely feasible small harmonic oscillations lead to the correlation diagram in Fig. 12b. The lifting of degeneracies is clearly seen. As explained before, the threefold degeneracy of $V_3 \rightarrow \infty$ is lifted to **A and E torsional sublevels**. This might be interpreted classically in a way, that the doubly degenerated E sublevels correspond to tunneling in two possible, but non distinguishable, directions and the A level corresponds to small oscillations within a potential well. In reality, this interpretation is falling short on the observed quantum mechanical effects but helps to get an understanding of the lifting of degeneracies. Furthermore, the $\pm m$ degeneracy of free internal rotors is removed for states with $m \bmod 3 = 0$. Most importantly, by consulting the correlation diagram, the labeling of the A and E sublevels is comprehensible, in particular the alternating order of A and E sublevels for increasing vibrational states, compare to Fig. 12. For higher torsional energies, identical to increasing v , the sublevels are observed to split more prominently as the tunneling probability increases with increasing energy of the molecule.

The Hamiltonian of an asymmetric rotor molecule undergoing internal rotation can be written as the sum of the internal rotation Hamiltonian $\hat{\mathcal{H}}_{int}$ and the overall rotational Hamiltonian $\hat{\mathcal{H}}_{rot}$ as

$$\hat{\mathcal{H}} = \hat{\mathcal{H}}_{int} + \hat{\mathcal{H}}_{rot} = F(\hat{p}_\alpha - \rho_a \hat{J}_a - \rho_b \hat{J}_b - \rho_c \hat{J}_c)^2 + V(\alpha) + A \hat{J}_a^2 + B \hat{J}_b^2 + C \hat{J}_c^2 \quad (2.46)$$

in the principle axis system [68, 70]. A major challenge of setting up proper Hamiltonians for molecules undergoing internal rotation is arising as the axis of internal rotation is typically not coinciding with one of the principal axes of rotation, leading

to off-diagonal cross terms of the internal rotation angular momentum conjugate with the overall rotation, $\hat{p}_\alpha \hat{J}_i$, and quadratic terms of the form $\hat{J}_i \hat{J}_j + \hat{J}_j \hat{J}_i$, see Eq. (2.46). In the literature, there are different approaches to overcome this challenge, like the principal axis method (PAM), internal-axis method (IAM), or ρ -axis method (RAM). PAM is making use of the molecular-fixed principal axis system introduced in Sec. 2.1 and is set up in Eq. (2.46). IAM is taking the symmetry axis of the internal rotor plus two arbitrarily, but beneficial for further calculations, fixed axes in the molecular framework as the reference system. The components of the ρ -vector, necessary for determining the coupling terms, can be calculated by

$$\rho_g = \frac{\lambda_g I_\alpha}{I_g} \quad (2.47)$$

with the principal moments of inertia I_g , the moment of inertia of the internal rotor I_α and the direction cosine $\lambda_g = \cos(\Theta(i, g))$ defined by the angle between the internal rotation axis i and one of the principal axes g [68]. The length of the dimensionless ρ -vector is given by

$$\rho = \sqrt{\rho_a^2 + \rho_b^2 + \rho_c^2}. \quad (2.48)$$

For RAM, the axis system is rotated in a way that the new z -axis is parallel to the ρ -vector. Here, from Eq. (2.47) it directly follows that $\rho_x = \rho_y = 0$. In this case, the internal rotation Hamiltonian simplifies dramatically to

$$\hat{\mathcal{H}}_{int} = F(\hat{p}_\alpha - \rho \hat{J}_z)^2 + V(\alpha) \quad (2.49)$$

and is diagonal in K , which is here meant to be the projection of the overall angular momentum onto the ρ -axis [68, 72]. A lucid and informative review by I. Kleiner is comparing different programs based on the aforementioned methods to treat molecules with one internal rotor [68].

The theoretical models, in particular the Hamiltonians of molecular fingerprints, and characteristics of expected molecular fingerprints of *syn*- and *gauche*-propanal, summarized within this chapter, allow for deciphering and analyzing measured spectra of propanal. Furthermore, the Autler-Townes effect is emphasized, which allows to apply a sophisticated MMW-MMW DR method.

3 Absorption Spectrometers

" We have the world's best spectrometer. Because it's ours."

- Frank Lewen -

The basic principle of absorption spectrometers is always the same. A radiation source produces electromagnetic waves which are guided through an absorption cell and which are finally received by a detector. Ideally, the absorption cell is filled solely with the molecule of interest in the gas phase, here with propanal. For measuring rotational transitions, represented by the green arrows in Fig. 6, (sub-)MMW spectrometers in Cologne are used and presented in Sec. 3.1. Ro-vibrational measurements, symbolized by the red arrows in Fig. 6, have been conducted at the AILES A beamline of the SOLEIL synchrotron in Paris, France, see Sec. 3.2.

3.1 (Sub-)Millimeter Wave Spectrometers

The most essential data of this work are taken using different (sub-)MMW spectrometers in Cologne, only differing in minor details, like synthesizer type, cell length, or optical, electrical, and cell arrangements [7, 8]. To allow for unambiguous assignments of rotational transitions, even of weak features which might be blended, one setup is extended in the framework of this thesis to be capable of DR measurements. Its schematics can be found in Fig. 13. Furthermore, a software based on LabView is developed, allowing for a (nearly) fully automatized change between the different setups, only limited by adaptations on the hardware side when switching between single or double modulation (DM) measurements. It even allows for various multi-measurement options to measure several frequency regions of interest automatically. A screenshot of the user interface, together with some more information, can be found in Fig. A10.

A typical absorption experiment uses only a single (probe-)radiation source, hereafter called the conventional setup (Sec. 3.1.1). In particular, the pump radiation is not applied (DR off). For DR experiments, additionally a pump radiation is applied (DR on) which might not (Sec. 3.1.2) or might be modulated (Sec. 3.1.3), referred to as the DM-DR setup, as two, probe and pump, sources are modulated.

3.1.1 Conventional Measurements - Measuring Rotational Fingerprints

The pump source and the optional second lock-in amplifier in Fig. 13 are not needed for conventional measurements. Key components of all experimental setups are synthesizers creating frequencies of up to 67 GHz. Either Rohde & Schwarz SMF100A or Agilent E8257D synthesizers are used, having similar characteristics, in particular in frequency stability and output powers. The synthesizers are locked to a 10 MHz

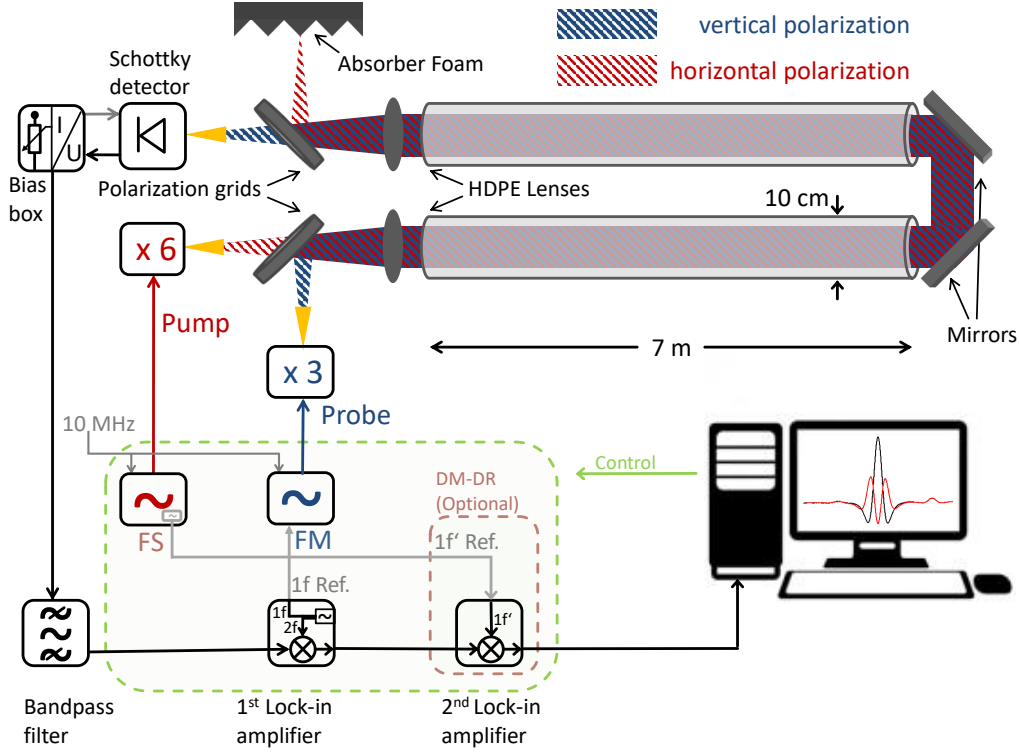


Figure 13: Unified schematics for the (sub-)millimeter wavelength spectrometer capable of DR measurements. The spectrometer can be operated in three modes: The pump source can be turned off (conventional) or on (DR) with an optional modulation (DM-DR) and is operating in the W-band. For more details see text. The figure is published in Ref. [73].

rubidium atomic clock guaranteeing a frequency accuracy of $\frac{\Delta\nu}{\nu} = 10^{-11}$. For measuring some transitions in the frequency region from 40 to 67 GHz, the synthesizer is directly coupled to a horn antenna. A tripler with in-house developed electronics for operating in full saturation mode is used, ensuring a stable output power of about 1 mW, for covering (more than) the W-band, here from 75 to 129 GHz. For various frequency regions between 169.2 and 500.4 GHz a commercial multiplier chain (Virginia Diodes, Inc.), intrinsically equipped with two triplers, is used, with adequate (cascaded) triplers and/or doublers to match the desired frequency regions. A lock-in amplifier submits a reference frequency for the frequency modulation (FM) of the probe radiation. The frequency of the FM is typically around 47 kHz (or 27 kHz) and the amplitude is usually chosen between 180–300 kHz. These parameters as well as all following measurement parameters are dependent on the measured frequency region and used setup. The modulated radiation is sent out by a gold-coated horn antenna. A polarizing grid is guiding the beam through a high-density polyethylene (HDPE) lens of 15 cm focal length, with the horn antenna located in one focal point, which is parallelizing the beam into the cell. The beams size diameter of the resulting plane

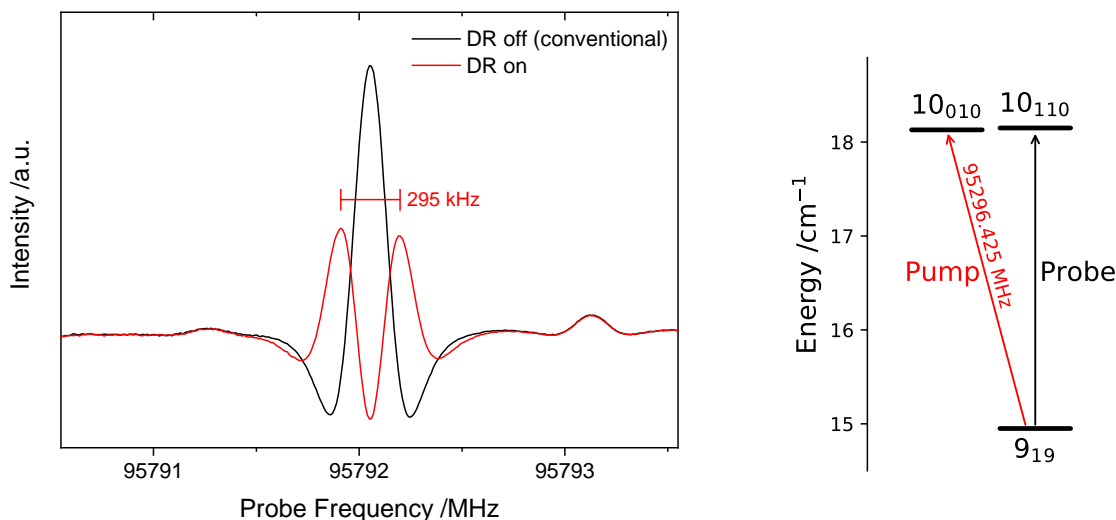


Figure 14: Conventional (black) vs. DR measurement (red), for the V -type regressive energy level arrangement of *syn*-propanal shown on the right hand side.

wave is of approximately 10 cm. The cell consists out of Pyrex (borosilicate glass) and the windows are made of Teflon (Polytetrafluoroethylene; PTFE). The majority of the broadband spectra are actually taken by using a single cell of 5 m length, in contrast to the cell arrangement shown in Fig. 13. It is used in a double pass setup, adding up to an effective absorption path length of 10 m. A roof-top mirror at one end of the cell tilts the polarization of the beam by 90° , so the polarizing grid can differentiate between incoming and outgoing beams. The single pass setup with two 7 m long cells mounted in parallel, shown in Fig. 13, is especially used to be able to overlap probe and pump radiation to allow for DR measurements, see Secs. 3.1.2 and 3.1.3. In this case, the total effective absorption path length adds up to 14 m. In both cell arrangements, the outgoing beam is now focused by a HDPE lens and subsequently steered by a polarization grid onto the receiving horn antenna. The signals are received by frequency matching low-noise room temperature Schottky detectors. The Schottky detector is connected to an in-house developed bias box for improving the SNR in the frequency regions below 129 GHz. Afterwards, the signal is passed to a bandpass filter (Model 189 selective amplifier, EG&G Parc or PAR) and is then arriving at the 7265 DSP lock-in amplifier (Signal Recovery or EG&G Instruments). Here, the signal is processed with a $2f$ demodulation. Basically, it is a phase sensitive multiplication of the detected signal with the $2f$ component of the modulation frequency. For this reason, the observed absorption lines appear close to the second derivative of a Gaussian, cf. to Sec. 2.1.3.f. A typical spectrum of a conventional measurement is plotted as a black line in Fig. 14. All experiments are conducted at room temperature. Typically the cell is pumped by a turbo molecular pump in cooperation with a mechanical forepump. Background pressures are typically better than 10^{-3} mbar. Afterwards, the cell is filled with gaseous

propanal by leaking the gas from a sample container. The liquid sample (97 % purity, Sigma-Aldrich) is vaporized into the cell, as the vapor pressure at room temperature of 341 mbar is much higher than the background pressure. Typically the cell is filled with pressures of 10–20 μ bar. In a stepwise manner the frequency is scanned by combining scans of increasing and decreasing frequencies to avoid systematic shifts which might be introduced for example by unwanted memory effects of the lock-in amplifier. Taking the average of the two scans results in the final spectrum. Usually, stepsizes of 10–20 kHz are chosen to derive smooth line shapes for selected single measurements, with spans of a few megahertz. For broadband measurements, frequency steps varied between 50–108 kHz due to time saving reasons. Each step is usually integrated for 50 ms (also called Time Constant, TC). As center frequencies are determined mainly from the broadband measurements, the frequency uncertainty is estimated to 20 kHz for strong and very symmetric lines and to 40 kHz or 80 kHz for weaker and less symmetric lines (cf. Fig. A24). The uncertainty of transition frequencies is mainly arising from their SNRs, FWHMs, standing waves, as well as from unknown blended features in the spectrum.

3.1.2 Double Resonance Measurements - Identifying Linkages

DR spectroscopy allows for identifying transitions which share an energy level as is explained in Sec. 2.3.3. Linkages and in particular series (cf. Fig. 8), can be assigned unambiguously in this way. The usefulness of the Autler-Townes effect for DR spectroscopy was already proven before as it can explain the observed phase shifts of regressive and progressive energy level arrangements in RF-MW experiments [13]. Furthermore, it was already directly observed in MW-MMW DR experiments [14].

In this work, one experimental setup is extended to be capable of MMW-MMW DR experiments. An additional, second (pump-)radiation is needed for doing so. The optional lock-in amplifier in Fig. 13 is still not used as the pump radiation is not modulated in classical DR experiments. An active frequency multiplier (AFM) with an output power of up to $P_{out} = 60$ mW (17.8 dBm) and a guaranteed output power of 25 mW (14 dBm) is used for reaching high enough output powers of the pump radiation in the frequency range of 70–110 GHz to create an observable Autler-Townes splitting. The W-band region is covered by upconversion of the synthesizer frequency by a factor of six (AFM6 70-110+14 from Radiometer Physics).

A MMW-MMW DR measurement with clearly observed Autler-Townes splitting is shown by the red line in Fig. 14. The observed splitting of roughly $\Delta\nu = 295$ kHz, which corresponds to the Rabi frequency ($\Delta\nu = \nu_R$ for zero detuning, cf. Sec. 2.3.3), in combination with a dipole moment component of $\mu_b = 1.85$ D of the pumped b -type transition results in an effective power intensity of the pump beam in the cell of

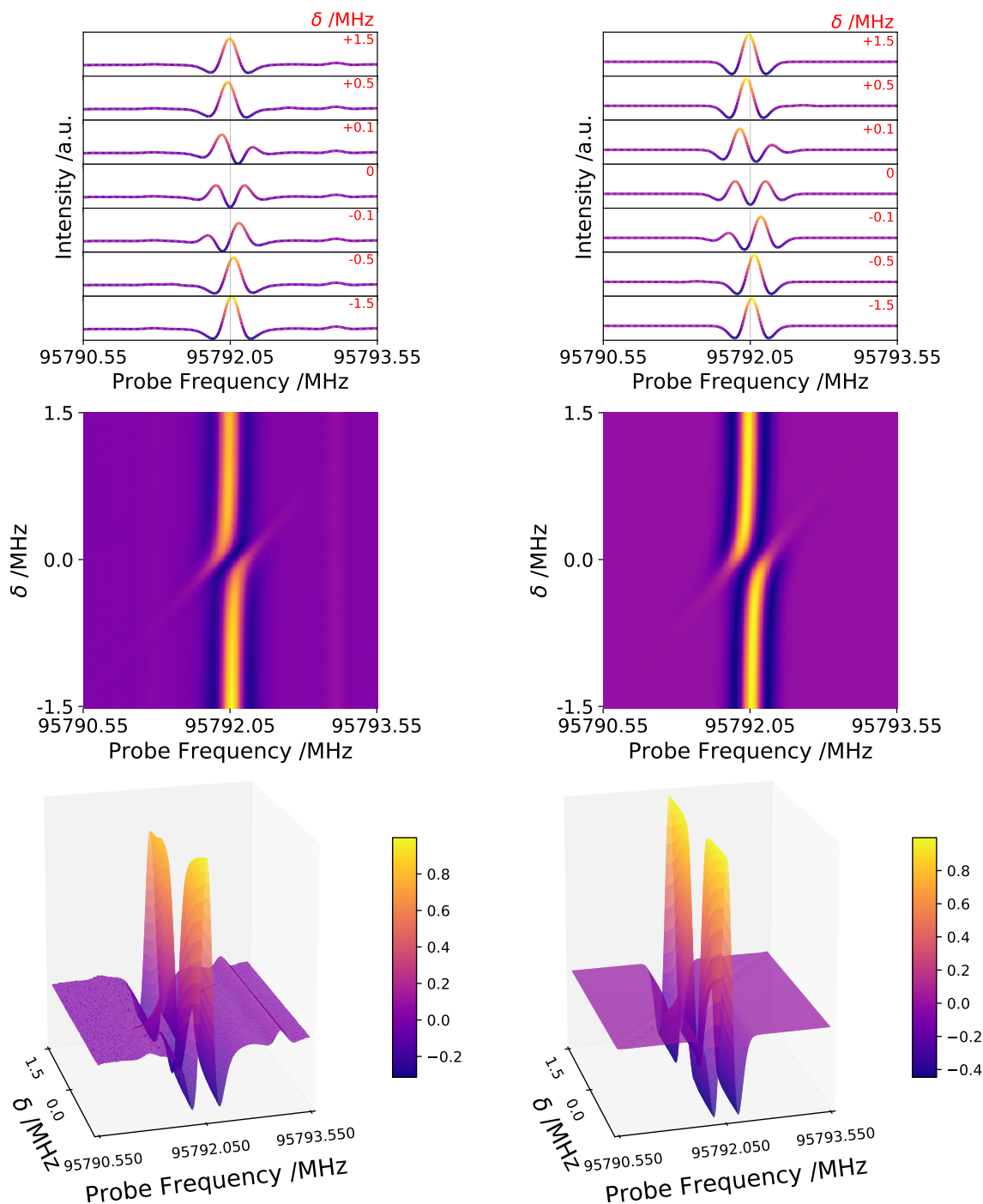


Figure 15: Autler-Townes effect in 2D DR spectra of *syn*-propanal. The same 2D DR spectra are shown for each row. Selected single measurements (top row), a heat map (middle row), and the resulting 3D spectra (bottom row) are shown. On the left hand side measurements and on the right hand side simulations are shown for comparison. The Autler-Townes splitting is clearly visible with a determined Rabi frequency of 295 ± 5 kHz. The zero detuned pump frequency is 95296.425 MHz. The observed regressive energy level arrangement can be seen in Fig. 14. For more details see text. The figure is published in Ref. [73].

1.3 W/m² (or 31.7 V/m field intensity; $\omega_R \propto \sqrt{P_{out}}$ [4]),¹³ assuming a beam diameter of 10 cm. The observed effective output power of 10 mW of the pump source in the cell seems reasonable, when compared to the nominal values from Radiometer Physics, as the polarization grid and the windows are assumed to have significant losses.

The explanation of the observed line shape by the Autler-Townes effect, in particular the avoided crossing, is manifested by a 2D DR spectrum of probe and pump frequencies with dimension 3×3 MHz, see Fig. 15. A pump step size of 20 kHz is applied in the range from $\delta = -1.5$ MHz up to +1.5 MHz which leads in total to 151 single measurements. A 3 MHz probe window with a step size of 10 kHz is measured for each pump frequency. This results in a 2D-grid of probe and pump frequencies with 301×151 measurement points (implemented as "2D DR" measurements in the newly developed software, see Fig. A10). Here, each probe frequency is integrated for 20 ms. The total measurement time of the 2D spectrum is roughly 77 min. Again, the *V*-type energy level arrangement shown on the right hand side of Fig. 14 is observed. Note the symmetric splitting with equally intense Autler-Townes components for on-resonant pumping ($\delta = 0$). On the other hand, the red or blue shifted component is more intense if the pump detuning is $\delta > 0$ or $\delta < 0$, respectively, which is in accordance to predictions for the observed regressive energy level arrangement, see Sec. 2.3.3. The determination of the energy level arrangement, whether it is progressive or regressive as explained in Sec. 2.3.3, is further demonstrated in Fig. A7 in the Appendix.

Thanks to the Autler-Townes effect, DR is an appropriate and useful tool also for spectroscopy in the MMW region. This is also further demonstrated in Ch. 5.

3.1.3 Double Modulation Measurements - Clearing up Molecular Spectra

Complex molecules regularly have very dense spectra, sometimes close to the confusion limit, as mentioned before. Occasionally, transitions containing valuable information on so far undetermined spectroscopic parameters might be blended by much stronger features or the linkage of a weak line is not as clear as in Fig. 14. In these cases, it helps sometimes to simply calculate the difference spectrum of the conventional and the DR measurement and to rescale it. However, it may happen that this procedure results in false positive signals, as can be seen in the two top rows of Fig. 16. These unwanted signals appear, e.g., due to pressure instabilities in the cell. The conventional and the DR measurements are recorded one after the other. The time difference between these measurements might be sufficient for a slight pressure change which results in changing intensities.

It would be desirable to measure with and without applied pump radiation (nearly) simultaneously because of instabilities or fluctuations of the experimental setup. This is

¹³ $I = P_{out}/A$, $A = \pi d^2/4$, $I = 0.5\epsilon_0 c E^2$, $\omega_R = \mu E/\hbar$, and $\hbar\omega_R = h\nu_R$ [4].

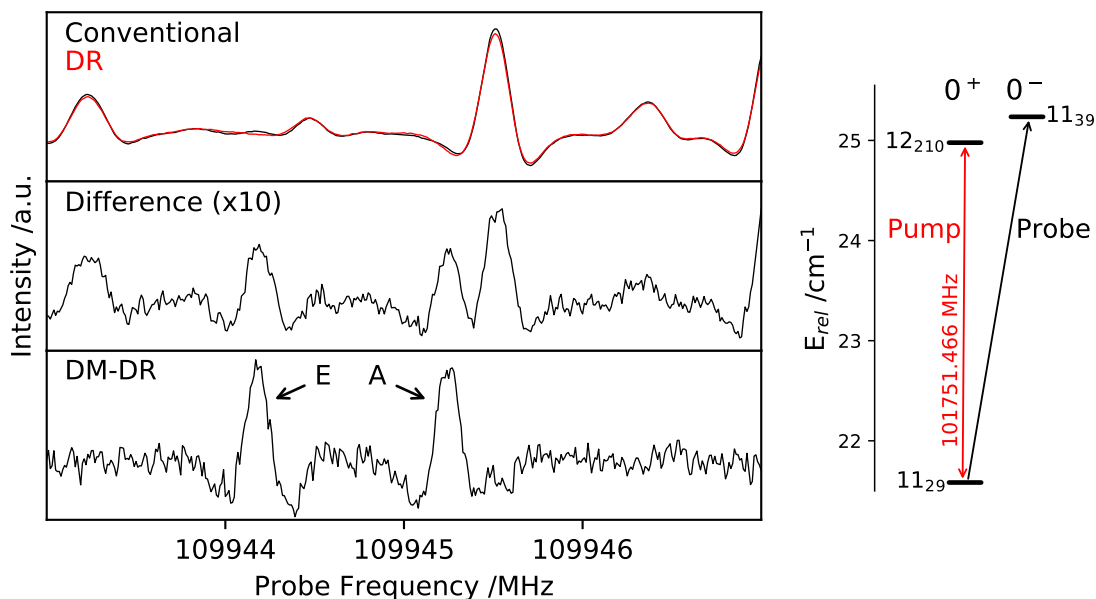


Figure 16: Comparison of a conventional measurement overlaid by a DR measurement (top row), their difference spectrum (conventional–DR; middle row), and a DM-DR spectrum (bottom row) of *gauche*-propanal for the energy term diagram on the right hand side. Two lines are appearing as the probed *c*-type transition shows methyl group internal rotation splitting (A and E components). In particular, the A component is heavily blended and thus not assignable in conventional measurements.

realized by an implementation of an additional modulation scheme of the pump source which is enabled by the use of a second lock-in amplifier, cf. Fig. 13. The probe source is still frequency modulated. Based on the DM and simultaneous DR character, this experimental setup is referred to as the DM-DR setup. Logically the pump source could be pulse modulated to directly switch between DR on and off. A sinusoidal amplitude modulation (AM) has a comparable effect. However, these solutions were excluded because for both approaches concerns about a possibly shortened lifetime of the AFM6 are suspected due to the power variations. Instead, a constant pump power is desirable. A chopper wheel is one solution, but is observed to transfer significant noise due to vibrations to the optical components. For these reasons, frequency switching (FS) from on-resonance to far enough off-resonance is adapted here. Typically a frequency throw of -120 MHz between on- and off-resonant frequencies is used. Measurements are also successful with smaller frequency throws, but a larger value is chosen to be on the safe side. A pump frequency far enough off-resonance has a similar effect as if no pump radiation is applied, which is the basic principle of DR experiments.

The additional lock-in amplifier, in comparison to conventional and DR experimental setups, is installed directly in series after the first lock-in amplifier. The applied $1f'$

demodulation is experimentally realizing the difference spectrum of the DR off and on measurements. The subtraction can be easily understood on closer inspection of the second demodulation process, or essentially the multiplication of the $1/f'$ reference signal with the output signal of the first lock-in amplifier, as the sign of the sinusoidal reference signal is chosen to be positive when the pump radiation is off and it is negative when the pump radiation is on. The second lock-in amplifier is (nearly) instantaneously doing a subtraction of DR off and on measurements in this way. This time, the synthesizer is creating the reference frequency f' and passes it to the second lock-in amplifier, not the other way around. An analog Model 128A lock-in amplifier from PAR is actually used as the first lock-in amplifier for DM-DR measurements (FM, $2f$ demodulation), instead of a digital one. Digital ones are observed to add signal spikes to the demodulated output signal without extra care. The analog lock-in amplifier has no internal reference frequency, which is therefore received externally by another digital lock-in amplifier. These details are neglected in Fig. 13 for uniformity, but are shown in full detail in Fig. A4. Most fundamentally, the FS frequency f' needs to be significantly lower than the FM frequency f , which is unchanged compared to conventional measurements. The value of f' is chosen to be around 200 Hz. Ideally, the TC is exactly a multiple of $T' = 1/f'$ such that always the same number of DR on and off measurements are taken into account for each measurement point. This circumvents unwanted drifting effects and lowered SNRs. A detailed explanation of the DM-DR experimental setup and its working principle including justifications of the applied measurement parameters can be found in Ref. [73]. Typical measurement parameters of DM-DR measurements are collected in Table 2.

Finally, this results in **baseline- and confusion-free spectra** containing only the line(s) of interest. This simplifies the observed spectra dramatically, as is shown for weak and blended lines in a DM-DR measurement plotted in the lowest panel of Fig. 16. Measured DM-DR line shapes are accidentally close to the second derivative of a Gaus-

Table 2: Typical measurement parameters of DM-DR measurements.

Parameter	Device	Value
f	1 st lock-in amplifier	≈ 47 kHz
FM amplitude	probe synthesizer	$\approx FWHM$
f'	2 nd lock-in amplifier	≈ 200 Hz
FS throw	pump synthesizer	-120 MHz
TC	2 nd lock-in amplifier	≥ 50 ms

Ideally:

$$mT = m/f = nT' = n/f' = TC \text{ with } m, n \in \mathbb{N}; f > f'$$

sian (cf. Fig. A8). If the pump frequency is off, but still close enough to create an AC Stark shift, the DM-DR line shape looks accidentally like a first derivative of a Gaussian (cf. Fig. A9). If by chance the far-enough off-resonance frequency, which is assumed to be DR off, is connecting a third energy level to the probed two-level system, it is noticed by an inverted line shape as it can be interpreted as a phase shift of the detected signal of π .

DM-DR measurements should be used, if possible, only for identifying linkages as systematic shifts occur even for slightly off-resonant pumping. Admittedly, off-resonant pumping is noticed by asymmetric line shapes and thus can be circumvented (cf. Fig. A9). Transition frequencies determined by DM-DR measurements are added to the line list with 100 kHz uncertainty (cf. Fig. A24), which is somewhat larger than for conventional measurements to account for unwanted frequency shifts, if a transition is heavily blended in conventional measurements but carries important information.

3.2 Synchrotron based Fourier-Transform Infrared Spectrometer

The ro-vibrational spectra of propanal were measured in the FIR region $80\text{--}700\text{ cm}^{-1}$ at the SOLEIL synchrotron facility using the AILES A beamline [74] under the standard proposal number 20190316. To record the spectrum, a Bruker IFS125 FT interferometer is used with a movable mirror of 5 m path length. One beam is passing a White-type multireflection cell containing gaseous propanal and both signals are finally detected by a liquid-helium cooled InSb bolometer. The FT of the resulting interferograms delivers a spectrum in the frequency domain.

A $6\text{ }\mu\text{m}$ thick Mylar beamsplitter, two $50\text{ }\mu\text{m}$ thick polypropylene windows, and a filter of mesoporous silicon material from Lakeshore are installed for a high IR flux in the range of $80\text{--}500\text{ cm}^{-1}$. An iris aperture of 2 mm is used. The interferometer is used with a total path difference of about 10 m (retardation δ) allowing for a maximum wavenumber resolution of $\Delta\tilde{\nu} = 1/\delta_{max} = 0.00102\text{ cm}^{-1}$. A White-type multireflection cell is set up to an effective absorption path length of 150 m [75, 76]. This cell is filled with propanal up to a pressure of 113 and $240\text{ }\mu\text{bar}$ to be able to properly measure strong and weak intensity bands, respectively, see Fig. 17. Synchrotron radiation is used as it allows for a significant gain in photon flux compared to a conventional FIR source (e.g. globar) and thus enables high resolution spectra to be recorded with a good SNR in a reasonable acquisition time. 220 and 400 interferograms are averaged, each interferogram taking 3 min, adding up to a total measurement time of 11 h and 20 h, respectively. Addressing bands at wavenumbers above 500 cm^{-1} and up to 700 cm^{-1} , the beamsplitter is changed to a KBr one and a 2 mm thick self-made polyethylene disk from the beamline is used as a filter. Here, 210 interferograms (10.5 h) are taken

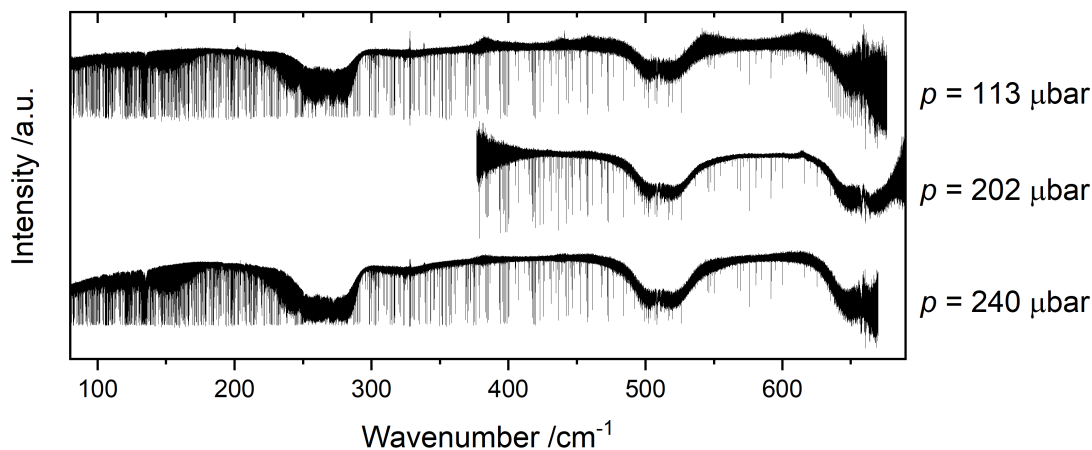


Figure 17: FIR spectra of propanal for the three measurement pressures of 113 μbar , 202 μbar , and 240 μbar . The measurement of $p = 202 \mu\text{bar}$ is optimized for wavenumbers above 500 cm^{-1} , whereas the other two are optimized for $80\text{--}500 \text{ cm}^{-1}$. The strong isolated features are impurities, mainly water lines. For more information see text.

at a propanal pressure of $p = 202 \mu\text{bar}$, see Fig. 17. Reference spectra are taken for each high-resolution measurement with an empty cell and 200 scans at a resolution of 0.025 cm^{-1} for deriving transmittance and absorbance spectra. The calibration of the 240 μbar spectrum is shown in Fig. A11 and is used for the analysis of the fundamental band ν_{24} of *syn*-propanal, see Sec. 5.1.2.b. The spectra are frequency calibrated using a script written by M.-A. Martin-Drumel [77]. The script uses frequencies of residual water lines for calibration [78–80], as the position of the mirror is not tracked accurately enough.

4 Analysis Procedure and Analytical Tools

In this chapter, the deciphering of molecular fingerprints is presented. More specifically, it is dedicated to the unambiguous assignment of transitions and most importantly to the derivation of the best possible quantum mechanical model. First of all the basic principles of a general iterative fitting procedure are explained in Sec. 4.1. This procedure guaranteed the optimal description of many molecular spectra and is also used for the analysis of all vibrational states of *syn*- and *gauche*-propanal within this work. Subsequently, a specific strategy is presented in Sec. 4.2 which makes use of DM-DR measurements to straightforwardly assign weak or blended transitions. The strategy is developed for nearly prolate molecules showing *a*- and *b*-type spectra and is successfully applied for assigning transitions of higher vibrationally excited states of *syn*-propanal, see Sec. 5.1.4. The SPFIT and ERHAM programs are shortly presented in Sec. 4.3 as they are used to fit the rotational spectra of *gauche*- and *syn*-propanal, respectively. Further programs, used for assigning transitions within this work, or which are expected to be beneficial for future analyses of propanal, are shortly summarized in Sec. "Assignment Software" in the Appendix.

4.1 General Assignment, Fitting, and Predicting Procedure

The iterative assignment, fitting, and predicting procedure is schematically shown in Fig. 18 and is based on a 3-step iterative procedure: i) New transitions are assigned and added to the data set, ii) followed by executing a fit with possibly implementation of additional parameters until the measured transitions are fit to experimental uncertainty and iii) based on the newly determined parameters more accurate predictions are derived. A thorough explanation for all three steps can be found in Sec. "Detailed Iterative Fitting Procedure" in the Appendix.

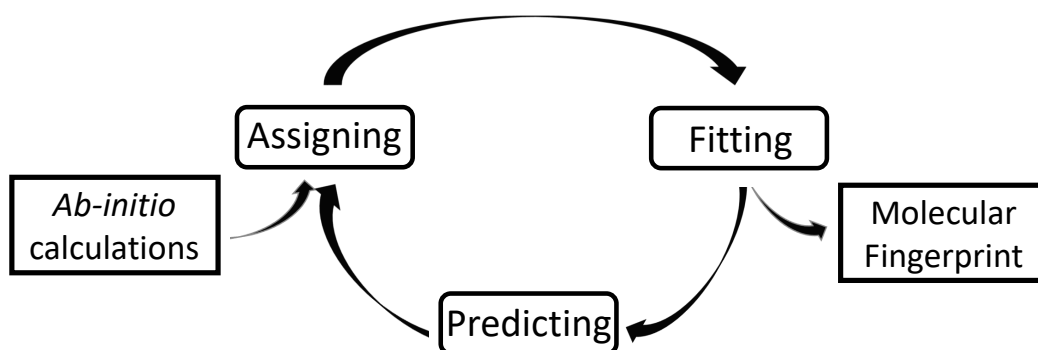


Figure 18: Schematic of the iterative assignment, fitting, and predicting procedure. *Ab-initio* calculations or literature values are used for predictions in the first place. The result is a quantum mechanical model of the spectroscopic molecular fingerprint.

Iterative analyses of rotational or ro-vibrational molecular spectra help to assign more transitions at every step. The iterative procedure is applied ideally until the spectroscopic parameters allow to properly reproduce the experimental spectrum. This may require tens of iterations. The ultimate goal is to find the best possible quantum mechanical model with the number of parameters being as little as possible. A measure of the fit quality and therefore also of the quality of the quantum mechanical model is the the weighted unitless root mean square

$$wrms = \sqrt{\sum_{i=1}^n \left[\frac{(\nu_{obs_i} - \nu_{calc_i})}{\Delta\nu_{obs_i}} \right]^2} / n \quad (4.1)$$

of the fit. In case n number of lines are fit to experimental uncertainty the *wrms* is close to 1.0 and the fit quality is said to be satisfactory. In this work, the difference of the observed and predicted transitions frequencies ($\nu_{obs_i} - \nu_{calc_i}$) are simply referred to as deviations. The *rms* is in units of Hertz and its formula is derived from Eq. (4.1) by omitting the weighting with the estimated experimental uncertainty of a line $\Delta\nu_{obs_i}$. The iterative fitting procedure is supposed to ensure parameter values close to their actual values at each step. Thus, the *wrms* is (hopefully) finally converging into the global minimum of the *wrms* surface. It is important to emphasize that a final selection of parameters may not represent an exclusive quantum mechanical model nor the global minimum of the *wrms* surface, even though the fit quality is considered to be satisfactory. It is more the best choice of parameters found.

The iterative assignment, fitting, and predicting procedure led to accurate predictions of spectra of many molecules, such as disulfur dioxide [7] and 2-cyanobutane [59]. The aforementioned molecules are partly measured or studied in the framework of this work, but the overall analysis is guided by other main contributors. Furthermore, the procedure leads to a proper description of molecular fingerprints of all studied vibrational states of propanal presented within this thesis.

4.2 Deciphering hidden Fingerprints - A specific Assignment Strategy

The DR or DM-DR experimental setups are used if assignments can not be made unambiguously otherwise. In particular, DM-DR measurements guarantee unambiguous assignments of linked transitions or series which would otherwise not be assignable or only in a very time consuming fashion, for example, because lines are blended or are not intense enough for showing an obvious pattern. In optimal cases, linked transitions allow to straightforwardly assign transitions or certain series. Based on these linkages, a systematic assignment strategy can be used as step i) of the general iterative fitting

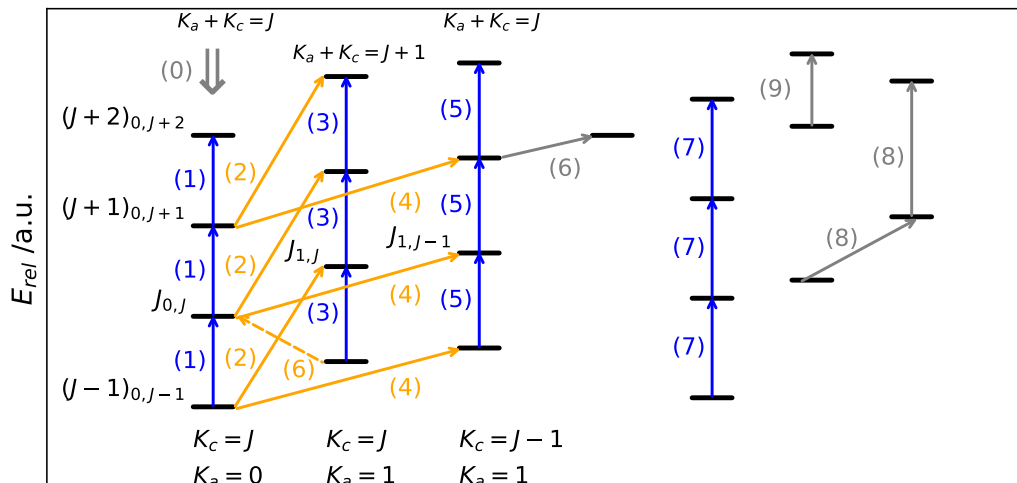


Figure 19: Visualized steps of the specific assignment strategy for near prolate asymmetric-top molecules with non-zero μ_a and μ_b dipole moment components. a - and b -type transitions are depicted by blue and orange arrows, respectively. If transitions can be either a - or b -type they are depicted in grey. The steps are to assign: (0) Candidate transitions; (1) $J_{0,J} \leftarrow (J-1)_{0,J-1}$; (2) $J_{1,J} \leftarrow (J-1)_{0,J-1}$; (3) $J_{1,J} \leftarrow (J-1)_{1,J-1}$; (4) $J_{1,J-1} \leftarrow J_{0,J}$; (5) $J_{1,J-1} \leftarrow (J-1)_{1,J-2}$; (6) Further directly linked transitions (e.g. $J_{0,J} \leftarrow (J-1)_{1,J-1}$); (7) Further qR series transitions; (8) Further linkages; (9) The (conventional) iterative assignment procedure. Transitions from previous steps are used as pump transitions for the next steps, if possible.

procedure presented in Sec. 4.1. The main idea is to merge the AUTOFIT [81], testing all possible combinations of candidate transitions in a fit to find the best model, and the AMDOR principle [82], verifying linkages of different types of transitions, see Sec. "Assignment Software" in the Appendix for some more detailed explanations of these methods. Here, a specific assignment strategy for near prolate asymmetric-top molecules with non-zero μ_a and μ_b dipole moment components is presented. The assignment strategy is visualized in Fig. 19 and is as follows:

(0) If a vibrationally excited state is studied and the ground vibrational state is already known, series may appear close to the ground state ones in Loomis-Wood plots or Fortrat diagrams. Blended transitions from oblate paired energy levels are usually intense and can easily be followed for example. A promising way is to start with a -type transitions of energy levels with $K_a = 0$, in particular as these may be blended in a quartet of lines for rather low J , see Sec. 2.1.3.c. If these lines are assigned, B and C may be determined quite accurately and possibly D_J . In this way, predictions to lower J reduce at best the size of the search frequency window of the next step.

(1) DM-DR measurements are used to unambiguously assign, in the best case the already localized, a -type transitions of qR series with $K_a = 0$ ($J_{0,J} \leftarrow (J-1)_{0,J-1}$).

If no candidates are found in step (0), a brute force 2D grid method may be applied. Transitions of the qR series with $K_a = 0$ should be assignable quite straightforwardly in the DR frequency region, in this work from 70 to about 120 GHz.

(2) Taking now a look at Fig. 8 and realizing that b -type transitions connect different qR series, the next logical step is to search for R -branch b -type transitions with $J_{1,J} \leftarrow (J-1)_{0,J-1}$. Fortunately, already unambiguously assigned a -type transitions with $K_a = 0$ can be used as pump transitions. To verify the first linkage, a rather broad search window might be applied as A is not determined yet. By verifying these linkages, A can be determined.

(3) If b -type transitions are identified and assigned in the previous step, a -type transitions of the qR series of the asymmetry side $J+1$ with $K_a = 1$ can be searched for ($J_{1,J} \leftarrow (J-1)_{1,J-1}$), using the aforementioned R -branch b -type transitions as pump transitions.

(4) Now Q -branch b -type transitions are tried to be assigned. Again, a -type transitions with $K_a = 0$ from step (1) are used as pump transitions. Q -branch b -type transitions link again energy levels with $K_a = 1$ but this time of the other asymmetry side J ($J_{1,J-1} \leftarrow J_{0,J}$).

(5) Using the Q -branch b -type transitions from the previous step as pump transitions, a -type transitions of qR series of asymmetry side J with $K_a = 1$ can be searched for ($J_{1,J-1} \leftarrow (J-1)_{1,J-2}$).

(6) Further transitions should be linked step-by-step in an alternating pump probe scheme as long as linkages are available. For example, a closed loop of transitions for energy levels with $K_a = 0$ and asymmetry side J and energy levels with $K_a = 1$ of $J+1$ can straightforwardly be derived, if R -branch b -type transitions are linked ($J_{0,J} \leftarrow (J-1)_{1,J-1}$), by either using transitions assigned in step (1), (2), or (3) as pump transitions. These lines form the typical quartet structure, see Fig. A5.

(7) At this point qR series with higher K_a , without a linkage to other series, should be easily assignable. Candidate lines of these series should be close to their predicted frequencies and can usually be linked quite straightforwardly.

(8) To constrain rotational parameters even more, basically all transitions which share an energy level in the W-band region may be assigned unambiguously by applying the pump probe scheme.

(9) Continuing of the assignment, fitting, and predicting procedure in the conventional way as presented in Sec. 4.1, in particular without DM-DR measurements. If no severe perturbations are observable, Loomis-Wood plots should allow for quick assignments.

The different steps can sometimes be performed simultaneously, if obvious series are observed. This is frequently the case after step (2) as rotational constants A , B , and C may be constrained quite well after the assignments of a - and b -type transitions.

The strategy is successfully applied for assigning transitions of higher vibrationally excited states of *syn*-propanal, see Sec. 5.1.4. It is observed that regressive pumping schemes have slightly larger SNRs than progressive ones for DM-DR measurements (cf. Fig. A7). Nevertheless, both schemes are applied successfully. Of course, this whole procedure is working only if linkages are available. For *syn*-propanal, usually up to six transitions can be found for each qR series with $K_a \leq 7$ in the frequency region of 70–120 GHz. It is expected that this procedure can be applied successfully to many other near prolate asymmetric-top rotors if their $B + C$ and A value is not much larger than that of propanal. $B + C$ is approximately the distance between two adjacent a -type transitions and determines therefore essentially the number of transitions in the given frequency window. The size of A determines if b -type transitions from steps (2), (4), or (6) can be linked by DR measurements. Furthermore, the method presented here may be automated in the future by combining the specific assignment strategy with the general fitting procedure presented in Sec. 4.1.

4.3 Analysis Software

To reproduce the observed spectra of propanal to experimental accuracy all effects presented in Ch. 2 need to be taken into account. Due to thousands of assigned transitions with quite a large coverage of quantum numbers, sufficient for astronomical detections, a satisfactory model is demanding for quite a number of spectroscopic parameters. For this reason, the analysis software has to guarantee stable and very fast operation. A thorough list of programs fitting molecular data is collected on the PROSPE website¹⁴ operated by Z. Kisiel [83]. Data of several example molecules with tips and proper documentation can be found on the CDMS website.¹⁵ Models for *syn*- and *gauche*-propanal have different specific foci, as for the former the methyl group internal rotation splittings are prominent and for the latter tunneling-rotation interaction as well as Fermi resonances and Coriolis interaction need to be treated satisfactorily. Well-established programs are chosen for this reason which satisfy the special needs of the conformers. Therefore, *gauche*- is fit with SPFIT and *syn*-propanal mainly with ERHAM. These programs are presented in Sec. 4.3.1 and 4.3.2, respectively.

4.3.1 SPFIT/SPCAT Suite of Programs

One of the most popular programs for fitting and predicting high-resolution molecular spectra is probably Herb Pickett's SPFIT/SPCAT suite of programs,¹⁶ based on

¹⁴Programs for ROTational SPEctroscopy (PROPSE); website: <http://www.ifpan.edu.pl/~kisiel/prospe.htm#introduction> [Online; accessed 26-July-2020].

¹⁵<https://cdms.astro.uni-koeln.de/classic/pickett> [Online; accessed 26-July-2020].

¹⁶The current version is available at <http://spec.jpl.nasa.gov> [Online; accessed 26-July-2020].

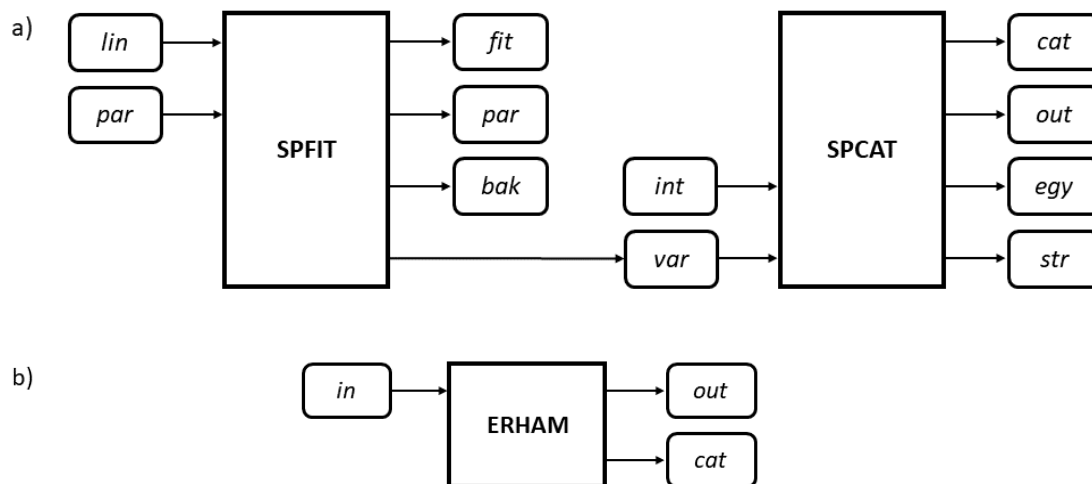


Figure 20: Schematic work flow of a) SPFIT/SPCAT suite of programs and b) ERHAM. Input and output files are depicted by round boxes.

a description in Ref. [84]. The work flow of SPFIT/SPCAT is visualized in Fig. 20a. With SPFIT and the user defined files containing all the assigned lines (*.lin) and definitions of the parameters (*.par), a fit is performed, with the major output containing the fit results (*.fit). The parameter file is overwritten with the new (fit) parameters, the old ones are saved to a backup file (*.bak). Furthermore, a file containing information on the resulting parameters with its uncertainties and the variance matrix is created (*.var). The *var*-file together with a file containing information regarding the predictions (*.int), in particular the transition dipole moment components, are used by SPCAT to predict the molecular spectra (*.cat). General information concerning the predictions are saved (*.out), as well as optional files containing all energy level information (*.egy) and transition dipole moments (*.str).

The big advantage of SPFIT/SPCAT is the great flexibility of setting up molecular Hamiltonians combined with robust and efficient diagonalization and quantum number assignment algorithms. Furthermore, H. M. Pickett introduced a RAS for properly fitting the tunneling-rotation interactions in molecules [65]. The complicated implementation of internal rotation parameters makes the program difficult to use. There are only a few examples of treating molecules with internal rotation with SPFIT, mainly by users with a considerable knowledge of SPFIT,¹⁷ other programs are more favorable, one of them being ERHAM.

¹⁷A list of publications using SPFIT for modeling molecules with internal rotation can be found here: <http://www.ifpan.edu.pl/~kisiel/introt/introt.htm#spfitint> [Online; accessed 26-July-2020].

4.3.2 ERHAM Program

Peter Groner developed a program based on an effective rotational hamiltonian (ERHAM) [72]. BELGI [85], RAM36 [86], and XIAM [87] are further examples of frequently used programs which are able to treat internal rotation in molecules. I. Kleiner classified ERHAM as a combined axis method, as it partly uses Hamiltonians in the ρ -axis system which are finally transformed to the principal axes system [68], whereas P. Groner prefers the declaration of ERHAM as stand-alone acronym, as it does not determine the potential function in comparison to other methods [71]. An informative review article about the program by the author itself can be found in Ref. [71]. The ERHAM code is written for treating molecules with up to two internal rotors.¹⁸ The fit process in other programs is often very time consuming as they try to reproduce the potential function, in particular the barrier height V_3 , sometimes hindering an iterative fitting work-flow outlined in Sec. 4.1. ERHAM fits spectra from molecules undergoing internal rotation to experimental accuracy in a computationally efficient way. The fast operation was one of the main reasons why the ERHAM program is chosen to fit the spectra of *syn*-propanal. ERHAM needs a single input file, including all the molecular information, parameters and assigned lines. The created output file contains the fit results and if specified by the user an additional file containing predictions in the SPCAT format is generated. The work flow of ERHAM is visualized in Fig. 20b.

In the following only a brief phenomenological outline of the effective rotational Hamiltonian is given, based on Refs. [72], [88], and [71], where the interested reader is also referred to for comprehensive mathematical derivations. Of central importance in ERHAM is that the overall wave function is a product of the symmetric rotor eigenfunctions with the wave functions of the internal rotation, described by free rotor functions $|j_i\sigma_i\rangle = (2\pi)^{-1/2} e^{i(n_i j_i + \sigma_i)\alpha_i}$ [71]. A consequence of the periodicity of the potential function is that eigenfunctions and eigenenergies of internal rotation can be expressed as Fourier series [71]. All matrix elements off-diagonal in σ vanish and neglecting matrix elements off-diagonal in the vibrational quantum number v are the reason of the fast performance of ERHAM, as only $(2J + 1) \times (2J + 1)$ -dimensional matrices need to be diagonalized. The general matrix elements of the full Hamiltonian can be looked up in Tables III or IV of Ref. [72], for identical or non-identical rotors, respectively.

The model uses rotational and centrifugal distortion constants as introduced in Sec. 2.1, energy tunneling parameters, rotational as well as centrifugal distortion constant tunneling parameters and some geometrical values of the molecule of interest. The energy tunneling parameters are labeled by $\epsilon_{qq'}$ and are basically the Fourier coefficients of the Fourier expansion approximating internal rotation energy levels. The subscript qq' is

¹⁸One internal rotor can be set (close) to zero, allowing to fit the experimental spectrum of molecules with only one internal rotor. More details can be found in Ref. [71].

denoting the order of the Fourier coefficients for two internal rotors. There is only one internal rotor for *syn*-propanal, therefore $q' = 0$ as it represents the expansion of the second rotor. The nomenclature of the tunneling parameters has its origin in the fact that they are describing integrals, each centered in a potential minimum, which can be interpreted as tunneling between two so-called localized states. Rotational as well as centrifugal distortion constant tunneling parameters are labeled in the same way as their pure rotational partners, as they are inter alia dependent on the respective operators, but are endowed with subscript qq' . Additionally, the length of the dimensionless ρ -vector and the polar angle β (or Θ_{RAM}) between the ρ -axis and the principal a axis are needed for transformation between the principal and ρ -axis system. The angle α between the ρ -axis and a plane spanned by the principal axes a and b is fixed to 0, due to C_s symmetry of *syn*-propanal.

5 Molecular Fingerprints of Propanal

” We are spectroscopists. We like to solve puzzles.”

- Marie-Aline Martin-Drumel -

Propanal is a complex molecule from the perspective of a spectroscopist as the spectrum is very rich in lines even at room temperature. The resulting density of lines is frequently a larger challenge for unambiguously assigning transitions in the (sub-)MMW region than the SNR, especially in higher frequency regions observed in this work. The analyses of both conformers are based on the same iterative procedure of assigning, fitting, and predicting molecular spectra, presented in Sec. 4.1. However, typical spectroscopic fingerprints of *syn*- and *gauche*-propanal have many facets and are very different even though they are conformers of the same molecule. Therefore, different assignment strategies for interpreting and finally modeling the spectroscopic fingerprints are needed, which benefit from typical patterns of *syn*- and *gauche*-propanal (cf. Sec. 2.1.3.c). Observable patterns simplify and enable a solid analysis of several vibrational states of both conformers. At room temperature, *syn*-propanal is significantly populated in a variety of excited states. Thus, several excited states are studied and methyl group internal rotation plays an important role in fitting all of the observed fingerprints, see Sec. 5.1. For example, a comprehensive study of internal rotation effects in the vibrational ground state of *syn*-propanal up to the sub-MMW region allowed for an improved refinement of its astronomical detection (cf. Fig. 5). For *gauche*-propanal, the sufficiently low barrier between the two equivalent configurations leads to a somewhat larger splitting due to tunneling between these configurations, in comparison to the torsional splittings in *syn*-propanal. A main result is the reassignment of the fundamental frequency of the first vibrationally excited state ν_{24} . This is accompanied by observing perturbations originating in interactions of $\nu_{24} = 1$ with the vibrational ground state $\nu = 0$, as is explained in detail in Sec. 5.2. A small portion of the observed MMW region is shown in Fig. 21, highlighting contributions of several vibrational states of both conformers.

5.1 *Syn*-Propanal

Syn-propanal is an asymmetric rotor with $\kappa = -0.7855$ in the vibrational ground state with the prolate limit being $\kappa = -1.0$, see Eq. (2.12). The asymmetry parameter has a comparable value for all studied vibrational states. The analyses benefit from the observations of rather strong *a*- and *b*-type transitions. The respective dipole moment components were determined from Stark-effect measurements as $\mu_a = 1.71$ D and $\mu_b = 1.85$ D [39]. The third dipole moment component is $\mu_c = 0$ D owing to the C_s symmetry of *syn*-propanal, see Fig. 4. From this figure, it is also seen that *syn*-propanal

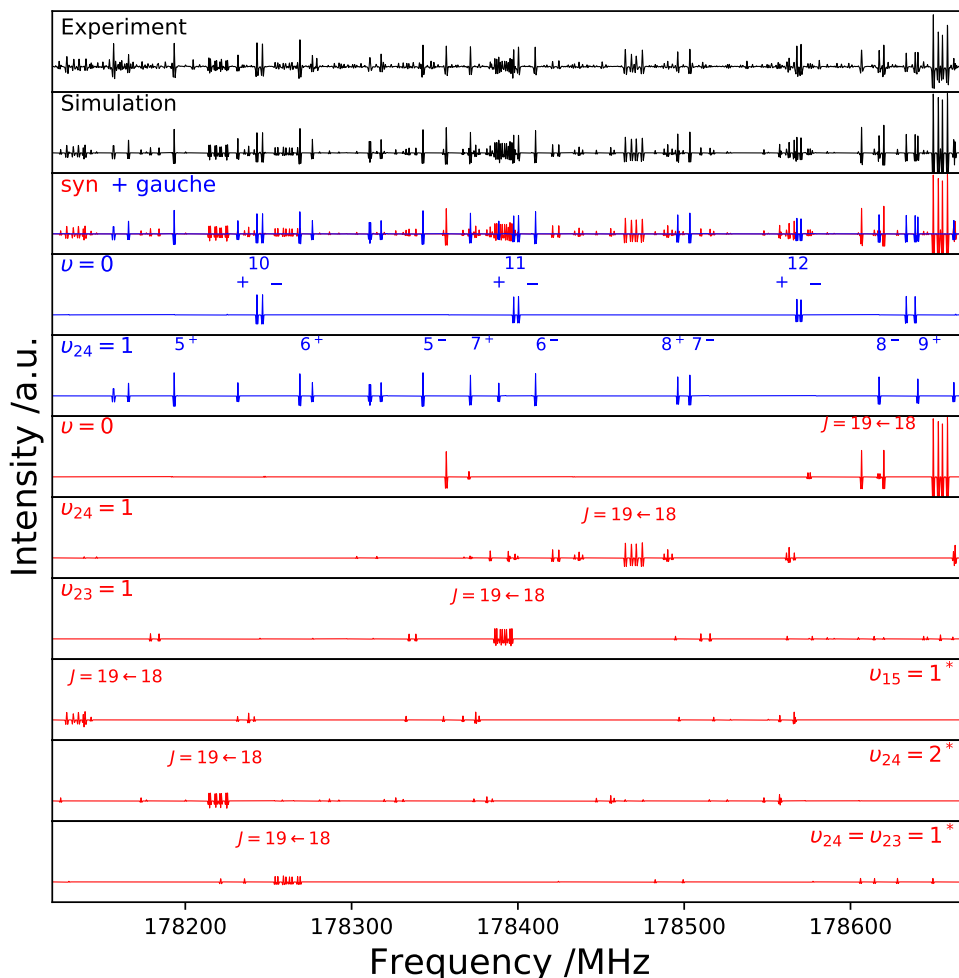


Figure 21: MMW spectrum of propanal around 178.4 GHz. The measured spectrum is shown in the top panel. In the second row from the top, a combined prediction of *syn*- and *gauche*-propanal is shown. One row beneath, predictions of *syn*- and *gauche*-propanal are shown in red and blue, respectively. Contributions of all studied vibrational states within this work are shown from the fourth row from the top to the bottom row, these are $v = 0$ and $v_{24} = 1$ of *gauche*-propanal (in blue), as well as $v = 0$, $v_{24} = 1$, $v_{23} = 1$ and tentatively assigned states $v_{15} = 1^*$, $v_{24} = 2^*$, and $v_{24} = v_{23} = 1^*$ (in red), respectively. For both states of *gauche*-propanal, *a*-type transitions with $J_{K_a, K_c} = 21_{K_a, K_c} \leftarrow 20_{K_a, K_c - 1}$ are highlighted for $K_a > 4$. The larger tunneling splitting of $v_{24} = 1$, compared to $v = 0$, is clearly visible (see splittings of X^+ and X^- for same K_a). For *syn*-propanal, the quartet of nearly oblate paired transitions with $J = 19_{K'_a, K'_c} \leftarrow 18_{K''_a, K''_c}$ and $K_a = 0 \leftarrow 1$, $K_a = 1 \leftarrow 1$, $K_a = 0 \leftarrow 0$, and $K_a = 1 \leftarrow 0$ is observable. Sometimes, even a further splitting due to methyl group internal rotation is clearly seen (see for example $v_{24} = v_{23} = 1^*$ at around 178260 MHz). This resulting octet structure played a key role in assigning transitions of so far unknown vibrational states.

is the lower energy conformer of propanal. Due to the energy difference between the two conformers, *syn*- is already detected in space in contrast to *gauche*-propanal [23]. However, discrepancies between astronomical observations and predicted fingerprints are the main reason to revisit the ground vibrational state of *syn*-propanal, as already mentioned and illustrated in Fig. 5. Furthermore, propanal is found in space with ALMA not only in colder environments but also in comparably warm gas environments of around 125 K, which may increase chances of a future detection of low lying vibrational states [49]. Therefore, in this work the lowest lying vibrational states of *syn*-propanal are also studied in detail. One of the major tasks is to satisfyingly model torsional splittings due to the methyl group internal rotation. The ERHAM program from P. Groner is used for proper modeling of observed splittings to experimental uncertainty [72]. A splitting into two equally intense components is observed, labeled with A and E. A detailed group-theoretical derivation of energy level splittings and spin statistics based on the molecular symmetry with allowed internal rotation can be found in Sec. "Group Theory of *Syn*-Propanal" in the Appendix. Treating the internal rotation is of even larger importance for higher vibrationally excited states as the observed splittings become larger. The initial internal rotation parameter ρ and the angle describing the orientation of the ρ -axis-system to the principle axis system Θ_{RAM} can be calculated with the components of the ρ -vector given in Eq. (2.47), resulting in the length of the ρ -vector, see Eq. (2.48), and $\Theta_{RAM} = \arctan(\rho_b/\rho_a)$ [68]. Necessary parameters for calculations of ρ and Θ_{RAM} in the aforementioned formulas – such as the direction cosines λ_g , the moments of inertia I_g , and the moment of inertia of the methyl group I_α – are taken, or calculated from the rotational constants as well as the angle $\angle(a, i)$ between the internal rotation axis i and the molecular axis a , given in Ref. [42]. The resulting values $\rho \approx 0.06$ and $\Theta_{RAM} \approx 28^\circ$ are the initially fixed values for the fit procedure. At first iteration steps, these values are kept fixed as they are strongly correlated with the energy tunneling parameter ϵ_{10} .

Several low-lying vibrationally excited states of *syn*-propanal are observable in room temperature spectra of propanal because of the rather strong dipole moment components and as *syn*-propanal is the lowest energy conformer. A schematic overview of expected vibrational energy levels of *syn*-propanal below 500 cm^{-1} is presented in Fig. 22. The ground vibrational state $v = 0$ as well as the two energetically lowest lying vibrationally excited states, the aldehyde torsion $v_{24} = 1$ and the methyl torsion $v_{23} = 1$, are well described and already published in Ref. [50]. The fingerprints of $v = 0$ and $v_{24} = 1$ can be described without limitations in the fit quality and are presented in Secs. 5.1.1 and 5.1.2.a. With the help of these rotational fingerprints the correct assignment of rotationally resolved FIR spectra can be made as is demonstrated with the reassignment of $v_{24} = 1 \leftarrow 0$ to $133.9754525(39) \text{ cm}^{-1}$ in Sec. 5.1.2.b. The analyses of these spectra is rather straightforward as the involved states can be considered as

of 2 GHz. Additional discrepancies were suspected at the beginning of this study. These issues along with largely identical observed frequency regions of Ref. [43] and the measurements performed in this work, lead to an omission of the literature data from the fit after first transitions are successfully assigned and an improved model is derived. Nevertheless, all literature data, especially the omitted MMW data, facilitate new assignments in the MMW region in the first place. In general, after deriving a first sophisticated model in the MMW region, transitions in frequency windows of about 30 GHz are assigned, almost independent of their quantum numbers. This results in a straightforward analysis of the spectra. A deterioration of up to 20% of the fit quality (*wrms*) is observed for iterations above 300 GHz. At an intermediate step, the *wrms* was lower when L_K was included instead of L_{KKJ} . L_K as well as L_J , which were included in intermediate steps, are both removed in the final fit, whereas L_{KKJ} is included. Finally, the *wrms* is comparable to fits in lower frequency ranges. This is one example of small ambiguities in the fit procedure. Here, the ambiguity is assumed to occur as higher order parameters are needed to properly describe energy levels with higher quantum numbers but not enough information in already assigned transitions is available at this point to determine these parameters. During the iterative fitting procedure, most of the omitted literature transitions are actually remeasured at the final stage of the fit. For testing the robustness of the model, the 112 omitted transitions from the literature are included to the final analysis with a total of 8551 transitions. It is observed that only four showed deviations, mainly from neglecting internal rotation splittings. Two of the reasons for the large number of assigned transitions are the strong μ_a - and μ_b -dipole moment components. More importantly, measuring different types of transitions allow for determining all rotational constants properly. In total, 3505 *a*-type transitions (2963 belonging to qR series, 542 to qQ -series), and 4403 *b*-type transitions (*R*-branch: 1567, *Q*-branch: 2832, and *P*-branch: 4) are assigned up to 500 GHz with $J \leq 77$ and $K_a \leq 40$. Furthermore, 372 nominally forbidden or false *c*-type transitions as well as 271 so called *x*-type transitions ($\Delta K_a = \Delta K_c = 0$) are assigned. These transitions originate either in mixed wave functions, i.e. when the torsional splitting is approximately equal to the asymmetry splitting, or from a mislabeling of the energy levels in ERHAM, as the levels are simply labeled by increasing eigenvalues of the Hamiltonian, see also Ref. [89] for an explanation of the author of ERHAM. A detailed quantum number coverage of the analysis can be found in Fig. A15. This detailed study of the ground vibrational state $v = 0$ results in the spectroscopic parameters presented in Table 3.

Table 3: Spectroscopic parameters^a (MHz) of the ground state ($v = 0$), first excited aldehyde torsion ($v_{24} = 1$), and first excited methyl torsion ($v_{23} = 1$) of *syn*-propanal.

Parameter	$v = 0$	$v_{24} = 1$	$v_{23} = 1$
A	16669.626420(154)	16712.057839(167)	16642.87187(61)
B	5893.503711(49)	5857.196275(49)	5871.180340(171)
C	4598.982111(48)	4595.250184(50)	4592.798935(116)
Δ_K	$\times 10^3$ 50.06225(63)	49.70451(84)	43.9445(37)
Δ_{JK}	$\times 10^3$ -19.370540(153)	-18.097558(232)	-17.5153(34)
Δ_J	$\times 10^3$ 5.354247(37)	5.236678(38)	5.223946(211)
δ_K	$\times 10^3$ 4.211646(164)	3.22843(30)	1.6032(32)
δ_J	$\times 10^3$ 1.5662438(66)	1.5132959(108)	1.527602(94)
Φ_K	$\times 10^9$ 986.40(80)	1070.36(179)	-221.1(104)
Φ_{KJ}	$\times 10^9$ -606.15(37)	-577.21(64)	143.2(109)
Φ_{JK}	$\times 10^9$ 77.271(65)	62.316(141)	-128.2(92)
Φ_J	$\times 10^9$ 2.1239(88)	2.0061(92)	0.827(124)
ϕ_K	$\times 10^9$ 292.50(58)	37.46(138)	-1471(46)
ϕ_{JK}	$\times 10^9$ 27.236(49)	25.349(112)	138.8(57)
ϕ_J	$\times 10^9$ 1.49907(138)	1.28486(267)	0.555(62)
L_K	$\times 10^{12}$ -	-79.43(120)	-
L_{KKJ}	$\times 10^{12}$ 14.082(239)	21.93(41)	-
L_{JK}	$\times 10^{12}$ -	-4.736(160)	-
L_{JJK}	$\times 10^{12}$ -	-	-71.7(56)
l_{KJ}	$\times 10^{12}$ -	-	-809(32)
l_{JK}	$\times 10^{12}$ -	-	-16.49(272)
ϵ_{10}	-3.0942(57)	38.7984(68)	130.5541(250)
ϵ_{20}	$\times 10^3$ -	-	68.4(71)
$[A - (B + C)/2]_{10}$	$\times 10^3$ -	-2.477(33)	-7.887(224)
$[(B + C)/2]_{10}$	$\times 10^3$ -	-0.7392(62)	-3.761(38)
$[(B - C)/4]_{10}$	$\times 10^3$ 0.09286(194)	-1.1251(80)	-3.8450(229)
$\Delta_{K_{10}}$	$\times 10^6$ -	-	-10.80(65)
$\Delta_{JK_{10}}$	$\times 10^6$ -	1.1215(216)	8.83(38)
$\delta_{J_{10}}$	$\times 10^6$ -	0.1903(33)	0.4833(83)
$d_{2_{10}}$	$\times 10^6$ -	0.26299(269)	0.5194(56)
$h_{2_{10}}$	$\times 10^{12}$ -	-29.11(97)	-
$h_{3_{10}}$	$\times 10^{12}$ -	-16.082(245)	-
$G_{a_{10}}$	$\times 10^3$ -	14.82(31)	67.0(33)
ρ^b	$\times 10^3$ 65.681(116)	63.8032(90)	61.9026(102)
$\Theta_{RAM} / ^\circ$	27.871(60)	28.5299(48)	28.4352(82)
Single state fits			
no. of lines	3901	5084	2085
no. of transitions	8551	6823 ^c	2760 ^d
standard deviation ^b	0.94	0.93	1.06

^a Watson's A reduction in the I^r representation is used in ERHAM. Numbers in parentheses are one standard deviation in units of the least significant figures. In the first block rotational and centrifugal distortion constants can be found, in the second ERHAM tunneling parameters and in the third geometrical values (not in MHz). The bottom row contains general information about the fits.

^b Weighted unitless value for the respective single state fit.

^c Two transitions from the literature are unweighted in the fit.

^d In total 3688 transitions are assigned, but presumably perturbed ones are unweighted in the fit.

5.1.2 Aldehyde Torsion ν_{24}

In the first place, the energetically lowest vibrationally excited states of *syn*-propanal, the aldehyde torsion $\nu_{24} = 1$, is measured and analyzed in the (sub-)MMW region to analyze its rotational spectrum and to derive very accurate spectroscopic parameters (Sec. 5.1.2.a). In combination with the spectroscopic parameters of the vibrational ground state, predictions are derived to reassign the fundamental frequency ν_{24} to $133.9754525(39) \text{ cm}^{-1}$ in the ro-vibrational spectra (Sec. 5.1.2.b).

5.1.2.a Aldehyde Torsion $\nu_{24} = 1$

The aldehyde torsion $\nu_{24} = 1$ was not studied as extensively as the ground vibrational state. Butcher and Wilson assigned in total 28 transitions (14 A and 14 E components) to 25 observed lines in the frequency region 15–31 GHz; Three observed lines were observed to be blends of the respective A and E components [39]. The coverage of the quantum numbers is small with J up to 6 and K_a up to 2 [39]. As for $\nu = 0$, ERHAM is used to refit the literature data. Fortunately, again, *a*- and *b*-type transitions were assigned thanks to the two rather strong dipole moment components, which allows to fit the rotational constants A , B , and C . Also the energy tunneling parameter ϵ_{10} could be fit due to the observed internal rotation splitting. All other parameters are initially fixed to the final values of the ground state analysis. With this approach the parameters $A = 16712.02(2) \text{ MHz}$, $B = 5857.21(1) \text{ MHz}$, $C = 4595.25(1) \text{ MHz}$ and $\epsilon_{10} = 37.3(11) \text{ MHz}$ are derived. In particular, the rotational constants are in a very good agreement with the values of the final fit, see Table 3, even though the standard deviation is not good with 2.98. First assignments in the MMW region (76–86 GHz) are done quite straightforward thanks to the close agreement of the rotational constants. Thereby, unambiguous assignments are supported by the prominent doublet structure arising from tunneling splitting into A and E components, as is demonstrated in Fig. 23. The nominal sensitivity limit of the experimental setup is around 75 GHz. Regions with less intense lines around 78 GHz and for frequencies below 76 GHz have to be taken into account, see Fig. 23. Even though predictions might be shifted by several megahertz, the rather strong lines can be easily assigned, even in less sensitive regions of the detector. The assignment of transitions in the frequency region of 75–129 GHz is divided into three iterations. First assignments of 64 transitions in the MMW region are followed by 219 and 341 transitions, adding up with the literature transitions to 652 ($= 28 + 64 + 219 + 341$) transitions. The quantum numbers covered values up to $J = 42$ and K_a up to 14. An overview of the frequency region of initially assigned transitions as well as the quantum number coverage is illustrated in Fig. A14 in the Appendix.

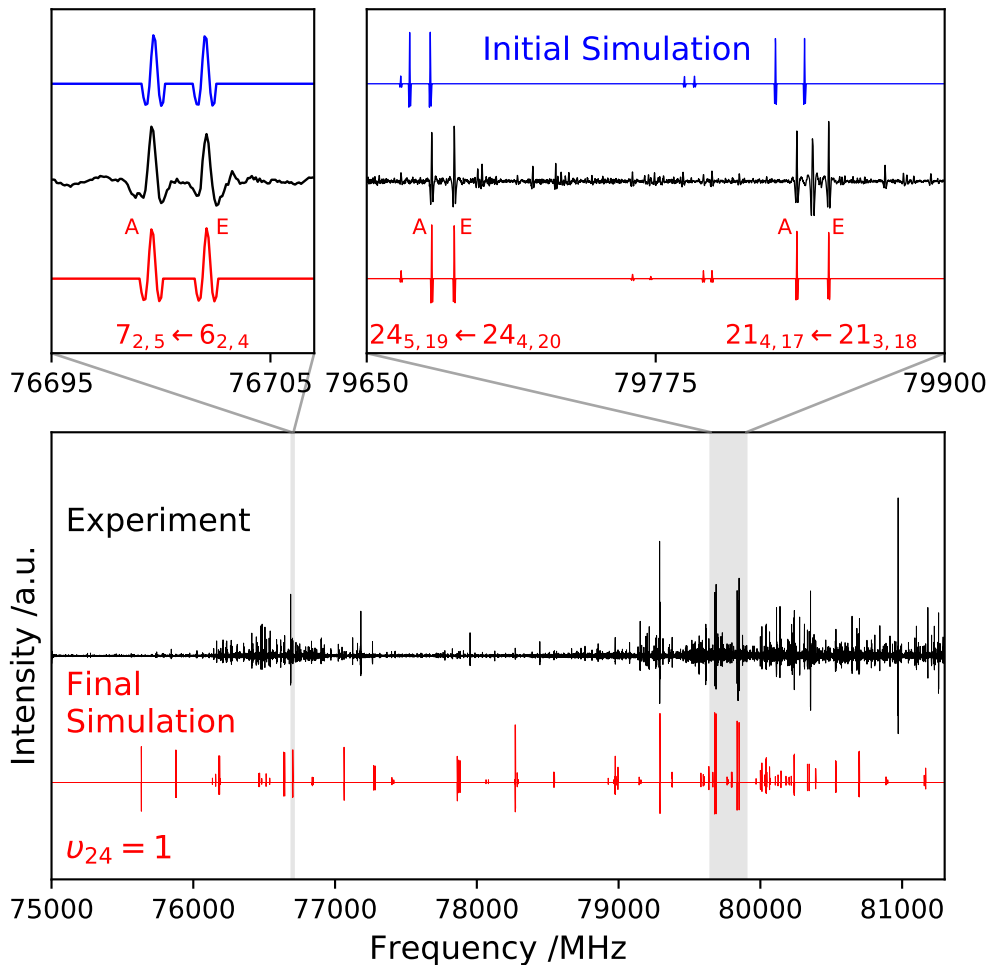


Figure 23: First assignments in the MMW region of $\nu_{24} = 1$ of *syn*-propanal.

The broad coverage in the 3 mm wavelength region allows for accurate predictions to higher frequency regions. Next, assignments are done in the frequency window of 170–200 GHz and from here on usually 30 GHz frequency windows are assigned with subsequent new predictions, identical to the procedure of the analysis of the ground vibrational state. However, during the analysis special care has to be taken on the treatment of *b*-type transitions with higher K_a quantum numbers than already included in the fit. Sometimes these transitions are weighted out in intermediate iterations, as they show deviations with σ much larger than 3 ($\sigma = (\nu_{obs} - \nu_{calc})/\Delta\nu_{obs}$), which is statistically not expected in the observed quantity. These transitions are weighted carefully step by step into the dataset at each iteration as far as the *wrms* does not increase too much. This is also observed for some transitions of the ground vibrational state, albeit to a lesser extend. The assignments of *Q*-branch *b*-type transitions is usually straightforward as these series can be easily followed in comparably small frequency windows, see Fig. 24. However, even in the final fit, a small fraction of these transitions show deviations to the finally derived model. This may also originate in the fact that

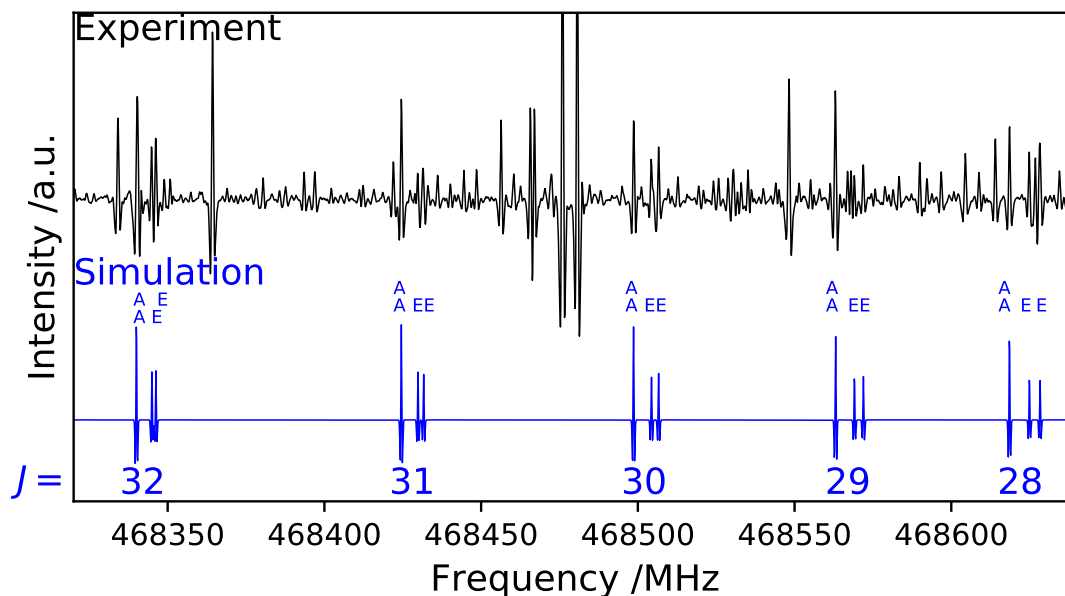


Figure 24: Q -branch b -type transitions of $\nu_{24} = 1$ of *syn*-propanal. The series, transitions with $J_{21,K_c-1} \leftarrow J_{20,K_c}$, are easy to identify, but often observed to be partly blended. The J quantum numbers are given as well as the tunneling components A and E of both asymmetry sides. Intense features which are not labeled may arise from other already assigned vibrational states. Their assignment is omitted for clarity. For example, the lines at 468475.96 MHz (A) and 468480.68 MHz (E) with truncated intensities are oblate paired transitions of $\nu_{23} = 1$.

these transitions are frequently partly blended as the respective frequency windows are close to the confusion limit. Besides these minor details, a satisfactory quantum mechanical description of $\nu_{24} = 1$ of *syn*-propanal is obtained. Spectroscopic parameters can be found in Table 3. Overall, the assignment and fitting procedure is identical to the vibrational ground state, except for the first assignments which required increased caution initially. In total, 6823 transitions are fit with a standard deviation of 0.93.

5.1.2.b Fundamental Band $\nu_{24} = 1 \leftarrow 0$

The analyses of the rotational spectra of $\nu = 0$ and $\nu_{24} = 1$ lead to very accurate spectroscopic parameters, see Table 3. In combination with the assignment of the fundamental frequency ν_{24} at 135.1 cm^{-1} from the literature [45], the assignment of the high-resolution FIR spectrum should be straightforward, even though no ro-vibrational transitions are available from the literature. However, ν_{24} turned out to be falsely determined and ERHAM does not support a direct fitting and/or predicting of ro-vibrational transitions, thus the SPFIT/SPCAT suite of programs is used instead. In this way, an accurate fundamental frequency ν_{24} is determined.

The accuracy of already determined spectroscopic parameters is not expected to increase substantially by including FIR transitions to the fit, since these have much larger uncertainties compared to MMW lines. Therefore, and in particular for time saving reasons, the SPFIT fitting procedure is kept as simple as possible. The A and E components of each of the two vibrational states $v = 0$ and $v_{24} = 1$ are effectively fit as single state fits without a special treatment of the effects from internal rotation. The aldehyde torsion is a motion out of the symmetry plane ($v_{24} = 1$ is of A'' symmetry), therefore the magnitude of μ_c is changing substantially and thus an intense c -type ro-vibrational spectrum is observed. Two bands are predicted as the ro-vibrational transitions also follow the selection rules $A \leftrightarrow A$ and $E \leftrightarrow E$ (cf. Fig. A1). As already mentioned, based on the ro-vibrational predictions no patterns or series of lines could be assigned initially by assuming $\nu_{24} = 135.1 \text{ cm}^{-1}$. An agreement of predictions and observations is quickly found with PGOPHER by shifting manually the energy differences of A and E levels to approximately 134.0 cm^{-1} (cf. Fig. 25), while all other parameters are kept fixed. New predictions with SPCAT are performed on the basis of the two manually adjusted energy differences. Even this rather simple approach allows for straightforward assignments of several series by using the LWW program [90,91].¹⁹ The line uncertainty is estimated to be $1 \cdot 10^{-4} \text{ cm}^{-1}$ for strong and $2 \cdot 10^{-4} \text{ cm}^{-1}$ for weak lines. In total, 5028 c -type transitions ($3868 \times A + 1160 \times E$) are assigned which cover a wavenumber region of $101\text{--}181 \text{ cm}^{-1}$ with $J \leq 75$ and $K_a \leq 38$ for A and with $J \leq 74$ and $K_a \leq 25$ for E. A more thorough treatment of internal rotation would probably allow for assigning more E transitions, but already this large number of transitions is more than sufficient to determine the energy difference very accurately. The energy differences²⁰ are determined in a global fit to $E_A = 4016568.098(79) \text{ MHz}$ (or $133.9782521(26) \text{ cm}^{-1}$) and $E_E = 4016442.202(173) \text{ MHz}$ (or $133.9740527(58) \text{ cm}^{-1}$). Finally, solely the ro-vibrational transitions are refit with fixed spectroscopic parameters, including the energy differences, to judge the quality of the ro-vibrational fit. The 5028 c -type transitions are fit with a *rms* of $1.3 \cdot 10^{-4} \text{ cm}^{-1}$ (*wrms* = 1.12). The agreement of final predictions with observations for both bands, A and E, is convincing as is demonstrated in Fig. 25.

The energy difference between E and A bands is $\Delta E^{vib} = E_E - E_A = 125.896(190) \text{ MHz}$. The energy difference between A and E substates within one vibrational state is approximately $3\epsilon_{10}$, see Eq. (A8). As A and E energy levels are inverted for the ground and first excited vibrational state, see Fig. 12, the energy differences of the substates in both vibrational states, determined by rotational spectroscopy, need to be added to

¹⁹Documentation at <http://lww.amu.edu.pl> [Online; accessed 28-July-2020]. The corresponding author is Wiesław Łodyga (Email: wlodyga@amu.edu.pl). The program is based on Loomis Wood plots.

²⁰Here presented in the frequency dimension ($\nu = E/h$).

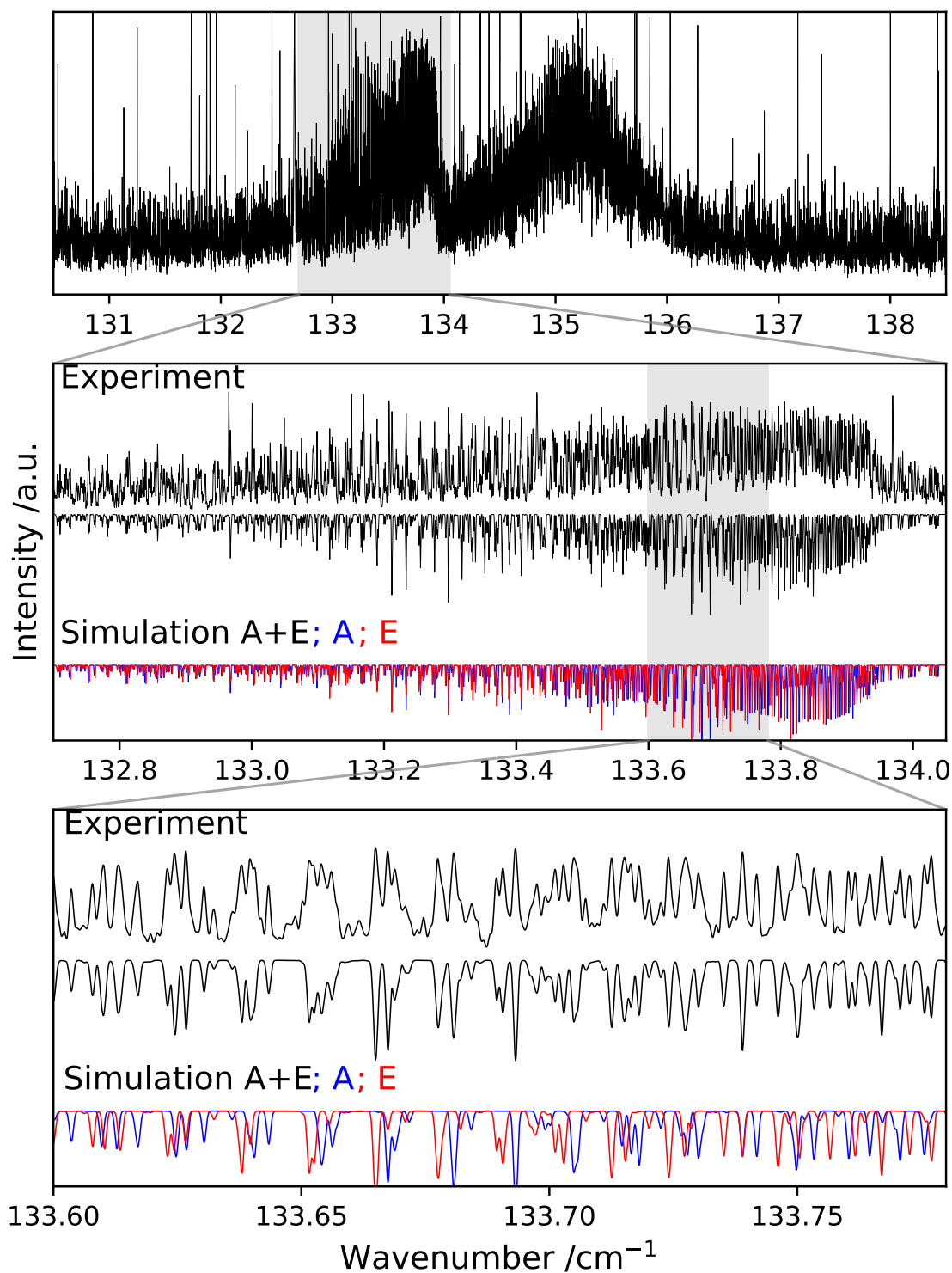


Figure 25: FIR spectrum of propanal. The fundamental band of ν_{24} of *syn*-propanal is reassigned to $133.9754525(39) \text{ cm}^{-1}$ based on the analysis with SPFIT. A and E bands are shown in blue and red, respectively. The band at 135.1 cm^{-1} is assumed to be the hot band $\nu_{24} = 2 \leftarrow 1$, see Sec. 5.1.4. The strong isolated lines are mainly originating from residual water in the cell.

derive the energy difference between A and E bands observed in the ro-vibrational spectrum (cf. Fig. A1). The expected energy difference, calculated from the rotational analysis with $\epsilon_{10}^{\nu=0} = -3.0942(57)$ MHz and $\epsilon_{10}^{\nu_{24}=1} = 38.7984(68)$ MHz (cf. Table 3), is $\Delta E^{rot} = |3 \cdot \epsilon_{10}^{\nu=0}| + |3 \cdot \epsilon_{10}^{\nu_{24}=1}| = 125.678(27)$ MHz. The (quasi) agreement of energy differences determined from ro-vibrational and rotational spectra within their uncertainties is a further confirmation of the correct assignment. Furthermore, from Fig. A1 it can be seen that the fundamental frequency can be calculated with $\nu = (2 \cdot E_E + E_A)/3$. Therefore, the fundamental frequency of ν_{24} is reassigned to $133.9754525(39)$ cm^{-1} (or $4016484.167(118)$ MHz).

5.1.3 Methyl Torsion $\nu_{23} = 1$

Analyzing the rotational spectra of the energetically second lowest vibrationally excited state, the methyl torsion $\nu_{23} = 1$, is more challenging compared to the ground vibrational state $\nu = 0$ or the first excited vibrationally excited state $\nu_{24} = 1$. First of all, the observed lines are less intense than for the other two states due to the higher energy of 219.9 cm^{-1} [45]; The intensities are estimated to be roughly a third of $\nu = 0$ ones. Moreover, perturbed transitions complicate the analysis. The basis for the analysis of $\nu_{23} = 1$ is comparable to the $\nu_{24} = 1$ one. Butcher and Wilson assigned 20 transitions ($10 \times A + 10 \times E$) with J up to 5 and K_a up to 1 in the frequency range of 13–31 GHz [39]. Again, the initially determined parameters with ERHAM of A , B , C , and ϵ_{10} with simultaneously fixing all other parameters to the ground state values are close to their final values, thanks to the assignment of a - and b -type transitions.

On account of larger splittings due to the methyl group internal rotation and less intense lines, the number of assigned lines in the first steps in the 3 mm wavelength region is somewhat smaller compared to $\nu_{24} = 1$ and in total four iterations, one more than for $\nu_{24} = 1$, are accomplished before predictions followed by assignments in the frequency regions above 170 GHz are done. From here on, identical to the analyses of $\nu = 0$ and $\nu_{24} = 1$, transitions are usually assigned in frequency windows of tens of gigahertz for each iteration. One of the most intense and easy assignable patterns is observable due to the oblate pairing of energy levels (reminder: two energy levels are oblate paired if they have identical energies, K_c 's, and J 's). This is true for the upper asymmetry side J of levels with K_a and the lower asymmetry side $J + 1$ with $K_a + 1$. A typical quartet structure of nearly oblate paired transitions is observable (reminder: b -, a -, a -, b -type pattern, described for simplicity by $K_a \leftarrow K_a + 1$, $K_a + 1 \leftarrow K_a + 1$, $K_a \leftarrow K_a$, and $K_a + 1 \leftarrow K_a$, see Sec. 2.1.3.c). Taking the internal rotation splitting into A and E components into account leads to a total of eight involved lines (octet structure). If energy levels are not oblate paired, four doublets significantly separated in frequency are observed, which will approach if the energy levels are close to oblate pairing until

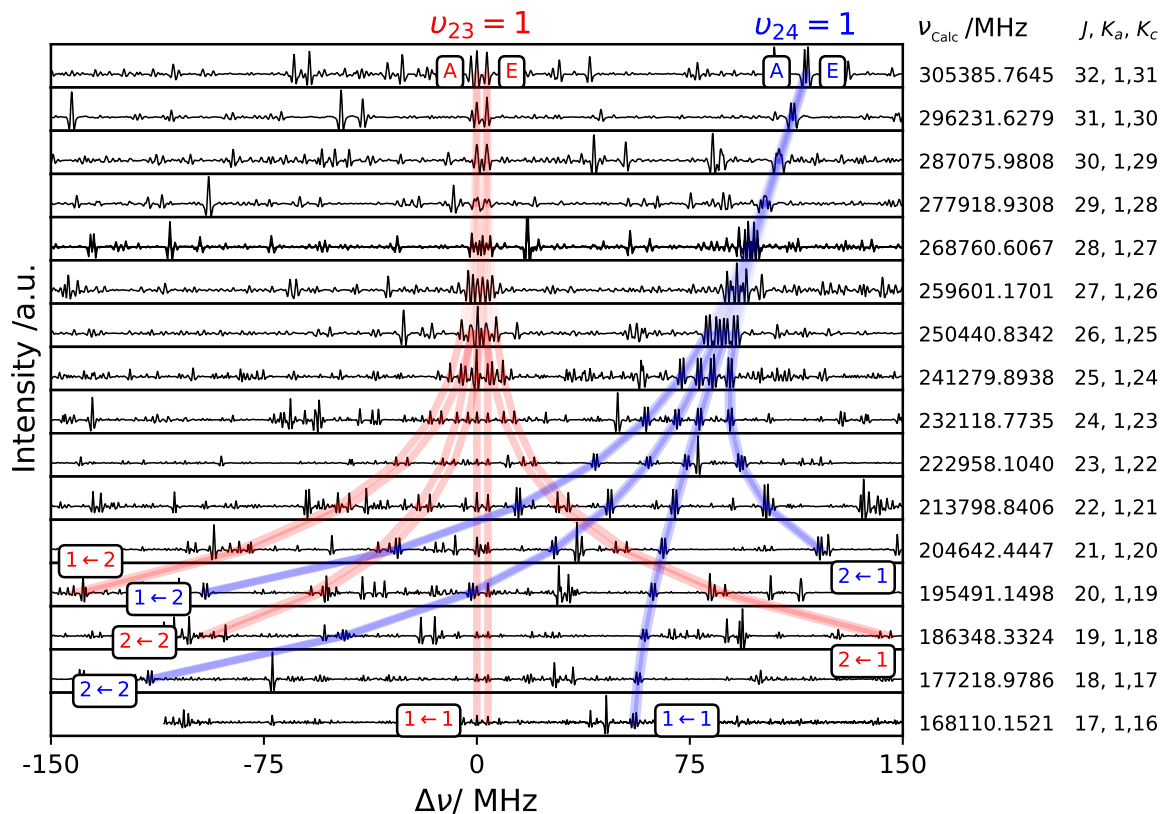


Figure 26: Oblate pairing of A and E components of $\nu_{23} = 1$ and $\nu_{24} = 1$ of *syn*-propanal (octet structure, see text for labeling and more information). Upper state quantum numbers of the predicted frequencies of the Loomis-Wood plot are given on the right hand side for the A component of a -type transitions $J_{1,J-1} \leftarrow (J-1)_{1,J-2}$ ($K_a = 1 \leftarrow 1$) of $\nu_{23} = 1$. Energy levels of the asymmetry side J of levels with $K_a = 1$ and the lower asymmetry side $J+1$ with $K_a = 2$ are oblate paired for high J . For this reason, a - and b -type transitions are blended for high J . K_a numbers are given in the figure.

they will be fully blended, at least all A and E components, respectively. This can be observed for the eight transitions of the energy levels with $K_a = 1$ (with $J = K_a + K_c$) and $K_a = 2$ (with $J+1 = K_a + K_c$) in Fig. 26. The respective rotational transitions of both vibrationally excited states $\nu_{24} = 1$ and $\nu_{23} = 1$ are close in frequency and thanks to the typical fingerprints, these transitions can be unambiguously assigned. Furthermore the larger splittings due to internal rotation of $\nu_{23} = 1$, compared to $\nu_{24} = 1$, is seen. The oblate pairing of transitions with increasing K_a occurs at increasing J . These clearly observable and easily assignable fingerprints played an important role in the analysis of $\nu_{23} = 1$, not only with respect to unambiguous assignments of transitions themselves, but more importantly for recognizing and localizing perturbations in the fingerprint of $\nu_{23} = 1$. For example, transitions arising from energy levels with $K_a = 3$

and 4, which are oblate paired for high J , can be easily assigned up to $J_{max} = 51$. However, transitions with $J = 39 - 46$ show deviations up to 5 MHz, see Fig. A21, and are excluded in the final fit. In case these perturbations are not localized yet, thus perturbed transitions are still included in the fit, the *wrms* deteriorates. Typically, these transitions show trends in their deviations if they are unweighted in the fit. In the end, 2760 out of 3688 transitions are assumed to be unperturbed and are satisfyingly reproduced within the derived model (cf. Fig. A17), whose spectroscopic parameters are shown in Table 3.

5.1.4 Vibrationally Excited States $v_{24} = 2$, $v_{15} = 1$, and $v_{24} = v_{23} = 1$

The reassignment of the fundamental band of v_{24} , see Sec. 5.1.2.b, is consequently followed by an unavoidable reassignment of the hot band $v_{24} = 2 \leftarrow 1$ as in the literature this hot band was mistakenly assigned to the newly assigned fundamental band v_{24} . Most likely the hot band is blue shifted in frequency in comparison to the fundamental band, in contrast to further observable hot bands (cf. Fig. A12). This indicates the so far unstudied Fermi resonance between $v_{24} = 2$ and $v_{15} = 1$. In addition, $v_{23} = 1$ is observed to show perturbations, see Sec. 5.1.3, which are assumed to originate in interactions with $v_{24} = 2$ or $v_{15} = 1$. The compulsory reassignment and the unstudied interactions are two prominent reasons to study the aforementioned excited vibrational states. Furthermore, it may be worth to verify the FIR assignments of various vibrational states from Refs. [45] and [46] with rotationally resolved rovibrational spectra. Another reason to study higher excited states is that several of them are low enough in energy to be populated considerably at room temperature and these may help to describe the potential energy surface of propanal in even more detail in the future.

The oblate paired transitions of A and E substates can be followed easily for $v = 0$, $v_{24} = 1$, and $v_{23} = 1$ in Loomis-Wood plots, see Fig. 27. These lines are rather intense as the various components of the typical quartet structure add up and therefore these blended lines are easily assignable. Apart from already assigned transitions, further oblate paired series are clearly observable, see Fig. 27. However, some of the series show severe perturbations even for energy levels with $K_a = 0$. For further complication, the non-blended quartet series of *a*- and *b*-type transitions are challenging to follow for low J in the W-band region. Many possible candidate lines may be present for these less intense lines, hampering an unambiguous assignment. Unfortunately, satellite patterns for low K_a are not as obvious as desirable to directly notice patterns. Assigning *a*- and *b*-type transitions in the W-band region, which are not oblate paired, is of fundamental interest. The importance of determining different types of transitions is proven with the analysis of $v_{24} = 1$ and $v_{23} = 1$, see Secs. 5.1.2.a and 5.1.3. In these analyses, on the

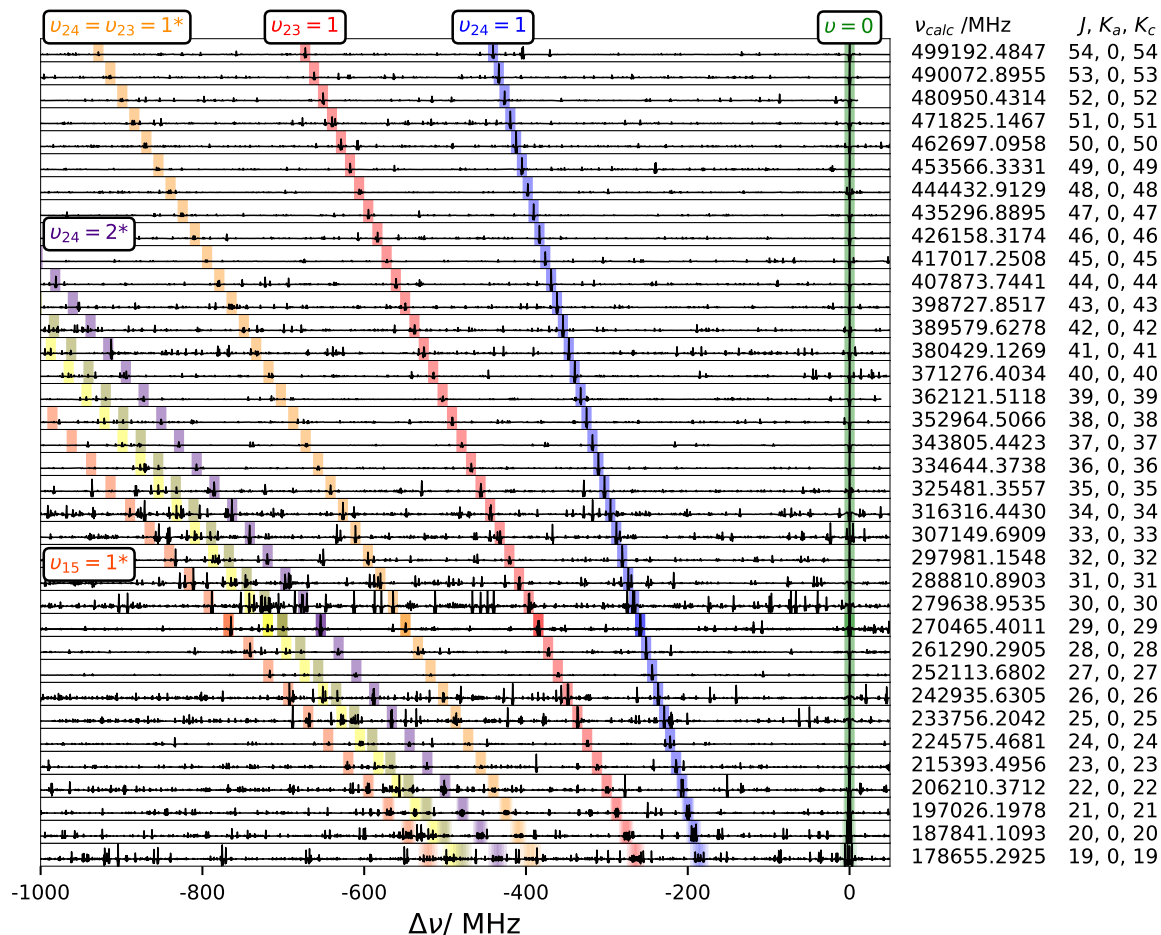


Figure 27: Satellite spectra of *syn*-propanal. The center frequencies of the Loomis-Wood plot are predicted *a*-type transitions $J_0, J \leftarrow (J-1)_0, J-1$ of the A component of $v = 0$. The intense satellite lines are originating in the typical oblate paired quartet of transitions. The labeling of vibrational states marked with an asterisk (*) might not be irrevocable, see text for more information.

basis of merely 28 and 20 transitions in the MW region, accurate enough predictions could be made to assign lines in the MMW region.

DM-DR measurements allow for secure assignments, as is explained in Sec. 3.1.3. This technique is particularly useful for finding additional vibrationally excited states without the need of *ab-initio* calculations and false assignments are avoided. A sophisticated assignment strategy is explained in detail in Sec. 4.2. At first, *a*-type transitions of qR series with $K_a = 0$, in particular $J_0, J \leftarrow (J-1)_0, J-1$, are tried to be linked in the W-band region. For doing so, candidate lines are ascertained either by visual inspection of a Loomis-Wood plot or by fitting the easy assignable oblate paired transitions to determine B , C , and D_J , see Fig. 27. In fact, both methods are applied successfully. Furthermore, if A and E components are observed to be split, also ϵ_{10} is determinable. Quite accurate predictions to lower transitions in the W-band region are derived in

this way for a -type transitions. Thus, the size of the search windows for DM-DR measurements decreases. Once the qR series with $K_a = 0$ are assigned, further transitions or series can straightforwardly be linked and assigned by simply following the specific assignment strategy presented in Sec. 4.2.

This strategy leads to a first solid description of three more vibrationally excited states in the W-band region. If the first series is found, the remainder of the analysis in the W-band region is quite straightforward for unperturbed transitions, at least for these newly described states. However, all vibrational states show perturbations at higher quantum numbers, limiting the quantum number coverage so far (cf. Figs. A18–A20). Untreated perturbations may be the reason for the unusual determination of ϕ_K in the early stage of the analysis of $\nu_{15} = 1^*$. The value may be rather effective but the parameter is kept in the fit as it reduces the *wrms* from 1.57 to 1.03. The spectroscopic parameters of $\nu_{24} = 2^*$, $\nu_{15} = 1^*$, and $\nu_{24} = \nu_{23} = 1^*$ are collected in Table 4.

Unfortunately, the assignment of the three vibrational bands is not straightforward. Determined rotational constants of all observed vibrationally excited states of *syn*-propanal are compared to *ab-initio* calculations on the CCSD(T)/ANO0 level of theory [92] for labeling these bands, see Table 5. First of all, a good agreement of experimental and theoretical values of the rotational constants B and C of $\nu_{24} = 1$ and $\nu_{23} = 1$ is observed. The theoretical values are calculated by taking the difference of the observed ground state rotational constants with the respective *ab-initio* vibration-rotation constants α . The A rotational constants are usually quite sensitive to small structural changes of the molecule and larger deviations are common. Unfortunately, the agreement of observed B and C rotational constants of the newly determined vibrational states with *ab-initio* ones is not as good as for $\nu_{24} = 1$ and $\nu_{23} = 1$. However, deviations of nearly the same magnitude but with opposite signs are observed for the two vibrational states $\nu_{15} = 1$ and $\nu_{24} = 2$, see red and blue numbers in Table 5. Here, $\nu_{24} = 2$ is calculated with the observed α and applying the harmonic approximation to it. The deviations may be caused by the Fermi resonance between these two bands, as their rotational parameters would mix in this case, see Eq. (2.33). The sums of the rotational constants with $(X_1^F + X_2^F)$ and without $(X_1^0 + X_2^0)$ the Fermi resonance are identical. As a reminder, evidence for the Fermi resonance is already noticed in the indispensable reassignment of the hot band $\nu_{24} = 2 \leftarrow 1$. Therefore, the two bands are tentatively assigned to $\nu_{24} = 2^*$ and $\nu_{15} = 1^*$. The assignment of A and E components of $\nu_{15} = 1^*$ should be verified in the future as $\epsilon_{10} > 0$ is expected for a singly excited state because $\epsilon_{10} < 0$ for $v = 0$, see Fig. A1.

The third vibrational state is tentatively assigned to $\nu_{24} = \nu_{23} = 1^*$, as the observed octet patterns of qR series seem to be the most intense ones among the remaining unassigned patterns and $\nu_{24} = \nu_{23} = 1$ is the energetically next higher vibrationally excited state. Butcher and Wilson assigned four lines in the microwave region to $\nu_{24} = 2$

[39]. In contrast to the hypothesis based on the Fermi resonance, these transitions agree with the third unknown vibrational state assigned in this thesis $\nu_{24} = \nu_{23} = 1^*$. However, the magnitude of the energy tunneling parameters ϵ_{10} is expected, and is in fact observed, to be larger for $\nu_{24} = \nu_{23} = 1^*$ than for $\nu_{24} = 2^*$, because the kinetic energy of the methyl group internal rotation is assumed to be higher in the former state, as the methyl torsional mode ν_{23} is excited, see ϵ_{10} 's in Table 4. This fact further supports the assignment done in this work.

The newly observed vibrational states are marked with an asterisk (*) as these assignments are somewhat more speculative than definite assignments (cf. Fig. 27 and Table 4). Even more qR series of higher vibrationally excited states are visible in Fig. 27 and are assignable above 220 GHz. These can be seen by the series surrounded by $\nu_{24} = 2^*$ and $\nu_{15} = 1^*$. Possible candidates for the vibrationally excited states may be found in Fig. 22. Final assignments remain speculative to this point but may be confirmed in the future with the help of the FIR spectrum, as is already successfully demonstrated in Sec. 5.1.2.b.

Table 4: Spectroscopic parameters^a (MHz) of $v_{24} = 2^*$, $v_{15} = 1^*$, and $v_{23} = v_{24} = 1^*$ of *syn*-propanal.

Parameter	$v_{24} = 2^*$	$v_{15} = 1^*$	$v_{23} = v_{24} = 1^*$
A	16789.3459(30)	16778.18986(279)	16824.5983(94)
B	5858.20647(78)	5841.34915(95)	5808.34395(120)
C	4587.919215(169)	4586.34328(75)	4591.09138(43)
Δ_K	$\times 10^3$ 57.727(69)	49.70451 ^b	60.51(79)
Δ_{JK}	$\times 10^3$ -21.3303(238)	-16.7421(189)	-19.308(47)
Δ_J	$\times 10^3$ 5.84526(287)	4.5159(35)	5.55736(157)
δ_K	$\times 10^3$ 15.1385(204)	-5.1552(271)	10.520(34)
δ_J	$\times 10^3$ 1.79674(155)	1.19570(79)	1.67096(83)
Φ_K	$\times 10^9$ 1070.36 ^b	1070.36 ^b	-221.1 ^c
Φ_{KJ}	$\times 10^9$ -577.21 ^b	-577.21 ^b	143.2 ^c
Φ_{JK}	$\times 10^9$ -2023(100)	62.316 ^b	-128.2 ^c
Φ_J	$\times 10^9$ -169.3(60)	2.0061 ^b	3.146(64)
ϕ_K	$\times 10^9$ 37.46 ^b	-22417(1444) ^d	-1471 ^c
ϕ_{JK}	$\times 10^9$ -3398(74)	25.349 ^b	138.8 ^c
ϕ_J	$\times 10^9$ -84.8(30)	1.28486 ^b	0.555 ^c
ϵ_{10}	-99.520(84)	-76.506(178) ^e	350.49(108)
$[A - (B + C)/2]_{10}$	$\times 10^3$ -	-	-
$[(B + C)/2]_{10}$	$\times 10^3$ -	-	13.38(107)
$[(B - C)/4]_{10}$	$\times 10^3$ 1.0329(269)	3.537(66)	-1.73(55)
$d_{2_{10}}$	$\times 10^9$ -	-	400.8(189)
ρ^f	$\times 10^3$ 57.647(47)	69.781(142)	51.114(145)
$\Theta_{RAM} / ^\circ$	30.8085(147)	27.410(30)	34.718(63)
Single state fits			
no. of lines	401	193	259
no. of transitions	605	203	392
standard deviation ^f	1.11	1.03	1.24

^a Watson's A reduction in the I^r representation is used in ERHAM. Numbers in parentheses are one standard deviation in units of the least significant figures. In the first block rotational and centrifugal distortion constants can be found, in the second ERHAM tunneling parameters and in the third geometrical values (not in MHz). The bottom row contains general information about the fits.

^b Parameter is fixed to the value of $v_{24} = 1$.

^c Parameter is fixed to the value of $v_{23} = 1$.

^d ϕ_K is only fit as it ameliorates the *wrms* from 1.57 to 1.03, see text for discussion.

^e The assignment of A and E lines should be verified in the future as $\epsilon_{10} < 0$, see text.

^f Weighted unitless value for the respective single state fit.

Table 5: Observed spectroscopic parameters (MHz) of *syn*-propanal in comparison to quantum chemical calculations on the CCSD(T)/ANO0 level of theory [92]. The colored deviations (Obs.-Calc.) of rotational constants of $v_{24} = 2$ and $v_{15} = 1$ may indicate Fermi resonances, see explanations in the text.

		$v_{24} = 1$	$v_{23} = 1$	$v_{15} = 1$	$v_{24} = 2$	$v_{24} = v_{23} = 1$
		α_v^a				
		-38.05	76.26	-185.68		
		34.48	20.41	14.40		
		2.95	5.98	18.42		
	Obs. ^e	Calc.				
		$(X_v = X_0 - \alpha_v)^{b,c}$			$(X_v = X_0 - \sum_v \alpha_v^{(obs)})^{b,d}$	
$v = 0$	16669.63	16707.68	16593.37	16855.31	16754.49	16685.30
	5893.50	5859.02	5873.09	5879.10	5820.89	5834.87
	4598.98	4596.03	4593.00	4580.57	4591.52	4589.07
		Obs.-Calc.				
$v_{24} = 1$	16712.06	4.38				
	5857.20	-1.83				
	4595.25	-0.78				
$v_{23} = 1$	16642.87		49.50			
	5871.18		-1.91			
	4592.80		-0.20			
$v_{15} = 1^*$	16778.19			-77.12	23.70	92.89
	5841.35			-37.75	20.46	6.48
	4586.34			5.78	-5.17	-2.72
$v_{24} = 2^*$	16789.35			-65.96	34.86	104.04
	5858.21			-20.90	37.32	23.33
	4587.92			7.35	-3.60	-1.15
$v_{24} = v_{23} = 1^*$	16824.60			-30.71	70.11	139.30
	5808.34			-70.76	-12.54	-26.53
	4591.09			10.53	-0.43	2.02

^a Vibration-rotation constants α_v of the CCSD(T)/ANO0 level of theory.

^b cf. $X_v = X_e - \sum_i \alpha_i(v_i + 1/2)$ with $X = A, B, C$ [51].

^c Values are derived from observed parameters of $v = 0$ and the respective *ab-initio* α .

^d Values are derived from observed parameters of $v = 0$ and the respective observed vibrational state parameters. The harmonic approximation is assumed to be valid.

^e Uncertainties are neglected for clarity but can be found in Tables 3 and 4.

5.2 *Gauche*-Propanal

Gauche-propanal is quite close to the limiting prolate case with $\kappa = -0.9849$, see Eq. (2.12). Perturbations due to tunneling-rotation interaction of the two degenerate *gauche* configurations, see also Fig. 4, are satisfactorily treated with the reduced axis system introduced by Pickett [65] and summarized in Sec. 2.3.5. The rotational data are fit with Pickett’s SPFIT program [84]. The dipole moment components of *gauche*-propanal were determined to $\mu_a = 2.645(5)$ D, $\mu_b = 0.417(6)$ D, and $\mu_c = 1.016(3)$ D [41]. Very strong *a*-type transitions, in particular qR series, can be followed quite securely, also supported by DR measurements, as is shown in Fig. 28. *C*-type transitions connect the different qR series, cf. Fig. 8. Thus, measuring these weak transitions plays a key role, as was already demonstrated in the literature [44]. In contrast, *b*-types are even more challenging to assign as the expected intensity is proportional to the square of the respective dipole moment component, see Eq. (2.21). Thus, the focus is on assigning *a*- and *c*-type transitions.

The analysis of a large portion of the vibrational ground state of *gauche*-propanal was already published in Ref. [50] and is explained in more detail in Sec. 5.2.1. The major focus is on understanding the tunneling-rotation interaction between the two tunneling states 0^+ and 0^- . Moreover, additional rather strong features are observed which cannot be assigned to the vibrational ground state of *gauche*- nor to vibrational states of *syn*-propanal (cf. Fig. A23). These features are too strong to arise from energetically higher lying vibrationally excited states of *syn*-propanal. They are observed to stand out next to the K_a structures of the ground state of *gauche*-propanal for every J quantum number, also seen by the green and orange linkages in Fig. 28. This is a decisive argument that these lines are arising from an excited state of *gauche*-propanal which could be finally assigned to the energetically lowest excited vibrational state $v_{24} = 1$ as is explained in Sec. 5.2.2. Again, tunneling-rotation interaction between the two tunneling states, labeled 24^+ and 24^- , can explain the rotational fingerprint to a large extend. On the other hand, for both vibrational states, $v = 0$ and $v_{24} = 1$, perturbations from single state fit predictions are observable in some qR series for several adjacent J that cannot be treated properly with single state models.²¹ These perturbations are found to originate in Fermi resonances as well as Coriolis interactions between the tunneling states of the two vibrational states as is shown in a global treatment of $v = 0$ together with $v_{24} = 1$ in Sec. 5.2.3. All four sub-states involved in the analysis are labeled with a fixed color coding throughout this section for clarification: The respective tunneling states of the vibrational states 0^+ , 0^- , 24^+ , and 24^- are labeled in

²¹In the following, the "single state" term is used to highlight that only one vibrational state of *gauche*-propanal is fit, in contrast to a global analysis of $v = 0$ and $v_{24} = 1$. In a strict sense two tunneling states X^+ and X^- are analyzed in a combined fit for each single (vibrational) state fit.

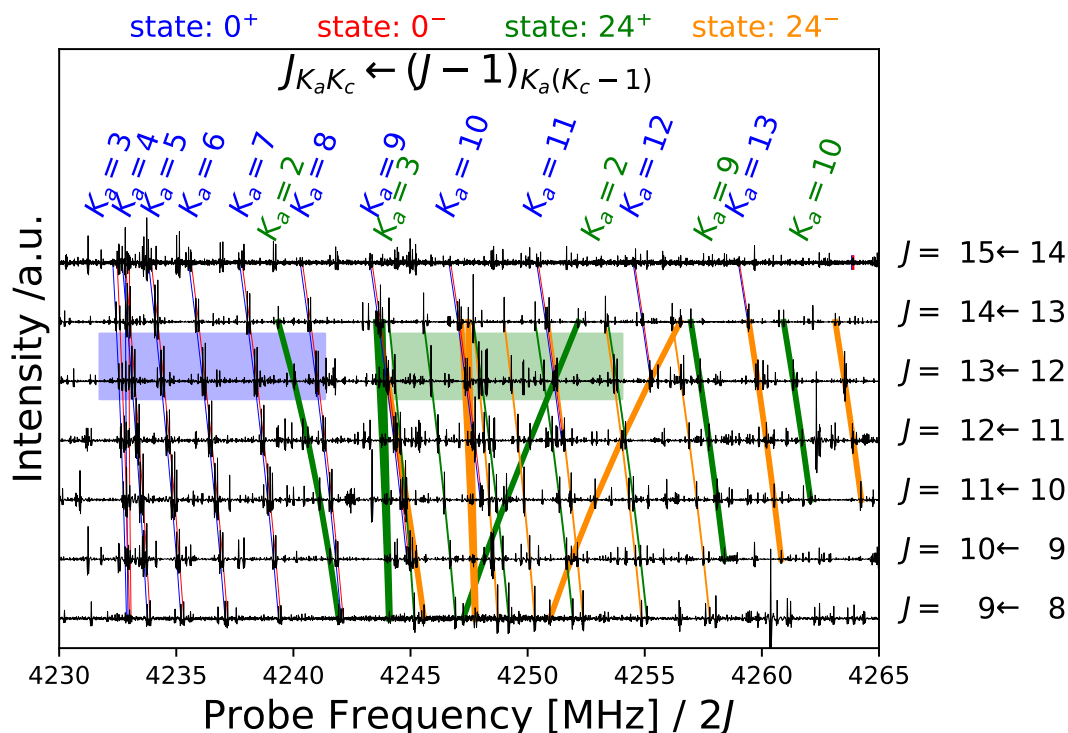


Figure 28: Fortrat diagram of propanal in the W-band region. Intense qR series transitions of *gauche*-propanal can be followed, schematically depicted in Fig. 8. The assignment of transitions of 0^+ and 0^- is quite straightforward, as indicated by the clear patterns of blue and red lines, respectively. On the other hand, the larger splitting of the tunneling states of the excited state $\nu_{24} = 1$ hampered assignments initially. DR measurements facilitate assignments and identified linkages are shown in green and orange for 24^+ and 24^- , respectively. The series in bold with $K_a = 9$ and $K_a = 10$ gave a first idea for labeling the whole fingerprint, likewise series in bold with $K_a = 2$ and $K_a = 3$, for more details see Sec. 5.2.2. Zoomed-in spectra highlighting the K_a structure for $\nu = 0$ and $\nu_{24} = 1$ marked by the blue and green squares can be seen in Figs. 30 and 33, respectively.

blue, red, green, and orange, respectively.

5.2.1 Single State Analysis of $\nu = 0$

In 1964, four out of twelve microwave transitions with $J_{max} = 4$ of the main isotopologue in the vibrational ground state of *gauche*-propanal were observed to be split into doublets [39]. Ten years later, Pickett and Scroggin studied this tunneling-rotation interaction in more detail [47]. A focus was put on describing strongly perturbed energy levels. The most important experimental results were the observations of three nominally forbidden transitions between the two tunneling states. In this case, these transitions become allowed as mixing of $J_{K_a, K_c} = 2_{11}$ of 0^+ and 2_{12} of 0^- is quite prominent and results in the aforementioned strong perturbation of the levels. In general,

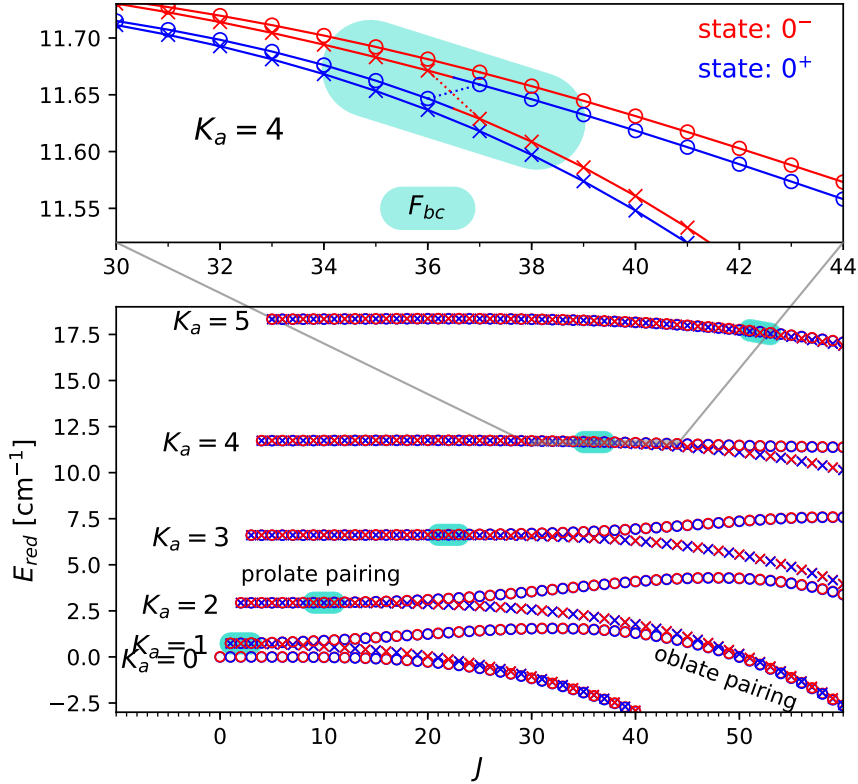


Figure 29: Reduced energy diagram of $v = 0$ of *gauche*-propanal, see Eq. (2.19). Marked in turquoise are tunneling-rotation interactions between energy levels of asymmetry side J ('o') of 0^+ and $J + 1$ ('x') of 0^- , which are described by a -type Coriolis parameters. The avoided crossing of energy levels for $K_a = 4$ is highlighted by the color change of the lines connecting the perturbed energy levels between $J = 36$ and $J = 37$.

a crossing of energy levels of the asymmetry side J of 0^+ with $J + 1$ of 0^- will occur as the two tunneling states are rather close in energy and energy levels of the lower asymmetry side $J + 1$ are shifting more to lower energies for higher J 's compared to the levels of the upper asymmetry side J . In simpler words, energy levels of the upper asymmetry side J of the lower tunneling state are crossing levels of the lower asymmetry side $J + 1$ of the upper tunneling state. The crossing of energy levels results in considerable mixing. Crossing energy levels have the same J and K_a quantum numbers leading to a principle connection by a -type transitions (cf. selection rules in Table 1), hence the tunneling-rotation interactions are described by a -type Coriolis interaction parameters in the RAS. The leading coefficient of this interaction is F_{bc} . In the covered frequency region of this work up to 500 GHz ($J_{max} = 60$), strong interactions occur for $K_a = 1$, $K_a = 2$, $K_a = 3$, $K_a = 4$, and $K_a = 5$ at $J = 2$, $J = 10$, $J = 22$, $J = 36$, and $J = 52$, respectively. The locations of strongly perturbed energy levels are highlighted in turquoise in the reduced energy diagram in Fig. 29 for energy levels

with $K_a \leq 5$ and $J_{max} = 60$. Both tunneling states, 0^+ and 0^- depicted in blue and red, respectively, seem to be blended in the reduced energy diagram as the energy difference is only about 476 MHz (or 0.016 cm^{-1}). In the zoomed inset of Fig. 29, a crossing for energy levels of asymmetry side J of 0^+ with $J+1$ of 0^- becomes clearer in the example of $K_a = 4$. The typical avoided crossing pattern is probably best observed for $K_a = 2$ of $v = 0$, see Fig. A25. Pickett and Scroggin measured nominally forbidden transitions as well as allowed transitions within tunneling states of the two perturbed energy levels with $K_a = 1$. In this way, a closed loop of energy levels connected by the transitions could be generated which allowed for determining the energy difference of the tunneling states [47]. The fundamental importance of that experimental result is the removal of the correlation between the energy difference and the magnitude of the perturbation, see also Eq. (2.29). However, different asymmetry sides within the two tunneling states were not linked. Up to this point only a -type transitions, excluding the nominally forbidden transitions, were measured within both tunneling states [39, 47], but another microwave study succeeded in measuring weaker b - and c -type transitions to determine an accurate A rotational constant. Its average value of both tunneling states was determined to be 26248.4079(50) MHz [44], in comparison to 23035(42) MHz in Ref. [47]. Here, the huge difference of more than 3 GHz is brought to the readers' attention because predictions of b - and c -type are strongly dependent on A .

The thorough investigations of the rotational spectrum of the ground state of *gauche*-propanal in the microwave region facilitated reliable predictions up to the MMW region [39, 41, 44, 47]. The typical doublet pattern, due to the tunneling splitting, in combination with the very strong dipole moment component of $\mu_a = 2.645(5) \text{ D}$ [41] allowed for easy and, more importantly, unambiguous assignments of qR series. This is demonstrated by the regular pattern of qR series highlighted in blue and red in Fig. 28. The splitting for transitions involving $K_a > 3$ is rather small and the doublet structure is hardly visible in this rather broad frequency window. A zoom into the blue box of Fig. 28 is shown in Fig. 30 and clarifies the typical doublet pattern of K_a structures. The typical doublet pattern for transitions with $K_a > 3$ is easily spotted in the plotted frequency window of 300 MHz. A doublet pattern is observed since the tunneling states are split in frequency but the two asymmetry sides are blended. This is not the case for $K_a \leq 3$ in the W-band region. In Fig. 30, a quartet structure is seen for $K_a = 3$ as each tunneling state has two unblended asymmetry sides, resulting in four distinct transitions.²² The shift in frequency for doublets with $K_a > 3$ to the next neighbor doublet, with $K_a + 1$, gets usually larger with increasing K_a value, see Fig. 30. Furthermore,

²²The frequency splitting of the two asymmetry sides for $K_a = 1$ and $K_a = 2$ is much larger than for transitions with $K_a = 3$. Asymmetry sides $J+1$ and J can be found to lower and higher frequencies compared to the quartet of $K_a = 3$ transitions, respectively. Typical K_a structures in the range for $0 \leq K_a \leq 13$ can be found in the Appendix in a much more crowded illustration in Fig. A26.

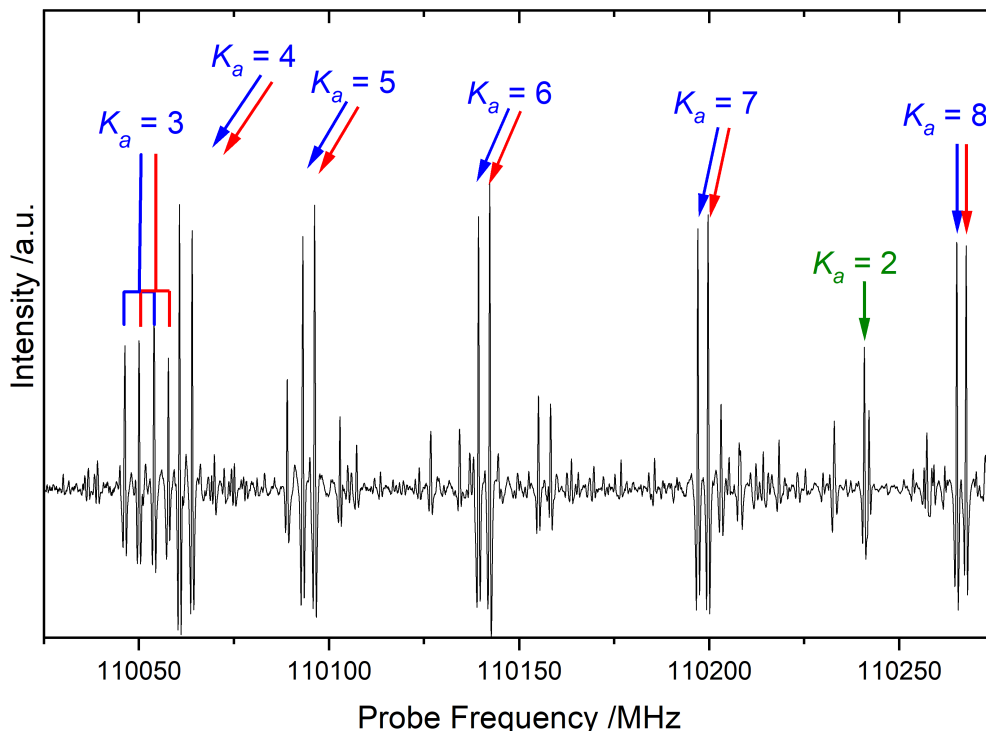


Figure 30: Typical rotational fingerprint of $\nu = 0$ of *gauche*-propanal. Shown here is a K_a structure with transitions $13_{K_a, K_c} \leftarrow 12_{K_a, K_c-1}$. The origin of the K_a structure is explained by the green arrows in Fig. 8. The doublet structure arises from the two tunneling states 0^+ and 0^- and is pointed out with blue and red arrows, respectively. Here, the two asymmetry sides are blended for transitions involving $K_a > 3$, but not for $K_a = 3$.

the asymmetry splitting is getting larger with increasing J , even lifting the doublet structure for transitions with $K_a > 3$ at higher J . Predicted intensities are usually decreasing for larger K_a values, for identical J , due to Boltzmann statistics. However, as the intensities of the absorption spectra are not easily comparable this trend cannot always be strictly followed as can be noticed in Fig. 30. Nevertheless, strong a -type transitions can be tracked easily thanks to typical fingerprints of qR series and K_a structures. The resulting fingerprint facilitates unambiguous assignments of rotational transitions to the observed upper frequency limit of 500 GHz. In this way, quantum numbers of the assigned R -branch a -type transitions cover transitions up to $J_{max} = 60$, only limited by the frequency cutoff, and K_a easily up to $K_a = 22$. The assignment of transitions involving higher K_a should be possible, but restrictions in modeling energy levels with $K_a > 17$ determined this task to be unnecessary, as will be explained later. The regular pattern of qR series (cf. Fig. 28) is lifted for transitions in case involved energy levels with J of 0^+ and $J + 1$ of 0^- are crossing (cf. Fig. 29). Notably the other series with asymmetry sides $J + 1$ of 0^+ and J of 0^- for the same K_a are locally not strongly affected. Thus they appear as usual qR series in Fortrat diagrams. Therefore,

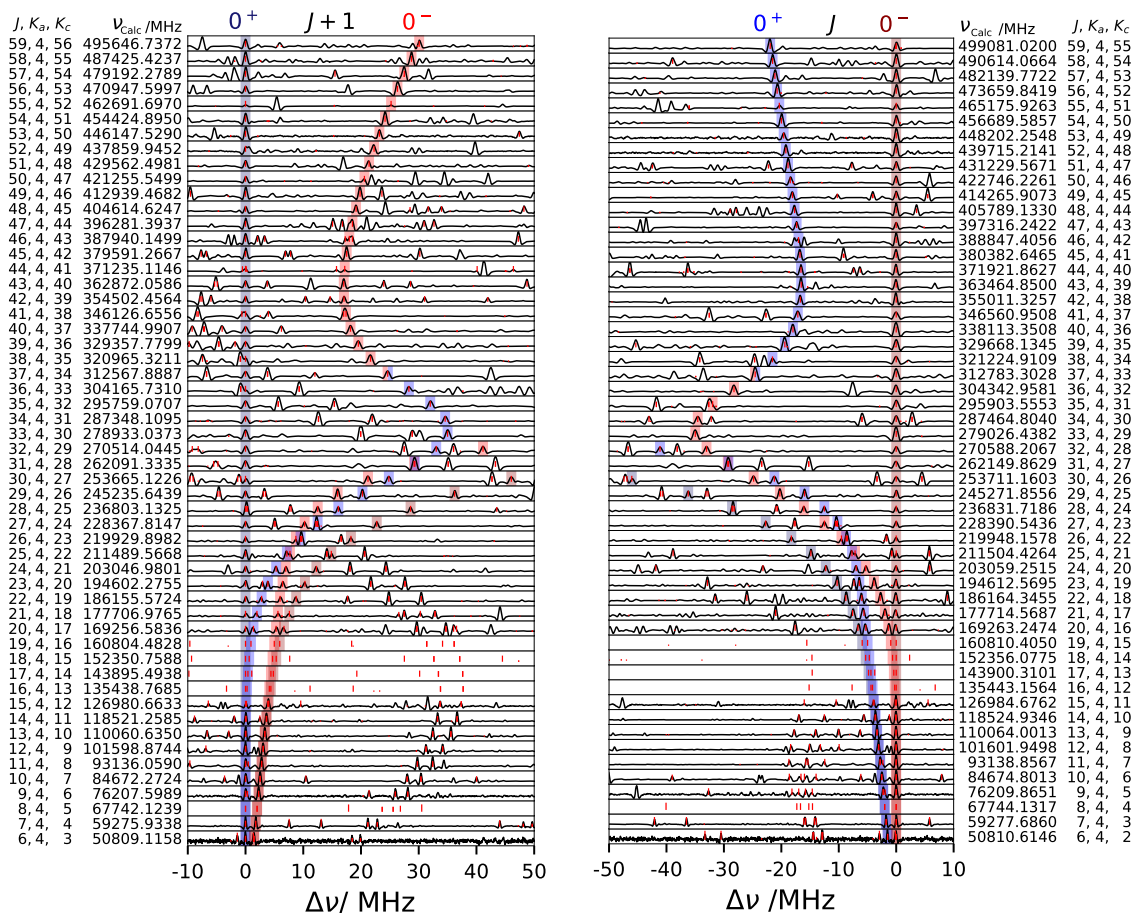


Figure 31: Loomis Wood plots of *gauche*-propanal showing qR series with $K_a = 4$. Colored boxes mark four predicted series which all consist of transitions $J_4, K_c \leftarrow (J-1)_4, K_{c-1}$. The asymmetry side $J+1$ of 0^+ and 0^- as well as the asymmetry side J of 0^+ and 0^- are shown in darkblue, red, blue, and darkred, respectively. Typical avoided crossing patterns are clearly visible for transitions of 0^- with $K_a + K_c = J+1$ and 0^+ with $K_a + K_c = J$. The nominally forbidden 'avoided crossing' transitions between 0^+ and 0^- occur for $37_4, K_c \leftarrow 36_4, K_{c-1}$, see Fig. 29. Vertical red lines mark all predicted transitions of *gauche*-propanal in the respective frequency windows.

transition frequencies of unperturbed series are used as center frequencies in Loomis-Wood plots. In this way, perturbed series become clearly visible and show typical avoided crossing patterns, as is shown in Fig. 31 for $K_a = 4$. The nominally forbidden transitions can be seen by the transitions marked by boxes half in blue and half in red for $37_4, K_c \leftarrow 36_4, K_{c-1}$. These transitions account for *a*-type transitions between the two tunneling states and can be understood as the avoided crossing transitions of the perturbed system. The interaction area of this system is shown enlarged in the zoom of the reduced energy diagram in Fig. 29. There, the avoided crossing behavior is nicely

seen by the color change, from blue to red and vice versa, of the lines connecting the perturbed energy levels.

In fact, Fig. 28 does not show all expected or even measured linkages which can be found in the plotted 3mm wavelength region. The intention of Fig. 28 is to emphasize the usually very easily trackable qR series and K_a structures of 0^+ and 0^- transitions. However, the illustration of the patterns is simplified consciously. Transitions involving $K_a \geq 3$ are shown only on purpose because strong perturbations of $K_a = 2$ at $J = 10$ are observed, which would have hampered the desired demonstration of the power of Fortrat diagrams. The complete picture is represented better by Fig. A26. This figure shows in principle the same qR series and K_a structures as are shown in Fig. 28, but with a broader frequency range. The qR series of $K_a = 2$ are highlighted with thicker lines and its nominally forbidden transitions can be seen by the color change within qR series from blue to red or vice versa. However, also a -type transitions within the tunneling states are still observed, which may be considered as crossing transitions, although with smaller intensities compared to the unperturbed system.

As was already mentioned before, deriving a proper description of $\nu = 0$ benefits from measuring additional b - or c -type transitions. This is particularly true for the perturbed energy levels. Possible candidates for the perturbed system around $K_a = 2$ at $J = 10$ are Q -branch c -type transitions (cf. left red arrow in Fig. 8), which connect the qR series of $K_a = 2$ with $K_a = 3$. An enlarged portion of the reduced energy diagram of $K_a = 2$ and $K_a = 3$ is shown in Fig. 32. Two example candidates of the aforementioned c -type transitions are plotted by the two vertical arrows connecting the two panels in Fig. 32. However, these transitions could not be measured in the framework of the single state analysis as their intensities are quite weak and a secure assignment was not possible. That is why the results in Ref. [50] could not benefit from information hidden in these transitions. Fortunately, the experimental setup is extended for DR and even DM-DR measurements in the process of this work, see Secs. 3.1.2 and 3.1.3. In fact, the successfully measured transition $11_{3,9} \leftarrow 11_{2,9}$ shown in Fig. 16, as an example of the benefits of DM-DR measurements, is identical to the candidate transition depicted by the right arrow in Fig. 32. The doublet structure is arising from the resolved splitting caused by the methyl group internal rotation in c -type transitions, but only the A components are fit (cf. Fig. A28). Many more c -type transitions could be measured thanks to the DR experimental setups, even from the most perturbed energy levels as highlighted by the left arrow in Fig. 32. Once possible candidates with linkages in the W-band region were identified, many more transitions of rQ series ($J_{3,K_c} \leftarrow J_{2,K_c}$, with asymmetry sides of $J \leftarrow J + 1$ as well as $J + 1 \leftarrow J$) with $\nu = 0^- \leftarrow 0^+$ as well as $\nu = 0^+ \leftarrow 0^-$ could be assigned unambiguously. Frequencies are determined by means of conventional spectroscopy if possible (typically $TC \geq 200$ ms, with TC up to seconds). New predictions even allow to assign further transitions of the aforementioned

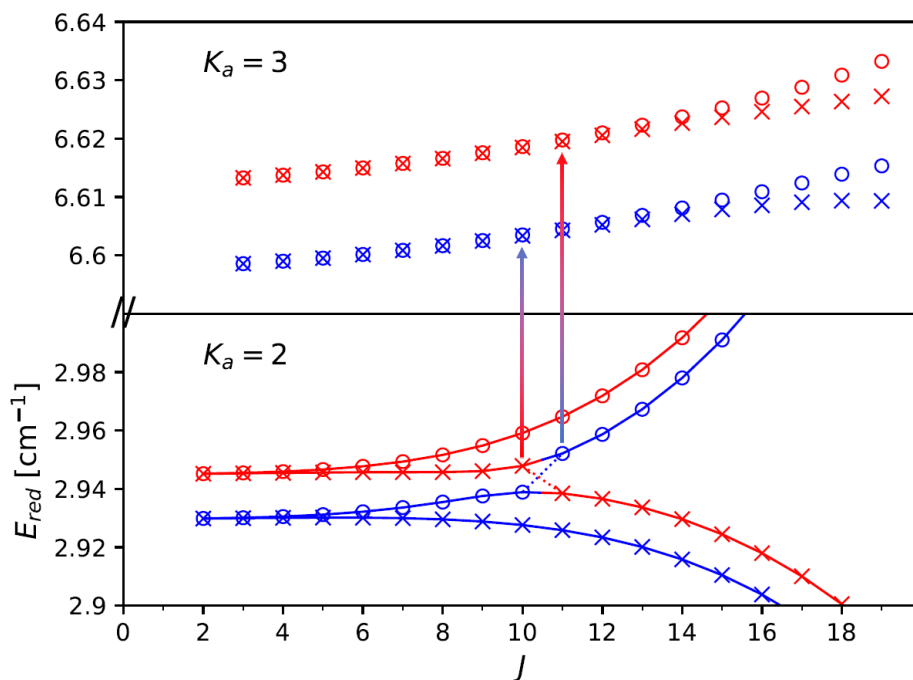


Figure 32: Reduced energy diagrams for $K_a = 2$ and $K_a = 3$ of $v = 0$ of *gauche*-propanal shown in the lower and upper panel, respectively, see Eq. (2.19). Notice that the y -axis is discontinuous. 0^+ and 0^- are plotted in blue and red, respectively. The energy levels marked with 'x' or 'o' are referring to the $J + 1$ or J asymmetry sides, respectively. A strong interaction is clearly visible for energy levels with $K_a = 2$ and J of 0^+ and $J + 1$ of 0^- around $J = 10$. This perturbation is resulting from tunneling-rotation interactions. Examples of c -type transitions connecting the different qR series are shown by the vertical arrows.

series entirely without DR measurements as longer integration times are feasible within small frequency windows. In the same way, some rQ series transition with $K_a = 2 \leftarrow 1$ and rR series transitions $K_a = 1 \leftarrow 0$ as well as pR series transitions with $K_a = 0 \leftarrow 1$ are included in the description of the global fit presented in Sec. 5.2.3.

To fit the data of $v = 0$ of *gauche*-propanal, all transitions with $K_a = 0$ up to $J = 45$ are added to the fit in a first step, followed by $K_a = 1$ up to $J = 45$ and increasing K_a incrementally. Later, transitions up to $J_{max} = 60$ are added to the fit. Some of the transitions showed clear perturbations for adjacent transitions in J for a fixed K_a , as already explained (cf. Fig. 29). It is advisable to include the unperturbed transitions with lower as well as with higher J at first, and finally adding the perturbed ones. The single state analysis is aborted at qR series with $0 \leq K_a \leq 13$ and $J_{max} = 60$ (cf. Figs. A30 and A31). However, some adjacent transitions of the same K_a are excluded, namely $J > 50$ for $K_a = 11$ and $J > 38$ for $K_a = 12$. Transitions with $K_a = 11$ show trends in the deviations, whereas transitions with $K_a = 12$ show typical perturbation patterns of avoided crossings. Additionally, transitions with $K_a \leq 17$ and $J \leq 31$

are included in the analysis as far as the *wrms* is not increasing considerably. In fact, the analysis was performed with linear combinations of spectroscopic parameters P^+ and P^- from the two substates 0^+ and 0^- in Ref. [50], respectively, explicitly $P = (P^+ + P^-)/2$ and $\Delta P = (P^+ - P^-)/2$ are used, see, e.g., Ref. [93]. This definition is sometimes beneficial for the analysis as P^+ and P^- might be quite similar and initially solely the average P is used if not enough information is available to properly determine both values. In this way, the dimension of the fit function is reduced at intermediate steps. The resulting linear combinations are presented in Ref. [50]. For this work, the data are refit with parameters defined in the conventional way, with a marginally lower *wrms*, to allow for a simpler comparison to the single state fit of $\nu_{24} = 1$ and the global fit, as these are fit in the conventional way, too. The best choice of spectroscopic parameters can be found in Table 6.

5.2.2 Single State Analysis of $\nu_{24} = 1$

The experimental basis for the study of the first vibrationally excited state $\nu_{24} = 1$ of *gauche*-propanal in the MMW region is not as luxurious as for the ground state $\nu = 0$. The fundamental frequency of $\nu_{24} = 1 \leftarrow 0$ was assigned in a FIR study to 113.1 cm^{-1} [45]. This rather low lying vibrational mode gives rise to rather strong rotational line intensities of nearly 58% of ground state intensities. However, there are only 15 rotational transitions assigned in the literature, all of them being *a*-type transitions with $J \leq 4$ and $K_a \leq 2$ [41]. The resulting rather coarse model, with deviations of more than 2 MHz for transition frequencies up to 34 GHz, where experimental uncertainties are presumably on the order of 100 kHz, is not a sophisticated starting point for extrapolating into the MMW region. The low quality of the model is not surprising for such small numbers of transitions of the same type and deriving a sophisticated model was not the intention of the authors. Their focus was on determining the fundamental frequency, or better verify the FIR value of 113.1 cm^{-1} [45], with microwave relative intensity measurements [41]. The energy was consistently confirmed with $109(15) \text{ cm}^{-1}$ [41]. As will be shown in the following section (Sec. 5.2.3), this value is far from the value determined in this work. The literature data are not used for the analysis, firstly, as incorrect assignments for such small numbers of transitions are not uncommon and would complicate the analysis unnecessarily and, secondly, strong qR series could be easily tracked by means of DR spectroscopy. Certainly, this is not the only or even the common procedure how to deal with literature data. On the other hand, by including all 15 transitions to the final fit of the global analysis the parameters converge to identical values, but 6 out of 15 transitions show anomalies. Two of them were used as pump transitions to probe the other four. Actually an off-resonance pumping of both pump transitions, predicted by the global model, can consistently

Table 6: Spectroscopic parameters^a (MHz) of $v = 0$ of *gauche*-propanal.

Parameter	0^+	0^-
E_{rel}	-237.7948(97)	237.7948(97)
E_{rel} / cm^{-1}	-0.00793180(27)	0.00793180(27)
A	26252.6975(151)	26248.6295(169)
B	4314.89027(116)	4314.95095(115)
C	4147.91130(116)	4148.12544(115)
$-D_K$	-2.1076(40)	-2.0916(40)
$-D_{JK}$	0.1798845(77)	0.1789630(70)
$-D_J$	-0.00659818(104)	-0.00658138(103)
d_1 $\times 10^3$	1.08611(84)	1.07826(84)
d_2 $\times 10^3$	-0.039962(168)	-0.037112(151)
H_K $\times 10^6$	-	-
H_{KJ} $\times 10^6$	8.233(67)	10.958(62)
H_{JK} $\times 10^6$	-3.3061(128)	-3.3644(126)
H_J $\times 10^6$	0.127026(204)	0.127706(203)
h_1 $\times 10^9$	-51.618(189)	-53.270(188)
h_2 $\times 10^9$	-0.8879(93)	-
h_3 $\times 10^9$	-0.0897(112)	-0.2868(113)
L_K $\times 10^9$	-	-
L_{KKJ} $\times 10^9$	-2.563(199)	-5.950(184)
L_{JK} $\times 10^9$	-2.313(57)	-2.258(56)
L_{JJK} $\times 10^9$	0.14815(186)	0.14300(187)
L_J $\times 10^{12}$	-3.323(32)	-3.182(32)
l_1 $\times 10^{12}$	2.1017(147) ^b	2.1017(147) ^b
P_{JK} $\times 10^{12}$	-0.1240(33) ^b	-0.1240(33) ^b
P_J $\times 10^{15}$	0.07108(298) ^b	0.07108(298) ^b
F_{bc}	23.9502(62)	
F_{bc}^K	-0.1033(37)	
F_{bc}^J $\times 10^3$	-3.3769(59)	
F_{bc}^{KK} $\times 10^3$	0.23557(229)	
F_{bc}^{JK} $\times 10^3$	-0.014540(152)	
F_{bc}^{JJ} $\times 10^6$	0.14990(75)	
F_{2bc} $\times 10^3$	-0.36326(243)	
Combined fit		
Number of transitions	2375	
<i>rms</i>	44.4 kHz	
<i>wrms</i>	0.97	

^a S reduction is used with SPFIT in the I^r -representation. Values of F_{bc} etc., given between column 2 and 3 are associated with operators between tunneling states. Numbers in parentheses are one standard deviation in units of the least significant figures.

^b Parameter value fixed to the other tunneling state.

explain the other blue and red shifted deviations with the help of the Autler-Townes effect. This endorses the approach of neglecting the data.

The constantly repeated emergence of additional strong lines next to ground vibrational state transitions of *gauche*-propanal in the MMW region is a clear hint of a satellite spectrum, see Fig. A23. In the observed spectra additional transitions, shifted to higher frequencies than $\nu = 0$ ones are observed. The energetically lowest vibrationally excited state $\nu_{24} = 1$ of *gauche*-propanal is obviously the first choice as the carrier of the additional lines because these lines have the next highest intensities compared to the ground state. A Fortrat diagram is used to find candidate lines of qR series of $\nu_{24} = 1$ (cf. Fig. 28). As a first step, the center frequencies of rather strong and not yet assigned transitions are determined. Candidates are searched at frequencies higher than the ones with $K_a = 3$ of the ground vibrational state. The idea is to find transitions belonging to series with $K_a \geq 3$, as they are expected to be unperturbed in the W-band region and the two asymmetry sides should be (nearly) blended, in particular the series should be well behaved and nearly parallel to the ones observed for the ground state. Quickly many transitions are successfully linked and different series are found. Well described series in the W-band region of $\nu_{24} = 1$ of *gauche*-propanal are highlighted by green and orange lines in Fig. 28. The J quantum numbers of the pump and probe transitions are already known from the Fortrat diagram, but the assignment of K_a quantum numbers is more difficult. As a reminder, the projection of J onto a molecular axis K cannot be larger than J , i.e. $K_a \leq J$. This leads to a first breakthrough in assigning K_a quantum numbers: The series with $K_a = 9$ and $K_a = 10$ need to have missing linkages to the lowest row ($J = 9 \leftarrow 8$) and to the two lowest rows ($J = 10 \leftarrow 9$ and $J = 9 \leftarrow 8$) in the Fortrat diagram shown in Fig. 28, respectively. The two asymmetry sides are blended for 24^+ and 24^- and thus two series are observed for each K_a . With this basic knowledge, the four qR series, $J_{9,K_c} \leftarrow (J-1)_{9,K_c-1}$ and $J_{10,K_c} \leftarrow (J-1)_{10,K_c-1}$ of 24^+ as well as of 24^- , can be fully assigned in the observed frequency region, without the help of any *ab-initio* quantum chemical calculations.

Further important observations and possible candidates for a full assignment are qR series belonging to $K_a = 2$ and $K_a = 3$, see Fig. 28. Two unknown series show nearly vertical linkages in the Fortrat diagram which is also observed for the series of $K_a = 3$ of $\nu = 0$. The two unassigned series are observed to show only a very small asymmetry splitting in the lowest row ($J = 9 \leftarrow 8$), less than 1 MHz, but a considerable splitting of several megahertz at the second top row ($J = 14 \leftarrow 13$). This lifting of the prolate pairing is also observed for qR series of $\nu = 0$ with $K_a = 3$. For these reasons the two, more specifically four series as prolate pairing is lifted, are unambiguously assigned to $J_{3,K_c} \leftarrow (J-1)_{3,K_c-1}$. Furthermore, four series are observed to have quite different slopes compared to all the other series as can be seen in Fig. 28. In particular, they are not nearly parallel to all the other series. However, each time two of the four series are

nearly parallel to themselves and the two doublet series appear to be roughly parallel to the unperturbed series with $K_a = 2$ of $v = 0$, compare to Fig. A26. Based on these observations, the four series could be assigned to the two asymmetry sides of both tunneling states with $J_{2,K_c} \leftarrow (J-1)_{2,K_c-1}$. Thus, all series belonging to series with $K_a = 2, 3, 8,$ and 9 could be unambiguously assigned.

At this point, qR series belonging to $4 \leq K_a \leq 8$ are expected to be surrounded by the already assigned series and doublets appear stepwise with increasing K_a . However, transitions with K_a belonging to 24^- may be higher in frequency than transitions with $K_a + 1$ belonging to 24^+ in the same K_a structure, see Fig. 33. The doublets are not as clearly separated from each other as for $v = 0$. An important information is the magnitude of the tunneling splitting of already assigned qR series. Intensity ratios are, unfortunately, more misleading than helping. Fortunately the DR measurements link series unambiguously. The missing series are assigned using the aforementioned information ending up in only small ambiguities. One alternative would be to test all possible combinations in a fit and use the best one. On the other hand, more experimental data is also able to clarify the open issues. Additional measurements were taken in the frequency range of 40–60 GHz to verify assignments. At lower frequencies, the K_a structures will get simpler as more qR series have no linkages anymore, as $K_a \leq J$. These new measurements allowed for an unambiguous assignment of the series from the MMW region. In this way, without the need of *ab-initio* calculations or predictions from the MW region the already assigned qR series and their respective K_a structures form a solid basis to extend the coverage of quantum numbers as well as frequency ranges. A typical fingerprint, the K_a structures with $13_{K_a, K_c} \leftarrow 12_{K_a, K_c-1}$, of $v_{24} = 1$ of *gauche*-propanal can be seen in Fig. 33. This figure is a zoom into the green area of Fig. 28.

Striking is that qR series with $K_a = 2$ do not seem to be strongly perturbed in the W-band region for $v_{24} = 1$ as is observed for $v = 0$, compare to Fig. A26. On the other hand this is not surprising as the tunneling splitting is often larger for vibrationally excited states which are closer to the barrier height. A crossing of energy levels with asymmetry side J of 24^+ and $J + 1$ of 24^- is expected to appear at higher J due to the larger tunneling splitting. This may lead to a possible interaction in the W-band region of levels with $K_a = 1$. Therefore, the next important step is to locate perturbed transitions to be able to determine accurately the energy difference between the tunneling states. For that, already assigned transitions with $2 \leq K_a \leq 9$ are fit to derive a first spectroscopic model. During the fitting procedure it was noticed that transitions with $3 \leq K_a \leq 9$ could be reproduced properly without using F_{bc} . Even though transitions with $K_a = 2$ looked well-behaved, the two likely perturbed asymmetry sides show clear deviations which followed a clear trend with opposite sign in the deviations ($\nu_{obs} - \nu_{calc}$). The a -type Coriolis interaction parameter had to be

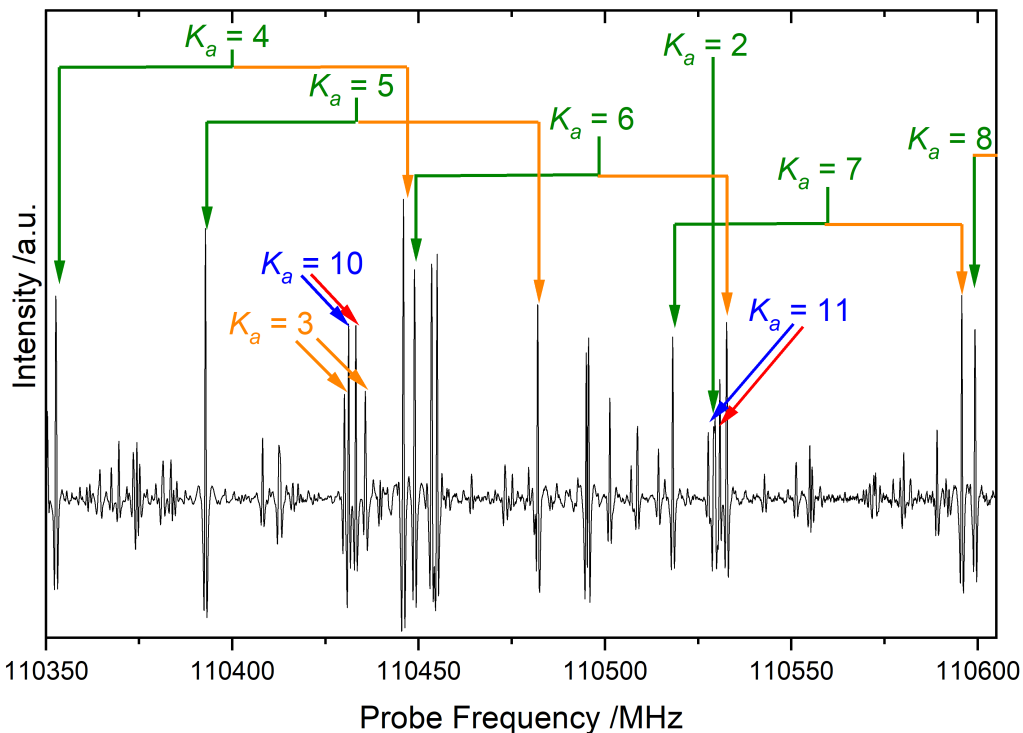


Figure 33: Typical rotational fingerprint of $\nu_{24} = 1$ of *gauche*-propanal. Shown here are K_a structure transitions with $13_{K_a, K_c} \leftarrow 12_{K_a, K_c-1}$. The doublet structure of 24^+ and 24^- is marked in green and orange, respectively. The two asymmetry components are blended in this case, except for $K_a = 2, 3$.

incorporated to the fit to reproduce these transitions to experimental uncertainty.

New predictions based on the derived rotational parameters allowed to assign many new transitions in the W-band regions with K_a up to 13. Also qR series with $K_a = 0$ and $K_a = 1$ could be linked by DR spectroscopy. The transitions with $K_a = 1$ of J of 24^+ and $J + 1$ of 24^- are heavily perturbed but they are assigned without doubt thanks to DR spectroscopy, see Fig. A26. In the covered frequency region up to 500 GHz ($J_{max} = 60$), the strongest interactions of $\nu_{24} = 1$ occur for $K_a = 1$, $K_a = 2$, and $K_a = 3$ at $J = 12$, $J = 26$, and $J = 42$, respectively, see the reduced energy diagram in Fig. 34. The avoided crossing behavior is very obvious in this figure. Important c -type transitions are measured by means of DR spectroscopy in the W-band region. In particular, also transitions with $K_a = 2 \leftarrow 1$ and $24^- \leftarrow 24^+$ with $J_{2,J-1} \leftarrow J_{1,J-1}$ addressing the energy difference of the strongly perturbed energy levels of asymmetry side J of 24^+ around $J = 12$ for $K_a = 1$. Because of the avoided crossing, a huge frequency offset of 5.4 GHz is observed between the Q -type transitions with $J = 12$ and $J = 13$ (cf. two vertical arrows of Fig. 34).

Fitting procedures with simultaneously increasing J and K_a turned out to be not successful. Consequently, the fitting procedure is restarted in a similar fashion to $\nu = 0$. This time the fitting is started with transitions of $K_a = 0, 1$, and 2 from the

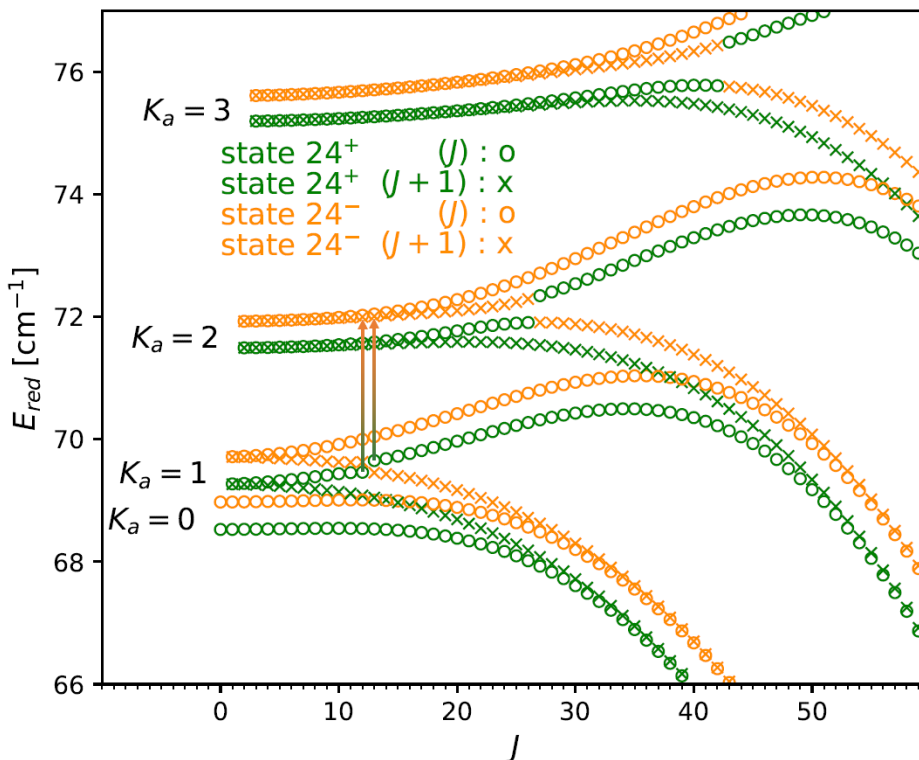


Figure 34: Reduced energy diagram of $v_{24} = 1$ of *gauche*-propanal, see Eq. (2.19). The avoided crossing behavior of energy levels due to tunneling-rotation interactions, described by *a*-type Coriolis parameters, are clearly seen by series which turn from green to orange, or vice versa. The strongest interactions occur for $K_a = 1$, $K_a = 2$, and $K_a = 3$ at $J = 12$, $J = 26$, and $J = 42$, respectively. The left and right vertical arrows show *Q*-type *c*-type transitions $12_{2,11} \leftarrow 12_{1,11}$ and $13_{2,12} \leftarrow 13_{1,12}$ (both with $24^- \leftarrow 24^+$), respectively. The avoided crossing leads to a frequency offset of about 5.4 GHz between these two transitions. These transitions are unambiguously assigned thanks to DM-DR measurements.

W-band region. Even at this stage, it is necessary to incorporate the *b*-type Coriolis interaction parameter F_{ca} together with F_{bc} and higher order ones of *a*-type Coriolis interaction. F_{ca} is included as a manually adjusted fixed parameter, without doing so the fit is diverging but a fixed parameter improved the *wrms* dramatically. Higher order *a*-type Coriolis interaction parameters are initially also fixed to the respective ground state values. The fixed values are released at later steps of the fit. From this point on, a similar strategy as for the ground state is applied. This time, transitions up to $J_{max} = 60$ are implemented stepwise for successive K_a quantum numbers, sometimes with more than one K_a at a time. The *c*-type Coriolis interaction parameter F_{ab} turned also out to be necessary and is therefore incorporated to the fit. Notably is that the *wrms* is most of the time between 1.5 and 2.0. A sophisticated model is only reached for the first time when lines up to $K_a = 8$ are used in the fit (*wrms* = 1.08), with most

of the qR series up to $J_{max} = 60$. Probably the large dataset allowed for recognizing perturbed transitions with so far unknown origin and by excluding them from the fit a solid model could be derived (cf. Fig. A29). In particular pairs of lines sharing one energy level are observed to have deviations with equal magnitude but opposite signs. It seems that one particular energy level is perturbed which cannot be described by tunneling-rotation interaction within the vibrational states nor by the global analysis, presented in Sec. 5.2.3. Nevertheless, assigning and fitting is continued until transitions up to $J_{max} = 60$ and $K_a = 11$ are well reproduced in the model with $wrms = 1.23$ (cf. Figs. A32 and A33). The best choice of spectroscopic parameters can be found in Table 7. Most striking, however, is that all lines with $K_a = 7$ and $J > 36$ could not be included into the model without a huge deterioration of the $wrms$. Similar problems occur for transitions with $K_a = 10$ and $J > 30$. Even more surprisingly, transition with $J > 45$ cannot be assigned straightforwardly. Also implementing transitions with $K_a = 12$ is not straightforward without deterioration of the $wrms$. Therefore, the single state analysis is aborted at this point.

5.2.3 Global Analysis of $v = 0$ and $v_{24} = 1$

Overall, the fits of $v = 0$ and $v_{24} = 1$ of *gauche*-propanal described in Secs. 5.2.1 and 5.2.2 provide respectable models. Nevertheless, following the single state analyses of the rotational spectra, it seems logical to combine both fits in a global one. First of all, it is noticed that predictions based on both single state fits in combination with the fundamental frequency ν_{24} , determined in the FIR to $113.1(2) \text{ cm}^{-1}$ [45], do not allow for any assignments in the FIR spectra taken within this work. On the other hand, the same procedure leads straightforwardly to the assignment of the fundamental band ν_{24} of *syn*-propanal, see Sec. 5.1.2.b. Even more surprisingly, no similar patterns nor equidistant line spacing between the predicted and observed bands in the FIR measurements are found. This observation led to the assumption of a wrong assignment of the fundamental band ν_{24} of *gauche*-propanal in the literature. For this reason, the perturbed transitions are revisited, reviving that first perturbations with so far unknown origin appear for $K_a = 12$ for $v = 0$, as was already shown by a nearest line plot in Fig. 4 in the supplementary material of Ref. [50], and for $K_a = 7$ of $v_{24} = 1$. The deviations from predicted to observed lines are depicted in Loomis-Wood plots which are shown in Fig. 35. The center frequencies of the Loomis-Wood plots are predicted frequencies of the qR series derived from the single state analyses presented in Secs. 5.2.1 and 5.2.2. The coinciding perturbations around transitions with adjacent J 's, with the strongest perturbation around $43_{K_a, K_c} \leftarrow 42_{K_a, K_c-1}$, for $K_a = 12$ of 0^+ and 0^- as well as for $K_a = 7$ of 24^+ , together with the observed deviations of opposite sign for $v = 0$ and $v_{24} = 1$, respectively, obtain the most important insights. The

Table 7: Spectroscopic parameters^a (MHz) of $v_{24} = 1$ of *gauche*-propanal.

Parameter	24 ⁺	24 ⁻
E_{rel}	-6708.368(33)	6708.368(33)
E_{rel} / cm^{-1}	-0.223767(1)	0.223767(1)
A	26460.7209(306)	26355.7061(246)
B	4326.01509(91)	4329.31158(68)
C	4159.09513(120)	4164.82842(107)
$-D_K$	-2.49474(307)	-2.1044(54)
$-D_{JK}$	0.218845(197)	0.189105(291)
$-D_J$	-0.00788577(44)	-0.00724399(70)
$d_1 \times 10^3$	1.31855(93)	1.14471(95)
$d_2 \times 10^3$	0.033294(311)	0.056931(211)
$H_K \times 10^6$	-	-
$H_{KJ} \times 10^6$	-84.22(62)	6.50(86)
$H_{JK} \times 10^6$	0.8116(256)	-2.6104(155)
$H_J \times 10^6$	0.092061(257)	0.136688(141)
$h_1 \times 10^9$	-9.759(314)	-31.063(313)
$h_2 \times 10^9$	-24.723(264)	-20.526(216)
$h_3 \times 10^9$	2.0639(303)	0.601(33)
$L_K \times 10^9$	-	-
$L_{KKJ} \times 10^9$	106.9(37)	-
$L_{JK} \times 10^9$	0.281(237)	3.765(245)
$L_{JJK} \times 10^9$	-0.11717(256)	-0.1127(41)
$L_J \times 10^9$	-0.003435(64)	-0.0018073(312)
$l_1 \times 10^{12}$	0.0663(290)	-0.1725(237)
$l_2 \times 10^{12}$	1.583(90)	2.684(77)
$l_3 \times 10^{12}$	0.0837(73)	-0.1898(78)
$l_4 \times 10^{12}$	-	-
$P_{KJ} \times 10^{12}$	-10.37(60)	-8.06(65)
$P_{JK} \times 10^{12}$	-0.2438(162)	-0.5442(162)
$P_J \times 10^{15}$	0.1391(72)	-
$p_2 \times 10^{15}$	-0.0561(105)	-0.1621(87)
F_{bc}		32.24988(59)
F_{bc}^K		0.37882(43)
$F_{bc}^J \times 10^3$		-2.9655(54)
$F_{bc}^{KK} \times 10^3$		-
$F_{bc}^{JK} \times 10^3$		-0.024112(133)
$F_{bc}^{JJ} \times 10^6$		0.07302(127)
$F_{bc}^{JJK} \times 10^9$		0.9205(220)
F_{ca}		151.923(69)
F_{ca}^K		-0.1463(120)
$F_{ca}^J \times 10^3$		-4.335(107)
$F_{ca}^{KK} \times 10^3$		-0.4136(135)
$F_{ca}^{JJ} \times 10^6$		0.1322(128)
$F_{ab}/2$		-4.3714(304)
$F_{ab}^J/2 \times 10^3$		-1.0862(114)
$F_{ab}^{JJ}/2 \times 10^6$		-0.1188(43)
Combined fit		
Number of transitions		1651
<i>rms</i>		56.2 kHz
<i>wrms</i>		1.23

^a S reduction is used with SPFIT in the I^T -representation. Values of F_{bc} , F_{ca} and higher orders, given between column 2 and 3 are associated with operators between tunneling states. Values of F_{ab} and higher orders are fit as linear combination $\Delta F_{ab} = (F_{ab}^+ - F_{ab}^-)/2$. Numbers in parentheses are one standard deviation in units of the least significant figures.

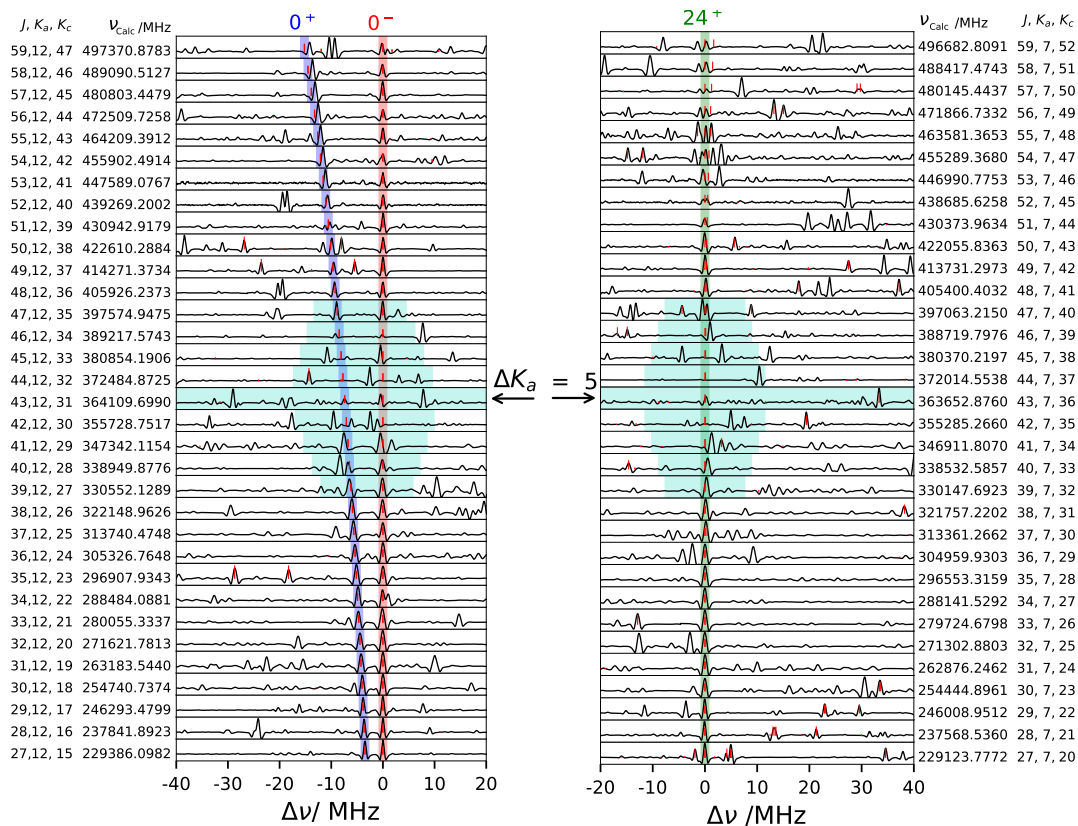


Figure 35: Loomis Wood plots of *gauche*-propanal showing qR series transitions, $J_{K_a, K_c} \leftarrow (J-1)_{K_a, K_c-1}$, with $K_a = 12$ (0^+ and 0^-) on the left and $K_a = 7$ (24^+) on the right hand side. The center frequencies of 0^- and 24^+ are derived from the single vibrational state models presented in Tables 6 and 7, respectively. Series of the ground and first excited state are strongly perturbed around $J = 43$ with trends in deviations from predicted to observed frequencies of opposite sign. This observation is a clear hint for ongoing interactions with $\Delta K_a = 5$ between $v = 0$ and $v_{24} = 1$ and the wrong assignment of the fundamental frequency $\nu_{24} = 113.1(2) \text{ cm}^{-1}$ in Ref. [45], see text.

fundamental frequency ν_{24} needs to be significantly lower than expected, approximately 44 cm^{-1} lower, to be able to explain the $\Delta K_a = 12 - 7 = 5$ interactions between $v = 0$ and $v_{24} = 1$ observed in Fig. 35. The fundamental frequency of 113.1 cm^{-1} of Ref. [45] is consistently confirmed by independent microwave relative intensity measurements, which determined a value of $109(15) \text{ cm}^{-1}$. Therefore, it seems to be necessary to test this value by MMW relative intensity measurements. A ratio of $I_{v_{24}=1}/I_{v=0} = 0.76(9)$ is determined for randomly selected transitions, see Table A11. This ratio translates via the Boltzmann factor to an energy difference of 57 cm^{-1} ($33 - 84 \text{ cm}^{-1}$) between $v_{24} = 1$ and $v = 0$. The derived ratio should be taken with caution because intensities cannot be compared easily in the MMW spectra, as can be seen by the large uncertainty and the resulting span of the estimated vibrational frequency. However, the assumption of a wrong assignment is supported further. Subsequently, the energy difference between the

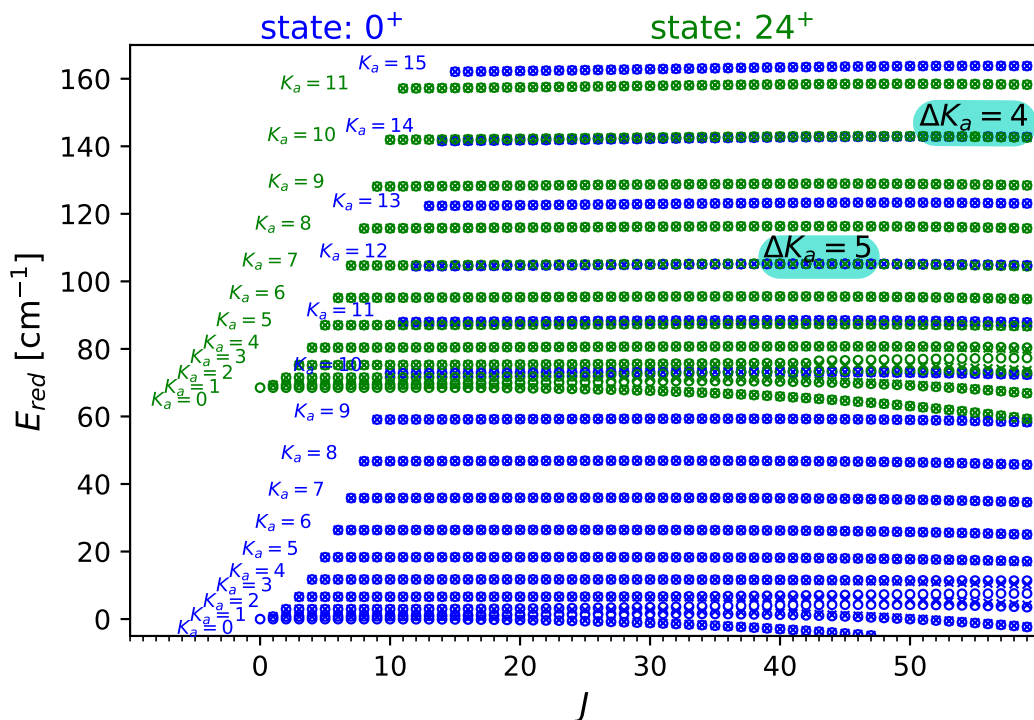


Figure 36: Reduced energy diagram of $v = 0$ and $v_{24} = 1$ of *gauche*-propanal, see Eq. (2.19). Only 0^+ and 24^+ tunneling states are shown for simplicity. Highlighted in turquoise are areas for fixed K_a and adjacent J 's with strongest perturbations between the two vibrational states.

two states is adjusted until the energy levels of $J_{K_a, K_c} = 43_{12, 31}$ of 0^+ and $J_{K_a, K_c} = 43_{7, 36}$ of 24^+ have the same energy. 0^+ is chosen instead of 0^- as in direct comparison 0^+ seems to be perturbed more strongly. This turned out to be a good starting point for the global analysis.

The final reduced energy diagram of $v = 0$ and $v_{24} = 1$ is shown in Fig. 36. Only 0^+ and 24^+ are shown for simplicity. It is easily seen that the energy levels with $K_a = 12$ of 0^+ (in blue) and $K_a = 7$ of 24^+ (in green) are very close in energy. Another interesting observation can explain two more observations. The single state analysis of the ground vibrational state ends at $K_a = 13$, which does not seem to be affected by the first vibrationally excited state. The next higher one, $K_a = 14$, could not be included into the fit without deterioration of the *wrms*. Likewise, transitions with $K_a = 10$ and $J > 30$ of $v_{24} = 1$ are excluded from the final single state analysis of $v_{24} = 1$. By reducing the fundamental frequency ν_{24} not only perturbations originating from $\Delta K_a = 5$ interactions but also $\Delta K_a = 14 - 10 = 4$ interactions indicate failures in the single state analyses. These findings gave confidence for a successful treatment of the interactions, starting by describing the $\Delta K_a = 5$ interactions and subsequently $\Delta K_a = 4$ interactions, in a global analysis of $v = 0$ and $v_{24} = 1$.

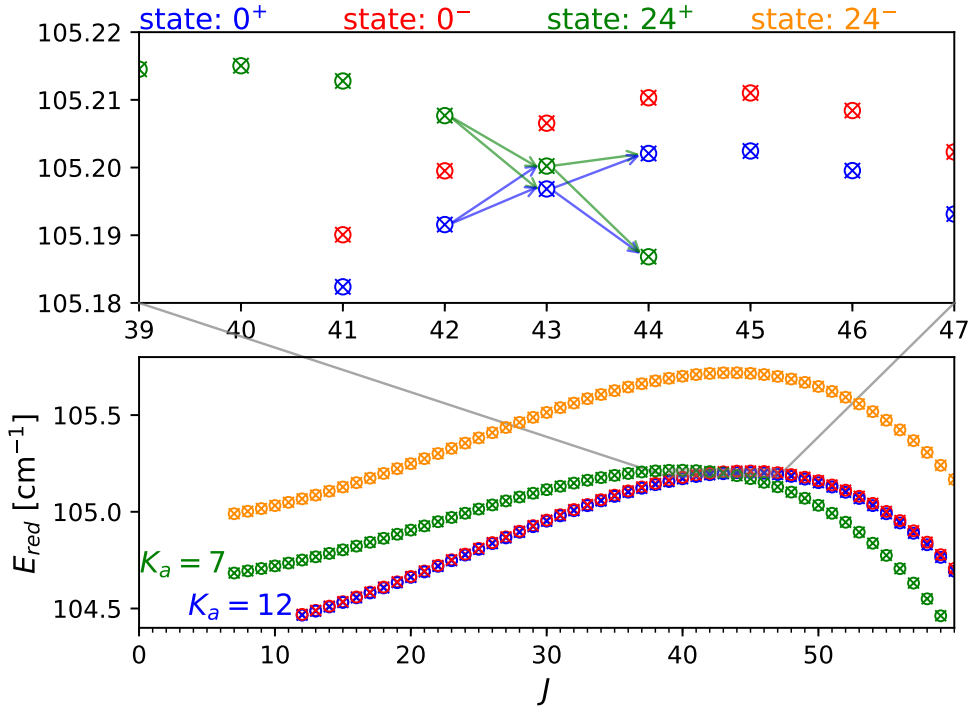


Figure 37: Reduced energy diagram of the $\Delta K_a = 5$ interaction in *gauche*-propanal, see Eq. (2.19). In the close up zoom nominally allowed and forbidden transitions, which occur between $0^+ \leftrightarrow 24^+$, respectively, are sketched by the arrows. All eight transitions are assigned within this work. The observed lines are shown in Fig. 38 and the resulting closed loops of transitions are key results to pin down the energy difference of the strongly interacting energy levels of 0^+ and 24^+ .

The $\Delta K_a = 5$ interactions are expected to explain the lowest occurring irregularities in K_a of both single state fits. Unfortunately, the analysis is not straightforward due to different interaction types which may cause the perturbations. To explain this in more detail, the reduced energy diagram of the tunneling states 0^+ and 0^- with $K_a = 12$ as well as of 24^+ and 24^- with $K_a = 7$ is presented enlarged in Fig. 37. The two asymmetry sides are blended, which can be noticed by the on top of each other plotted 'x' and 'o' markers. The energy levels are prolate paired. Furthermore, the much larger splitting of the two tunneling states of the vibrationally excited state in comparison to the ground state is clearly visible, compare to the energy difference of the green and yellow series and to the nearly not visible energy difference of the blue and red series in the lower panel of Fig. 37. Here, also the apparent crossing of the energy levels of 24^+ with both ground state tunneling states, 0^+ and 0^- , can be clearly seen. The energy levels of 24^- are quite isolated in comparison. In particular no crossing of 24^- with the ground state energy levels is existent for $J \leq 60$ for these values of K_a . In the upper panel of Fig. 37, an even closer zoom to the interaction area is shown to study possible interactions in more detail. In a first step, all combinations of energy levels which may interact with

each other are considered. Here, the state 24^- is neglected as it is considered to be isolated from the others. Therefore, 0^+ , 0^- , and 24^+ may interact with each other, leading to three possible two level system interaction partner: $0^+ \leftrightarrow 0^-$, $0^+ \leftrightarrow 24^+$, and $0^- \leftrightarrow 24^+$. Identifying all possible interaction parameters is the next step to find the one which ameliorates the *wrms* the most.²³ Moreover, five parameters are tested for each new type of possible Coriolis interactions to find the best one. The five examined parameters are always the ones with the five lowest orders of the rotational operator (cf. Eq. (A3)). The time consuming procedure of testing many parameters is applied as *ab-initio* calculations are too expensive and furthermore not practicable to reproduce the magnitude of the various interaction parameters properly. The tunneling states 0^+ and 24^+ are of the same symmetry and are observed to be closest in energy for $J = 43$ for all considered energy levels in the upper panel of Fig. 37. Consequently, the off-diagonal Fermi parameter F_2 is observed to reduce the *wrms* the most. Further testing also indicated an amelioration of the *wrms* when the parameter G_{2b} (and G_{2b}^J) is incorporated. These parameters are sufficient for properly describing the observed perturbations. Transitions with adjacent J 's are without exception well described in the fit. Finally, all eight possible transitions connecting the most strongly perturbed energy levels with $J = 43$ of 0^+ and 24^+ , see the arrows in the upper panel of Fig. 37, are unambiguously assigned as can be seen in Fig. 38. In this case, four nominally allowed transitions within each tunneling state as well as four nominally forbidden transition between 0^+ and 24^+ are observed due to the strong mixing of the energy levels with $J = 43$. Interestingly, the line shapes of all eight transitions are asymmetric, sometimes even a partial splitting into two components with unequal intensities is observed, see Fig. 38. The origin of this asymmetry/splitting is not known with certainty, however, the special line shapes of all eight strongly perturbed transitions are considered as an additional confirmation that the assignments are correct.²⁴ Usually these lines would be neglected in the fitting procedure. However, due to their fundamental importance

²³Interactions between $0^+ \leftrightarrow 0^-$ are described by the already used *a*-type Coriolis interactions, as they link the tunneling states of the ground vibrational state with same K_a ($\Delta K_a = 0$, $\Delta K_c = 1$ and $\Delta J = 0$). Furthermore *b*-type Coriolis interactions might occur when interactions between 0^- and 24^+ are considered ($\Delta K_a = 5$, $\Delta K_c = 5$, and $\Delta J = 0$). The tunneling states 0^+ and 24^+ are of the same symmetry, that is why Fermi resonances might appear. Last but not least, also *c*-type Coriolis interactions can occur between 0^+ and 24^+ , as they appear within the states of same symmetry ($\Delta K_a = 5$, $\Delta K_c = 4$ or 6 , and $\Delta J = 0$), see Sec. 2.3.5.

²⁴Even though the origin is not clarified securely, one hypothesis is that the asymmetry/splitting is originating in methyl group internal rotation splittings which are too small to observe them in regular *a*-type transitions. Usually vibrational states swap A and E levels with $\Delta v = 1$ which gives rise to larger splittings of A and E transitions, cf. Fig. 12. The resulting perturbation for A and E levels might differ due to the different energy differences. By further taking into account the two asymmetry sides, the resulting four components might explain the asymmetric line shape.

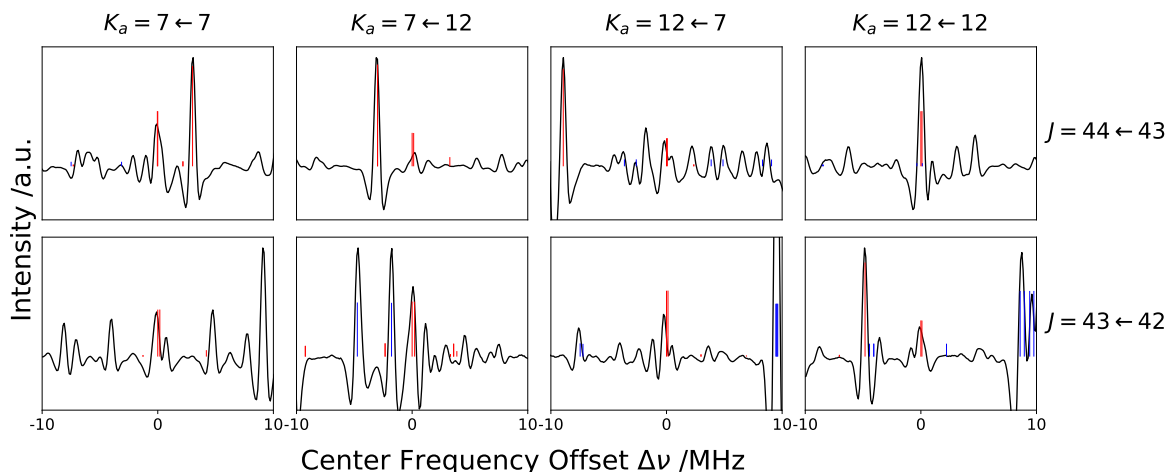


Figure 38: Strongly perturbed transitions of the $\Delta K_a = 5$ interaction of 0^+ (with $K_a = 7$) and 24^+ (with $K_a = 12$) in *gauche*-propanal (in red). Eight transitions can be observed, four nominally allowed and furthermore four nominally forbidden lines between the vibrational states with $K_a = 7 \leftrightarrow 12$. The center frequencies are predictions from the global analysis and the shown transitions are depicted by the arrows in the upper panel of Fig. 37. Further assigned transitions of *gauche*- and *syn*-propanal are shown by the red and blue stick spectrum, respectively.

as they are able to determine directly the energy difference of the strongly perturbed energy levels with closed loops, the eight lines, or 16 prolate paired transitions, are included in the fit with a somewhat larger uncertainty of 100 kHz (cf. Fig. A24). Including these transitions fostered a model which is able to describe the $\Delta K_a = 5$ interactions to experimental uncertainty.

After successfully treating the $\Delta K_a = 5$ interactions, the next step is to also properly include transitions affected by $\Delta K_a = 4$ interactions. The perturbed transitions are observed in qR series with $K_a = 14$ for $\nu = 0$ as well as $K_a = 10$ for $\nu_{24} = 1$. A reduced energy diagram zoomed to the interaction area is shown in Fig. 39. Again, the lower tunneling state 24^+ of the vibrationally excited state is crossing the two tunneling states of the ground state, 0^+ and 0^- . However, the pattern of the perturbed energy levels looks rather different than for $\Delta K_a = 5$ interactions. Due to $\Delta K_a = 4$ and $\Delta J = 0$ between the involved energy levels of $\nu = 0$ and $\nu_{24} = 1$ solely *a*-type Coriolis interaction parameters are tested. Here, F_{bc} improves the *wrms* the most and is therefore incorporated to the parameter set. In the region of the strongest perturbations merely transitions which would be considered as avoided crossing transitions and are nominally forbidden are assigned. This is not ideal as the energy difference is not measured directly, see Fig. 39. Besides, perturbations at energy levels with such high *J*'s impede an ideal description because transitions connecting nearly unperturbed or much less perturbed energy levels above the center of interaction cannot be measured

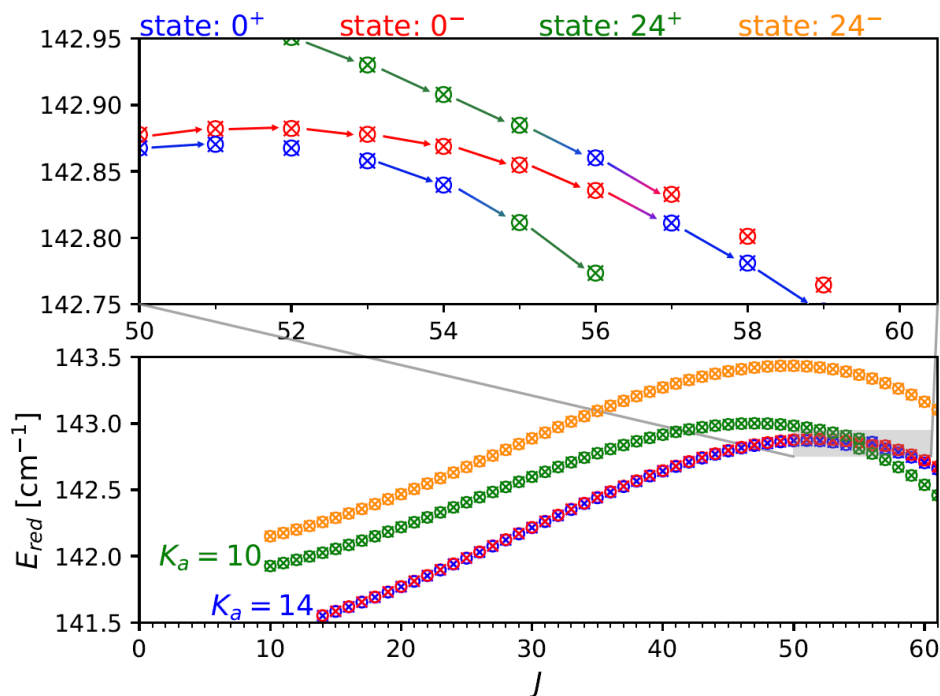


Figure 39: Reduced energy diagram of the $\Delta K_a = 4$ interaction in *gauche*-propanal. The arrows in the upper panel indicate assigned and fit transitions.

within the observed frequency range ($J_{max} = 60$). Noteworthy are the two prolate paired energy levels of 24^+ and the missing levels of 0^+ at $J = 55$. It is not possible that four energy levels of one state have the same K_a value and closer examination reveals that the one higher in energy is not an energy level with $K_a = 10$. Due to the strong perturbations a mislabeling arises. Usually energy levels with identical J and increasing K_a are increasing in energy for both tunneling states (cf. Fig. 7). An interaction can lift the steady ladder arrangement, but energy levels are still labeled by SPFIT depending on the ladder scheme. Two energy levels which are close in energy might swap the order within the fitting procedure, followed by a renaming and therefore objection of assigned transitions as they might appear far off in frequency. It is advisable to put a zero weight to transitions in question and only implement them at the end as they can be renamed within the fit procedure. Extending the frequency range to measure involved and nearly unperturbed qR series transitions with $J > 60$ and ideally using DM-DR spectroscopy at these high frequencies to assign closed loop transitions might further improve the model. Despite all these obstacles, a first description of $\Delta K_a = 4$ interactions is reached in the global analysis.

After $\Delta K_a = 5$ and $\Delta K_a = 4$ interactions between $v = 0$ and $v_{24} = 1$ are treated satisfactorily in the derived global model, more transitions with higher K_a than already described can be straightforwardly implemented to the fit, like is done in the single state analyses. qR series with the next higher K_a are stepwise implemented to the

fit for each tunneling state of both vibrational states. In the end, qR series up to J_{max} and $K_a = 15$ for $v = 0$ and $K_a = 11$ for $v_{24} = 1$ with J_{max} up to 60 are fit to experimental uncertainty. K_a is even up to 17 for lower J of $v = 0$. The total coverage of quantum numbers of observed transitions and their deviations to predictions of the global analysis of $v = 0$ and $v_{24} = 1$ can be seen in the lower panels of Figs. A30–A33. Series with higher K_a can only be included in the model when a significant deterioration of the *wrms* is accepted. One hypothesis for this might originate in interactions with the second vibrationally excited state $v_{24} = 2$ of *gauche*-propanal or other vibrational states. The treatment of this is beyond the scope of this work. In summary, the global analysis allows for the assignment of many more transitions which could be, more importantly, fit to experimental uncertainty, in comparison to the single state fits. The final spectroscopic parameters of the global analysis are collected in Table 8. The most fundamental result of the global analysis is the determination, associated with a reassignment, of the fundamental frequency $\nu_{24} = 68.75037(30) \text{ cm}^{-1}$ of *gauche*-propanal.

Table 8: Spectroscopic parameters^a (MHz) of the global fit of $v = 0$ and $v_{24} = 1$ of *gauche*-propanal.

Parameter	0^+	0^-	24^+	24^-
$\Delta E^v/2^b$		237.7893(81)		6708.3692(235)
ΔE			2061084.2(90)	
E_{rel}^c	-237.7893(81)	237.7893(81)	2054375.8(90)	2067792.6(90)
E_{rel}^c / cm^{-1}	-0.00793180(27)	0.00793180(27)	68.52660(30)	68.97414(30)
ΔE^{vc}		475.5786(115)		13416.8(13)
ΔE^{vc} / cm^{-1}		0.01586359(38)		0.44753(42)
ΔE^c / cm^{-1}			68.75037(30)	
A	26252.5958(75)	26248.5661(79)	26460.7047(155)	26355.6568(204)
B	4314.88778(67)	4314.95158(62)	4326.01733(78)	4329.30966(59)
C	4147.91471(61)	4148.12679(59)	4159.09496(106)	4164.83173(96)
$-D_K$	-2.06977(62)	-2.05824(63)	-2.49135(150)	-2.0896(39)
$-D_{JK}$	0.1798841(50)	0.1789892(47)	0.218507(51)	0.188766(78)
$-D_J$ $\times 10^3$	-6.580854(308)	-6.56201(32)	-7.90169(37)	-7.26255(53)
d_1 $\times 10^3$	1.08499(57)	1.07526(57)	1.31865(45)	1.14660(37)
d_2 $\times 10^3$	-0.044125(68)	-0.039849(38)	0.038543(150)	0.063808(93)
H_K $\times 10^6$	-	-	-	-
H_{KJ} $\times 10^6$	8.709(32)	11.200(34)	-83.926(268)	5.338(290)
H_{JK} $\times 10^6$	-3.2406(35)	-3.3057(34)	1.1632(76)	-2.2458(99)
H_J $\times 10^6$	0.127377(111)	0.128224(113)	0.092240(215)	0.138476(219)
h_1 $\times 10^9$	-51.703(158)	-52.556(156)	-9.608(76)	-32.140(55)
h_2 $\times 10^9$	-0.8131(85)	-	-23.001(63) ^d	-23.001(63) ^d
h_3 $\times 10^9$	-	-0.19834(244)	2.2481(57)	0.5638(248)
L_K $\times 10^9$	-	-	-	-
L_{KKJ} $\times 10^9$	-2.265(87)	-5.299(88)	94.94(142)	-
L_{JK} $\times 10^9$	-2.3217(182)	-2.2200(182)	-1.522(75)	2.476(81)
L_{JJK} $\times 10^9$	0.14531(87)	0.14138(88)	-0.15456(145)	-0.16335(225)

Continued on next page

Table 8 – continued from previous page

Parameter	0^+	0^-	24^+	24^-	
L_J	$\times 10^{12}$	-3.3327(284)	-3.2059(284)	-3.864(60)	-2.458(60)
l_1	$\times 10^{12}$	2.1378(128)	2.0364(128)	–	–
l_2	$\times 10^{12}$	–	–	1.0502(103)	3.3197(278)
l_3	$\times 10^{12}$	–	–	–	-0.2006(61)
l_4	$\times 10^{12}$	–	–	–	–
P_{JK}	$\times 10^{12}$	-0.15475(281) ^d	-0.15475(281) ^d	-0.2404(105)	-0.3999(132)
P_J	$\times 10^{15}$	0.07456(286) ^d	0.07456(286) ^d	0.1630(62)	0.0813(63)
p_2	$\times 10^{15}$	–	–	–	-0.2204(40)
F_{bc}^-		23.96486(229)		32.22732(54)	
F_{bc}^K		-0.10958(81)		0.399567(297)	
F_{bc}^J	$\times 10^3$	-3.3607(40)		-2.96460(216)	
F_{bc}^{KK}	$\times 10^3$	0.24036(86)		–	
F_{bc}^{JK}	$\times 10^3$	-0.013551(106)		-0.023756(97)	
F_{bc}^{JJ}	$\times 10^6$	0.14945(63)		0.07229(40)	
F_{bc}^{JKK}	$\times 10^9$	–		0.5455(163)	
F_{bc}^{KKK}	$\times 10^6$	0.1473(39)		–	
F_{2bc}	$\times 10^3$	-0.34902(47)		–	
F_{ca}		–		151.909(61)	
F_{ca}^K		–		-0.1580(32)	
F_{ca}^J	$\times 10^3$	–		-4.489(45)	
F_{ca}^{KK}	$\times 10^3$	–		-0.4677(61)	
F_{ca}^{JJ}	$\times 10^6$	–		0.2043(78)	
$F_{ab}/2^b$		5.17(38)		4.3454(139)	
$F_{ab}^K/2^b$		0.066 ^e		–	
$F_{ab}^J/2^b$	$\times 10^3$	–		1.1419(57)	
$F_{ab}^{JJ}/2^b$	$\times 10^6$	–		0.10361(207)	
F_{bc}^f			7.2891(115)		
G_{2b}^f			0.020888(188)		
G_{2b}^{Jf}	$\times 10^6$		2.906(57)		
F_2^{-g}			-3.1298(64)		
F_2^{+g}			-2.6569(122)		
Global fit					
Number of transitions ^h	1414	1419	985	992	
Total number of transitions		4810			
Total number of lines		3426			
<i>rms</i>		55.2 kHz			
<i>wrms</i>		1.17			

^a S reduction is used with SPFIT in the I^r -representation. Values of F_{bc} etc., given either between column 2+3 or 4+5, are associated with operators between tunneling states. Values of F_{bc} etc., given between column 3+4, are associated with operators between the vibrational states.

^b Parameter is fit as linear combination $X^v = (X^{v'} - X^{v''})/2$.

^c Value not fit. Only given for clarification and calculated from the fit $\Delta E^v/2$ and ΔE .

^d Parameter is fit as linear combination $X^v = (X^{v'} + X^{v''})/2$ (it is fixed to the other tunneling state).

^e Parameter value is manually fixed.

^f Parameter acts between 0^+ and 24^- as well as between 0^- and 24^+ .

^g Parameter acts between 0^+ and 24^+ (+) or between 0^- and 24^- (-).

^h Transitions between different tunneling states are counted to the respective lower level of a transition.

6 Summary, Discussion, and Conclusions

Rotational and ro-vibrational spectra of propanal are measured and analyzed in the course of this thesis. The rotational spectra are measured with (sub-)millimeter wave spectrometers in Cologne mainly in the frequency ranges of 75–129 GHz and 169.2 – 500.4 GHz. Ro-vibrational spectra are measured in the FIR region 80–700 cm^{-1} at the SOLEIL synchrotron facility in Paris. The two stable conformers of propanal, *syn*- and *gauche*-propanal, are analyzed in several energetically low-lying vibrational states. In this section, main results are summarized and the accuracy of predictions for possible astronomical detection are evaluated. Based on this evaluation it is concluded whether the derived quantum mechanical models are solid up to the maximum observed frequency of 500 GHz, and beyond, and whether the accuracy of derived models would benefit from a revisit in future investigations, in particular as part of an extended global analysis. First of all, the extensive analyses of $v = 0$, $v_{24} = 1$, and $v_{23} = 1$ of *syn*-propanal as well as further analyses of the three tentatively assigned vibrationally excited states $v_{24} = 2^*$, $v_{15} = 1^*$, and $v_{24} = v_{23} = 1^*$ are discussed in Sec. 6.1. Thereafter, the advantage of a global analysis of *gauche*-propanal in its vibrational ground state $v = 0$ and its first vibrationally excited state $v_{24} = 1$, compared to single state analyses of both states, are discussed in Sec. 6.2. The derived description of *gauche*-propanal is compared to other molecules with two stable degenerate configurations and feasible tunneling between these. Finally, the newly established DR and in particular DM-DR experimental setups in Cologne are examined and benefits for the analyses of *syn*- and *gauche*-propanal are pointed out in Sec. 6.3.

6.1 *Syn*-Propanal

The quantum number coverage of the analyses of rotational spectra of various analyzed vibrational states of *syn*-propanal are displayed in Figs. A15–A20. A brief overview of the most important facts of these analyses can be found in Table 9. All vibrational states of *syn*-propanal are analyzed using the ERHAM program to properly describe the torsional splittings due to the methyl group internal rotation [72].

The three lowest vibrational states of *syn*-propanal, the ground vibrational state $v = 0$, the first excited aldehyde torsion $v_{24} = 1$, and the first excited methyl torsion $v_{23} = 1$, are well described up to 500 GHz. The results of $v = 0$, $v_{24} = 1$, and $v_{23} = 1$ have already been published in Ref. [50] and spectroscopic parameters are listed in Table 3. In this work, *a*- and *b*-type transitions, as well as some incorrectly labeled or nominally forbidden *c*- and *x*-types, of all three vibrational states are assigned in the frequency regions of 75–129 GHz and 170–500 GHz. Additional transitions from the MW region 8–40 GHz [39, 42] are included in the final analyses. The final analyses of the three

Table 9: Summary of the analyses of rotational spectra of vibrational states of *syn*-propanal studied within the framework of this thesis. Key data of derived quantum mechanical models and their predictive power for possible astronomical detection are listed.

Vibrational state	Quantum mechanical model					Expected Predictive Power		
	J_{max}	$K_{a, max}$	ν_{max} ^a	No. ^b	σ ^c	ALMA B3 ^{d,e}	500 GHz ^{d,f}	THz ^{d,g}
$v = 0$	77	40	500	8551	0.94	✓	✓	✓
$v_{24} = 1$	64	36	500	6823	0.93	✓	✓	✓
$v_{23} = 1$	54	18	500	2760	1.06	✓	✓	✗
$v_{24} = 2^*$	54	9	498	605	1.11	✓	✗	✗
$v_{15} = 1^*$	20	7	123	203	1.03	✓	✗	✗
$v_{24} = v_{23} = 1^*$	53	4	490	392	1.24	✓	✗	✗

^a The maximum frequency of assignments in the final fit (in GHz); ^b Number of transitions in the fit; ^c Unitless standard deviation of the fit; ^d Yes (✓) or No (✗); ^e Is the model accurate enough for astronomical searches for this vibrationally excited state in ALMA Band 3?; ^f Is a firm model up to 500 GHz available?; ^g Are predictions into the terahertz region expected to be reliable (or: Are all observed lines included in the final fit)?

states cover a broad quantum number range with $J \leq 77$ and $K_a \leq 40$, $J \leq 64$ and $K_a \leq 36$, $J \leq 54$ and $K_a \leq 18$ for $v = 0$, $v_{24} = 1$, and $v_{23} = 1$, respectively.

The ground vibrational state can be considered as an isolated state over the full observed range and is described to experimental uncertainty with a single state analysis. The same holds for $v_{24} = 1$ for which special care is taken to incorporate some of the *b*-type transitions at the upper limit of $K_{a, max}$ and J_{max} included in the fit. This is also observed for $v = 0$, albeit to a much lesser extend. Some of these transitions still show larger deviations ($\sigma > 3$) in the final model of $v_{24} = 1$. Nevertheless, all assigned transitions within this work are included in the final fit. More centrifugal distortion terms, compared to $v = 0$, are needed to fit the observed transitions to experimental uncertainty, in particular this is true for the internal rotation parameters. The larger ϵ_{10} in $v_{24} = 1$ results in larger internal rotation splittings, therefore centrifugal distortion terms are also expected to play a decisive role. On the basis of derived quantum mechanical models of $v = 0$ and $v_{24} = 1$, and with a detour of refitting the data with SPFIT, a main result is the reassignment of the fundamental frequency ν_{24} to $133.9754525(39) \text{ cm}^{-1}$. Therefore, astronomical observations of the rotational spectra as well as of the fundamental band are not limited by quantum mechanical models anymore, see also Fig. 5. Rotational predictions should be reliable up to the terahertz region (cf. Fig. A13). Thanks to the derived quantum mechanical models the spectrum can also be simulated for any temperature, with reliable intensities, which is important for the determination of column densities and temperatures of molecules in the ISM. Observers should only be careful with *b*-type transitions with K_a and J much higher

than those in the fit, as deviations may arise from the model.

A firm model is derived for $\nu_{23} = 1$ as well. Many predicted transitions should be accurate enough for astronomical observations up to the terahertz region, but should be viewed with caution if the predicted uncertainty is larger than 0.3 MHz, or if $J + 2K_a > 50$, as severe perturbations are observed which are not treated by the single state model. Because of these perturbations, only transitions with quantum numbers actually covered by this analysis should be used in conservative treatments to derive column densities and other physical parameters from astronomical detection. A global analysis involving $\nu_{23} = 1$ at 219.9 cm^{-1} and potentially perturbing vibrational states that are close in energy, such as $\nu_{15} = 1$ at 264.0 cm^{-1} as well as $\nu_{24} = 2$ at 269.3 cm^{-1} [45, 46], is desirable for the future to ensure also an accurate prediction of perturbed transitions. Possible interactions of the triad of vibrational states are visualized in Fig. 40. As $\nu_{23} = 1$ is of A'' symmetry, Coriolis interaction may occur from $\nu_{15} = 1$ with A' symmetry. In addition, $\nu_{24} = 2$ with A' symmetry gives rise to further rotational or Coriolis-type interactions. These may be less prominent due to the higher order coupling term compared to Coriolis interaction between two fundamentals and furthermore due to the larger energy difference between the two interacting states. A global analysis may even be more difficult because of a Fermi resonance between $\nu_{15} = 1$ and $\nu_{24} = 2$ whose strength may be considerable. Also Coriolis interaction can occur between these states. The vibrational frequency of $\nu_{24} = 2$ is expected to be shifted to higher frequencies because of the Fermi resonances between $\nu_{24} = 2$ and $\nu_{15} = 1$, as $\nu_{24} = 2$ is expected to be slightly higher in energy than $\nu_{15} = 1$, see

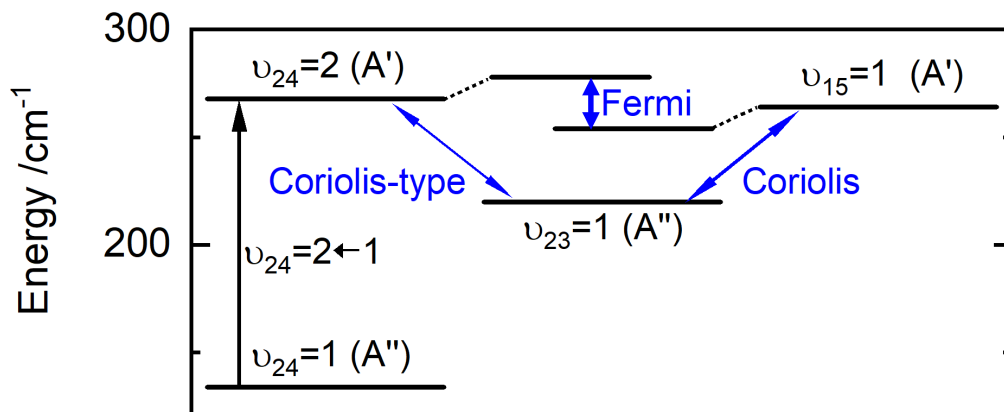


Figure 40: Possible interactions between the triad of vibrational states $\nu_{23} = 1$, $\nu_{15} = 1$, and $\nu_{24} = 2$ of *syn*-propanal are marked by blue arrows. A strong Fermi resonance between $\nu_{15} = 1$ and $\nu_{24} = 2$ is expected to shift $\nu_{24} = 2$ to higher frequency. This results in a blue-shifted hot band of $\nu_{24} = 2 \leftarrow 1$ compared to the transition of the unperturbed system, which is shown by the black arrow. Possible Coriolis-type interactions between $\nu_{15} = 1$ and $\nu_{24} = 2$ are not shown for clarity.

Fig. 40. Based on this assumption, the hot band $\nu_{24} = 2 \leftarrow 1$ is assumed to be shifted to higher frequencies from its unperturbed position. The band at 135.1 cm^{-1} , which was previously assigned to the fundamental band ν_{24} [45], is most likely the hot band $\nu_{24} = 2 \leftarrow 1$, see Fig. A12. The assignments of the fundamental band $\nu_{24} = 1 \leftarrow 0$ and its hot band $\nu_{24} = 2 \leftarrow 1$ would be exchanged from Ref. [45], if the suggested re-assignment is confirmed by the rotationally resolved FIR spectrum.

The analyses of vibrationally excited states of higher energies are successfully performed with the systematic DM-DR measurement scheme introduced in Sec. 4.2. This scheme facilitates the deciphering of less intense fingerprints. In this way, *a*- and *b*-type transitions could be assigned unambiguously. First models for three newly assigned vibrationally excited states are derived in this work. The analyses cover a smaller quantum number range than for example $\nu = 0$ (cf. Figs. A18–A20). Nevertheless, accurate rotational constants A , B , C , and the tunneling parameter ϵ_{10} are derived for each of these states, see Table 4. A systematic shift in deviations of the same magnitude but reversed in sign is observed for two of the three states, based on observed and predicted parameters B and C , see Table 5. Fermi resonances are assumed to be the origin of this effect, already noticed by the inevitable re-assignment of $\nu_{24} = 2 \leftarrow 1$ (cf. also Fig. 40). Therefore, the two states are assigned to $\nu_{24} = 2^*$ and $\nu_{15} = 1^*$. The third one is tentatively assigned as the next energetically lowest lying vibrationally excited state which is not assigned so far, namely $\nu_{24} = \nu_{23} = 1^*$, as observed qR series seem to be the next most intense ones. Astronomical searches for these states are now possible in the W-band region (ALMA Band 3). All three vibrational states show more or less severe perturbations above 170 GHz even for low K_a . All of these states should be revisited in a global analysis, after their assignment is confirmed with the help of the already measured FIR spectra, like is done for $\nu_{24} = 1 \leftarrow 0$. In addition to these vibrational states, more qR series belonging to further vibrationally excited states are identified, see Fig. 27, which may be the starting point for the analyses of further vibrational states.

6.2 *Gauche*-Propanal

The quantum mechanical models of the ground vibrational state $\nu = 0$ and the first excited aldehyde torsion $\nu_{24} = 1$ of *gauche*-propanal are described in the reduced axis system proposed by Pickett [65] and are fit and predicted with his SPFIT/SPCAT suite of programs [84]. Both vibrational states are described by single state fits first, see Tables 6 and 7, but the quantum number coverage could be increased within a global analysis (cf. Figs. A30–A33). Within this global analysis, the maximum K_a for series of *a*-type transitions (qR series) up to $J_{max} = 60$ are $K_a = 15$ and $K_a = 11$ for $\nu = 0$ and for $\nu_{24} = 1$, respectively. K_a is even up to 17 for lower J of $\nu = 0$ ($J \leq 47$ for

$K_a = 16$ and $J \leq 26$ for $K_a = 17$). Notably, strongly perturbed qR series with $K_a = 12$ and $K_a = 14$ of $\nu = 0$ as well as with $K_a = 7$ and $K_a = 10$ of $\nu_{24} = 1$ are included in the final fit and are well described by $\Delta K_a = 5$ and $\Delta K_a = 4$ interaction parameters. Fermi as well as Coriolis interaction terms are needed for a satisfying description, see the best choice of spectroscopic parameters in Table 8. The $\Delta K_a = 4$ interaction may possibly be described even better if transitions with $J > 60$ above 500 GHz are assigned as these are less perturbed. It is observed that implementing at first transitions below and above interaction areas help to derive best possible solutions. Ongoing interactions within one vibrational state as well as between two vibrational states can be seen by plotting the mixing coefficients for energy levels of one asymmetry side of one tunneling state in a contour plot (cf. Fig. A27). Including transitions with even higher K_a is expected to be only possible if $\nu_{24} = 2$ is added to the global fit, as may be seen from Fig. 41. Astronomical detection of both states should not be limited by the quality of the derived quantum mechanical model. Predictions (cf. Fig. A22) are expected to be accurate into the terahertz region for qR series transitions if they are fit up to J_{max} (cf. Figs. A30–A33). Caution is advised if predicted qR series with adjacent $J > 60$ show systematic deviations to observed spectra. These deviations may easily be ignored in astronomical spectra since they most probably originate in so far untreated interactions.

Interactions between $\nu = 0$ and $\nu_{24} = 1$ were initially not expected as the fundamental frequency ν_{24} was determined to $113.1(2) \text{ cm}^{-1}$ [45], which was supported by relative intensity measurements [41]. The energy difference of the two vibrational states does not explain the observed (perturbed) fingerprint. Certainly, the states interact as is proven in a global analysis, see Sec. 5.2.3. Here, the fundamental frequency ν_{24} is redetermined to $68.75037(30) \text{ cm}^{-1}$. Unfortunately, this low lying fundamental frequency was not expected at the time the FIR spectra were taken, therefore the conditions were not optimized for this region and this band can currently not be confirmed additionally by means of ro-vibrational spectroscopy. The review of the fundamental frequency ν_{24} by independent microwave relative intensity measurements in the literature was initially based on the suspicion that the fundamental frequency ν_{24} of *gauche*-propanal was too high in comparison to similar molecules [41]. For example, the fundamental frequencies ν_{24} of the isoelectronic molecule nitrosoethane ($\text{CH}_3\text{CH}_2\text{NO}$) are 70 cm^{-1} for *gauche*- $\text{CH}_3\text{CH}_2\text{NO}$ and 130 cm^{-1} for *syn*- $\text{CH}_3\text{CH}_2\text{NO}$ [41]. These values agree well with the values of propanal, which are determined in this work to $68.75037(30) \text{ cm}^{-1}$ for *gauche*-propanal and to $133.9754525(39) \text{ cm}^{-1}$ for *syn*-propanal. A justified precaution of microwave relative intensity measurements may be noticed by the fact that only 6 years later the same authors redetermined the values of *gauche*- $\text{CH}_3\text{CH}_2\text{NO}$ to $61(19) \text{ cm}^{-1}$ and *syn*- $\text{CH}_3\text{CH}_2\text{NO}$ to $182(17) \text{ cm}^{-1}$ [94].

The rather low maximum value of K_a for both vibrational states of *gauche*-propanal,

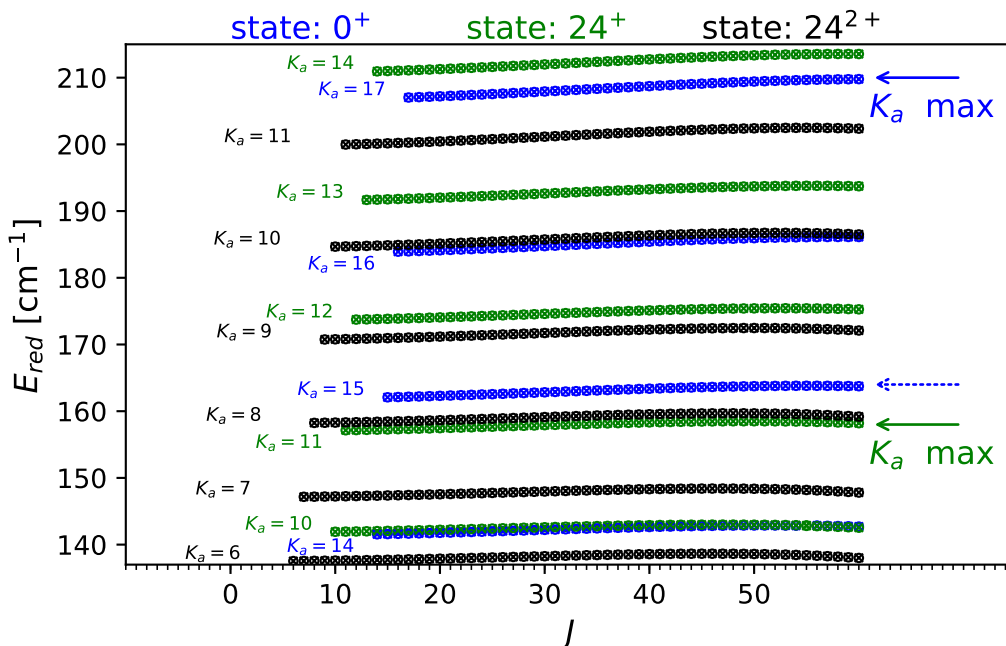


Figure 41: Reduced energy diagram for $v = 0$, $v_{24} = 1$, and $v_{24} = 2$ of *gauche*-propanal. Even though the exact energies of $v_{24} = 2$ are highly speculative, the significance of a global analysis including $v_{24} = 2$ is illustrated. The tunneling states 24^{2+} and 24^{2-} of $v_{24} = 2$ are assumed to be roughly split by 5.8 cm^{-1} with the overtone frequency at 113.6 cm^{-1} (cf. Fig. A12). The splitting would be clearly visible on this scale. However, only 0^+ , 24^+ , and 24^{2+} are shown for simplicity. The rotational parameters up to the quartic order of $v_{24} = 2$ are derived by assuming the harmonic approximation. The maximum K_a of $v = 0$ for transitions fit up to $J_{max} = 60$ is $K_a = 15$. For example, $K_a = 16$ of $v = 0$ is included up to $J = 46$, at this point deviations become to large which might arise from interactions with $v_{24} = 2$.

for example in comparison to $v = 0$ and $v_{24} = 1$ of *syn*-propanal, or in other words the challenge of describing a molecule with two stable degenerate configurations with feasible tunneling, which leads to a necessary treatment of tunneling-rotation interaction, is known from the literature [95–97]. The analysis of *gauche*-propanal is compared to some similar molecules in Table 10. The collection of these molecules highlights the challenge of describing molecules with two stable degenerate configurations. One of them, the most stable conformer I of cyanoacetaldehyde (NCCH_2CHO), which is the *gauche* conformer with a C-C-C-O dihedral angle of $151(3)^\circ$, can only be satisfactorily described for the tunneling state 0^+ up to $K_a = 2$ and for 0^- up to $K_a = 7$ with J up to 40 [95]. Furthermore also in the aforementioned work adjacent transitions involving energy levels with $J = 30, 31, 32$ of $J_{1,J}$ for 0^- had to be excluded from the fit because they were not reproduced properly. *Gauche*-ethanetellurol ($\text{CH}_3\text{CH}_2\text{TeH}$) is described with solely *a*-type transitions up to $J = 53$ with $K_a = 19$ [96]. The maximum K_a is 22

for $J = 34$. Another example is mercaptoacetonitrile (HSCH_2CN) where the estimated uncertainty of center frequencies is 100 kHz, but the standard deviation is roughly four times larger. Transitions in the fit have values up to $K_a = 12$ with $J \leq 20$ and for $20 < J \leq 55$ up to $K_a = 4$. Again, some series of lines were excluded, for example of qR series with $K_a = 2$. Exceptional in the work of this thesis, in comparison to the aforementioned analyses, is the direct measurement of the energy difference of the tunneling states of the most perturbed energy levels with c -type transition. This might be one of the reasons why the energy difference is at least an order of magnitude better determined than for the other presented molecules in Table 10. Besides, determined energy differences may be far off from its given uncertainty ranges if no transitions connecting the tunneling states are measured. In these cases the energy difference is still strongly correlated to the interaction parameters (cf. Eq. (2.29)). In fact, weaker c -type transitions were also tried to assign in the literature, but attempts failed.²⁵ This highlights also the advantage of the DM-DR experimental setup.

Table 10: Selected overview of analyses of molecules with two stable degenerate *gauche*-configurations^a and observed splitting due to tunneling between them including a necessary treatment of tunneling-rotation interaction. The selection highlights difficulties of modeling these kind of molecules.

Molecule ^a	Molecular formula	ΔE /MHz	J_{max}	$K_{a, max}$	ν_{max} ^b /GHz	No. ^c	<i>rms</i> /kHz	Ref.
Propanal ^d	$v = 0$	475.5786(115)	60	17	500	2833	55	TW ^e
	$v_{24} = 1$	13416.8(13)	60	11	500	1977		
Cyanoacetaldehyde	NCCH_2CHO	58735(17)	40	7	200	413	204 ^f	[95] ^f
Ethantellurol	$\text{CH}_3\text{CH}_2^{130}\text{TeH}$	656.59(14)	53	22	300	734	67	[96]
Mercaptoacetonitrile	HSCH_2CN	8044(36)	56	12	124	439	382	[97]

^a *Gauche* or *synclinal* conformers; ^b The maximum frequency of a transition included to the fit;

^c Number of transitions included to the fit; ^d Global analysis including $v = 0$ and $v_{24} = 1$;

^e This Work; ^f Fit 2. A *rms* of 0.204 kHz is presented which is assumed to be 204 kHz.

6.3 Millimeter-Millimeter Wave Double Resonance Spectroscopy

The conventional measurements with (sub-)millimeter wave spectrometers are well established in Cologne and in many places around the world. On the other hand, MMW-MMW DR experiments are not established and are made possible, to the best of the

²⁵It is seen [...] that rather significant values of μ_c [=1.27 D] are predicted in the theoretical calculations for conformer I. Searches were therefore undertaken in an attempt to assign c -type transitions using the separation by about 58794 MHz [editor's note: value of Fit 1 with solely 199 transitions; Fit 2 58735(17) MHz] to guide the efforts. However, no c -type lines could be assigned in this dense spectrum in this manner.”; p. 4053 of Ref. [97].

authors knowledge, for the first time, thanks to a 60 mW amplifier in the W-band region. Within this work, the DM-DR experimental setup is built and tested. Changes between different operation modes are done quick thanks to a newly written software and are only limited by connecting or disconnecting a second lock-in amplifier. The advantage of this measurement technique is demonstrated by measuring and assigning weak transitions, which may be blended by stronger features, as is shown in Fig. 16. It needs to be noted that the magnitude of the splitting due to the Autler-Townes effect is not fully understood yet. Based on Eq. (2.32) the splitting should only depend on the detuning and the Rabi frequency, which itself depends on the electric field and the dipole moment component of the pump transition. Assuming comparable output powers and identical dipole moments for the different pump transitions in Fig. A7, the different magnitudes of the observed splittings for regressive and progressive pumping schemes cannot be explained. Higher powers are required for progressive pump schemes for maximized DM-DR signals. It should be pointed out, though, that both schemes can satisfactorily be employed in DM-DR pumping schemes.

The analysis of *gauche*-propanal benefits for two reasons on this newly established technique. First of all, quite weak *c*-type transitions, compared to stronger *a*-type ones, could be measured and assigned. The importance of these transitions lies in the connection of the two tunneling states, a direct measurement of the energy difference. Furthermore, strongly perturbed transitions can be assigned unambiguously in the MMW region, which played an important role for the analysis of $\nu_{24} = 1$ as the first level crossings of 24^+ and 24^- can be observed with *a*-type transitions in the W-band region, see heavily perturbed qR -series with $K_a = 1$ shown by crossing green and orange lines in Fig. A26. Otherwise, an assignment, if possible at all, would have been cumbersome. Last but not least, solid models of new and less intense vibrationally excited states of near prolate molecules can straightforwardly be derived by applying the specific assignment strategy presented in Sec. 4.2. This is demonstrated on the example of three vibrationally excited states of *syn*-propanal, see Sec. 5.1.4. The manually performed systematic procedure of DM-DR measurements turned out to be a fruitful and straightforward assignment scheme, which leads to accurate spectroscopic parameters despite exclusive measurements in the MMW region.

In summary, the DR and especially the DM-DR experimental setups facilitate a better understanding of both conformers of propanal. These experimental techniques are now well established in the W-band region in Cologne and may help to decipher the fingerprints of more molecules in the future.

7 Prospects

” *Can we automatize it?*”

- Luis Bonah -

From the conclusions drawn in the previous section, possible next steps in the analyses of *syn*- and *gauche*-propanal (Secs. 7.1 and 7.2) as well as further applications of the newly established MMW-MMW DR experimental setups in Cologne are pointed out (Sec. 7.3).

7.1 *Syn*-Propanal

The accurate spectroscopic models of *syn*-propanal derived within this work allow to search for its molecular fingerprints in space. There is no urgent need to extend the analysis even further considering the deciphering of astronomical observations for *syn*-propanal. However, the analysis of rotational spectra of the vibrational ground state $v = 0$ and the first excited aldehyde torsion $v_{24} = 1$ could be extended up to the terahertz region quite straightforwardly. This may also lead to an even better description of Q -branch b -type transitions. The most interesting objective is probably the proper description of the triad of interacting vibrational states, see Fig. 40. Next steps to derive a global analysis of the triad are presented in the following and are summarized in Table 11.

(1) The analysis of the first excited methyl torsion $v_{23} = 1$ is certainly worth to be extended to the terahertz region because of the observed, but so far unstudied perturbations, to guarantee the accuracy of predictions above 500 GHz. More importantly, a global analysis including vibrationally excited states that are close in energy would allow to reproduce perturbed transitions of $v_{23} = 1$, which are excluded in the current single state analysis. A combined analysis of the interacting triad of vibrationally excited states $v_{23} = 1$, $v_{24} = 2$, and $v_{15} = 1$, shown in Fig. 40, is desirable for the future to predict all observable transitions to experimental uncertainty. Therefore, it is necessary to extend the rotational analysis of (2) $v_{24} = 2$ and (3) $v_{15} = 1$ to be able to derive a proper global analysis. This also requires the proper assignment of the rotational spectrum of $v_{24} = 2$ and $v_{15} = 1$ with the help of the FIR spectrum. It is advisable to start with (4) the assignment of the hot band $v_{24} = 2 \leftarrow 1$ as this band, at least the Q -branch, seems to be quite isolated in the FIR spectrum, in contrast to the overtone $v_{24} = 2 \leftarrow 0$ and the fundamental band $v_{15} = 1 \leftarrow 0$, both located around 267 cm^{-1} . For simplifying the deciphering of the vibrational bands, (5) assigning rovibrational transitions of the fundamental band $v_{23} = 1 \leftarrow 0$ are recommended because the center of this band, around 219.9 cm^{-1} [45], is quite isolated and many lines should be assignable straightforwardly. In particular R -branch transitions should further help

to decipher the molecular fingerprints around 267 cm^{-1} . If the hot band $\nu_{24} = 2 \leftarrow 1$ and the fundamental band $\nu_{23} = 1 \leftarrow 0$ are unambiguously assigned, the next step (6) is to assign the overtone band $\nu_{24} = 2 \leftarrow 0$. Based on this assignment the lines around 267 cm^{-1} can be disentangled with (7) a subsequent analysis of $\nu_{15} = 1 \leftarrow 0$. Finally, spectroscopic parameters as well as the vibrational frequencies of the interacting vibrational bands may be known. (8) This would allow to describe the possible interactions of the triad in detail.

Further possible steps are, of course, the assignments and fitting of even more vibrationally excited states in the rotational spectrum with the help of the assignment strategy presented in Sec. 4.2. With help of the ASAP software [98], also further fundamental bands, overtone bands and hot bands can be assigned in the FIR spectra. For example, the tentatively assignment of $\nu_{24} = \nu_{23} = 1^*$ could be verified by means of already measured rotationally resolved FIR spectra.

Table 11: Overview of recommended next steps for deciphering molecular fingerprints of *syn*-propanal. The main objective is to finally describe the interacting triad ($\nu_{24} = 2$, $\nu_{15} = 1$, and $\nu_{23} = 1$), see Fig. 40.

Step	Vibrational state	Main objective
(0a)	$\nu = 0, \nu_{24} = 1$	<ul style="list-style-type: none"> • Extend the analysis to the THz-region • Proper description of <i>Q</i>-branch <i>b</i>-type transitions
(0b)	$\nu_{24} = \nu_{23} = 1$	<ul style="list-style-type: none"> • Verify the tentatively assignment of the rotational analysis of $\nu_{24} = \nu_{23} = 1^*$
(1)	$\nu_{23} = 1$	<ul style="list-style-type: none"> • Extend the analysis to the THz-region • Localize perturbed transitions
(2)	$\nu_{24} = 2$	<ul style="list-style-type: none"> • Accurate spectroscopic parameters
(3)	$\nu_{15} = 1$	<ul style="list-style-type: none"> • Accurate spectroscopic parameters
(4)	$\nu_{24} = 2 \leftarrow 1$	<ul style="list-style-type: none"> • Verify the tentatively assignment at 135.1 cm^{-1} • Verify the tentatively assignment of the rotational analysis of $\nu_{24} = 2^*$
(5)	$\nu_{23} = 1 \leftarrow 0$	<ul style="list-style-type: none"> • Assign <i>R</i>-branch transitions • Determine the fundamental frequency ν_{23}
(6)	$\nu_{24} = 2 \leftarrow 0$	<ul style="list-style-type: none"> • Determine the first overtone frequency ν_{24}
(7)	$\nu_{15} = 1 \leftarrow 0$	<ul style="list-style-type: none"> • Verify the assignment of the rotational analysis of $\nu_{15} = 1^*$ • Determine the fundamental frequency ν_{15}
(8)	$\nu_{24} = 2, \nu_{15} = 1, \nu_{23} = 1$	<ul style="list-style-type: none"> • Accurate spectroscopic (and interaction) parameters (Global analysis of the interacting triad)

7.2 *Gauche*-Propanal

An important result of this work is the re-determination of the fundamental frequency $\nu_{24} = 68.75037(30) \text{ cm}^{-1}$. One logical next step (a) is to confirm this result by means of rotationally resolved FIR measurements, which have to be measured first. The SNRs of current measurements are not high enough for any assignments below 80 cm^{-1} . An option (b) to further confirm the assignment of the fundamental frequency are absolute line intensity measurements, which can be done with a newly developed emission spectrometer [99,100]. Another indirect confirmation (c), without the need of further high-resolution FIR measurements, is the assignment of the overtone band, $\nu_{24} = 2 \leftarrow 0$, in the already measured FIR spectrum by using the ASAP software [98]. If one vibrational state of the vibrational band is known from rotational spectroscopy, here the ground vibrational state $\nu = 0$ is studied in detail, the FIR lines may be assignable with ASAP, see Sec. "Assignment Software" in the Appendix for some more details. This would not only confirm the observed overtone band and consequently also indirectly the fundamental frequency, but it would also result in the determination of first rotational parameters of $\nu_{24} = 2$. An alternative procedure (d) is to study the rotational spectrum of $\nu_{24} = 2$ in a global analysis together with $\nu = 0$ and $\nu_{24} = 1$. A global analysis including $\nu_{24} = 2$ may also allow to increase the K_a ranges of $\nu = 0$ and $\nu_{24} = 1$ even further, as is expressed by a predicted reduced energy diagram in Fig. 41. It may be also of interest to study further vibrationally excited states as has been done for *syn*-, but astronomers should search for *gauche*-propanal in space at first.

Table 12: Overview of possible next steps for deciphering molecular fingerprints of *gauche*-propanal. There is no recommended chronological order among the different steps. Each step may be performed first, without any disadvantages.

Step	Vibrational state	Main objective
(a)	$\nu_{24} = 1 \leftarrow 0$	<ul style="list-style-type: none"> • Verify the fundamental frequency ν_{24} (Measure the FIR spectrum below 80 cm^{-1})
(b)	$\nu = 0, \nu_{24} = 1$	<ul style="list-style-type: none"> • Verify the fundamental frequency ν_{24} with absolute intensity measurements (emission spectroscopy)
(c)	$\nu_{24} = 2 \leftarrow 0$	<ul style="list-style-type: none"> • (Indirectly) Verify the fundamental frequency ν_{24} • Verify the tentatively assignment at 113.6 cm^{-1} • Determine the first overtone frequency • First spectroscopic parameters
(d)	$\nu = 0, \nu_{24} = 1, \nu_{24} = 2$	<ul style="list-style-type: none"> • Accurate spectroscopic (and interaction) parameters (Global analysis) • Increase K_a for J_{max}

7.3 Future Experimental Ideas

Based on the newly established DR and DM-DR experimental setups in Cologne, see Secs. 3.1.2 and 3.1.3, future experimental ideas are discussed. The focus is put on deciphering hidden molecular fingerprints with experimental techniques. First of all, the DM character may be adopted in further experimental setups, see Sec. 7.3.1. Furthermore, a promising idea for a fully automated experiment and analysis is advertised in Sec. 7.3.2.

7.3.1 Baseline-free Spectroscopy

The DM-DR experimental setup allows for confusion- and baseline-free spectra, which facilitate the assignment of less intense lines, even if they are blended, see Figs. 16 and 42. In fact, there are several more options to make use of the double modulation technique, in particular to visualize and study confusion- and baseline-free difference spectra [101]. For example, an IR laser could excite a certain vibrational state, which would naturally change the spectrum of the two involved vibrational states in the MMW region as well. If the laser radiation is modulated, only lines of the two vibrational states would be apparent in the rotational spectrum. Actually, even the two involved states can be distinguished if they are clearly separated in energy, as the lower one will be populated less, whereas the upper state will be populated more in regard to the thermal equilibrium, which leads in optimal cases to opposite signs of the observed lines in the difference spectrum. This should simplify the analysis of high energy vibrational states dramatically. In general, all sources which are used in addition to a conventional spectrometer may be modulated as well. In this way, only the molecular fingerprint affected by the additional source is expected to be visible in the spectrum. This can also be employed in discharge experiments as exemplified by microwave taxonomy experiments [12]. Furthermore, the DM-DR technique could also be extended to chirped pulse experiments. Spectra taken with a 180° phase shift can simply be added in the time domain, which results in a difference spectrum. If one FID is influenced by an additional source, while the FID of the phase shifted is not, a comparable difference spectrum as for the DM-DR experimental setup performed in this work is created. In general, greatly simplified spectra facilitate the deciphering of complex molecular fingerprints.

7.3.2 Automated Deciphering of Molecular Fingerprints

The main idea of an automated DM-DR measurement scheme is basically the combination of automated assignment features, such as AUTOFIT [81], and the AMDOR principle [82]. Automated analyses search for the best possible fit, which is applied

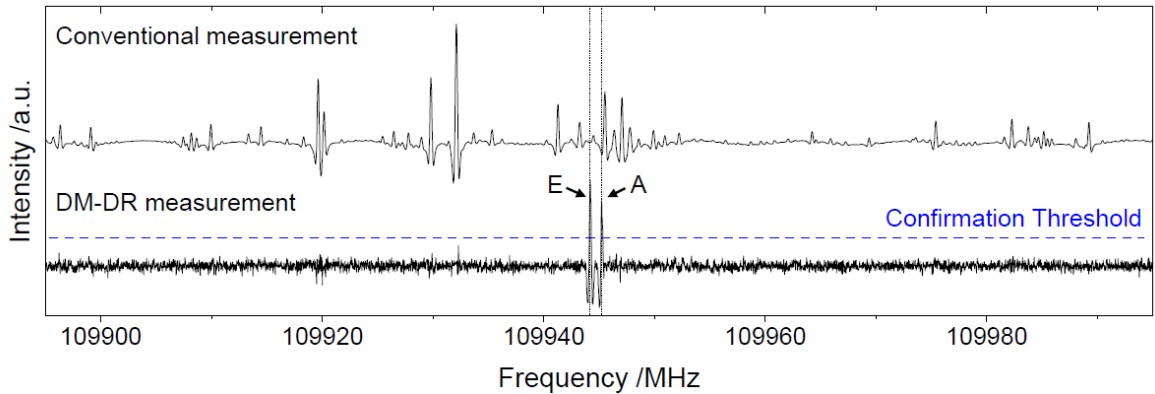


Figure 42: Broadband DM-DR measurement of $11_{3,9} \leftarrow 11_{2,9}$ of $v = 0$ of *gauche*-propanal (cf. Fig. 16). The A and E components are not straightforwardly assignable in the conventional measurement. A threshold could be used in the future for automated assignments thanks to baseline- and confusion-free DM-DR measurements.

successful. However, the right choice of search parameters can be critical and the results are only the statistically most relevant assignments. The crucial step is to verify experimentally the first few transitions beyond any doubt. Thereby, the most time consuming step is usually to find the first linkage of two transitions and another linkage of one of the two transitions to a third one not belonging to the same type of series. *A*, *B*, and *C* can be determined quite accurately if two different kind of transitions are assigned. A secure, but admittedly time consuming, starting point is to apply a 2D DR grid search, which is a brute force method and implemented in a newly developed control software of the experiment (cf. Fig. A10). As soon as a linkage is identified, for example in case a certain intensity threshold is exceeded, illustrated in Fig. 42, the search could be aborted in the future. Finding linkages can be speed up even more, as it may be possible to test the linkage only at one frequency step. If the intensity of a DM-DR measurement is above or below the intensity threshold, a positive linkage or no linkage is found, respectively. This is only possible because of the baseline- and confusion-free measurement and for doing so candidate "probe" and "pump lists" should be created. A first scheme for systematically testing near prolate molecules is given by the instruction in Sec. 4.2. This manually step-by-step demonstration may lead to a promising approach of a fully automated measurement, assignment and fitting procedure, if the measurement setup is combined with an analyzing software. For molecules with κ far away from the prolate limit and for molecules with rather strong nonvanishing dipole moments other than μ_a and μ_b , the assignment and fitting strategy needs to be adapted. In the best case, this would allow for a fully automated deciphering of molecular fingerprints.

In the first chapter of this thesis, the need for more accurate molecular fingerprints of propanal is emphasized by deviations between observed and predicted spectra and, generally, by means of astronomical observations close to the confusion limit. Nowadays astronomical detection of *syn*- and *gauche*-propanal, up to the terahertz region, are not limited by laboratory data nor by the analysis of molecular fingerprints, thanks to the **accurate quantum mechanical models of propanal** presented in this thesis. Deciphering of molecular fingerprints of propanal benefits from the **newly established MMW-MMW DR experimental technique**. DR and in particular baseline- and confusion-free DM-DR measurements are expected to facilitate proper analyses of complex molecular fingerprints in the future. **The results of this work can support next steps in revealing the level of complexity of COMs in space.**

Appendix

Data Storage and Used Programs

All measurement data taken in the framework of this thesis plus the fit files and line lists of propanal, as well as the PDF version of this thesis will be saved on the AFS of the "I. Physikalisches Institut" of the University of Cologne. External programs used for the spectroscopic molecular data analysis within this thesis are listed in the following:

- ERHAM - Fit rotational spectra – with up to two internal rotors
- LWW - Assign ro-vibrational spectra
- PGOPHER - Fit molecular spectra
- SMAP - Assign molecular spectra
- SPFIT/SPCAT - Fit molecular spectra – with interacting states

Abbreviations

- AFM - Active Frequency Multiplier
- ALMA - Atacama Large Millimeter Array
- AM - Amplitude Modulation
- CDMS - Cologne Database for Molecular Spectroscopy
- COM - Complex Organic Molecule
- CP - Chirped Pulse
- CRC - Collaborative Research Center
- DM - Double Modulation
- DR - Double Resonance
- EMoCA - Exploring Molecular Complexity with ALMA
- FID - Free Induction Decay
- FIR - Far InfraRed
- FM - Frequency Modulation
- FS - Frequency Switching
- FT - Fourier Transform
- FWHM - Full Width Half Maximum
- HDPE - High-Density PolyEthylene

-
- HWHM - Half Width Half Maximum
 - IAM - Internal-Axis Method
 - IR - InfraRed
 - ISM - InterStellar Medium
 - LAM - Large Amplitude Motion
 - MMW - MilliMeter Wave
 - MW - MicroWave
 - NMR - Nuclear Magnetic Resonance
 - PAM - Principal Axis Method
 - PROSPE - PRograms for ROtational SPEctroscopy
 - PTFE - PolyTetraFluoroEthylene
 - RAM - ρ -Axis Method
 - RAS - Reduced Axis System
 - RF - Radio Frequency
 - RMS - Root Mean Square
 - SGR - Sagittarius
 - SNR - Signal to Noise Ratio
 - TC - Time Constant
 - UV - UltraViolet
 - WRMS - Weighted unitless Root Mean Square

Equations

Angular Momentum Matrix Elements [51]

$$\langle J, K, M | \hat{J}^2 | J, K, M \rangle = \hbar^2 J(J+1) \quad (\text{A1a})$$

$$\langle J, K, M | \hat{J}_z | J, K, M \rangle = \hbar K \quad (\text{A1b})$$

$$\langle J, K, M | \hat{J}_z^2 | J, K, M \rangle = \hbar^2 K^2 \quad (\text{A1c})$$

$$\langle J, K, M | \hat{J}_z^2 | J, K, M \rangle = \hbar^2 M^2 \quad (\text{A1d})$$

$$\langle J, K, M | \hat{J}_y | J, K \pm 1, M \rangle = \frac{\hbar}{2} \sqrt{J(J+1) - K(K \pm 1)} \quad (\text{A1e})$$

$$\langle J, K, M | \hat{J}_x | J, K \pm 1, M \rangle = \frac{i\hbar}{2} \sqrt{J(J+1) - K(K \mp 1)} \quad (\text{A1f})$$

$$\langle J, K, M | \hat{J}_x^2 | J, K, M \rangle = \frac{\hbar^2}{2} [J(J+1) - K^2] \quad (\text{A1g})$$

$$\langle J, K, M | \hat{J}_y^2 | J, K, M \rangle = \frac{\hbar^2}{2} [J(J+1) - K^2] \quad (\text{A1h})$$

$$\langle J, K, M | \hat{J}_y^2 | J, K \pm 2, M \rangle = \frac{\hbar^2}{4} \sqrt{[J(J+1) - K(K \pm 1)][J(J+1) - (K \pm 1)(K \pm 2)]} \quad (\text{A1i})$$

$$\langle J, K, M | \hat{J}_x^2 | J, K \pm 2, M \rangle = -\frac{\hbar^2}{4} \sqrt{[J(J+1) - K(K \pm 1)][J(J+1) - (K \pm 1)(K \pm 2)]} \quad (\text{A1j})$$

$$\langle J, K-2, M | \hat{J}_+^2 | J, K, M \rangle = \hbar^2 \sqrt{(J+K)(J-K+1)(J+K-1)(J-K+2)} \quad (\text{A1k})$$

$$\langle J, K+2, M | \hat{J}_-^2 | J, K, M \rangle = \hbar^2 \sqrt{(J-K)(J+K+1)(J-K-1)(J+K+2)} \quad (\text{A1l})$$

Coriolis Interaction Parameters

The Coriolis interaction parameter and its operators (in the S-reduction, I' representation with $z = a$), which are needed to reproduce the assigned transition frequencies of *gauche*-propanal to experimental uncertainty, are of the form

$$\begin{aligned}
 H_{vv'} = & \quad iG_a \hat{J}_a + iG_b \hat{J}_b + iG_c \hat{J}_c \\
 & + F_{bc}(\hat{J}_b \hat{J}_c + \hat{J}_c \hat{J}_b) + F_{ca}(\hat{J}_a \hat{J}_c + \hat{J}_c \hat{J}_a) + F_{ab}(\hat{J}_a \hat{J}_b + \hat{J}_b \hat{J}_a) \\
 & + F_{ab}^J \hat{J}^2(\hat{J}_a \hat{J}_b + \hat{J}_b \hat{J}_a) + F_{ab}^K \{\hat{J}_a \hat{J}_b + \hat{J}_b \hat{J}_a, \hat{J}_z^2\}/2 \\
 & + F_{bc}^J \hat{J}^2(\hat{J}_b \hat{J}_c + \hat{J}_c \hat{J}_b) + F_{bc}^K \{\hat{J}_b \hat{J}_c + \hat{J}_c \hat{J}_b, \hat{J}_z^2\}/2 \\
 & + F_{ca}^J \hat{J}^2(\hat{J}_a \hat{J}_c + \hat{J}_c \hat{J}_a) + F_{ca}^K \{\hat{J}_a \hat{J}_c + \hat{J}_c \hat{J}_a, \hat{J}_z^2\}/2 \\
 & + F_{bc}^{JJ} \hat{J}^4(\hat{J}_b \hat{J}_c + \hat{J}_c \hat{J}_b) + F_{bc}^{JK} \{\hat{J}_b \hat{J}_c + \hat{J}_c \hat{J}_b, \hat{J}^2 \hat{J}_z^2\}/2 + F_{bc}^{KK} \{\hat{J}_b \hat{J}_c + \hat{J}_c \hat{J}_b, \hat{J}_z^4\}/2 \\
 & + F_{bc}^{JJJ} \hat{J}^6(\hat{J}_b \hat{J}_c + \hat{J}_c \hat{J}_b) + F_{bc}^{JJK} \{\hat{J}_b \hat{J}_c + \hat{J}_c \hat{J}_b, \hat{J}^4 \hat{J}_z^2\}/2 \\
 & + F_{bc}^{KKKJ} \{\hat{J}_b \hat{J}_c + \hat{J}_c \hat{J}_b, \hat{J}^2 \hat{J}_z^4\}/2 + F_{bc}^{KKKK} \{\hat{J}_b \hat{J}_c + \hat{J}_c \hat{J}_b, \hat{J}_z^6\}/2 \\
 & + F_{bc}^{JJJJ} \hat{J}^8(\hat{J}_b \hat{J}_c + \hat{J}_c \hat{J}_b) + F_{bc}^{JJJK} \{\hat{J}_b \hat{J}_c + \hat{J}_c \hat{J}_b, \hat{J}^6 \hat{J}_z^2\}/2 \\
 & + F_{bc}^{JJKK} \{\hat{J}_b \hat{J}_c + \hat{J}_c \hat{J}_b, \hat{J}^4 \hat{J}_z^4\}/2 + F_{bc}^{JKKK} \{\hat{J}_b \hat{J}_c + \hat{J}_c \hat{J}_b, \hat{J}^2 \hat{J}_z^6\}/2 \\
 & + F_{bc}^{KKKK} \{\hat{J}_b \hat{J}_c + \hat{J}_c \hat{J}_b, \hat{J}_z^8\}/2 \\
 & + iG_{2b} \{\hat{J}_b, (\hat{J}_b \hat{J}_c + \hat{J}_c \hat{J}_b)\}/2 + iG_{2b}^J \{\hat{J}_b, \hat{J}^2(\hat{J}_b \hat{J}_c + \hat{J}_c \hat{J}_b)\}/2 \\
 & + F_{2bc} \{\hat{J}_b \hat{J}_c + \hat{J}_c \hat{J}_b, \hat{J}_b^2 - \hat{J}_c^2\}/2
 \end{aligned} \tag{A2}$$

where $\{, \}$ is the anticommutator [63, 65]. If a new Coriolis interaction of a particular type is expected in the global analysis of $v = 0$ and $v_{24} = 1$ of *gauche*-propanal, each time the five lowest order parameters are tested to determine the one which lowers the *wrms* the most. For example, for *a*-type Coriolis interaction the operators of the five lowest orders are given in the S-reduction as [63]

$$\begin{aligned}
 H_{vv'} = & \quad iG_a \hat{J}_a & (n = 1) \\
 & + F_{bc}(\hat{J}_b \hat{J}_c + \hat{J}_c \hat{J}_b) & (n = 2) \\
 & + iG_{2a} \{\hat{J}_a, (\hat{J}_b^2 - \hat{J}_c^2)\}/2 & (n = 3) \\
 & + F_{2bc} \{\hat{J}_b \hat{J}_c + \hat{J}_c \hat{J}_b, \hat{J}_b^2 - \hat{J}_c^2\}/2 & (n = 4) \\
 & + iG_{3a} \{\hat{J}_a, (\hat{J}_b^4 - \hat{J}_c^4)\}/2 & (n = 5). \tag{A3}
 \end{aligned}$$

Line Intensities

The line intensities are calculated by SPFIT with (given in Eqs. (1)+(2) in Ref. [102])

$$\begin{aligned}
 I(T) &= \frac{8\pi^3}{3hc} \nu S\mu_x^2 \left[\exp\left(\frac{-E''}{k_B T}\right) - \exp\left(\frac{-E'}{k_B T}\right) \right] / Q_{rot+spin} \\
 &= 4.16231 \cdot 10^{-5} \nu S\mu_x^2 \left[\exp\left(\frac{-E''}{k_B T}\right) - \exp\left(\frac{-E'}{k_B T}\right) \right] / Q_{rot+spin} \quad (A4)
 \end{aligned}$$

with line frequency ν in units of MHz, dipole moment along the molecular axis x in units of Debye, line strength S and the rotation-spin partition function $Q_{rot+spin}$. The line intensity $I(T)$ is given in units of $\text{nm}^2 \cdot \text{MHz}$.

ERHAM calculates the relative line intensity as (given on page 3 in Ref. [103])

$$I_{rel}(T) = g_l S\mu_x^2 \exp\left(\frac{-E''}{k_B T}\right) \left(1 - \exp\left(\frac{-h\nu}{k_B T}\right)\right) \cdot \nu \quad (A5)$$

which is basically derived from Eq. (A4) by factoring out the Boltzmann factor of the lower state and considering the spin weight g_l to be not included in the line strength.

Energy Level Splittings in ERHAM:

It turns out, that the energy difference between the two substates A and E, originating in the methyl group internal rotation, in the non-rotating case ($K_1 = K_2 = 0$) is dependent on the energy tunneling parameters $\epsilon_{qq'}$ ($\epsilon_{qq'}$ are the respective Fourier coefficients). By using

$$\sum_0 = \epsilon_{00} + 2 \sum_{q>0} \left[C'_{qq} \epsilon_{qq} + C'_{q-q} \epsilon_{q-q} + \sum_{q'=-q+1}^{q-1} \left(C'_{qq'} \epsilon_{qq'} + C'_{q'q} \epsilon_{q'q} \right) \right] \quad (\text{A6})$$

the energy difference can be determined [71]. Note that the second index has to be 0 for molecules containing only a single internal rotor ϵ_{q0} . For this reason, often the parameter is written as ϵ_q . From Ref. [71], $C'_{qq'}$ can be calculated as

$$C'_{qq'} = \cos \left[2\pi \left\{ q(\sigma_1 - \rho_1 K_1)/n_1 + q'(\sigma_2 - \rho_2 K_2)/n_2 \right\} \right]. \quad (\text{A7})$$

The energy difference for no rotation of the A ($\sigma_1 = 0 \Rightarrow C'_{qq'} = 1$) and E energy levels ($\sigma_1 = \pm 1 \Rightarrow C'_{qq'} = -0.5$) can be approximated ($q \leq 1$) to

$$|\Delta E| = |E_{E0} - E_{A0}| = |(\epsilon_{00} - \epsilon_{10}) - (\epsilon_{00} + 2\epsilon_{10})| = |-\epsilon_{10} - 2\epsilon_{10}| = 3\epsilon_{10}. \quad (\text{A8})$$

The resulting energy difference of A and E tunneling states are schematically shown for the ground state and the first excited state in Fig. A1. The order of A and E substates is alternating for higher vibrational states, usually with $\epsilon_{10} < 0$ for $\nu = 0$ (cf. Fig. 12). The resulting energy differences and in particular the fundamental frequency $\nu = 1 \leftarrow 0$ can be determined as shown in Fig. A1.

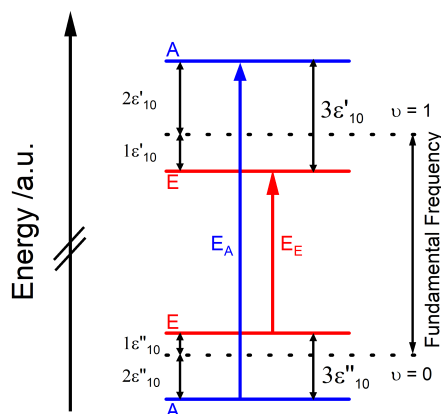


Figure A1: Schematic energy level diagram of torsional substates A and E of two vibrational states $\nu = 0$ and $\nu = 1$ for a single rotor molecule ($|\epsilon''_{10}| < |\epsilon'_{10}|$; $\epsilon''_{10} < 0$; $\epsilon'_{10} > 0$). In ERHAM, A and E splitting for the non-rotating case can be approximated to a first order by the energy tunneling parameter ϵ_{10} [72].

Group Theory of *Syn*-Propanal

This whole section "Group theory of *syn*-propanal" is taken from the Appendix of Ref. [50] and is only slightly adapted.

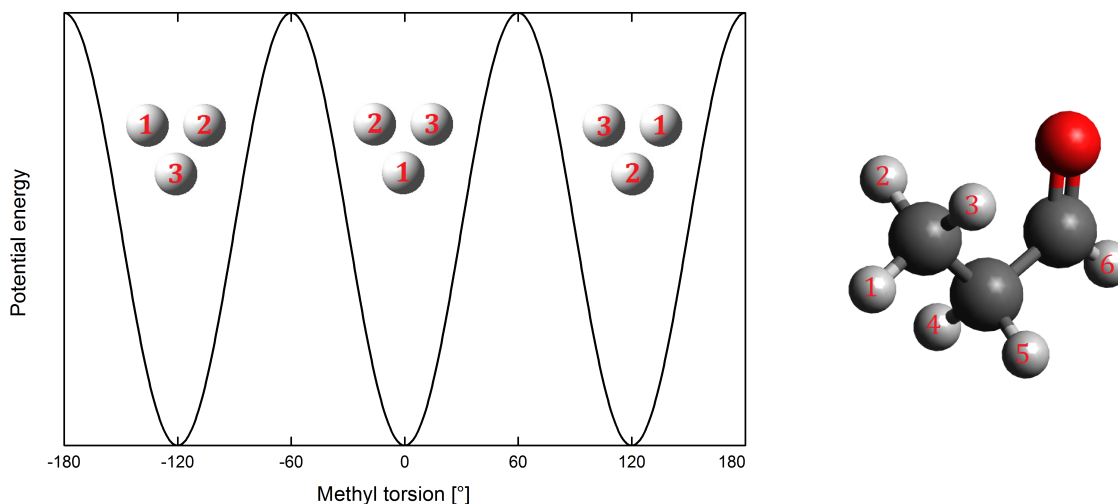


Figure A2: The threefold degenerate potential describes the internal rotation of the methyl group (in *syn*-propanal). The relative position of the three hydrogen atoms of the methyl group is shown with the numbered spheres. The ordering at 0° methyl torsion corresponds to the configuration of *syn*-propanal with numbered hydrogen atoms shown on the right hand side. Figures are taken from Ref. [50].

The following group theory of propanal is based on Refs. [104, 105].²⁶ The molecular symmetry group for *syn*-propanal in the rigid rotor assumption is the $C_s(M)$ -group (see Table A1), whereas with allowed internal rotation the molecular symmetry group is $C_{3v}(M) \simeq C_s \times C_3$ (cf. Table A2), with C_3 describing the internal rotation. The potential function of the internal rotation of the methyl group is shown on the left hand side in Fig. A2.

For determining the characters in the reducible representation of spin statistical weights of the total wave function χ_{rve}^{sw} , in the last row of Tables A1 and A2, the formulas according to Landau-Lifshitz were used:

$$\chi_{rve}^{sw}[P^*] = 0 \quad (\text{A9})$$

$$\chi_{rve}^{sw}[P] = 2\Pi_a(2I_a + 1)(-1)^{(2I_a)(n_a - 1)}. \quad (\text{A10})$$

²⁶A instructive introduction to 'Fundamentals of molecular symmetry can be found in form of an online lecture by P. Jensen <https://www.ptc.uni-wuppertal.de/de/team/dozenten/prof-per-jensen-phd/fundamentals-of-molecular-symmetry.html>; [Online; accessed 21-July-2020].

Table A1: Character table of *syn*-propanal for the rigid rotor assumption.

$C_s(M)$	E	(23)(45)*
$h = 2$	1	1
A'	1	1
A''	1	-1
$\chi_{rve}^{sw}[P]$	128	0

 Table A2: Character table of *syn*-propanal with allowed internal rotation.

$C_{3v}(M)$	E	(123)	(23)(45)*
$h = 6$	1	2	3
A ₁	1	1	1
A ₂	1	1	-1
E	2	-1	0
$\chi_{rve}^{sw}[P]$	128	32	0

Since for carbon and oxygen $I_a = 0$ their contribution is always 1, consequently only sets of n_a hydrogen nuclei with spin $I_a = 1/2$ which are permuted by permutation P need to be taken into account. This results in:

$$\begin{aligned} \chi_{rve}^{sw}[E] &= 2 \cdot 2^6 &= 2^7 = 128 \\ \chi_{rve}^{sw}[(123)] &= 2 \cdot 2 \cdot 2^3 &= 2^5 = 32 \\ \chi_{rve}^{sw}[(23)(45)^*] & &= 0 \end{aligned}$$

Now the "frequency" of irreducible representations a_j can be calculated via

$$a_j = \frac{1}{h} \sum_R \chi^\Gamma[R] \chi^{\Gamma_i}[R]^*. \quad (\text{A11})$$

This results in:

$$\begin{aligned} a_{A'} &= \frac{1}{2}(1 \cdot 1 \cdot 128 + 1 \cdot 1 \cdot 0) &= 64 \\ a_{A''} &= \frac{1}{2}(1 \cdot 1 \cdot 128 + 1 \cdot (-1) \cdot 0) &= 64 \\ a_{A_1} &= \frac{1}{6}(1 \cdot 1 \cdot 128 + 2 \cdot 1 \cdot 32 + 3 \cdot 1 \cdot 0) &= 32 \\ a_{A_2} &= \frac{1}{6}(1 \cdot 1 \cdot 128 + 2 \cdot 1 \cdot 32 + 3 \cdot (-1) \cdot 0) &= 32 \\ a_E &= \frac{1}{6}(1 \cdot 2 \cdot 128 + 2 \cdot (-1) \cdot 32 + 3 \cdot 0 \cdot 0) &= 32 \end{aligned}$$

Now it is important how A_1 , A_2 , and E from $C_{3V}(M)$ are generated from C_s . Therefore the columns with the same permutation operations of Tables A1 and A2 are compared.

For A_1 yields:

$$\begin{aligned} a_{A'} &= \frac{1}{2}(1 \cdot 1 \cdot 1 + 1 \cdot 1 \cdot 1) &= 1 \\ a_{A''} &= \frac{1}{2}(1 \cdot 1 \cdot 1 + 1 \cdot (-1) \cdot 1) &= 0 \end{aligned}$$

For A_2 yields:

$$\begin{aligned} a_{A'} &= \frac{1}{2}(1 \cdot 1 \cdot 1 + 1 \cdot 1 \cdot (-1)) &= 0 \\ a_{A''} &= \frac{1}{2}(1 \cdot 1 \cdot 1 + 1 \cdot (-1) \cdot (-1)) &= 1 \end{aligned}$$

For E yields:

$$\begin{aligned} a_{A'} &= \frac{1}{2}(1 \cdot 1 \cdot 2 + 1 \cdot 1 \cdot 0) &= 1 \\ a_{A''} &= \frac{1}{2}(1 \cdot 1 \cdot 2 + 1 \cdot (-1) \cdot 0) &= 1 \end{aligned}$$

Therefore, if internal rotation is feasible, the energy levels A' and A'' split into:

$$\begin{aligned} A'(64) &\longmapsto A_1(32) + E(32) \\ A''(64) &\longmapsto A_2(32) + E(32) \end{aligned}$$

When different permutations act on the dipole moments (i.e. $P(\mu_x) = +\mu_x$ or $P(\mu_x) = -\mu_x$) it is obvious that in *syn*-propanal μ_a and μ_b have A_2 symmetry. The selections rules can be obtained employing the nonvanishing integral rule. The product of the wave function from the final state ψ_f and of the wave function from the initial state ψ_i must contain A_2 . This can be read of directly from the product table of $C_{3V}(M)$ in Table A3.

Table A3: Product table of $C_{3v}(M)$.

$C_{3v}(M)$	A_1	A_2	E
A_1	A_1	A_2	E
A_2	A_2	A_1	E
E	E	E	$A_1 \oplus A_2 \oplus E$

The selection rules for *syn*-propanal with allowed internal rotation are:

$$A_1 \longleftrightarrow A_2 \quad (\text{A12})$$

$$E \longleftrightarrow E \quad (\text{A13})$$

With the help of the "rotational recipe" and considering the molecule in the prolate (I^r representation: $xyz = bca$) and oblate limit (III^r representation: $xyz = abc$) equivalent rotations and their characters are derived, see Table A4. Calculating the "frequency" of irreducible representations and looking for the common symmetry of different combinations of even and odd K_a and K_c values, the correlation table in Table A5 follows. In the schematic energy level diagram for *syn*-propanal in Fig. A3 it becomes obvious that transitions with allowed internal rotation are split with an intensity ratio of 1:1 in comparison to the rigid rotor assumption.

Table A4: Equivalent rotations of *syn*-propanal in the (a) prolate (I^r representation: $xyz = bca$) and (b) oblate limit (III^r representation: $xyz = abc$).

a)	$C_S(M)$	E	(23)(45)*
	equiv. rot.	R^0	$R_{\Pi/2}^{\Pi}$
	$K_a = 0$	1	$(-1)^J$
	$ K_a \neq 0$	2	0
b)	$C_S(M)$	E	(23)(45)*
	equiv. rot.	R^0	R_z^{Π}
	$K_c = 0$	1	1
	$ K_c \neq 0$	2	$2 \cdot (-1)^{K_c}$

Table A5: Correlation table of *syn*-propanal for the rigid rotor assumption and with allowed internal rotation.

$C_S(M)$	$K_a \ K_c$	$C_{3V}(M)$
A'	ee/oe	$A_1 \oplus E$
A''	oo/eo	$A_2 \oplus E$

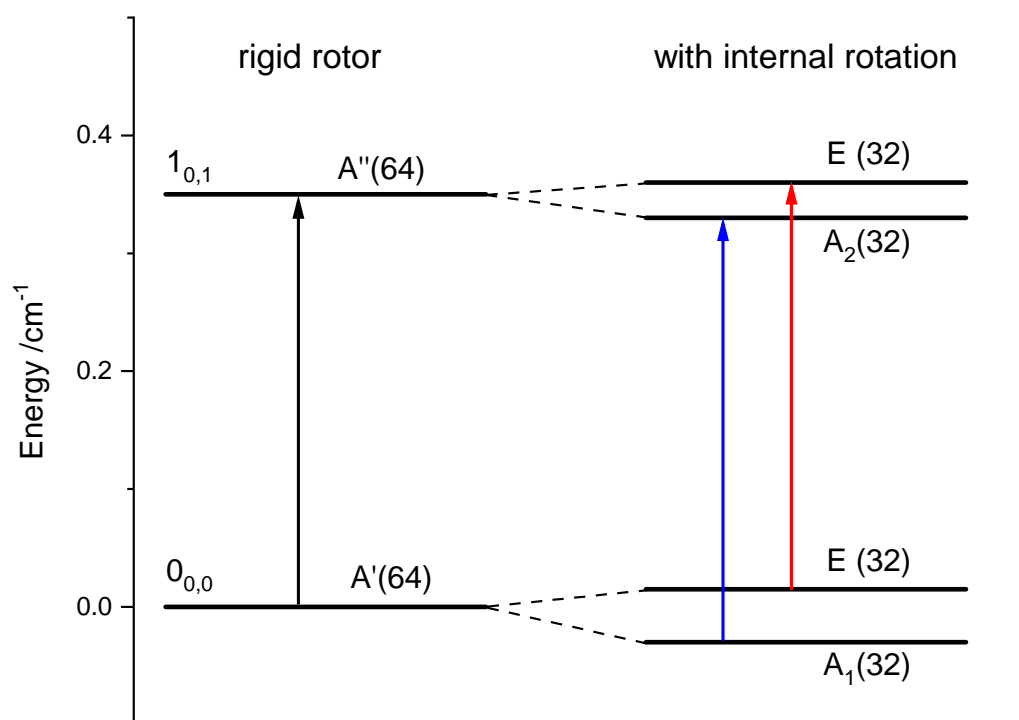


Figure A3: The two lowest rotational energy levels are shown for the rigid rotor assumption and for allowed internal rotation of *syn*-propanal. The splittings are enlarged for clarification. A and E components are red and blue shifted compared to the rigid rotor transitions since splittings of various energy levels have different magnitudes. Symmetries of energy levels are given together with their spin statistical weights. The figure is adapted from Ref. [50].

Tables

Table A6: Overview of the six possible representations for correlation of the x,y,z axis system with the a,b,c axis system. A right- and left-handed orientation is shown by superscripts r and l .

	Γ^r	Π^r	III^r	Γ^l	Π^l	III^l
x	b	c	a	c	a	b
y	c	a	b	b	c	a
z	a	b	c	a	b	c

Table A7: Character Table for the Four Group $V(a, b, c)$.

$V(a, b, c)$	E	C_2^a	C_2^b	C_2^c
A	1	1	1	1
B_a	1	1	-1	-1
B_b	1	-1	1	-1
B_c	1	-1	-1	1

Table A8: Character Table for the Point Group C_3^a .

C_3	E	C_3	C_3^2
A	+1	+1	+1
E_1	+1	ϵ	ϵ^*
E_2	+1	ϵ^*	ϵ

^a $\epsilon = \exp(i2\pi/3)$

Table A9: Character Table for the Point Group C_s , if the symmetry plane is spanned by the molecular axes a and b .

C_s	E	σ_h
A'	+1	+1 : a, b, R_c
A''	+1	-1 : c, R_a, R_b

Table A10: Character Table for the Point Group C_1 .

C_1	E
A	+1

Table A11: MMW Relative Intensity Measurements of $v = 0$ and $v_{24} = 1$ of *gauche*-propanal.

Transition	Frequency ^a /MHz	Intensity ^b /a.u.				R^c	\bar{R}
		0^+	0^-	24^+	24^-		
$J_0, J \leftarrow (J-1)_{0, J-1}$							
$J = 10$	84433.3080	27555	27006	20145	23525	0.80	
$J = 13$	109592.1802	12673	11678	9227	10849	0.82	
$J = 14$	117952.3133	5045	4301	4055	4413	0.91	
$J = 22$	184344.5475	185815	180231	127299	146387	0.75	
$J = 33$	274651.7827	49280	42338	32034	29777	0.67	
$J = 49$	404836.5234	5251	7002	4720	2745	0.61	0.76(11)
$11_{K_a, K_c} \leftarrow 10_{K_a, K_c-1}$							
$K_a = 4$	93136.0761	31346	35416	31820	27102	0.88	
$K_a = 5$	93165.8352	33457	35058	21810	25410	0.69	
$K_a = 6$	93206.2575	28107	32080	19931	20957	0.68	
$K_a = 7$	93255.8588	26711	23473	18544	16524	0.70	
$K_a = 8$	93314.0764	20306	22892	18017	14072	0.74	
$K_a = 9$	93380.6683	15614	16589	16244	12175	0.88	0.76(9)
							0.76(9)

^a The frequency is given for the 0^+ state.

^b The Intensity is derived by the difference of maximum and minimum intensities of a measured line.

^c The Ratio is simply calculated by considering all Intensities I_i with $R = (I_{24^+} + I_{24^-}) / (I_{0^+} + I_{0^-})$. All considered transitions are *a*-type transitions and differences in line shapes as well as frequencies are neglected as transitions within one row appear in a small frequency window, in particular $(\mu_a^2 \nu^2 S_{Doppler})$ is assumed to be equal for transitions in the same row.

Detailed Iterative Fitting Procedure

The three steps of the iterative i) assignment, ii) fitting, and iii) predicting procedure are schematically shown in Fig. 18 and are explained in somewhat more detail here than in Sec. 4.1.

i) Ideally, the most intense lines in a spectral region are assigned for low J and K_a for a prolate rotor molecule first. As high intensities are often unique in a certain frequency window, in particular in the range of the uncertainty of the predicted frequency, the intense features are a good starting point as they can be assigned unambiguously quite often. In fact, full series are assigned rather than single lines as trends in deviations of observed and predicted frequencies are important indications of correct assignments. These linkages might even be experimentally proven with DR measurements (cf. Secs. 3.1.2 and 3.1.3). In these cases, the assignment is beyond any reasonable doubt. Another important tool for unambiguous assignments are intensity ratios. Patterns of lines in a small frequency window, or even single lines which are already assigned and are accidentally close to the candidate line, facilitate unambiguous assignments. In this respect, internal rotation splittings or splittings due to tunneling between different configurations support the assignment procedure as they are an additional confirmation for correct assignments. This can be compared to hyperfine structures or isotopic patterns of molecules which permitted, for example, the definitive identification of GeC_2 and the determination of its T-shaped structure in the course of this work in the McCarthy lab at the Harvard-Smithsonian Center for Astrophysics [106].²⁷ Finding spectroscopic patterns is a main task as they simplify the analysis, which hopefully reveals the characteristic spectral features of a molecule. Choosing the optimal series or patterns for assignments is dependent on the asymmetry of a molecule and on its type of spectrum. If deviations between observed and predicted transition frequencies become too large or spectroscopic assignments cannot be made unambiguously anymore, new fits are executed to generate better predictions.

ii) A measure of the fit quality is the the *wrms* of the fit, see Eq. (4.1). In case n number of lines are fit to experimental uncertainty the *wrms* is close to 1.0 and the fit quality is said to be satisfactory. Sometimes a *wrms* > 1.0 has to be excepted in first iterations as there may not be enough spectral information to model the data in full detail yet. The fit will certainly deteriorate significantly at many iteration steps. This means that the *wrms* value is enlarged by more than 10%. This may happen especially if frequencies of newly added transitions are observed to deviate quite much from their predicted frequencies. One explanation, which is often the root of the problem and is fortunately easily solvable, is that the parameter set is too small to describe the observed fingerprint. Therefore, new parameters need to be included. The ulti-

²⁷<https://www.cfa.harvard.edu/amp/mccarthygroup/> [Online; accessed 09-August-2020]

mate goal is to find the best possible solution with the number of parameters being as little as possible. In general, all potential parameters are tested for performance, but only the best one is used in the model. Including a new parameter is solely done if an amelioration of the *wrms* of at least 10% is observed and if the parameter is well determined, which means that the uncertainty value is at least an order of magnitude lower than the parameter value. These are rules of thumb and are dependent on the number of assigned transitions, the threshold values may be lowered for larger data sets with thousands of assigned transitions. Furthermore, they can be lifted if no progress is made without doing so or if a specific series is described much better with an additional parameter. For finding the best parameter, first, missing parameters of the same orders (quartic, sextic, ...) of already implemented ones are tested, starting by the lowest order. Then, parameters of the next higher order are tested, but only of the next higher one, as gaps in the parameter set should be avoided. In general, higher order parameters should only be implemented if a respective lower one is already implemented. Eventually, additional sets of parameters are tested, such as internal rotation, Fermi or Coriolis interaction parameters. Testing of new parameters is repeated in the same fashion until no improvement of the *wrms* by more than 10% is monitored.

Sometimes it may even be advisable not to choose the best parameter, but maybe the second best, if the *wrms* of their fits are similar and the parameter value of the best fit seems to be odd, for example, if its value is far from *ab-initio* calculations or expectations. The neglected parameter gets special attention at later iteration steps and it is checked whether a similar parameter value is observed again. If so, this parameter will be also implemented. It is advisable to make educated guesses which parameters may be the most reasonable ones to add. For example, the next higher order parameter with an operator of the form \hat{J}^n may be the required parameter if only transitions of the qR series with $K_a = 0$ and J higher than the ones already implemented in the fit are newly added for a nearly prolate molecule. However, even this may be challenging as operators of different parameters may have similar effects on energy levels. It happened, that best parameters turned out to be undetermined or a proper fit convergence is hampered at a later iteration step. In the case of unsuitable fits, going back to a previous step and implementing second best parameters may help to derive suitable models. Finally, several promising options are tested. However, the *wrms* surface, which is depending on the parameter values, is not studied in detail as it is not practicable and far beyond the scope of this work. Connecting the fit software with an external software, which allows for the usage of several fit algorithms, in particular, to check wider ranges of the *wrms* surface, such as MAGIX [107],²⁸ may help to find the

²⁸Download from: <https://magix.astro.uni-koeln.de/> [Online; accessed 08-August-2020].

global minimum more securely in the future.

The iterative fitting procedure, with implementing sets of series together with a step-wise implementation of parameters which are describing new series the best, should lead to starting values which are close to the overall global minimum at each step, thus the fit is (hopefully) converging into the global minimum in the end. In this context, it is important to emphasize that a final selection of parameters may not represent an exclusive quantum mechanical model nor the global minimum of the *wrms*, it is more the best choice of parameters found. Most importantly, the applied procedure results in reasonable quantum mechanical models in the end.

iii) New predictions can be carried out straightforwardly to higher (or even lower) frequency regions to allow for further assignments if the fit quality is satisfactory. In case a firm model is derived, the laboratory work is finished and a search for the molecular fingerprint in space can be started.

Assignment Software

Used programs for assigning transitions within this work (SMAP and LWW) and programs which are expected to be beneficial for future analyses of propanal (PGOPHER, AABS, and ASAP) as well as automation solutions (AUTOFIT and AMDOR) are shortly summarized here.

There are several applications available in the literature that facilitate a quick assignment and fitting of lines. The center frequencies of lines are usually determined by polynomial fits to the central part of the line profile. The rotational data of this work are analyzed with the **SubMillimeter Analysis Program (SMAP)**.²⁹ No documentation nor a help file nor an example procedure of this program is publicly available, but the program is rather self-explanatory. The software used to assign the FIR spectrum of the fundamental band ν_{24} of *syn*-propanal within this work is the **LWW program** [90,91],³⁰ with the corresponding author Wiesław Łodyga.³¹ The program is based on Loomis Wood plots. In Loomis Wood plots transitions which make up a series are plotted for adjacent quantum numbers in adjacent rows above each other. The alignment of each row is based on the predicted center frequencies of the transitions. In this way, series or systematic deviations become obvious and easily assignable.

PGOPHER [108–110] is frequently used in the framework of this thesis for a quick overview of molecular spectra. This program is one of the most popular programs for assigning and fitting molecular spectra as the graphical interface is rather user-friendly and an extensive documentation is available.³² The program is maintained and developed by Colin Western. Further software, not used for deriving spectroscopic results presented within this thesis, but powerful and probably beneficial for future analyses of propanal are AABS and ASAP. A purely keyboard controlled assignment software, written by Z. Kisiel, is the **Assignment and Analysis of Broadband Spectra (AABS)** software [111], which allows for rather quick assignments. A program facilitating the assignment and analysis of vibrational bands ($\nu' \leftarrow \nu''$), if the lower vibrational state ν'' is already studied by means of rotational spectroscopy, is the **Automated Spectral Assignment Procedure (ASAP)** [98], originally developed by Christian Endres. It is assumed that the spectroscopic parameters of lower vibrational state ν'' and its predicted energy levels do not have an uncertainty. This is legitimated as the rotational transitions are usually about two orders of magnitude more accurate than ro-vibrational ones, as uncertainties of transitions in the MMW are estimated to ~ 20 kHz and in the FIR to ~ 0.0001 cm⁻¹ (≈ 3 MHz). Transitions which all end

²⁹Download from <http://spec.jpl.nasa.gov/ftp/pub/calpgm/SMAP/> [Online; accessed 28-July-2015]. The PROPSE website lists Brian Drouin as the author.

³⁰Documentation at <http://lww.amu.edu.pl> [Online; accessed 28-July-2020]

³¹Email: wlodyga@amu.edu.pl

³²<http://pgopher.chm.bris.ac.uk/> [Online; accessed 28-July-2020]

up in the same energy level of the unknown upper state v' have a common frequency offset and by stacking these transitions the energy offset is figured out. This is repeatedly done for several unknown energy levels, see Ref. [98] for a much more detailed explanation.

Some (nearly) autonomous assignment and fitting procedures of broadband rotational spectra can be found in the literature, see for example Refs. [81, 112, 113]. Probably the most commonly known algorithm is **AUTOFIT** [81], which is a brute force algorithm and is also implemented in PGOPHER [109, 110]. It simply needs three transitions from *ab-initio* calculations and a defined search frequency window around the predicted transition frequencies. The size of the frequency windows may display the uncertainty of *ab-initio* calculations. All center frequencies of observed lines within the windows are determined. Then all combinations of three observed transitions, one from each predicted frequency window, are fit to determine the rotational constants A , B , and C . From these fits, further selected transitions are predicted and the quality of the agreement of measured and predicted spectra is rated. Usually with the best fit further transitions and spectroscopic parameters are determined. Another brute force method is the **Automated Microwave DOuble Resonance (AMDOR) spectroscopy** [82], but here possible linkages of various observed transitions in broadband measurements are probed by means of DR spectroscopy, in particular these DR measurements are computer controlled and part of the automation. If five linked transitions, four a - plus one b - or c -type transitions (a -type transitions show typical pattern in the 2D AMDOR spectrum, comparable to Fortrat diagrams, and are thus known), are found, their quantum numbers are simply guessed in a certain range. Out of all possible assignments the best fit is chosen on the basis of the lowest standard deviation and is expected to determine accurate A , B , and C rotational constants. The overall idea of this method is to identify the molecular composition of a sample (or mixture) without a priory knowledge of the chemical compounds.

To facilitate the visual inspection in the process of this research and for the creation of revealing figures highlighting the results of this work, in particular series of molecular fingerprints, self-written python based algorithms for Loomis Wood plots and Fortrat diagrams are developed. If no predictions are available Fortrat diagrams can be used. Here the frequency axis of broadband spectra are divided by $2J$ and plotted in adjacent rows for increasing J .³³ The principle idea is the same as for Loomis Wood plots. Furthermore to study interactions, in particular to locate possible interaction areas of different vibrational states and, again, also for visualization purposes, also self-written algorithms for reduced energy diagrams are developed.

³³Transitions of rigid linear molecules would show up as vertical series as they follow $\nu_{J \leftarrow J-1} = 2BJ$, derived from Eq. (2.8) with the selection rule $\Delta J = \pm 1$.

Figures

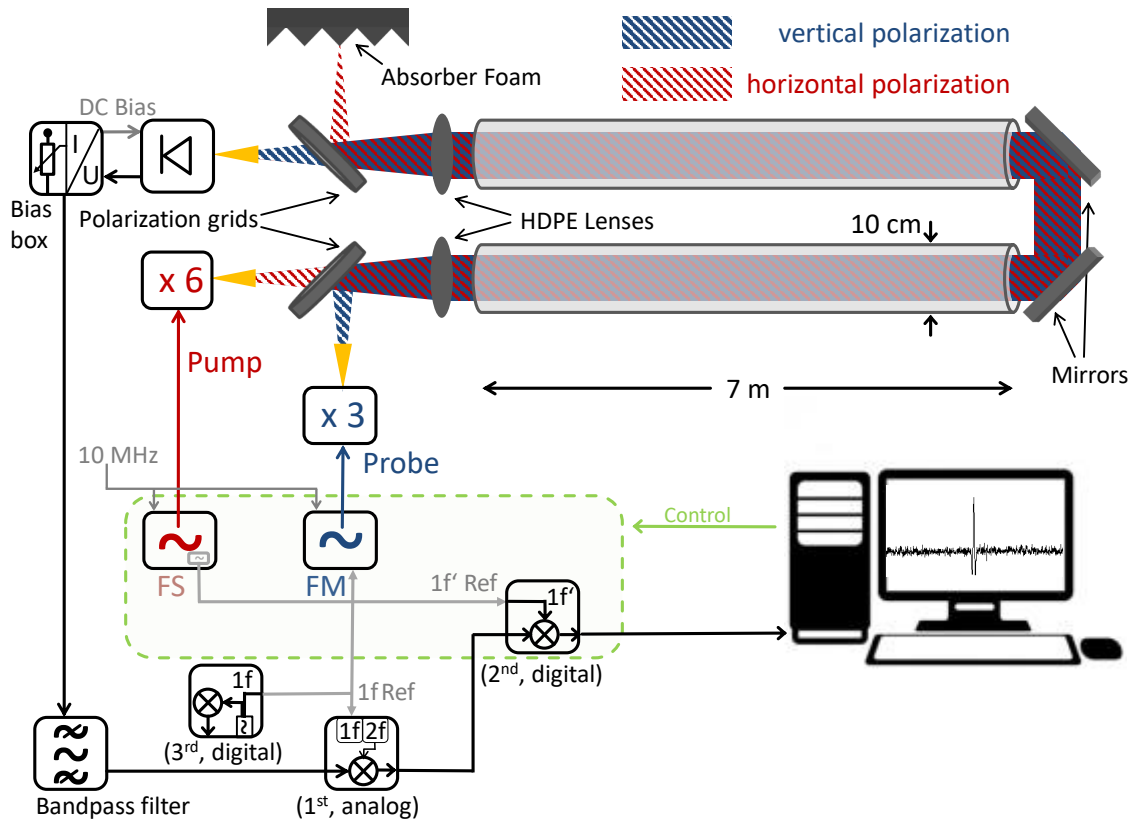


Figure A4: DM-DR W-band absorption spectrometer. The pump source is additionally modulated (the frequency is switching from on-resonance to far enough off-resonance, usually with a frequency throw of -120 MHz) in comparison to classical DR measurements. The $1f'$ demodulation of the second lock-in amplifier is experimentally realizing the difference spectrum of the DR off and on measurements. The pump synthesizer is creating the reference frequency f' and passes it to the digital lock-in amplifier. An analog Model 128A lock-in amplifier from PAR is used as the first lock-in amplifier (FM, $2f$ demodulation) as digital ones are observed to add signal spikes to the demodulated signal without extra care. The reference signal is generated by a third (digital) lock-in amplifier because the analog lock-in amplifier has no internal reference frequency. The first and third lock-in amplifier are not computer controlled as settings do not need to be changed. This results in baseline- and confusion-free spectra containing only the line(s) of interest. For more details see Sec. 3.1.3.

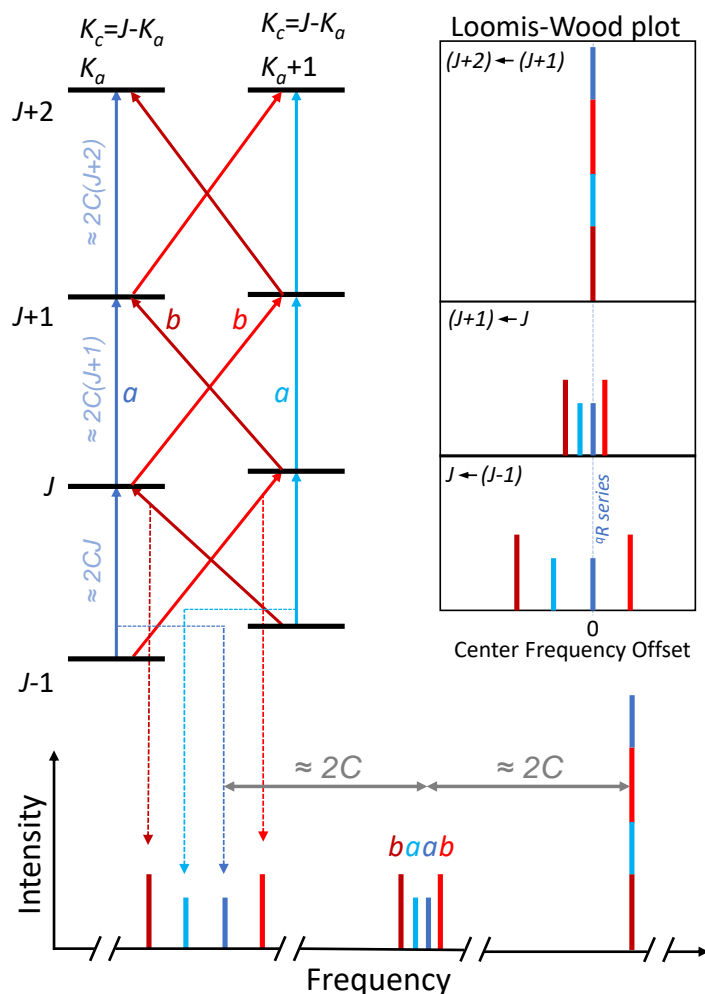


Figure A5: Schematic visualization of a typical quartet of lines for (nearly) oblate paired energy levels with $J_{K_a, J-K_a}$ of asymmetry side J and $J_{K_a+1, J-K_a}$ of $J+1$ for near prolate rotor molecules. The respective energy term diagram is shown on the upper left (rotational constant C may be given in MHz). The resulting spectrum is shown on the bottom. Note that the x -axis is interrupted. The μ_b dipole moment component is somewhat larger than μ_a , such as for *syn*-propanal. Caution: For qR series, **the spacing of (nearly) prolate paired energy levels is only approximately $B+C$** for molecules close to the prolate limit ($\kappa = -1.0$) and is noticeably reduced depending on $B-C$ for higher J until the spacing is approximately $B+C - (B-C) = 2C$ **for nearly oblate paired energy levels**. The (nearly) oblate paired pattern of the quartet of lines (b -, a -, a -, b -type) is best observed in Loomis-Wood plots (upper right). The spacing of the quartet of lines of *syn*-propanal is $2C \approx 9.2$ GHz as can be seen in Fig. 26 ($\kappa = -0.7855$). Furthermore, a typical qR series is highlighted for $J_{K_a, J-K_a} \leftarrow (J-1)_{K_a, J-K_a-1}$ in the Loomis-Wood plot. qR series are of fundamental importance, in particular if μ_b is rather small, or if the quartet structure is not observable. The spacing is about $B+C \approx 8.5$ GHz ($\kappa = -0.9849$) for qR series of (nearly) prolate paired energy levels of *gauche*-propanal in Fig. 31.

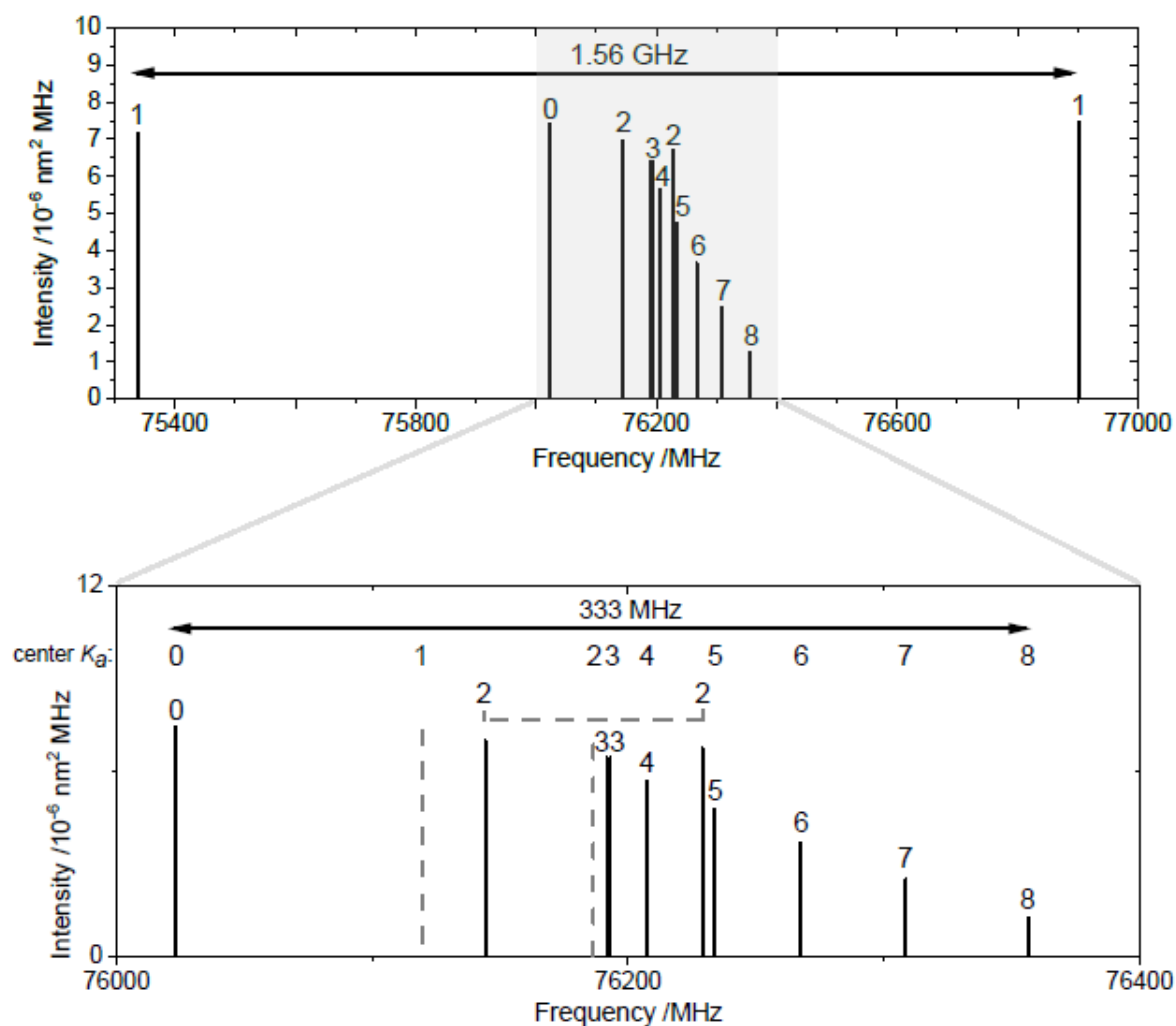


Figure A6: Typical K_a structure of near prolate asymmetric-top molecules, on the example of 0^+ of *gauche*-propanal ($\kappa = -0.9849$). Transitions of the K_a structure follow all the selection rule $9_{K_a, K_c} \leftarrow 8_{K_a, K_c-1}$. K_a values are given in the figure. Transitions of the asymmetry side $J+1$ appear at lower frequencies compared to ones of the asymmetry side J for identical K_a . If only one K_a value is shown, the two asymmetry components are blended (prolate paired). All transitions appear in close frequency windows as they are arising from the lifting of the $(2J+1)$ K -degeneracy (cf. green arrows in Fig. 8).

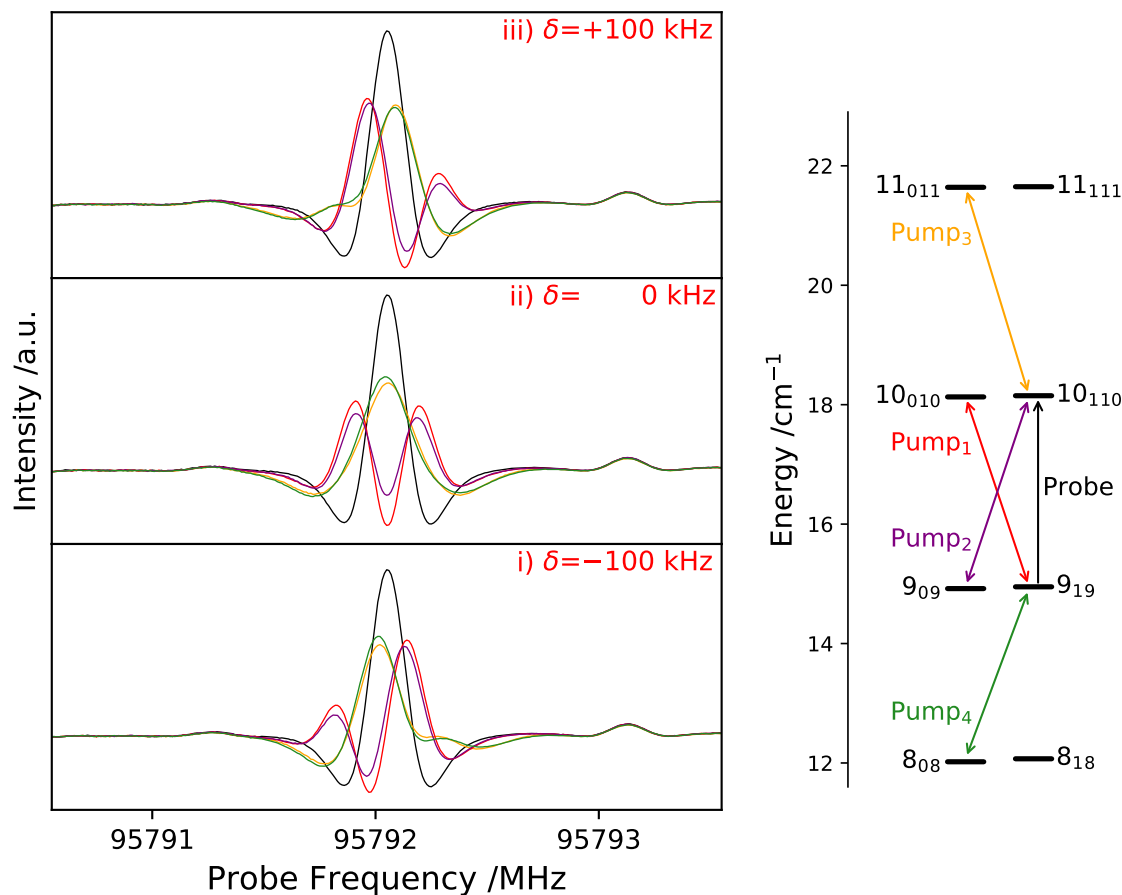


Figure A7: DR measurements of *syn*-propanal for all four possible energy level arrangements. Regressive energy level arrangements are shown 1) in red (V-type) and 2) in violet (Λ -type) and progressive ones 3) in orange and 4) in green. A conventional measurement is also shown for comparison (in black). On the left hand side DR spectra are shown for three different detunings $\delta = \omega - \omega_{21} = +100$ kHz, 0 kHz, -100 kHz. The probed frequency window is always the same and measured spectra are plotted in the respective color of the pump transition. Obviously, regressive (red and violet) and progressive (orange and green) energy level arrangements can be distinguished if off-resonant pumping is applied. The more intense Autler-Townes component is red- or blue-shifted in frequency for regressive or progressive arrangements if $\omega > \omega_{21}$ ($\delta = +100$ kHz), respectively, and vice versa if $\omega < \omega_{21}$ ($\delta = -100$ kHz). Furthermore, a larger splitting can be observed for regressive pumping schemes. The two Autler-Townes components are split but still blended for progressive pumping schemes with on-resonant pumping ($\delta = 0$ kHz). This can be seen by the broader and less intense line shape in comparison to the conventional measurement. The origin of different splittings is unknown to this point. The larger splittings in regressive energy level arrangements lead to slightly higher SNRs in DM-DR measurements, in comparison to progressive ones. The figure is published in Ref. [73].

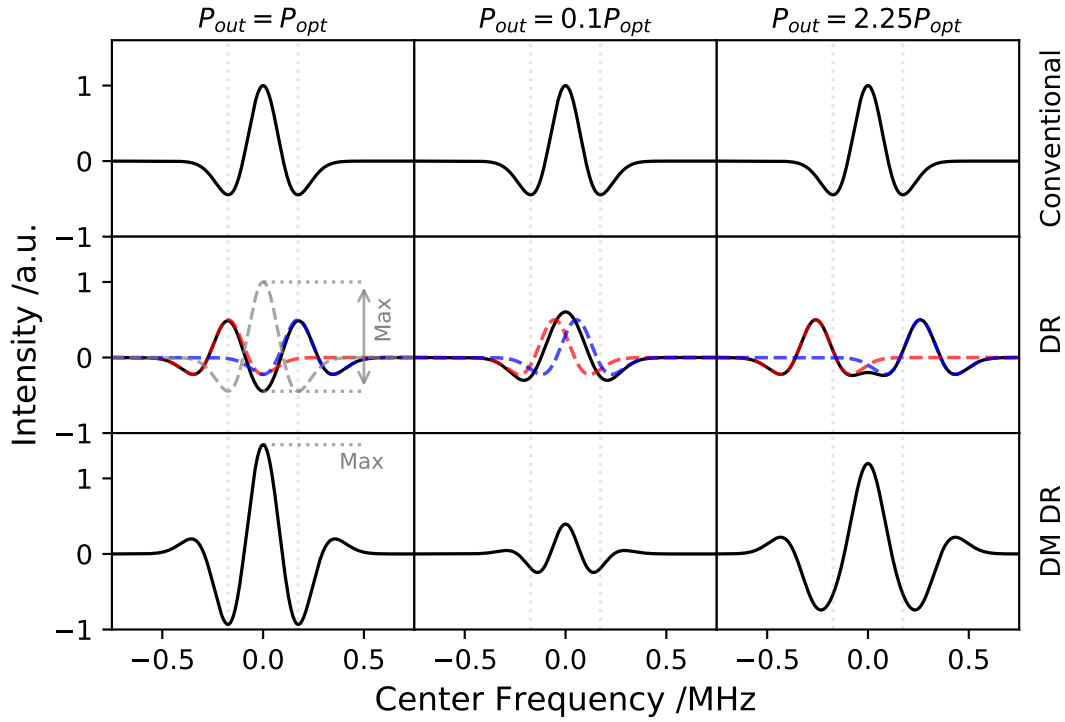


Figure A8: Simulated DM-DR line shapes for different output powers of the pump source P_{out} . The DM-DR signal (bottom row) is basically the difference of a conventional (top row) and a DR measurement (middle row). The pump source is off for conventional measurements (DR off: $P_{out} = 0$ W). The two Autler-Townes components and their sum are shown in blue, red, and black for DR measurements, respectively. The maximum signal at DM-DR measurements is obtained if the left minimum of the blue shifted component and the right minimum of the red shifted component are blended at the unperturbed center frequency ($P_{out}=P_{opt}$; $\omega_R \propto \sqrt{P_{out}}$ [4]). The figure is published in Ref. [73].

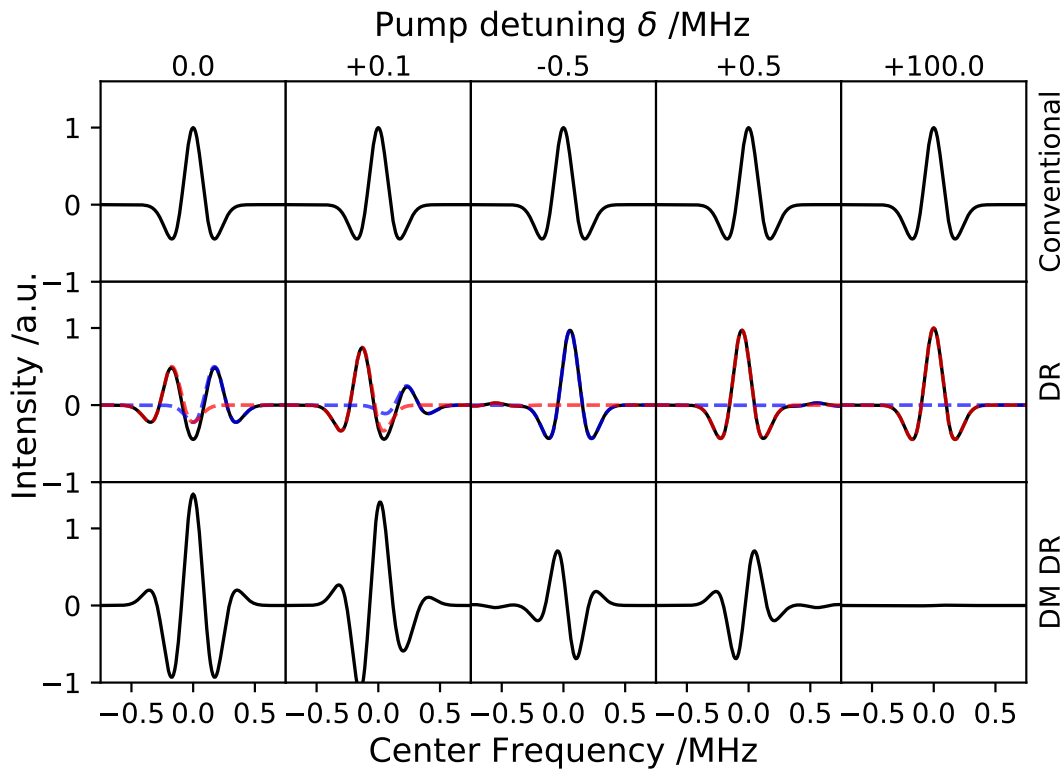


Figure A9: Simulated DM-DR line shapes for different detunings of the pump frequency δ of a regressive energy level arrangement. The DM-DR signal (bottom row) is basically the difference of a conventional (top row) and a DR measurement (middle row). The output power is the same for all DR and DM-DR spectra and is chosen to maximize the DM-DR signal for zero detuning ($P_{out}=P_{opt}$, cf. Fig. A8). The two Autler-Townes components and their sum are shown in blue, red, and black for DR measurements (middle row), respectively. The DM-DR line shapes are accidentally close to a first derivative of a Gaussian, or close to the $1f$ line shape of a conventional measurement, for slightly detuned pump frequencies, here $\delta = \pm 0.5$ MHz. Slightly off-resonant pumping is noticed by asymmetric line shapes for DR and DM-DR measurements, see $\delta = +0.1$ MHz. On the other hand, DM-DR line shapes are accidentally close to a second derivative of a Gaussian, or close to the $2f$ line shape of a conventional measurement, for on-resonant pumping. The figure is published in Ref. [73].

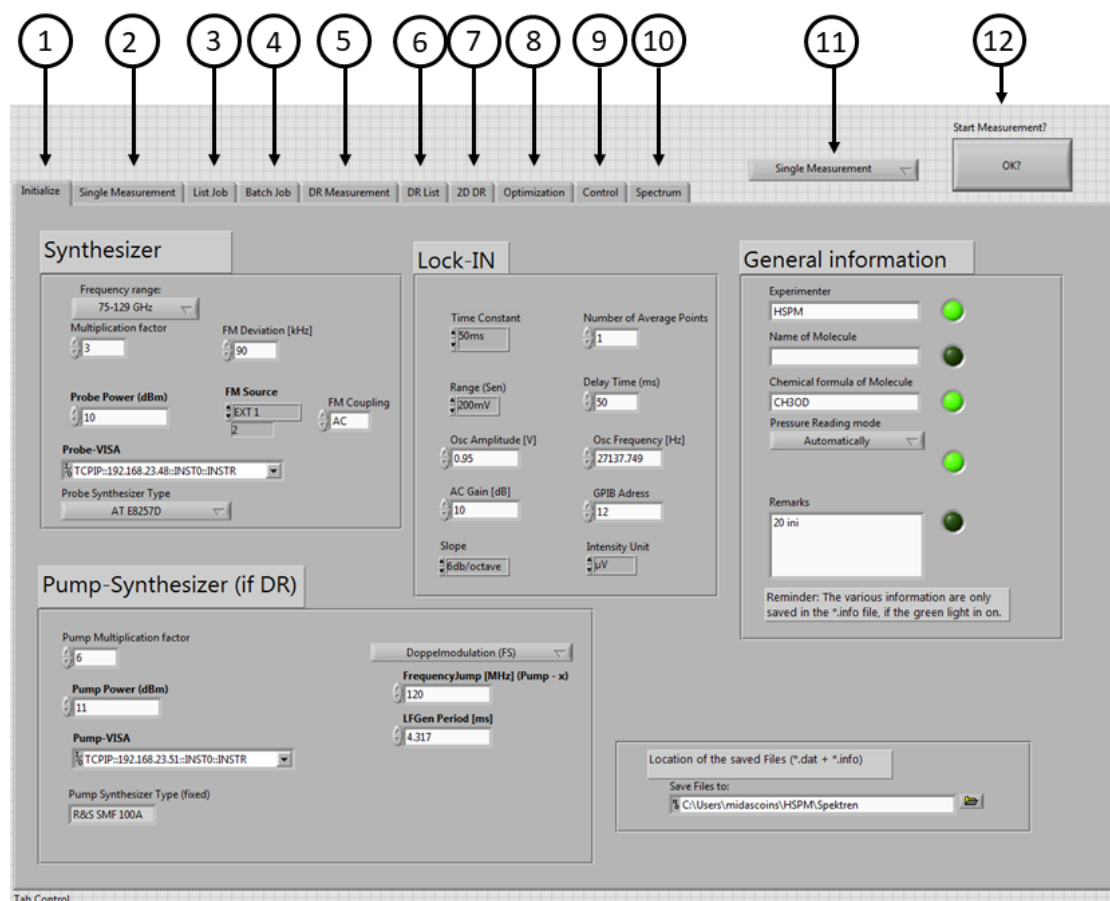


Figure A10: Screenshot of the user interface of the measurement software, written in LabVIEW. For the actual measurement, the user can choose between several options, which are divided in different tabs: (1) Initialize: Control of general parameters of the measurement, such as modulation depth, Time Constant and so on (required); (2) Single measurement; (3) List job: Subsequent measurement of several user defined single measurements; (4) Batch Job: Several single measurement of the same window size are measured, which are adjacent in frequency. This option is ideal for broadband measurements; (5) (Single) DR measurement (DM-DR is optional); (6) DR List (DM-DR is optional); (7) 2D DR spectra (DM-DR is optional); (8) Optimization: Tracking of line intensities for optimizing experimental conditions (activated in the tab); (9) Control: Summary of current measurement parameters; (10) Spectrum: xy -graph displaying the current measurement $I(\nu)$; (11) Toggle button which defines the active tab (2–7); (12) 'Start measurement' button.

The software code of the program basically consists out of four different parts: (i) A while loop which allows the user to toggle between several options on the fly, if available; (ii) Calculating all necessary parameters and initializing of the hardware; (iii) The actual measurement procedure of increasing and decreasing frequencies and subsequent storage of the data; (iv) terminating the communication with the hardware.

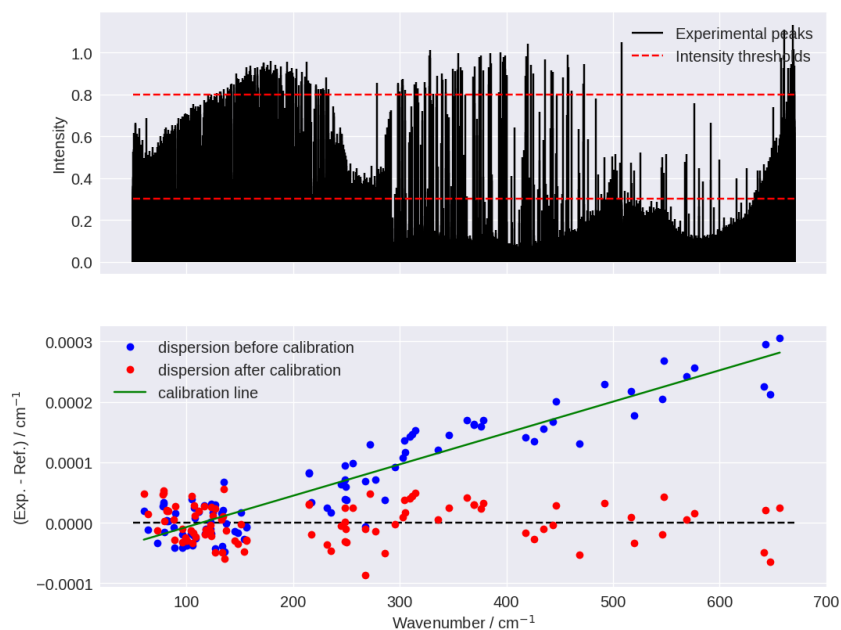


Figure A11: Calibration of the FIR measurement of propanal at a pressure of 240 μbar . A script written by M.-A. Martin-Drumel is used [77]. Residual water lines are used for calibration [78–80].

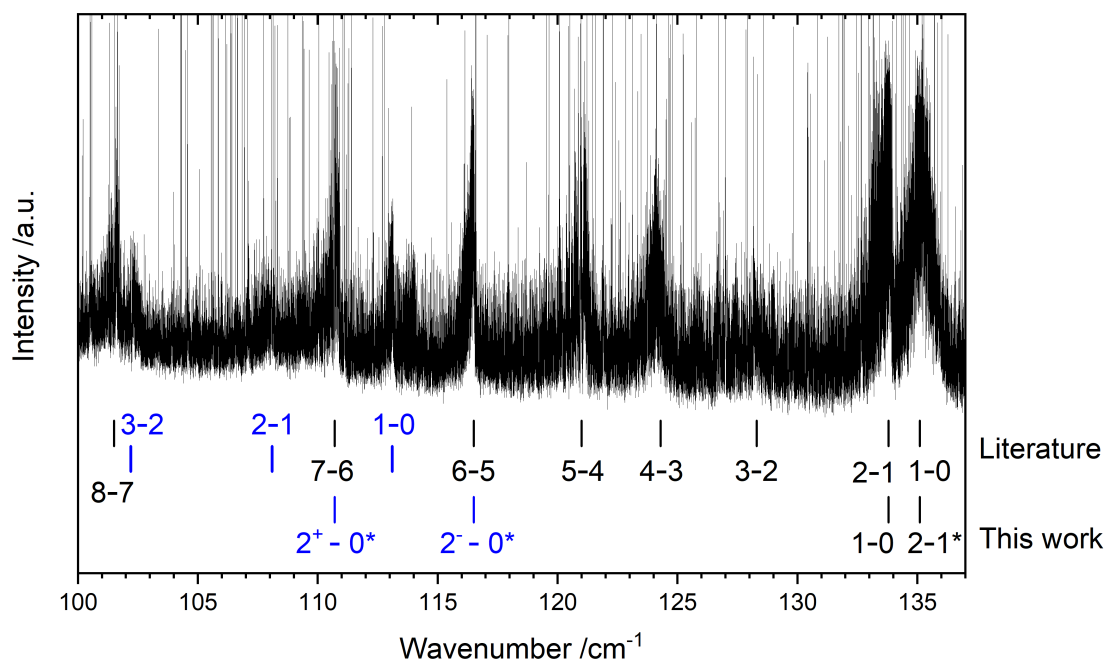


Figure A12: Assignments of FIR bands of *syn*- and *gauche*-propanal of this work vs. literature ones [45]. Solid black lines show the assignment of *syn*- and blue ones of *gauche*-propanal. Tentative assignments from this work are marked with (*).

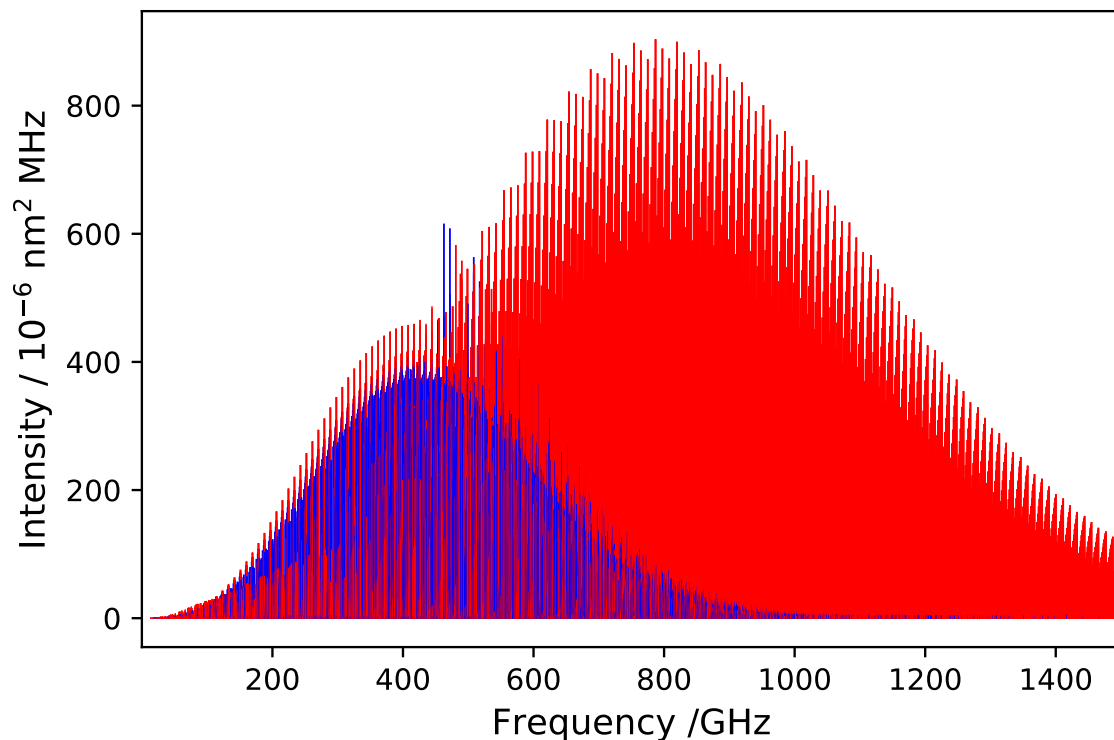
Figures: *Syn*-Propanal

Figure A13: Calculated stick spectrum of $v = 0$ of *syn*-propanal. The spectrum is shown up to 1.5 THz with $J_{max} = 99$, calculated for $T = 300$ K with $Q = 82649.4356$. Blue and red sticks depict *a*- and *b*-type transitions (nominally forbidden or falsely labeled *c*- and *x*-type transitions are also depicted by red sticks, see Sec. 5.1.1), respectively. Note that intensities of transitions that may be blends are not summed up.

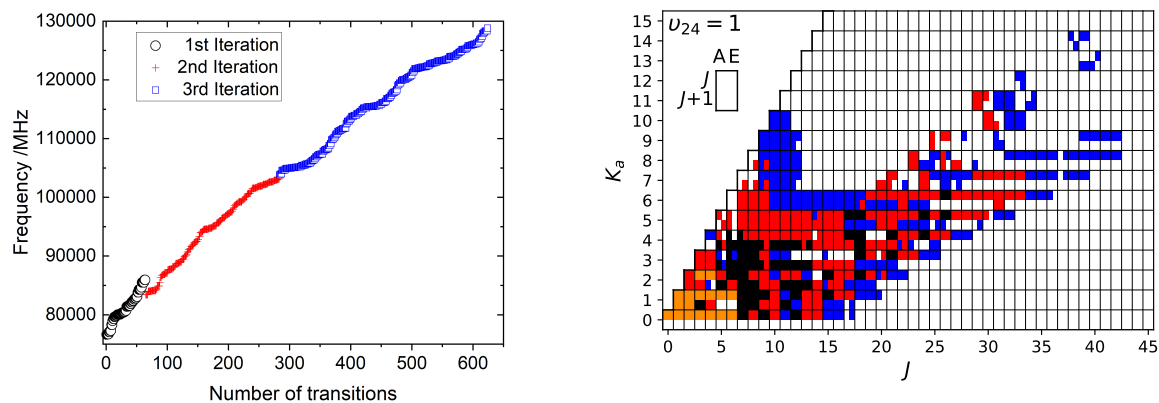


Figure A14: Frequency coverage of assigned and fit transitions in the MMW region (left; without literature data) and quantum number coverage of all involved energy levels (right) of the first three iterations of the analysis of $v_{24} = 1$ of *syn*-propanal. The literature data are shown in orange and the first, second, and third iteration of new assignments in the MMW region are shown in black, red, and blue, respectively. In total 652 transitions with J up to 42 and K_a up to 14 are fit with a standard deviation of 1.14.

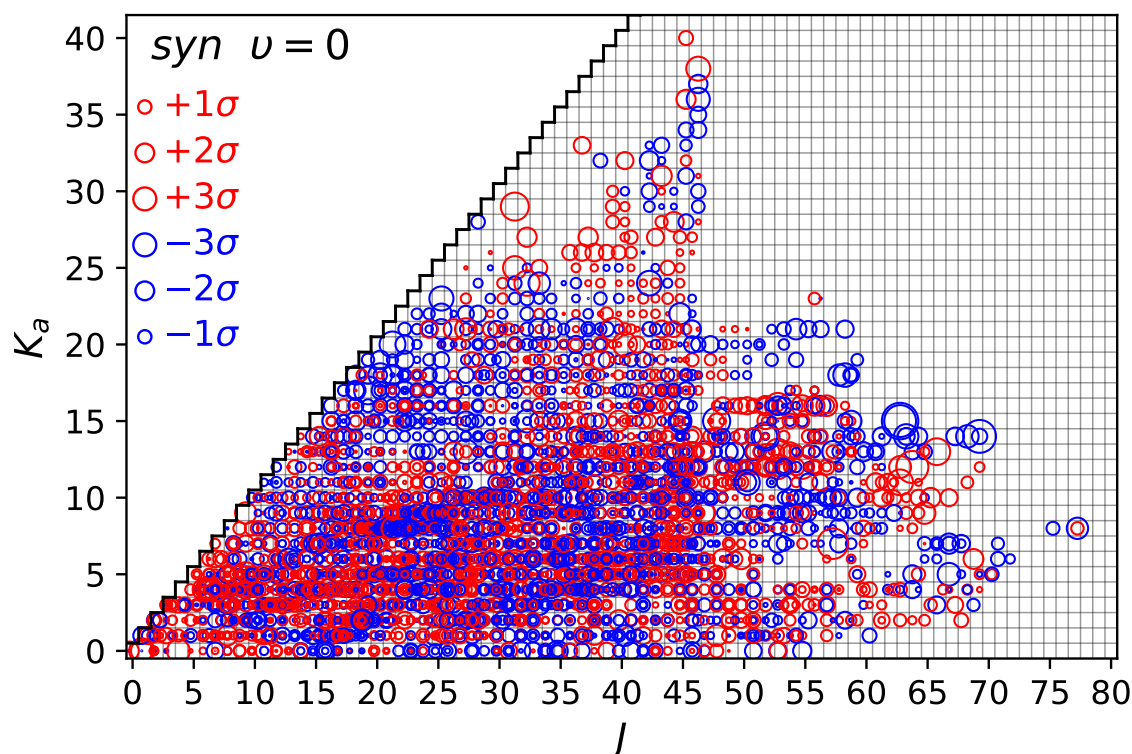
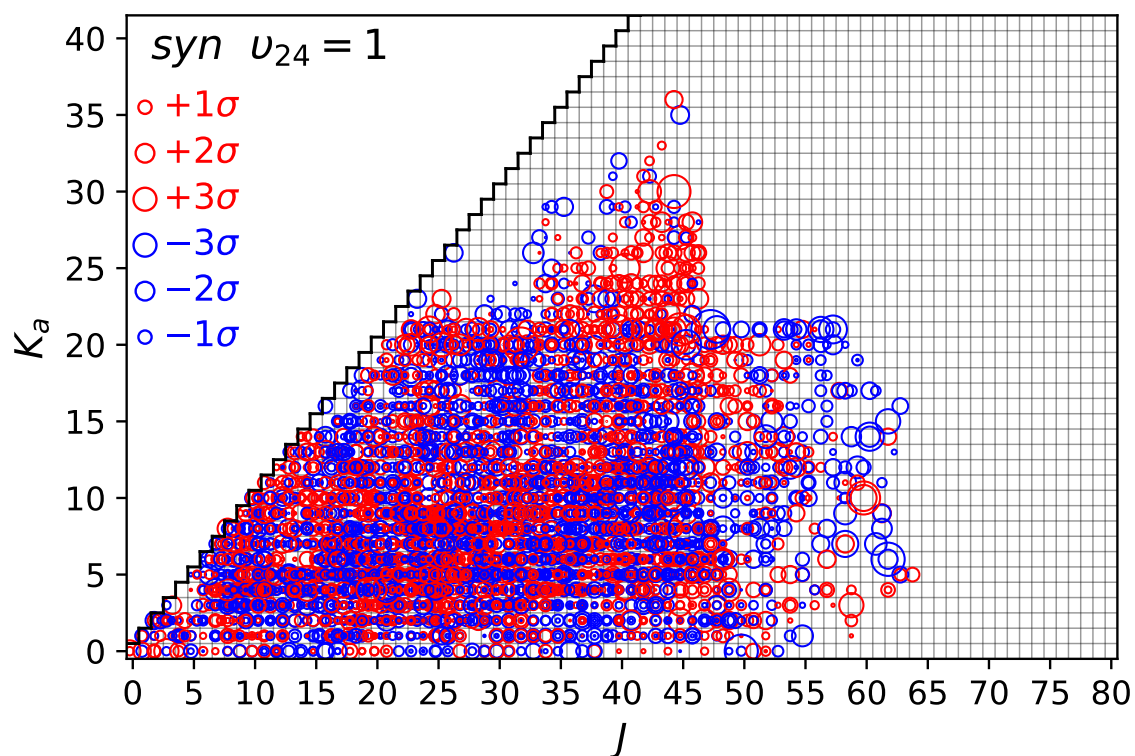
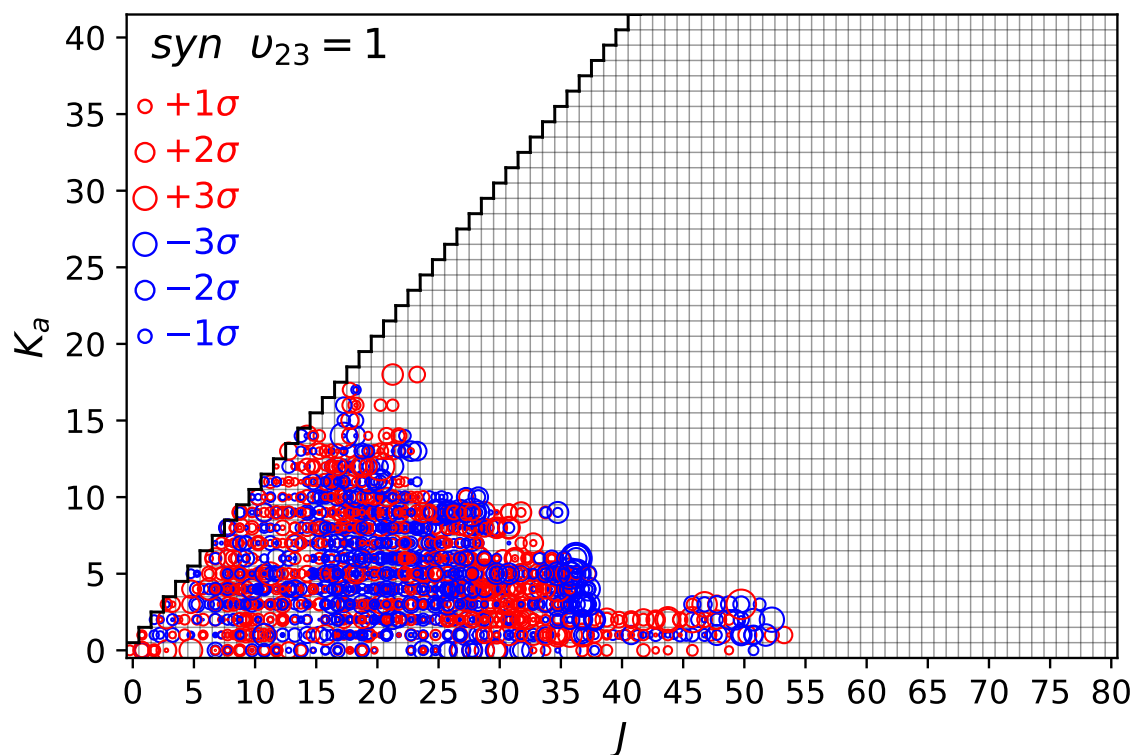


Figure A15: Quantum number coverage of $v = 0$ of *syn*-propanal.

Figure A16: Quantum number coverage of $v_{24} = 1$ of *syn*-propanal.Figure A17: Quantum number coverage of $v_{23} = 1$ of *syn*-propanal.

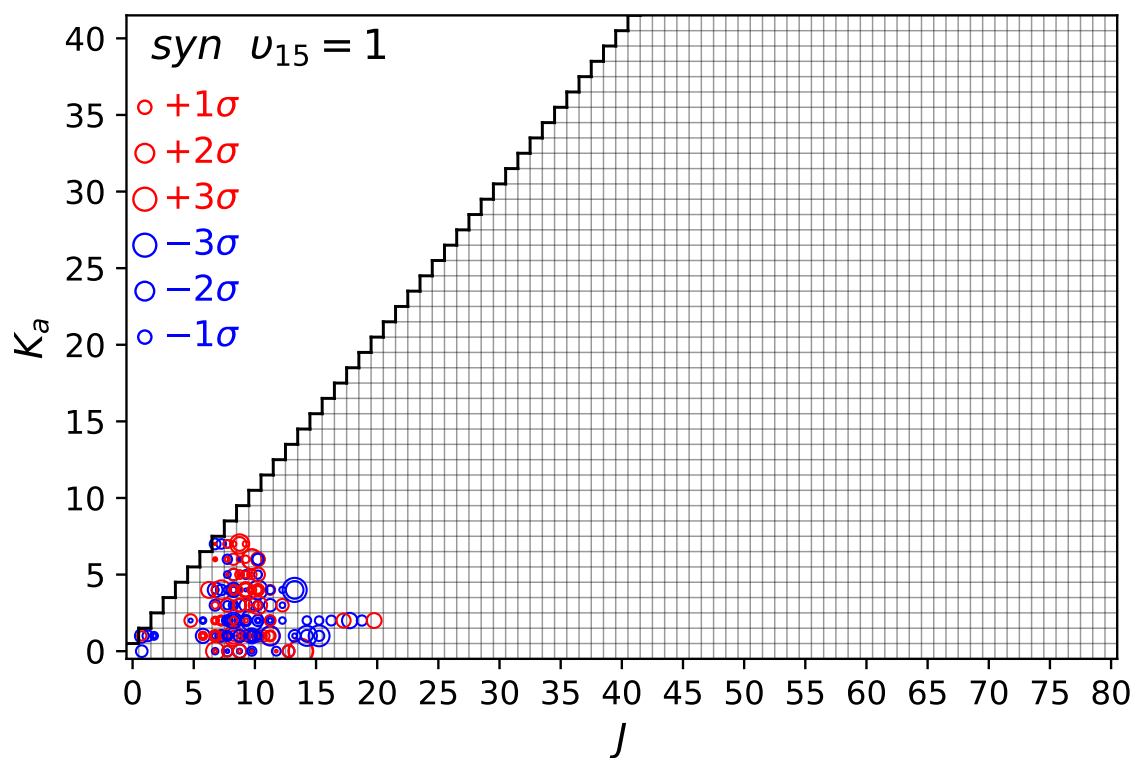


Figure A18: Quantum number coverage of $v_{15} = 1^*$ of *syn*-propanal.

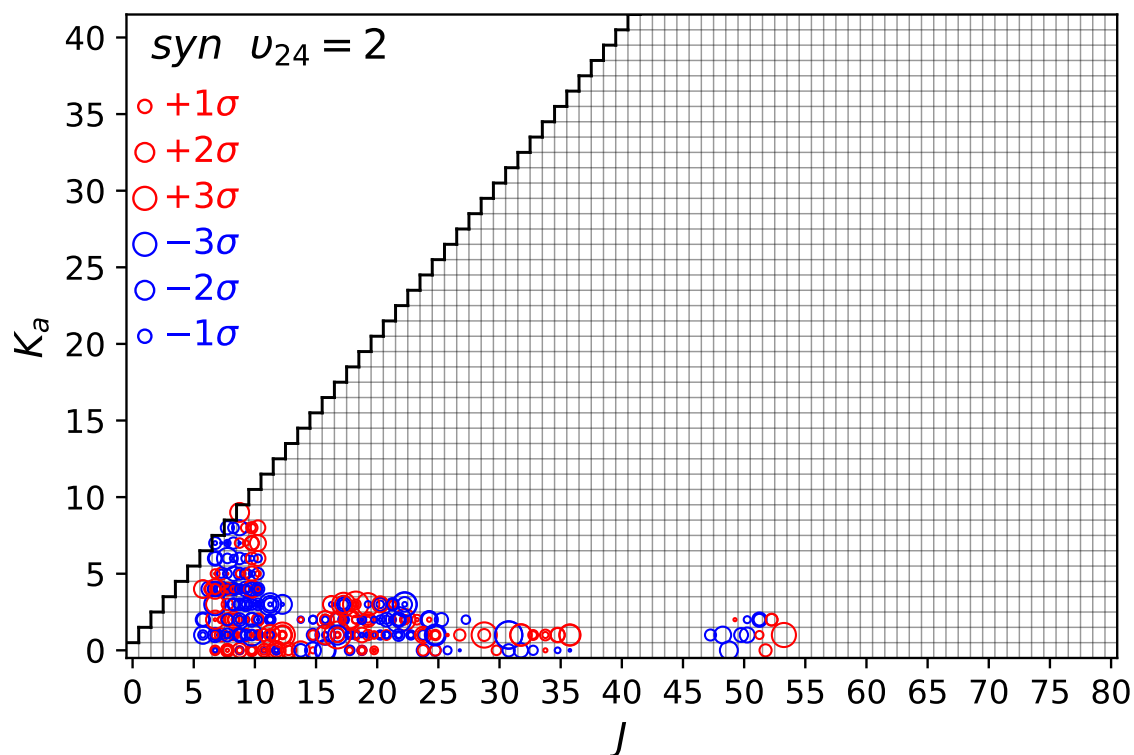


Figure A19: Quantum number coverage of $v_{24} = 2^*$ of *syn*-propanal.

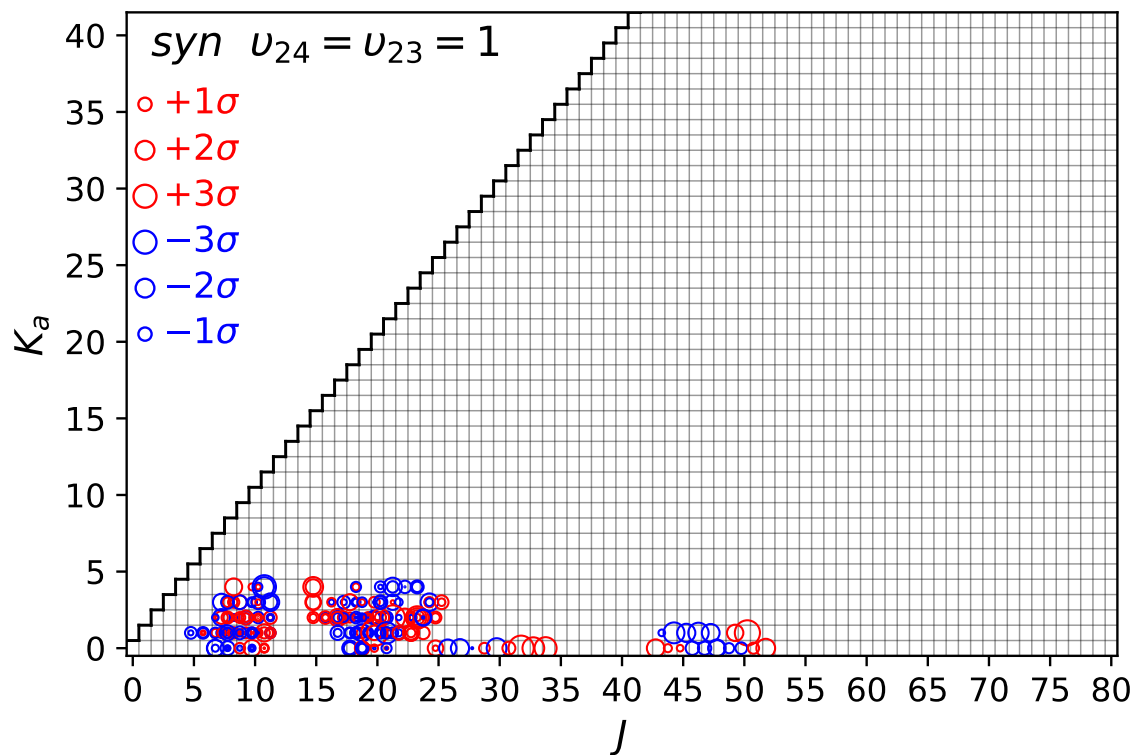


Figure A20: Quantum number coverage of $v_{24} = v_{23} = 1^*$ of *syn*-propanal.

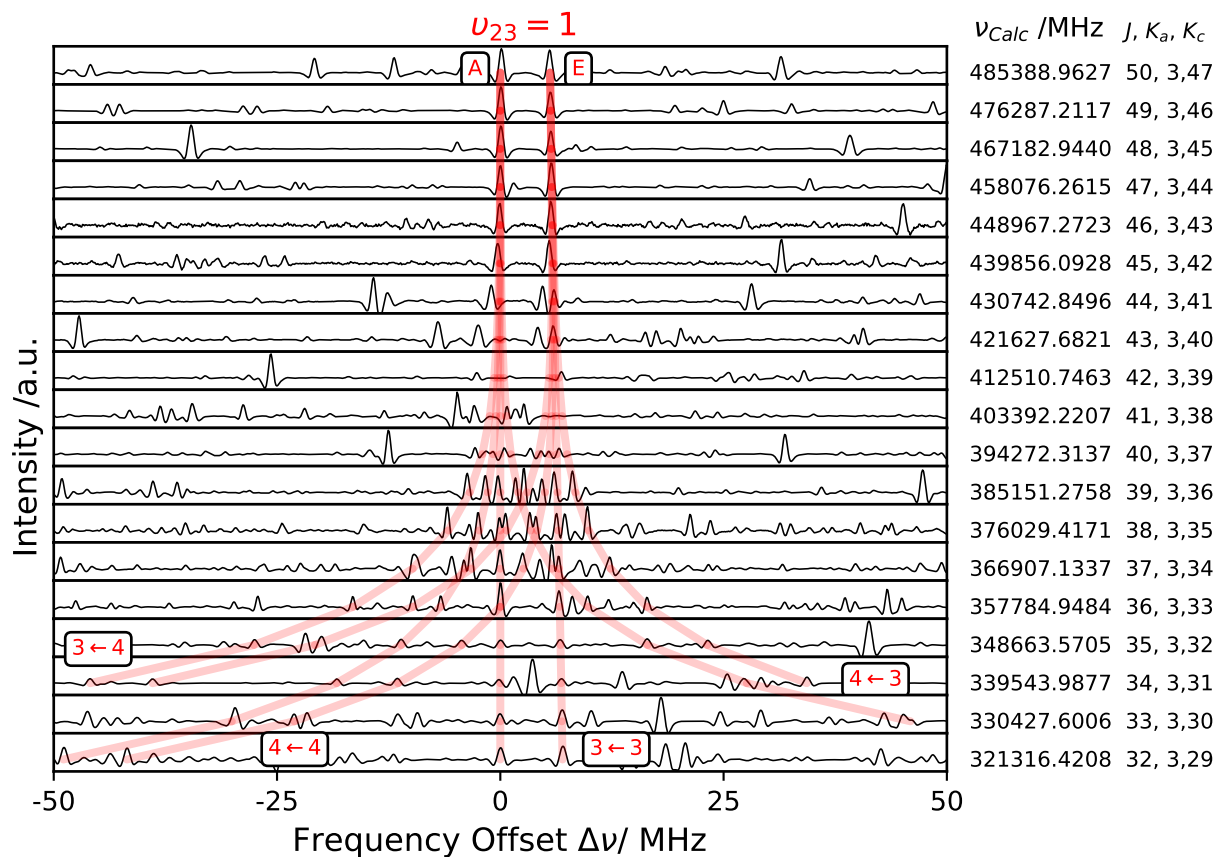


Figure A21: Oblate pairing of A and E components of $\nu_{23} = 1$ of *syn*-propanal. Energy levels of the asymmetry side J of levels with $K_a = 3$ and the lower asymmetry side $J + 1$ with $K_a = 4$ are oblate paired for high J numbers. For this reason, the typical quartet structure made of a - and b -type transitions are blended for high J (i: b -type $K_a = 3 \leftarrow 4$, ii: a -type $K_a = 4 \leftarrow 4$, iii: a -type $K_a = 3 \leftarrow 3$, iv: b -type $K_a = 4 \leftarrow 3$), see Fig. A5. K_a numbers are given in the figure. Upper state quantum numbers of the predicted frequencies of the Loomis-Wood plot are given on the right hand side for the A component of a -type transitions $J_{3,J-3} \leftarrow (J-1)_{3,J-4}$ ($K_a = 3 \leftarrow 3$). Transitions with $J = 39-46$ show deviations up to 5 MHz due to perturbations with so far unknown origin and are unweighted in the final fit.

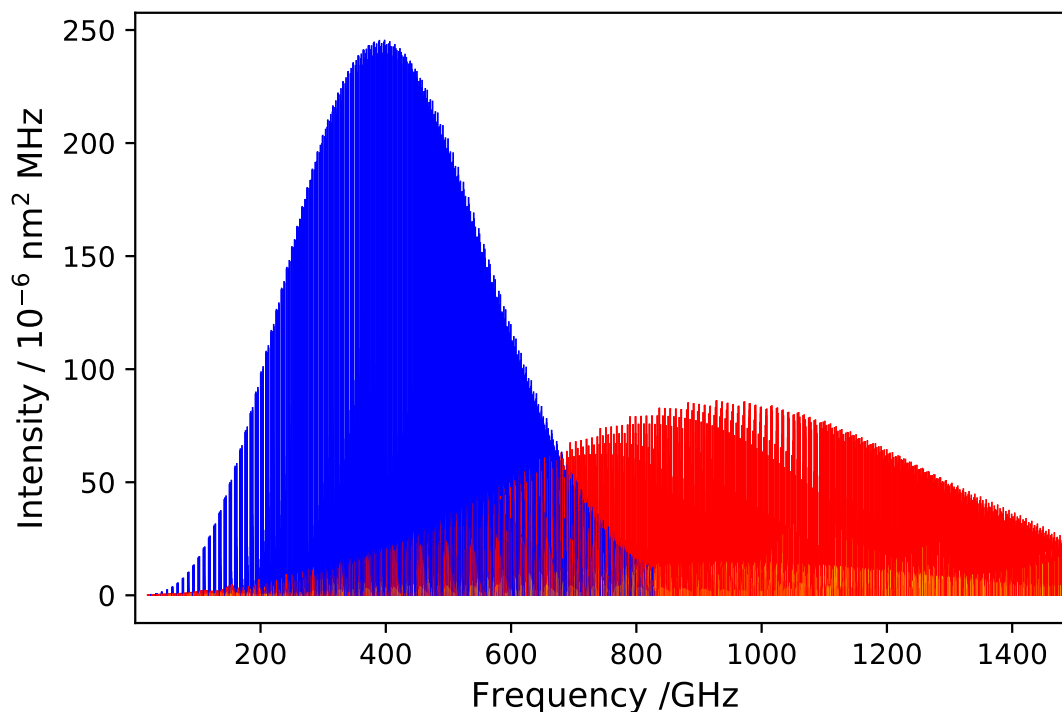
Figures: *Gauche*-PropanalOverview of the analysis of *gauche*-propanal:

Figure A22: Calculated stick spectrum of $v = 0$ of *gauche*-propanal. The spectrum is shown up to 1.5 THz with $J_{max} = 99$, calculated for $T = 300 \text{ K}$ with $Q = 41324.7178$ and $E_g = 420 \text{ cm}^{-1}$ [41]. Blue, orange, and red sticks depict *a*-, *b*-, and *c*-type transitions, respectively. Note that intensities of transitions that may be blends are not summed up.

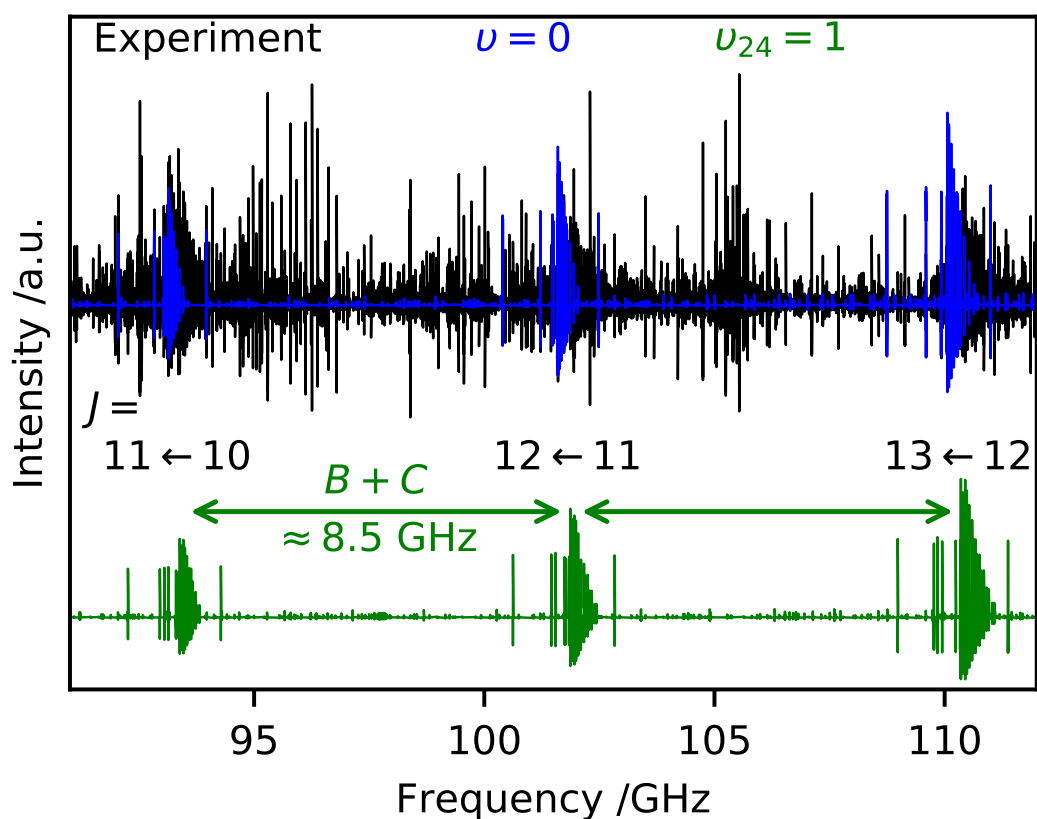


Figure A23: Satellite spectrum of *gauche*-propanal in the W-band region. The broadband measurement of propanal in the W-band region is shown in black. The constantly repeated emergence of rather strong and unassigned lines next to predicted K_a structure vibrational ground state transitions of *gauche*-propanal ($\nu = 0$ in blue) reveal the presence of a satellite spectrum belonging to $\nu_{24} = 1$ (in green).

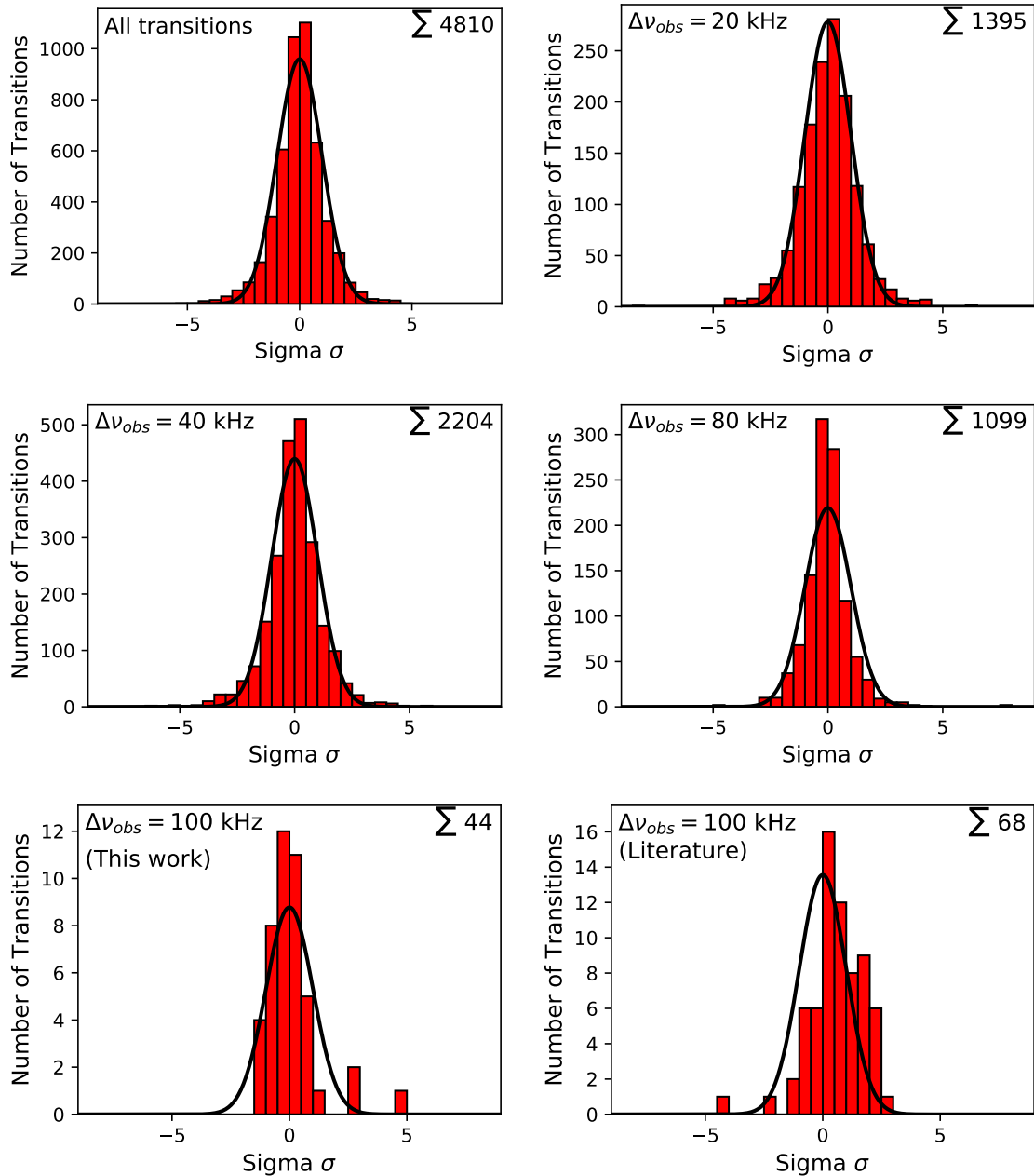


Figure A24: Statistical analysis of deviations of observed and predicted transition frequencies of *gauche*-propanal. 4810 transitions are fit in the global analysis of $\nu = 0$ and $\nu_{24} = 1$, see Table 8. The deviations are calculated as $\sigma = (\nu_{obs} - \nu_{calc})/\Delta\nu_{obs}$. The number of transitions with a given σ , within bin width 0.5, are plotted as red bars and the theoretically expected distributions are shown as black curves. This analysis supports the choice of uncertainties of 20 kHz for strong and very symmetric lines as observed and expected distributions match quite well. A rather conservative choice of 40 kHz and especially of 80 kHz for weaker and less symmetric lines is noticed. The DM-DR measurements from this work (26 assigned *c*-type transitions) and assigned transitions with asymmetric line shapes (16 transitions from $\Delta K_a = 5$ and 2 from $\Delta K_a = 4$ interactions), both with $\Delta\nu_{obs} = 100$ kHz, do not show systematic shifts. Transition frequencies from the literature show systematical shifts.

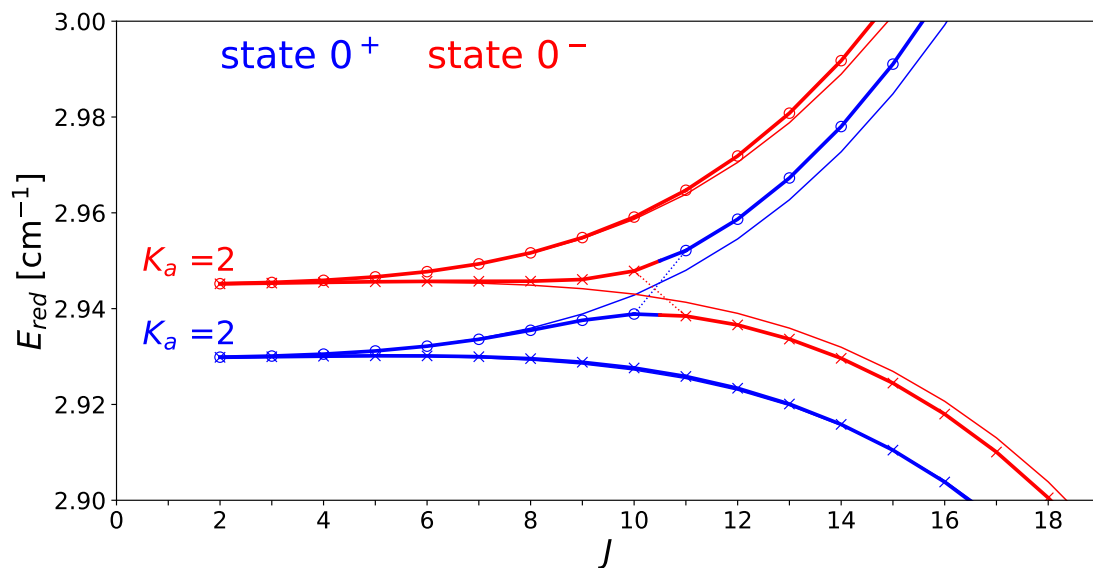


Figure A25: Reduced energy diagram for $K_a = 2$ of $v = 0$ of *gauche*-propanal, see Eq. (2.19). The two states, 0^+ and 0^- , are plotted in blue and red, respectively. Energy levels of asymmetry side J are marked by a circle (\circ), whereas $J + 1$ levels are marked with a cross (\times). The observed perturbation is resulting from tunneling-rotation interaction and is described by a -type Coriolis parameters in the RAS. The avoided crossing behavior is seen by thicker lines, connecting the energy levels, which change from blue to red, or vice versa. Quasi unperturbed energy level predictions of $K_a = 2$ are shown by the thin solid lines. The a -type Coriolis interaction parameters are simply neglected for these predictions.

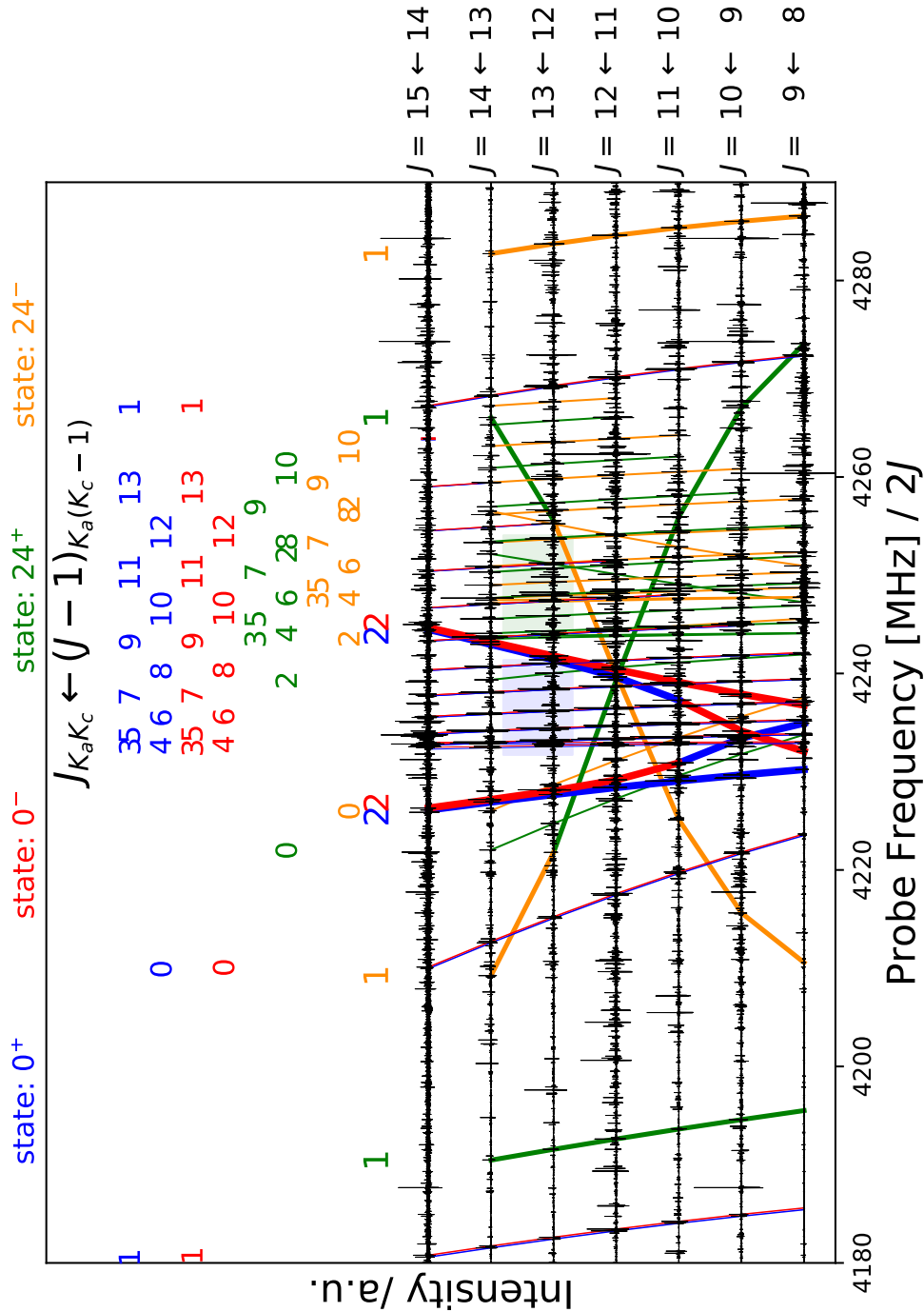


Figure A26: Fortrat diagram of *gauche*-propanal in the W-band region. qR series transitions of *gauche*-propanal are highlighted. In each layer K_a structures for 0^+ and 0^- as well as for 24^+ and 24^- are shown. The K_a structures are fully shown for $0 \leq K_a \leq 13$ and $0 \leq K_a \leq 10$, respectively. The numbers in the upper part of the figure represent the K_a quantum number of qR series ($J_{K_a, K_c} \leftarrow (J-1)_{K_a, K_c-1}$). The lowest row shows the K_a quantum numbers of perturbed transitions in the W-band region, in particular $K_a = 2$ for the ground state $v = 0$ and $K_a = 1$ for the first excited state $v_{24} = 1$. The energy term diagram for $K_a = 2$ of $v = 0$ can be seen in Fig. A25. Avoided crossing transitions are seen by a color change within qR series.

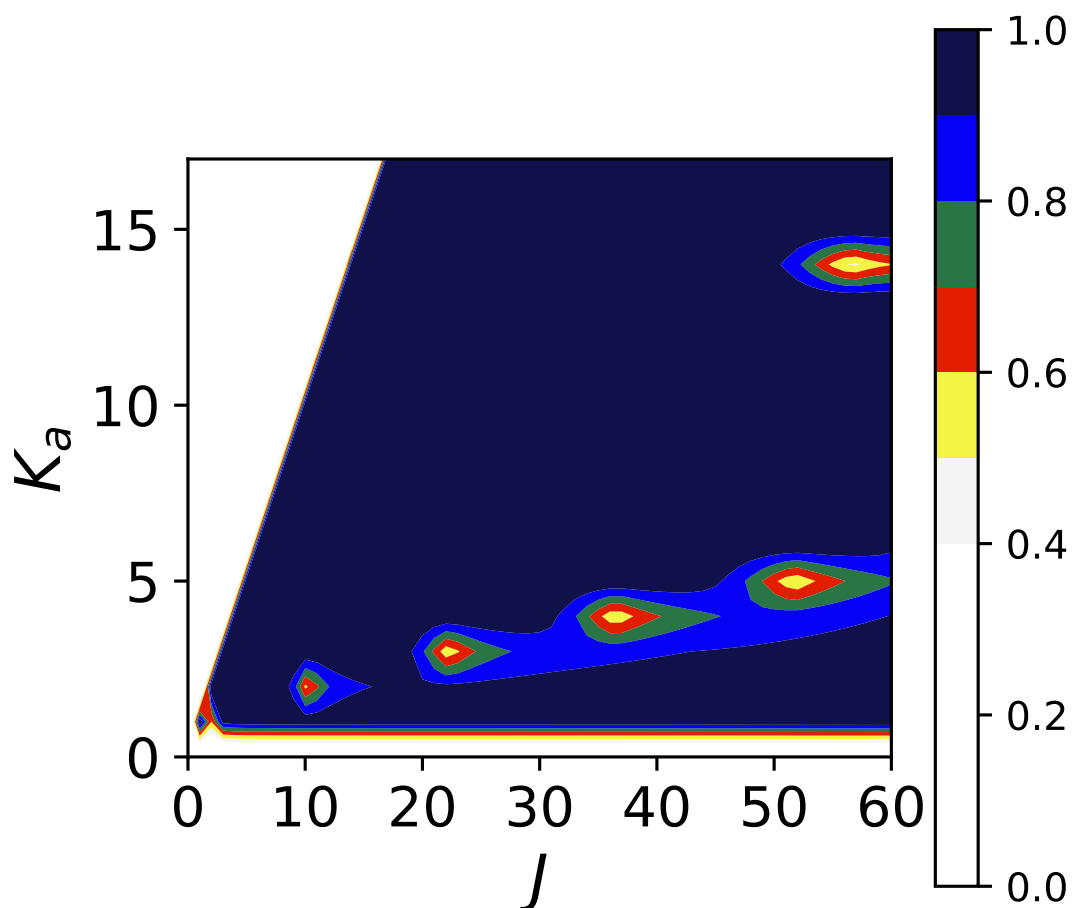


Figure A27: Contour plot of mixing coefficients of the asymmetry side $J + 1$ of 0^- of *gauche*-propanal. The mixing coefficients of the energy levels are plotted in dependence on their J and K_a . This contour plot is presented as an example, out of eight possible ones, as it illustrates the interaction areas clearly. Strong tunneling-rotation interactions occur within one vibrational state (here between energy levels from asymmetry side J of 0^+ with the ones of $J + 1$ of 0^- , the latter ones are plotted in this contour plot) for $K_a = 1$, $K_a = 2$, $K_a = 3$, $K_a = 4$, and $K_a = 5$ at $J = 2$, $J = 10$, $J = 22$, $J = 36$, and $J = 52$, respectively. Furthermore $\Delta K_a = 4$ interactions between $v = 0$ and $v_{24} = 1$ can be seen for $K_a = 14$.

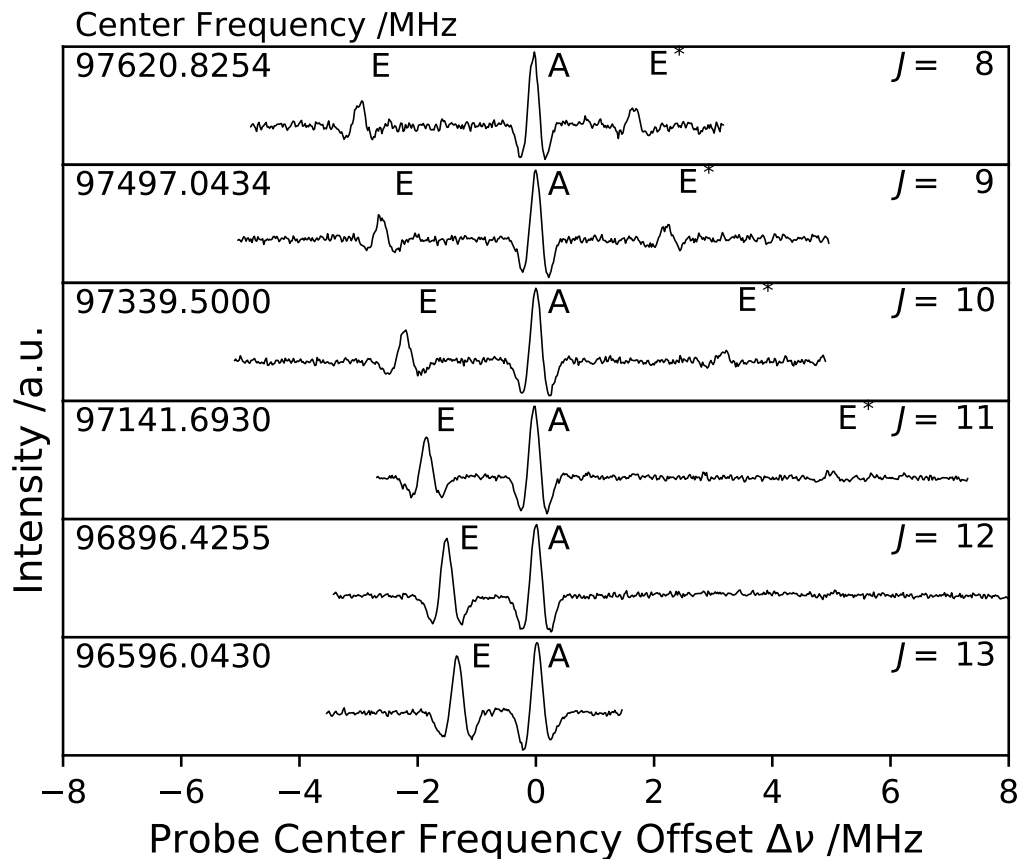


Figure A28: DM-DR measurements of *c*-type transitions of *gauche*-propanal. Shown here is the series $J_{3, J-2} \leftarrow J_{2, J-2}$ for asymmetry sides with $J+1 \leftarrow J$ with $\nu = 24^+ \leftarrow 24^-$. The measurement of $J_{K_a, K_c} = 11_{3, 9} \leftarrow 11_{2, 9}$ took about 4 minutes ($TC = 200$ ms). "Forbidden" transitions (E^*) of the internal rotation splitting lead to two observable E components if the asymmetry splitting is comparable to the internal rotation splitting [51]. As a consequence, A and E components can be assigned unambiguously without a proper model as E and E^* share intensities. The A components can be fit to a first approximation like a molecule without internal rotation.

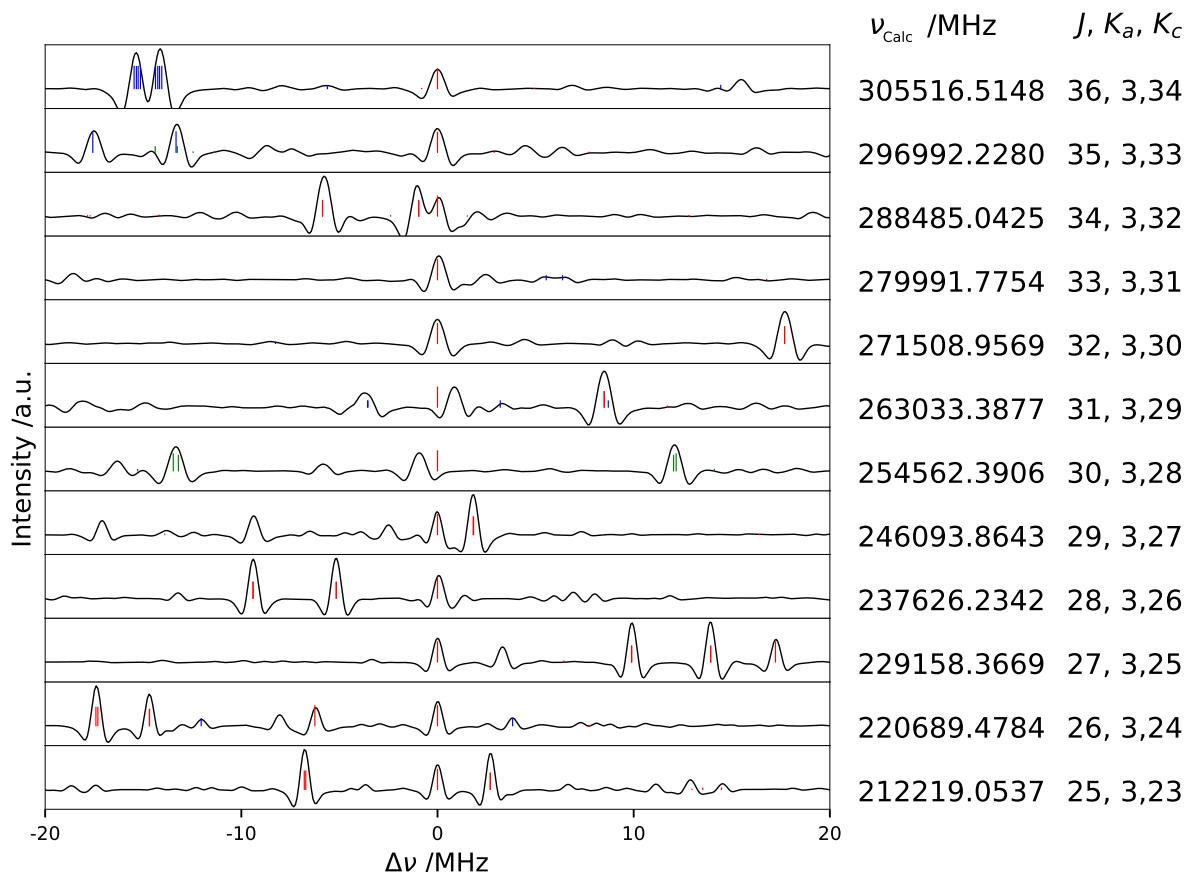


Figure A29: Single perturbed energy level of $\nu_{24} = 1$ of *gauche*-propanal. Presented here is a Loomis Wood plot of *gauche*-propanal showing a 9R series with $K_a = 3$ of asymmetry side $J+1$ of 24^- . The center frequencies and quantum numbers are given for the upper energy level of $J_3, J_{-2} \leftarrow (J-1)_3, J_{-3}$. The two transitions $31_{3,29} \leftarrow 30_{3,28}$ and $30_{3,28} \leftarrow 29_{3,27}$ show deviations of roughly the same magnitude, but opposite signs. This is a clear hint of a singly perturbed energy level $J_{K_a, K_c} = 30_{3,28}$ which can not be explained by tunneling-rotation interaction within $\nu_{24} = 1$. Furthermore, no other vibrational state of *gauche*-propanal is expected to be the origin of this perturbation. The origin is unknown up to this point. Some further energy levels of 24^+ and 24^- show similar behavior, albeit with smaller magnitudes than shown here. Observed deviations are in the range of 0.1 – 1.0 MHz. These transitions are not included in the fit. Large data sets with hundreds, or better thousands, of lines help to localize these perturbations of unknown origin. This is important to derive solid models. These local perturbations are not observed in $\nu = 0$ of *gauche*-propanal. Predictions of $\nu_{24} = 1$ of *gauche*-propanal, $\nu = 0$ of *syn*-propanal, and $\nu_{24} = 1$ of *syn*-propanal are indicated by red, green, and blue sticks, respectively.

The quantum number coverage of the tunneling states 0^+ , 0^- , 24^+ and 24^- of *gauche*-propanal of their single state analyses in comparison to the global analysis of $v = 0$ and $v_{24} = 1$ are shown in Figs A30, A31, A32, and A33, respectively. The size of the circles is proportional to the standard deviation $\sigma = (\nu_{obs} - \nu_{calc})/\Delta\nu_{obs}$ of each transitions and is plotted for the quantum numbers of the lower energy level.

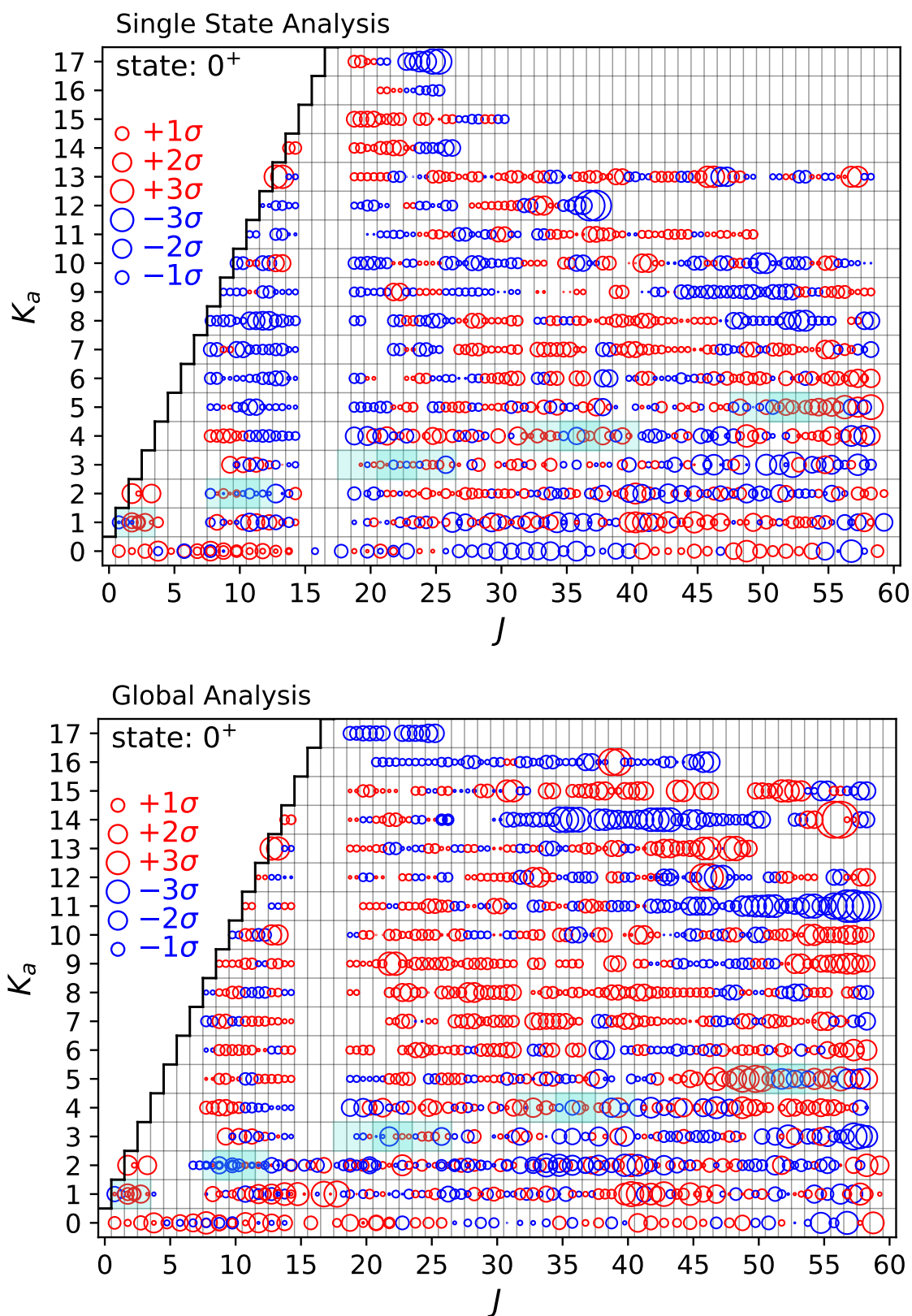


Figure A30: Quantum number coverage of the tunneling state 0^+ of *gauche*-propanal of the single state analysis of $v = 0$ (top row) and of the global analysis of $v = 0$ and $v_{24} = 1$ (bottom row).

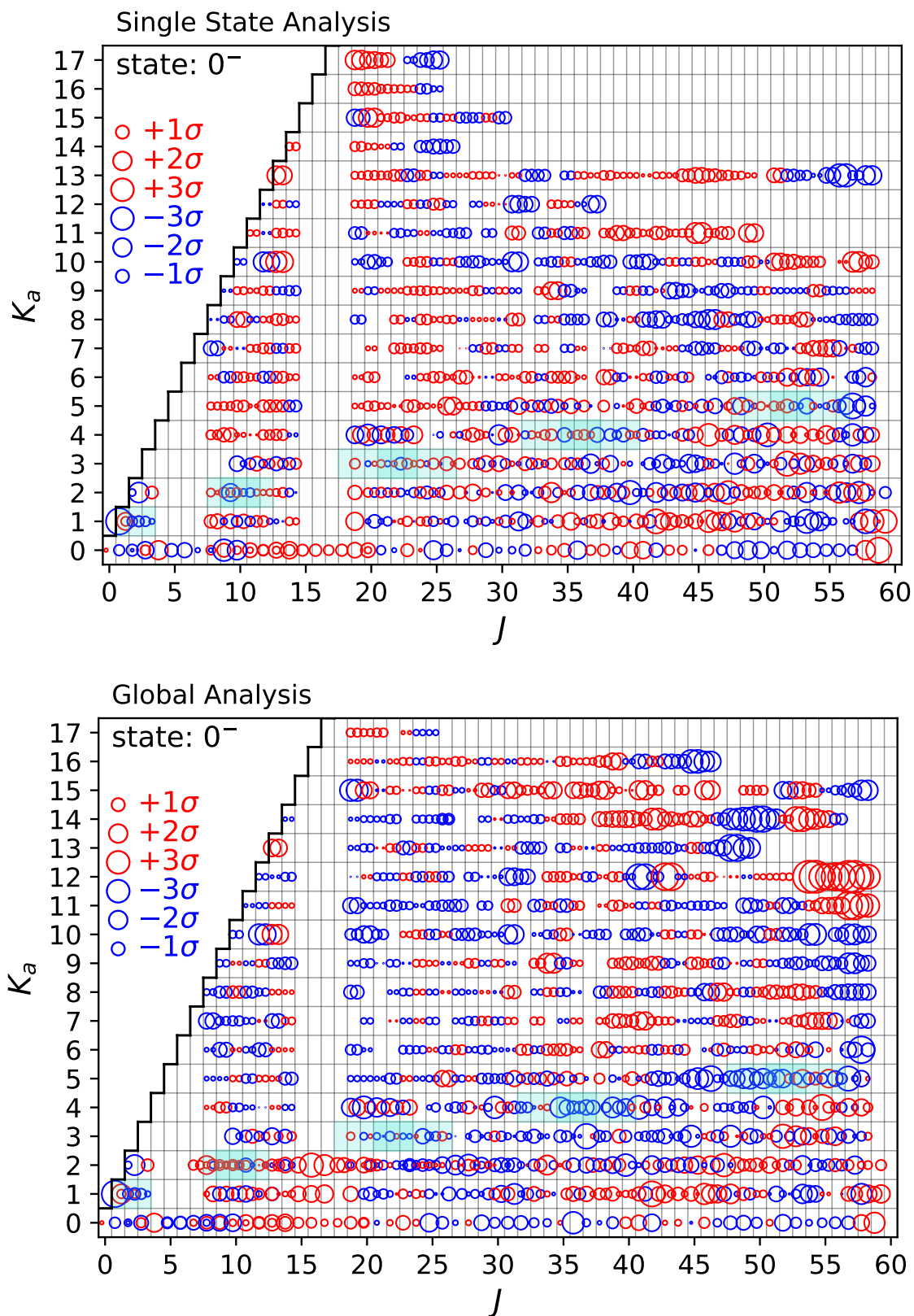


Figure A31: Quantum number coverage of the tunneling state 0^- of *gauche*-propanal of the single state analysis of $v = 0$ (top row) and of the global analysis of $v = 0$ and $v_{24} = 1$ (bottom row).

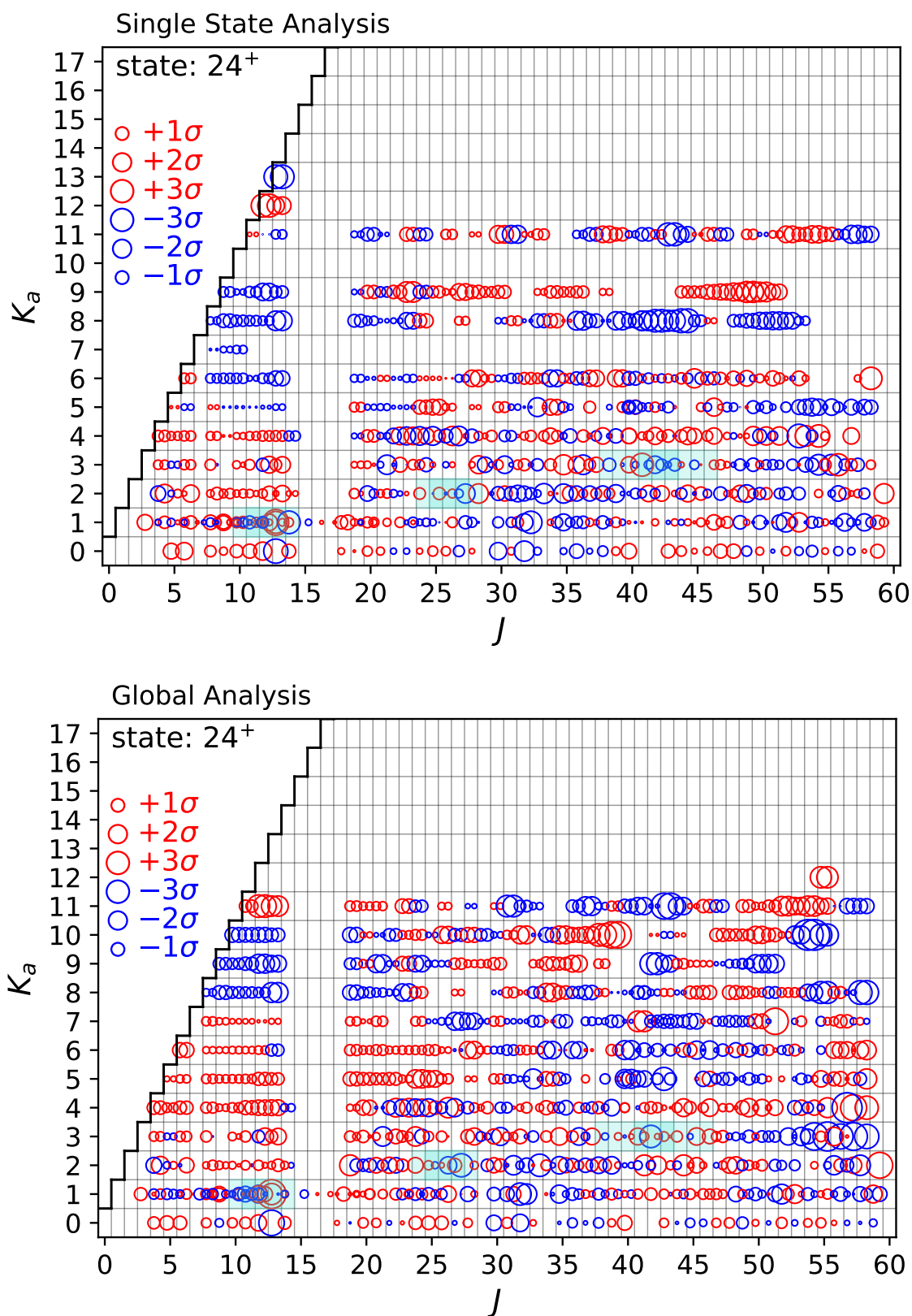


Figure A32: Quantum number coverage of the tunneling state 24^+ of *gauche*-propanal of the single state analysis of $v_{24} = 1$ (top row) and of the global analysis of $v = 0$ and $v_{24} = 1$ (bottom row).

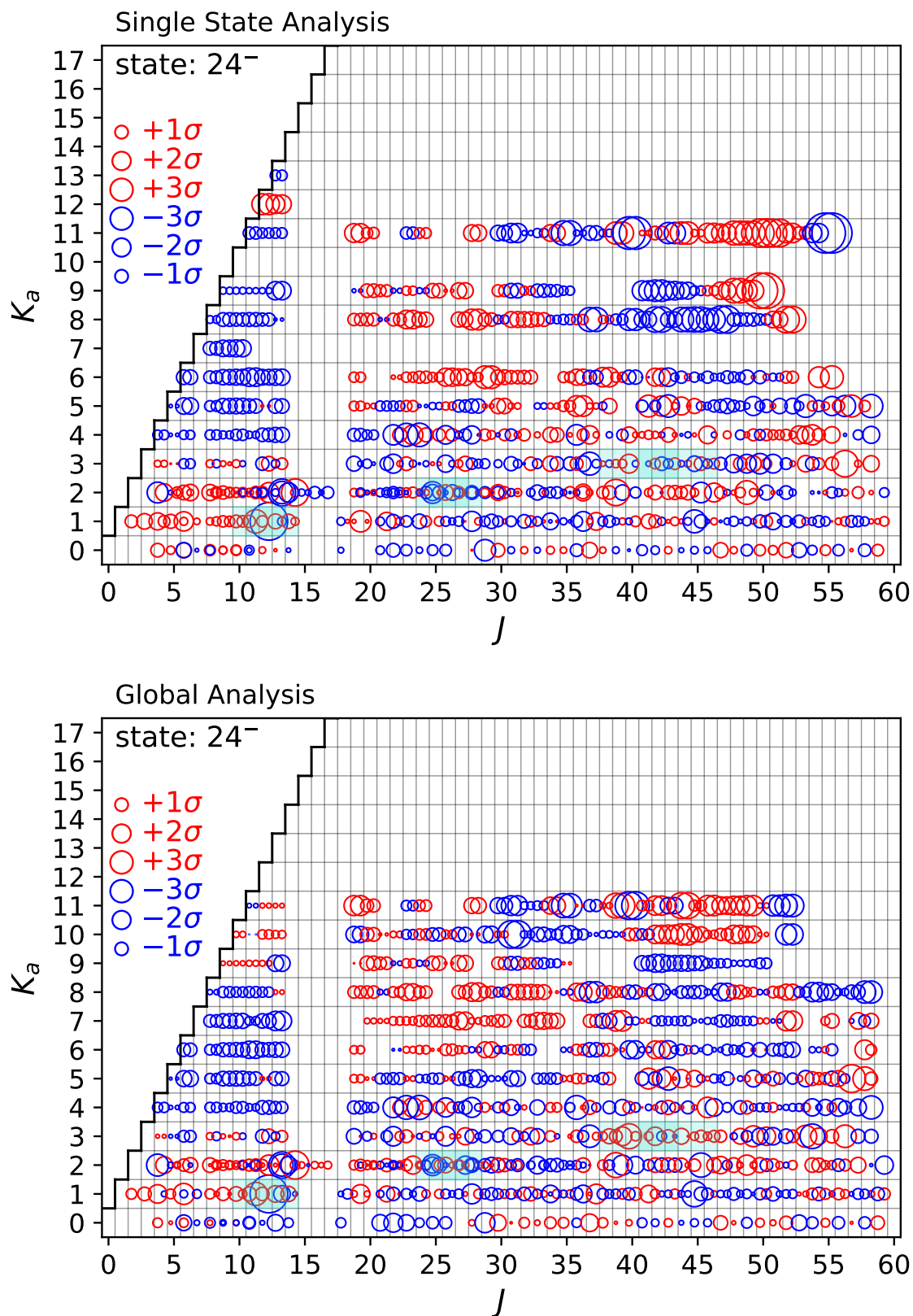


Figure A33: Quantum number coverage of the tunneling state 24^- of *gauche*-propanal of the single state analysis of $v_{24} = 1$ (top row) and of the global analysis of $v = 0$ and $v_{24} = 1$ (bottom row).

References

- [1] https://www.eso.org/public/germany/images/atm_opacity/ [Online; accessed 26-July-2020].
- [2] B. P. Abbott, R. Abbott, and T. D. Abbott, et al. Observation of gravitational waves from a binary black hole merger. *Physical Review Letters*, 116:061102, Feb 2016. <https://doi.org/10.1103/PhysRevLett.116.061102>.
- [3] T. Oka. Observation of the Infrared Spectrum of H_3^+ . *Physical Review Letters*, 45:531–534, Aug 1980. doi:10.1103/PhysRevLett.45.531.
- [4] P. F. Bernath. *Spectra of Atoms and Molecules*. Oxford University Press, New York, 1995. ISBN: 978-0195075984.
- [5] J. M. Hollas. *High Resolution Spectroscopy*. John Wiley & sons Ltd, Chichester, England, second edition, 1998. ISBN: 978-0471974215.
- [6] S. L. Widicus Weaver. Millimeterwave and Submillimeterwave Laboratory Spectroscopy in Support of Observational Astronomy. *Annual Review of Astronomy and Astrophysics*, 57(1):79–112, 2019. doi:10.1146/annurev-astro-091918-104438.
- [7] M.-A. Martin-Drumel, J. van Wijngaarden, O. Zingsheim, F. Lewen, M. E. Harding, S. Schlemmer, and S. Thorwirth. Millimeter- and submillimeter-wave spectroscopy of disulfur dioxide, OSSO. *Journal of Molecular Spectroscopy*, 307:33 – 39, 2015. doi:10.1016/j.jms.2014.11.007.
- [8] M. H. Ordu, O. Zingsheim, A. Belloche, F. Lewen, R. T. Garrod, K. M. Menten, S. Schlemmer, and H. S. P. Müller. Laboratory rotational spectroscopy of isotopic acetone, $\text{CH}_3^{13}\text{C}(\text{O})\text{CH}_3$ and $^{13}\text{CH}_3\text{C}(\text{O})\text{CH}_3$, and astronomical search in Sagittarius B2(N2). *Astronomy & Astrophysics*, 629:A72, 2019. doi:10.1051/0004-6361/201935887.
- [9] G. W. Hills, R. S. Lowe, J. M. Cook, and R. F. Curl Jr. Microwave optical double resonance spectrum of NH_2 . IV. Observation of an unusual rotational transition in ${}^2\text{B}_1$. *The Journal of Chemical Physics*, 68(9):4073–4076, 1978. doi:10.1063/1.436319.
- [10] H. Jones and J. M. Brown. Infrared-microwave double-resonance spectroscopy of the ClO_2 radical: A textbook example. *Journal of Molecular Spectroscopy*, 90(1):222–248, 1981. doi:10.1016/0022-2852(81)90343-X.
- [11] W. Jäger and M. C. L. Gerry. Microwave–millimeter-wave double resonance experiments on Ar–CO. *The Journal of Chemical Physics*, 102(9):3587–3592, 1995. doi:10.1063/1.468581.

- [12] K. N. Crabtree, M.-A. Martin-Drumel, G. G. Brown, S. A. Gaster, T. M. Hall, and M. C. McCarthy. Microwave spectral taxonomy: A semi-automated combination of chirped-pulse and cavity Fourier-transform microwave spectroscopy. The Journal of Chemical Physics, 144(12):124201, 2016. doi:10.1063/1.4944072.
- [13] D. Schmitz, V. A. Shubert, D. Patterson, A. Krin, and M. Schnell. Phase Dependence of Double-Resonance Experiments in Rotational Spectroscopy. The Journal of Physical Chemistry Letters, 6(8):1493–1498, 2015. PMID: 26263157, doi:10.1021/acs.jpcllett.5b00494.
- [14] K. M. Roenitz, B. M. Hays, C. R. Powers, M. N. McCabe, H. Smith, S. L. Widicus Weaver, and S. T. Shipman. AC Stark Effect Observed in a Microwave–Millimeter/Submillimeter Wave Double-Resonance Experiment. The Journal of Physical Chemistry A, 122(30):6321–6327, 2018. PMID: 29993251, doi:10.1021/acs.jpca.8b02116.
- [15] D. Patterson, M. Schnell, and J. M. Doyle. Enantiomer-specific detection of chiral molecules via microwave spectroscopy. Nature, 497:475–477, 2013. doi:10.1038/nature12150.
- [16] S. Gärtner, J. Krieg, A. Klemann, O. Asvany, S. Brünken, and S. Schlemmer. High-Resolution Spectroscopy of CH_2D^+ in a Cold 22-Pole Ion Trap. The Journal of Physical Chemistry A, 117(39):9975–9984, 2013. PMID: 23621684 doi:10.1021/jp400258e.
- [17] C. R. Markus, S. Thorwirth, O. Asvany, and S. Schlemmer. High-resolution double resonance action spectroscopy in ion traps: vibrational and rotational fingerprints of CH_2NH_2^+ . Physical Chemistry Chemical Physics, 21:26406–26412, 2019. doi:10.1039/C9CP05487A.
- [18] S. H. Autler and C. H. Townes. Stark Effect in Rapidly Varying Fields. Physical Review, 100:703–722, 1955. doi:10.1103/PhysRev.100.703.
- [19] C. Cohen-Tannoudji, J. Dupont-Roc, and G. Grynberg. The Dressed Atom Approach, chapter 6, pages 407–514. John Wiley & Sons, Ltd, 2008. doi:10.1002/9783527617197.ch6.
- [20] M. H. Ordu. Rotational spectroscopy of acetone and its mono - ^{13}C isotopologues. PhD thesis, University of Cologne, Germany, 2016.
- [21] A. Belloche, H. S. P. Müller, R. T. Garrod, and K. M. Menten. Exploring molecular complexity with ALMA (EMoCA): Deuterated complex organic

- molecules in Sagittarius B2(N2). *Astronomy & Astrophysics*, 587:A91, 2016. doi:10.1051/0004-6361/201527268.
- [22] Dr. A. Belloche. private communication. July 2020, present adress at: Max-Planck-Institut für Radioastronomie, Auf dem Hügel 69, 53121 Bonn; Email: belloche@mpifr-bonn.mpg.de.
- [23] J. M. Hollis, P. R. Jewell, F. J. Lovas, A. Remijan, and H. Møllendal. Green Bank Telescope Detection of New Interstellar Aldehydes: Propenal and Propanal. *The Astrophysical Journal*, 610(1):L21–L24, jun 2004. doi:10.1086%2F423200.
- [24] D. R. Johnson, F. J. Lovas, C. A. Gottlieb, E. W. Gottlieb, M. M. Litvak, M. Guelin, and P. Thaddeus. Detection of interstellar ethyl cyanide. *The Astrophysical Journal*, 218:370–376, December 1977. doi:10.1086/155691.
- [25] A. Belloche, R. T. Garrod, H. S. P. Müller, K. M. Menten, C. Comito, and P. Schilke. Increased complexity in interstellar chemistry: detection and chemical modeling of ethyl formate and n-propyl cyanide in Sagittarius B2(N) ***. *Astronomy & Astrophysics*, 499(1):215–232, 2009. doi:10.1051/0004-6361/200811550.
- [26] A. Belloche, R. T. Garrod, H. S. P. Müller, and K. M. Menten. Detection of a branched alkyl molecule in the interstellar medium: *iso*-propyl cyanide. *Science*, 345(6204):1584–1587, 2014. doi:10.1126/science.1256678.
- [27] B. A. McGuire, P. B. Carroll, R. A. Loomis, I. A. Finneran, P. R. Jewell, A. J. Remijan, and G. A. Blake. Discovery of the interstellar chiral molecule propylene oxide (CH₃CHCH₂O). *Science*, 352(6292):1449–1452, 2016. doi:10.1126/science.aae0328.
- [28] H. S. P. Müller, S. Thorwirth, D. A. Roth, and G. Winnewisser. The Cologne Database for Molecular Spectroscopy, CDMS. *Astronomy and Astrophysics*, 370(3):L49 – L52, 2001. doi:10.1051/0004-6361:20010367.
- [29] H. S. P. Müller, F. Schlöder, J. Stutzki, and G. Winnewisser. The Cologne Database for Molecular Spectroscopy, CDMS: a useful tool for astronomers and spectroscopists. *Journal of Molecular Structure*, 742(1):215 – 227, 2005. doi:10.1016/j.molstruc.2005.01.027.
- [30] C. P. Endres, S. Schlemmer, P. Schilke, J. Stutzki, and H. S. P. Müller. The Cologne Database for Molecular Spectroscopy, CDMS, in the Virtual Atomic and Molecular Data Centre, VAMDC. *Journal of Molecular Spectroscopy*,

- 327:95 – 104, 2016. *New Visions of Spectroscopic Databases, Volume II*, doi:10.1016/j.jms.2016.03.005.
- [31] L. E. Snyder, D. Buhl, B. Zuckerman, and P. Palmer. Microwave Detection of Interstellar Formaldehyde. *Physical Review Letters*, 22:679–681, 1969. doi:10.1103/PhysRevLett.22.679.
- [32] C. A. Gottlieb. Detection of Acetaldehyde in Sagittarius. In M. A. Gordon and L. E. Snyder, editors, *Molecules in the Galactic Environment*, page 181–186, New York, 1973. Wiley-Interscience.
- [33] M.-A. Martin-Drumel, K. L. K. Lee, A. Belloche, O. Zingsheim, S. Thorwirth, H. S. P. Müller, F. Lewen, R. T. Garrod, K. M. Menten, M. C. McCarthy, and S. Schlemmer. Submillimeter spectroscopy and astronomical searches of vinyl mercaptan, C_2H_3SH . *Astronomy & Astrophysics*, 623:A167, 2019. doi:10.1051/0004-6361/201935032.
- [34] B. E. Turner and A. J. Apponi. Microwave Detection of Interstellar Vinyl Alcohol, $CH_2=CHOH$. *The Astrophysical Journal*, 561(2):L207–L210, 2001. doi:10.1086%2F324762.
- [35] J. C. McGurk, T. G. Schmalz, and W. H. Flygare. Fast passage in rotational spectroscopy: Theory and experiment. *The Journal of Chemical Physics*, 60(11):4181–4188, 1974. doi:10.1063/1.1680886.
- [36] G. G. Brown, B. C. Dian, K. O. Douglass, S. M. Geyer, S. T. Shipman, and B. H. Pate. A broadband Fourier transform microwave spectrometer based on chirped pulse excitation. *Review of Scientific Instruments*, 79(5):053103, 2008. doi:10.1063/1.2919120.
- [37] G. B. Park, A. H. Steeves, K. Kuyanov-Prozument, J. L. Neill, and R. W. Field. Design and evaluation of a pulsed-jet chirped-pulse millimeter-wave spectrometer for the 70–102 GHz region. *The Journal of Chemical Physics*, 135(2):024202, 2011. doi:10.1063/1.3597774.
- [38] N. Wehres, M. Hermanns, B. M. Heyne, K. von Schoeler, M. Töpfer, C. E. Honingh, U. U. Graf, F. Lewen, and S. Schlemmer. Broadband high-resolution rotational spectroscopy using chirped-pulse spectroscopy in combination with low noise amplifiers. Unpublished, to be submitted soon.
- [39] S. S. Butcher and E. B. Wilson Jr. Microwave Spectrum of Propionaldehyde. *The Journal of Chemical Physics*, 40(6):1671–1678, 1964. doi:10.1063/1.1725377.

- [40] J. Randell, A. P. Cox, K. W. Hillig, M. Imachi, M. S. LaBarge, and R. L. Kuczkowski. Cis and Gauche Propanal: Microwave Spectra and Molecular Structures. Zeitschrift für Naturforschung A, 43(3):271 – 276, 1988. doi:10.1515/zna-1988-0314.
- [41] J. Randell, J. A. Hardy, and A. P. Cox. The microwave spectrum and potential function of propanal. Journal of the Chemical Society, Faraday Transactions 2, 84:1199–1212, 1988. doi:10.1039/F29888401199.
- [42] J. A. Hardy, A. P. Cox, E. Fliege, and H. Dreizler. Determination of a High Potential Barrier Hindering Internal Rotation from the Ground State Spectrum The Methylbarrier of cis-Propanal. Zeitschrift für Naturforschung A, 37(9):1035 – 1037, 1982. doi:10.1515/zna-1982-0910.
- [43] J. Demaison, H. Maes, B. P. Van Eijck, G. Wlodarczak, and M. C. Lasne. Determination of the moment of inertia of methyl groups: Analysis of the millimeterwave spectra of *cis*-propanal and methylthioethyne. Journal of Molecular Spectroscopy, 125(1):214 – 224, 1987. doi:10.1016/0022-2852(87)90208-6.
- [44] J. Randell, A. P. Cox, and H. Dreizler. Gauche Propanal: Microwave Spectrum and Methyl Barrier. Zeitschrift für Naturforschung A, 42(9):957 – 962, 1987. doi:10.1515/zna-1987-0908.
- [45] J. R. Durig, D. A. C. Compton, and A. Q. McArver. Low frequency vibrational spectra, methyl torsional potential functions, and internal rotational potential of propanal. The Journal of Chemical Physics, 73(2):719–724, 1980. doi:10.1063/1.440173.
- [46] G. A. Guirgis, B. R. Drew, T. K. Gounev, and J. R. Durig. Conformational stability and vibrational assignment of propanal. Spectrochimica Acta Part A: Molecular and Biomolecular Spectroscopy, 54(1):123 – 143, 1998. doi:10.1016/S1386-1425(97)00200-X.
- [47] H. M. Pickett and D. G. Scroggin. Microwave spectrum and internal rotation potential of propanal. The Journal of Chemical Physics, 61(10):3954–3958, 1974. doi:10.1063/1.1681688.
- [48] J. K. Jørgensen, M. H. D. van der Wiel, A. Coutens, J. M. Lykke, H. S. P. Müller, E. F. van Dishoeck, H. Calcutt, P. Bjerke, T. L. Bourke, M. N. Drozdovskaya, C. Favre, E. C. Fayolle, R. T. Garrod, S. K. Jacobsen, K. I. Öberg, M. V. Persson, and S. F. Wampfler. The ALMA Protostellar Interferometric Line Survey (PILS) - First results from an unbiased submillimeter wavelength line survey of the Class

- 0 protostellar binary IRAS 16293-2422 with ALMA. *Astronomy & Astrophysics*, 595:A117, 2016. doi:10.1051/0004-6361/201628648.
- [49] J. M. Lykke, A. Coutens, J. K. Jørgensen, M. H. D. van der Wiel, R. T. Garrod, H. S. P. Müller, P. Bjerkeli, T. L. Bourke, H. Calcutt, M. N. Drozdovskaya, C. Favre, E. C. Fayolle, S. K. Jacobsen, K. I. Öberg, M. V. Persson, E. F. van Dishoeck, and S. F. Wampfler. The ALMA-PILS survey: First detections of ethylene oxide, acetone and propanal toward the low-mass protostar IRAS 16293-2422. *Astronomy & Astrophysics*, 597:A53, 2017. doi:10.1051/0004-6361/201629180.
- [50] O. Zingsheim, H. S. P. Müller, F. Lewen, J. K. Jørgensen, and S. Schlemmer. Millimeter and submillimeter wave spectroscopy of propanal. *Journal of Molecular Spectroscopy*, 342:125 – 131, 2017. Spectroscopy of Large Amplitude Vibrational Motions, on the Occasion of Jon Hougen’s 80th Birthday - Part I, doi:10.1016/j.jms.2017.07.008.
- [51] W. Gordy and R. L. Cook. *Microwave Molecular Spectra*. Wiley-Interscience, 1984. ISBN: 978-0471086819.
- [52] C. H. Townes and A. L. Schawlow. *Microwave Spectroscopy*. Dover Publications, Inc, 1975. ISBN: 978-0486617985.
- [53] S. C. Wang. On the Asymmetrical Top in Quantum Mechanics. *Physical Review*, 34:243–252, 1929. doi:10.1103/PhysRev.34.243.
- [54] D. Kivelson and E. B. Wilson Jr. Approximate Treatment of the Effect of Centrifugal Distortion on the Rotational Energy Levels of Asymmetric-Rotor Molecules. *The Journal of Chemical Physics*, 20(10):1575–1579, 1952. doi:10.1063/1.1700219.
- [55] J. K. G. Watson. Centrifugal Corrections for Asymmetric-Top Molecules. *The Journal of Chemical Physics*, 45(4):1360–1361, 1966. doi:10.1063/1.1727763.
- [56] J. K. G. Watson. Determination of Centrifugal Distortion Coefficients of Asymmetric-Top Molecules. *The Journal of Chemical Physics*, 46(5):1935–1949, 1967. doi:10.1063/1.1840957.
- [57] G. Winnewisser. Millimeter Wave Rotational Spectrum of HSSH and DSSD. II. Anomalous K Doubling Caused by Centrifugal Distortion in DSSD. *The Journal of Chemical Physics*, 56(6):2944–2954, 1972. doi:10.1063/1.1677629.

- [58] B. P. van Eijck. Reformulation of quartic centrifugal distortion Hamiltonian. Journal of Molecular Spectroscopy, 53(2):246 – 249, 1974. doi:10.1016/0022-2852(74)90129-5.
- [59] H. S. P. Müller, O. Zingsheim, N. Wehres, J.-U. Grabow, F. Lewen, and S. Schlemmer. Rotational Spectroscopy of the Lowest Energy Conformer of 2-Cyanobutane. The Journal of Physical Chemistry A, 121(38):7121–7129, 2017. PMID: 28862854, doi:10.1021/acs.jpca.7b06072.
- [60] D. T. Petkie, T. M. Goyette, P. Helminger, H. M. Pickett, and F. C. De Lucia. The Energy Levels of the $\nu_5/2\nu_9$ Dyad of HNO_3 from Millimeter and Submillimeter Rotational Spectroscopy. Journal of Molecular Spectroscopy, 208(1):121 – 135, 2001. doi:10.1006/jmsp.2001.8367.
- [61] Z. Kisiel, L. Pszczólkowski, B. J. Drouin, C. S. Brauer, S. Yu, and J. C. Pearson. The rotational spectrum of acrylonitrile up to 1.67THz. Journal of Molecular Spectroscopy, 258(1):26 – 34, 2009. doi:10.1016/j.jms.2009.08.011.
- [62] H. S. P. Müller, E. A. Cohen, and D. Christen. The Rotational Spectrum of ClClO_2 in Its $\nu_4 = 1$ and $\nu_6 = 1$ Vibrationally Excited States: An Example of Strong Coriolis Interaction. Journal of Molecular Spectroscopy, 216(2):335 – 344, 2002. doi:10.1006/jmsp.2002.8629.
- [63] B. J. Drouin. Practical uses of SPFIT. Journal of Molecular Spectroscopy, 340:1 – 15, 2017. doi:10.1016/j.jms.2017.07.009.
- [64] H. S. P. Müller, L. R. Brown, B. J. Drouin, J. C. Pearson, I. Kleiner, R. L. Sams, K. Sung, M. H. Ordu, and F. Lewen. Rotational spectroscopy as a tool to investigate interactions between vibrational polyads in symmetric top molecules: Low-lying states $\nu_8 \leq 2$ of methyl cyanide, CH_3CN . Journal of Molecular Spectroscopy, 312:22 – 37, 2015. doi:10.1016/j.jms.2015.02.009.
- [65] H. M. Pickett. Vibration—Rotation Interactions and the Choice of Rotating Axes for Polyatomic Molecules. The Journal of Chemical Physics, 56(4):1715–1723, 1972. doi:10.1063/1.1677430.
- [66] J. D. Swalen and J. A. Ibers. Potential Function for the Inversion of Ammonia. The Journal of Chemical Physics, 36(7):1914–1918, 1962. doi:10.1063/1.1701290.
- [67] W. J. Orville-Thomas, editor. Internal Rotation in Molecules. Wiley-Interscience, 1974. ISBN: 9780471657071.

- [68] I. Kleiner. Asymmetric-top molecules containing one methyl-like internal rotor: Methods and codes for fitting and predicting spectra. Journal of Molecular Spectroscopy, 260(1):1 – 18, 2010. doi:10.1016/j.jms.2009.12.011.
- [69] I. Kleiner. Spectroscopy of Interstellar Internal Rotors: An Important Tool for Investigating Interstellar Chemistry. ACS Earth and Space Chemistry, 3(9):1812–1842, 2019. doi:10.1021/acsearthspacechem.9b00079.
- [70] C. C. Lin and J. D. Swalen. Internal Rotation and Microwave Spectroscopy. Reviews of Modern Physics, 31:841–892, 1959. doi:10.1103/RevModPhys.31.841.
- [71] P. Groner. Effective rotational Hamiltonian for molecules with internal rotors: Principles, theory, applications and experiences. Journal of Molecular Spectroscopy, 278:52 – 67, 2012. doi:10.1016/j.jms.2012.06.006.
- [72] P. Groner. Effective rotational Hamiltonian for molecules with two periodic large-amplitude motions. The Journal of Chemical Physics, 107(12):4483–4498, 1997. doi:10.1063/1.474810.
- [73] Oliver Zingsheim, Luis Bonah, Frank Lewen, Sven Thorwirth, Holger S.P. Müller, and Stephan Schlemmer. Millimeter-millimeter-wave double-modulation double-resonance spectroscopy. J. Mol. Spectrosc., 381:111519, 2021.
- [74] J.-B. Brubach, L. Manceron, M. Rouzières, O. Pirali, D. Balcon, F. Kwabia-Tchana, V. Boudon, M. Tudorie, T. Huet, A. Cuisset, and P. Roy. Performance of the AILES THz-Infrared beamline at SOLEIL for High resolution spectroscopy. In WIRMS 2009, volume 1214 of AIP Conference Proceedings, pages 81–84, 2010. doi:10.1063/1.3326356.
- [75] O. Pirali, V. Boudon, J. Oomens, and M. Vervloet. Rotationally resolved infrared spectroscopy of adamantane. The Journal of Chemical Physics, 136(2):024310, 2012. doi:10.1063/1.3666853.
- [76] O. Pirali, M. Goubet, T. R. Huet, R. Georges, P. Soulard, P. Asselin, J. Courbe, P. Roy, and M. Vervloet. The far infrared spectrum of naphthalene characterized by high resolution synchrotron FTIR spectroscopy and anharmonic DFT calculations. Physical Chemistry Chemical Physics, 15:10141–10150, 2013. doi:10.1039/C3CP44305A.
- [77] Dr. M.-A. Martin-Drumel. private communication. Jan. 2020, present adress at: Institut des Sciences Moléculaires d’Orsay (ISMO), CNRS, Univ. Paris-Sud, Université Paris-Saclay, F-91405 Orsay (France); Email: marie-aline.martin@universite-paris-saclay.fr.

- [78] V.-M. Horneman, R. Anttila, S. Alanko, and J. Pietilä. Transferring calibration from CO₂ laser lines to far infrared water lines with the aid of the ν_2 band of OCS and the ν_2 , $\nu_1-\nu_2$, and $\nu_1+\nu_2$ bands of ¹³CS₂: Molecular constants of ¹³CS₂. Journal of Molecular Spectroscopy, 234(2):238–254, 2005. doi:10.1016/j.jms.2005.09.011.
- [79] F. Matsushima, H. Odashima, T. Iwasaki, S. Tsunekawa, and K. Takagi. Frequency measurement of pure rotational transitions of H₂O from 0.5 to 5 THz. Journal of Molecular Structure, 352-353:371–378, 1995. doi:10.1016/0022-2860(94)08531-1.
- [80] F. Matsushima, N. Tomatsu, T. Nagai, Y. Moriwaki, and K. Takagi. Frequency measurement of pure rotational transitions in the $\nu_2 = 1$ state of H₂O. Journal of Molecular Spectroscopy, 235(2):190–195, 2006. doi:10.1016/j.jms.2005.11.003.
- [81] N. A. Seifert, I. A. Finneran, C. Perez, D. P. Zaleski, J. L. Neill, A. L. Steber, R. D. Suenram, A. Lesarri, S. T. Shipman, and B. H. Pate. AUTOFIT, an automated fitting tool for broadband rotational spectra, and applications to 1-hexanal. Journal of Molecular Spectroscopy, 312:13 – 21, 2015. doi:10.1016/j.jms.2015.02.003.
- [82] M.-A. Martin-Drumel, M. C. McCarthy, D. Patterson, B. A. McGuire, and K. N. Crabtree. Automated microwave double resonance spectroscopy: A tool to identify and characterize chemical compounds. The Journal of Chemical Physics, 144(12):124202, 2016. doi:10.1063/1.4944089.
- [83] Z. Kisiel. Spectroscopy from Space. Kluwer Academic Publishers, Dordrecht, 2001. ISBN: 978-0792369936.
- [84] H. M. Pickett. The fitting and prediction of vibration-rotation spectra with spin interactions. Journal of Molecular Spectroscopy, 148(2):371 – 377, 1991. doi:10.1016/0022-2852(91)90393-O.
- [85] J. T. Hougen, I. Kleiner, and M. Godefroid. Selection Rules and Intensity Calculations for a C_s Asymmetric Top Molecule Containing a Methyl Group Internal Rotor. Journal of Molecular Spectroscopy, 163(2):559 – 586, 1994. doi:10.1006/jmsp.1994.1047.
- [86] V. V. Ilyushin, Z. Kisiel, L. Pszczółkowski, H. Mäder, and J. T. Hougen. A new torsion-rotation fitting program for molecules with a sixfold barrier: Application to the microwave spectrum of toluene. Journal of Molecular Spectroscopy, 259(1):26 – 38, 2010. doi:10.1016/j.jms.2009.10.005.

- [87] H. Hartwig and H. Dreizler. The Microwave Spectrum of trans-2,3-Dimethyloxirane in Torsional Excited States. Zeitschrift für Naturforschung A, 51(8):923–932, 1996. doi:10.1515/zna-1996-0807.
- [88] P. Groner. Large-amplitude motion tunneling parameters in effective rotational Hamiltonians from rotation-internal rotation theory. Journal of Molecular Spectroscopy, 156(1):164 – 189, 1992. doi:10.1016/0022-2852(92)90101-S.
- [89] P. Groner, S. Albert, E. Herbst, and F. C. De Lucia. Dimethyl Ether: Laboratory Assignments and Predictions through 600 GHz. The Astrophysical Journal, 500(2):1059–1063, 1998. doi:10.1086%2F305757.
- [90] W. Łodyga, M. Kręglewski, P. Pracna, and Š. Urban. Advanced graphical software for assignments of transitions in rovibrational spectra. Journal of Molecular Spectroscopy, 243(2):182 – 188, 2007. PRAHA2006, The 19th International Conference on High Resolution Molecular Spectroscopy, doi:10.1016/j.jms.2007.02.004.
- [91] M. Kręglewski and W. Łodyga. Assigning the vibration-rotation spectra using the lww program package. In Conference: 71st International Symposium on Molecular Spectroscopy, pages 1–1, 2016. doi:10.15278/isms.2016.TF07.
- [92] Dr. S. Thorwirth. private communication. December 2018, present address at: I. Physikalisches Institut, Universität zu Köln, Zùlpicher Straße 77, 50937 Köln; Email: sthorwirth@ph1.uni-koeln.de.
- [93] D. Christen and H. S. P. Müller. The millimeter wave spectrum of aGg’ ethylene glycol: The quest for higher precision. Physical Chemistry Chemical Physics, 5:3600–3605, 2003. doi:10.1039/B304566H.
- [94] A. P. Cox, J. A. Hardy, and J. Randell. The microwave spectrum and potential function of nitrosoethane, CH₃CH₂NO. Journal of Molecular Structure, 352-353:299 – 307, 1995. Molecular Structure and Spectroscopy, doi:10.1016/0022-2860(94)08514-I.
- [95] H. Møllendal, L. Margulès, R. A. Motiyenko, N. W. Larsen, and J.-C. Guillemin. Rotational Spectrum and Conformational Composition of Cyanoacetaldehyde, a Compound of Potential Prebiotic and Astrochemical Interest. The Journal of Physical Chemistry A, 116(16):4047–4056, 2012. PMID: 22432569, doi:10.1021/jp212306z.
- [96] R. A. Motiyenko, L. Margulès, M. Goubet, H. Møllendal, A. Konovalov, and J.-C. Guillemin. First High Resolution Spectroscopic Studies and Ab Initio Calcula-

- tions of Ethanetellurol. The Journal of Physical Chemistry A, 114(8):2794–2798, 2010. PMID: 20136116, doi:10.1021/jp912082b.
- [97] H. Møllendal, S. Samdal, and J.-C. Guillemin. Rotational Spectrum, Conformational Composition, Intramolecular Hydrogen Bonding, and Quantum Chemical Calculations of Mercaptoacetonitrile (HSCH₂CN), a Compound of Potential Astrochemical Interest. The Journal of Physical Chemistry A, 120(12):1992–2001, 2016. PMID: 26974178, doi:10.1021/acs.jpca.6b01600.
- [98] M.-A. Martin-Drumel, C. P. Endres, O. Zingsheim, T. Salomon, J. van Wijngaarden, O. Pirali, S. Gruet, F. Lewen, S. Schlemmer, M. C. McCarthy, and S. Thorwirth. The SOLEIL view on sulfur rich oxides: The S₂O bending mode ν_2 at 380cm⁻¹ and its analysis using an Automated Spectral Assignment Procedure (ASAP). Journal of Molecular Spectroscopy, 315:72 – 79, 2015. Spectroscopy with Synchrotron Radiation, doi:10.1016/j.jms.2015.02.014.
- [99] N. Wehres, J. Maßen, K. Borisov, B. Schmidt, F. Lewen, U. U. Graf, C. E. Honingh, D. R. Higgins, and S. Schlemmer. A laboratory heterodyne emission spectrometer at submillimeter wavelengths. Physical Chemistry Chemical Physics, 20:5530–5544, 2018. doi:10.1039/C7CP06394F.
- [100] N. Wehres, B. Heyne, F. Lewen, M. Hermanns, B. Schmidt, C. Endres, U. U. Graf, D. R. Higgins, and S. Schlemmer. 100 GHz Room-Temperature Laboratory Emission Spectrometer. Proceedings of the International Astronomical Union, 13(S332):332–345, 2017. doi:10.1017/S1743921317007803.
- [101] Prof. Dr. S. Schlemmer. private communication. 2018-2020, present adress at: I. Physikalisches Institut, Universität zu Köln, Zùlpicher Straße 77, 50937 Köln; Email: schlemmer@ph1.uni-koeln.de.
- [102] H. M. Pickett, E. A. Cohen, B. J. Drouin, and J. C. Pearson. Submillimeter, Millimeter, and Microwave Spectral Line Catalog. <https://spec.jpl.nasa.gov/ftp/pub/catalog/doc/catdoc.pdf>, 2003. [Online; accessed 21-July-2020].
- [103] P. Groner. The latest revision of the ERHAM code. <http://www.ifpan.edu.pl/~kisiel/introt/erham/wh01.pdf>, 2013. [Online; accessed 21-July-2020].
- [104] P. R. Bunker and P. Jensen. Molecular Symmetry and Spectroscopy. NRC Research Press, Ottawa, 2nd edition, 1998. ISBN: 978-0660175195.
- [105] P. R. Bunker and P. Jensen. Fundamentals of Molecular Symmetry. IOP Publishing, Bristol, 2004. ISBN: 978-0750309417.

- [106] O. Zingsheim, M.-A. Martin-Drumel, S. Thorwirth, S. Schlemmer, C. A. Gottlieb, J. Gauss, and M. C. McCarthy. Germanium Dicarbide: Evidence for a T-Shaped Ground State Structure. The Journal of Physical Chemistry Letters, 8(16):3776–3781, 2017. PMID: 28742354, doi:10.1021/acs.jpcclett.7b01544.
- [107] T. Möller, I. Bernst, D. Panoglou, D. Muders, V. Ossenkopf, M. Röllig, and P. Schilke. Modeling and Analysis Generic Interface for eXternal numerical codes (MAGIX). Astronomy & Astrophysics, 549:A21, 2013. doi:10.1051/0004-6361/201220063.
- [108] C. M. Western. PGOPHER: A program for simulating rotational, vibrational and electronic spectra. Journal of Quantitative Spectroscopy and Radiative Transfer, 186:221 – 242, 2017. doi:10.1016/j.jqsrt.2016.04.010.
- [109] C. M. Western and B. E. Billinghurst. Automatic assignment and fitting of spectra with pgopher. Physical Chemistry Chemical Physics, 19:10222–10226, 2017. doi:10.1039/C7CP00266A.
- [110] C. M. Western and B. E. Billinghurst. Automatic and semi-automatic assignment and fitting of spectra with PGOPHER. Physical Chemistry Chemical Physics, 21:13986–13999, 2019. doi:10.1039/C8CP06493H.
- [111] Z. Kisiel, L. Pszczółkowski, I. R. Medvedev, M. Winnewisser, F. C. De Lucia, and E. Herbst. Rotational spectrum of *trans-trans* diethyl ether in the ground and three excited vibrational states. Journal of Molecular Spectroscopy, 233(2):231 – 243, 2005. doi:10.1016/j.jms.2005.07.006.
- [112] D. Schmitz, V. A. Shubert, T. Betz, and M. Schnell. Exploring the conformational landscape of menthol, menthone, and isomenthone: a microwave study. Frontiers in Chemistry, 3:15, 2015. doi:10.3389/fchem.2015.00015.
- [113] D. P. Zaleski and K. Prozument. Automated assignment of rotational spectra using artificial neural networks. The Journal of Chemical Physics, 149(10):104106, 2018. doi:10.1063/1.5037715.

List of Figures

1	Electromagnetic spectrum and transmission of earth atmosphere.	1
2	EMoCA survey in the region of 95.64–96.34 GHz.	4
3	The homologous series of alkanales.	5
4	Calculated potential energy function of propanal with respect to the aldehyde group rotation.	8
5	Detection of propanal in space in the ALMA-PILS survey.	9
6	Schematic potential energy function of a diatomic molecule.	12
7	Schematic correlation diagram for labeling asymmetric rotor energy levels.	18
8	Schematic energy level diagram of a nearly prolate rotor molecule.	23
9	Reduced energy diagram of a nearly prolate rotor molecule.	24
10	Autler-Townes effect of a 3-level system.	32
11	Autler-Townes effect for off-resonant pumping.	33
12	Threefold degenerate potential function for internal rotation.	37
13	(Sub-)Millimeter wavelength absorption spectrometer.	42
14	Conventional vs. DR measurement.	43
15	Autler-Townes effect in 2D DR spectra of <i>syn</i> -propanal.	45
16	Conventional vs DR vs DM-DR measurements.	47
17	FIR spectra of propanal.	50
18	Schematic of the iterative assignment, fitting, and predicting procedure.	51
19	Visualized steps of a specific assignment strategy.	53
20	Schematic workflow of SPFIT/SPCAT suite of programs and ERHAM.	56
21	MMW spectrum of propanal around 178.4 GHz.	60
22	Vibrational energy levels of <i>syn</i> -propanal below 500 cm^{-1}	62
23	First assignments in the MMW region of $\nu_{24} = 1$ of <i>syn</i> -propanal.	66
24	<i>Q</i> -branch <i>b</i> -type transitions of $\nu_{24} = 1$ of <i>syn</i> -propanal.	67
25	FIR spectrum of the fundamental band ν_{24} of <i>syn</i> -propanal.	69
26	Oblate pairing of transitions of $\nu_{23} = 1$ and $\nu_{24} = 1$ of <i>syn</i> -propanal.	71
27	Satellite spectra of <i>syn</i> -propanal.	73
28	Fortrat diagram of <i>gauche</i> -propanal in the W-band region.	79
29	Reduced energy diagram of $\nu = 0$ of <i>gauche</i> -propanal.	80
30	Typical rotational fingerprints of $\nu = 0$ of <i>gauche</i> -propanal.	82
31	Loomis Wood plots of <i>gauche</i> -propanal showing qR series with $K_a = 4$	83
32	Reduced energy diagram for $K_a = 2, 3$ of $\nu = 0$ of <i>gauche</i> -propanal.	85
33	Typical rotational fingerprint of $\nu_{24} = 1$ of <i>gauche</i> -propanal.	90
34	Reduced energy diagram of $\nu_{24} = 1$ of <i>gauche</i> -propanal.	91
35	Loomis Wood plots of <i>gauche</i> -propanal showing qR series with $K_a = 12$ (0^+ and 0^-) and $K_a = 7$ (24^+).	94

36	Reduced energy diagram of $v = 0$ and $v_{24} = 1$ of <i>gauche</i> -propanal. . . .	95
37	Reduced energy diagram of the $\Delta K_a = 5$ interaction in <i>gauche</i> -propanal.	96
38	Perturbed transitions of the $\Delta K_a = 5$ interaction in <i>gauche</i> -propanal. .	98
39	Reduced energy diagram of the $\Delta K_a = 4$ interaction in <i>gauche</i> -propanal.	99
40	Possible interactions between $v_{23} = 1$, $v_{15} = 1$, and $v_{24} = 2$ of <i>syn</i> - propanal.	104
41	Reduced energy diagram of $v = 0$, $v_{24} = 1$, and $v_{24} = 2$ of <i>gauche</i> - propanal.	107
42	Broadband DM-DR measurement of $v = 0$ of <i>gauche</i> -propanal.	114
A1	Schematic energy level diagram of two vibrational states with internal rotation.	121
A2	Internal rotation of <i>syn</i> -propanal with numbered hydrogen atoms. . . .	122
A3	Energy levels of <i>syn</i> -propanal for the rigid rotor assumption and with feasible internal rotation.	126
A4	DM-DR W-band absorption spectrometer.	134
A5	Schematic visualization of a typical quartet of lines (and a qR series). .	135
A6	Typical K_a structure of near prolate asymmetric-top molecules.	136
A7	DR measurements of <i>syn</i> -propanal for all four possible energy level ar- rangements.	137
A8	Simulated DM-DR line shapes for different output powers of the pump source P_{out}	138
A9	Simulated DM-DR line shapes for different detunings of the pump fre- quency δ	139
A10	Screenshot of the user interface of the measurement software.	140
A11	Calibration of the FIR data.	141
A12	Assignments of FIR bands of <i>syn</i> - and <i>gauche</i> -propanal.	141
A13	Calculated stick spectrum of $v = 0$ of <i>syn</i> -propanal up to 1.5 THz. . . .	142
A14	Frequency and quantum number coverage of first iterations of the anal- ysis of $v_{24} = 1$ of <i>syn</i> -propanal.	143
A15	Quantum number coverage of $v = 0$ of <i>syn</i> -propanal.	143
A16	Quantum number coverage of $v_{24} = 1$ of <i>syn</i> -propanal.	144
A17	Quantum number coverage of $v_{23} = 1$ of <i>syn</i> -propanal.	144
A18	Quantum number coverage of $v_{15} = 1^*$ of <i>syn</i> -propanal.	145
A19	Quantum number coverage of $v_{24} = 2^*$ of <i>syn</i> -propanal.	145
A20	Quantum number coverage of $v_{24} = v_{23} = 1^*$ of <i>syn</i> -propanal.	146
A21	Oblate pairing of transitions of $v_{23} = 1$ of <i>syn</i> -propanal.	147
A22	Calculated stick spectrum of $v = 0$ of <i>gauche</i> -propanal up to 1.5 THz. .	148
A23	Satellite spectrum of <i>gauche</i> -propanal in the W-band region.	149

A24	Statistical analysis of deviations of observed and predicted transition frequencies of <i>gauche</i> -propanal.	150
A25	Reduced energy diagram for $K_a = 2$ of $v = 0$ of <i>gauche</i> -propanal.	151
A26	Large Fortrat diagram of <i>gauche</i> -propanal.	152
A27	Contour plot of mixing coefficients of <i>gauche</i> -propanal.	153
A28	DM-DR measurements of <i>c</i> -type transitions in <i>gauche</i> -propanal.	154
A29	Single perturbed energy level of $v_{24} = 1$ of <i>gauche</i> -propanal.	155
A30	Quantum number coverage of the tunneling state 0^+ of <i>gauche</i> -propanal.	157
A31	Quantum number coverage of the tunneling state 0^- of <i>gauche</i> -propanal.	158
A32	Quantum number coverage of the tunneling state 24^+ of <i>gauche</i> -propanal.	159
A33	Quantum number coverage of the tunneling state 24^- of <i>gauche</i> -propanal.	160

List of Tables

1	Selection rules of asymmetric-top molecules for the quasi-good quantum numbers K_a and K_c	22
3	Spectroscopic parameters of $v = 0$, $v_{24} = 1$ as well as $v_{23} = 1$ of <i>syn</i> -propanal.	64
4	Spectroscopic parameters (MHz) of $v_{24} = 2^*$, $v_{15} = 1^*$, and $v_{23} = v_{24} = 1^*$ of <i>syn</i> -propanal.	76
5	Observed spectroscopic parameters (MHz) of <i>syn</i> -propanal in comparison to quantum chemical calculations.	77
6	Spectroscopic parameters of $v = 0$ of <i>gauche</i> -propanal.	87
7	Spectroscopic parameters of $v_{24} = 1$ of <i>gauche</i> -propanal.	93
8	Spectroscopic parameters of the global fit of $v = 0$ and $v_{24} = 1$ of <i>gauche</i> -propanal.	100
9	Summary of the analyses of rotational spectra of vibrational states of <i>syn</i> -propanal.	103
10	Selected overview of analyses of molecules with two stable degenerate <i>gauche</i> -configurations.	108
11	Recommended next steps for deciphering molecular fingerprints of <i>syn</i> -propanal.	111
12	Possible next steps for deciphering molecular fingerprints of <i>gauche</i> -propanal.	112
A1	Character table of <i>syn</i> -propanal for the rigid rotor assumption.	123
A2	Character table of <i>syn</i> -propanal with allowed internal rotation.	123
A3	Product table of $C_{3v}(M)$	124
A4	Equivalent rotations of <i>syn</i> -propanal.	125
A5	Correlation table of <i>syn</i> -propanal for the rigid rotor assumption and with allowed internal rotation.	125
A6	Overview of the six possible representations.	127
A7	Character Table for the Four Group $V(a, b, c)$	127
A8	Character Table for the Point Group C_3^a	127
A9	Character Table for the Point Group C_s	127
A10	Character Table for the Point Group C_1	128
A11	MMW Relative Intensity Measurements of $v = 0$ and $v_{24} = 1$ of <i>gauche</i> -propanal.	128

Acknowledgments

These are a rather long acknowledgments, but there are many people I would like to thank from the bottom of my heart...

First of all, thank you **Prof. Dr. Stephan Schlemmer** for being the supervisor and first reviewer of this thesis. Thanks also to **Prof. Dr. Laurent Margulès** for being the second reviewer, **Prof. Dr. Mathias Schäfer** for being the chair of the thesis defense committee and **Dr. Holger S. P. Müller** for taking the job as a minutes taker.

This work is financially supported by the Collaborative Research Centre 956, project B3, and the Gerätezentrum “Cologne Center for Terahertz Spectroscopy”, both funded by the Deutsche Forschungsgemeinschaft (DFG). I would like to acknowledge the general support from the Bonn-Cologne Graduate School of Physics and Astronomy (BCGS) in addition to a financial one through the H2 stipend and also giving me the chance to attend conferences/summer schools, SFB 956 for financing the student exchange to Boston and DAAD PPP for the trip to Hiroshima. I acknowledge the SOLEIL facility for provision of synchrotron radiation under the proposal 20190316.

The non literal quotations at the beginning of the chapters are devoted to the people who influenced this thesis the most. During the last years I realized more than ever that having a great mentor can change your life. As a young student I was fascinated by many subjects and struggled to find the best direction. After my Bachelor thesis this uncertainty was blown away. Thanks **Stephan** for fascinating me so much (we still need to record the fingerprint of Kölsch). Having one great supervisor might be cool, but having a handful of them is incredibly fortunate. In fact, starting as an undergraduate with **Sven** and his passion on spectroscopy and **Frank** with his technical knowledge was the ideal combo and their support lasted until now. **Marie**, I am simply missing words how grateful I am that our ways crossed. You opened up a new world of puzzles for me and showed me how to solve them. Maybe this is adequate: I really hope the Vengabus will not stop to come. I am deeply thankful to **Holger** for his professionally and very time consuming supervision of this thesis, everyday we chatted about various details of molecular fingerprints. My greatest attitude goes to all of you for your endurance. The point I appreciated the most is that my ideas were always listened to. The topic of this thesis could have been dramatically different, as may be seen from the quotation by Holger. Propanal was initially planned as a one year project and in fact the targeted problem was solved within this time frame. But I was given the chance to develop and follow some own ideas. Thanks for giving me this chance! Thank you all for never being bossy while on the same time being highly critical. I enjoyed the numerous and long discussion on science and all the others as well. I guess, I learned a lot. You five, you are a great team!

I would also like to thank **Mike C. McCarthy** and his team for hosting me as a student intern in Boston as well as **Hiroshi Kohguchi** for his unbelievable hearty welcome in Hiroshima. **Oskar**, thank you for making this possible. Besides, I would like to thank the younger students to make my stay abroad purely enjoyable. Arigato Gozaimasu. **Olivier Pirali**, I would like to thank you for making the Soleil trips successful and on the same time very familiar. Thanks to **Arnaud Belloche** for creating a figure based on my wishes. Many thanks **Hanno**, for enthusing about group theory, I am still enjoying it. Thanks to **Peter Groner** and **Christian Endres** for some discussions on ERHAM. **Colin Western** for a very quick beta version of PGOPHER including further interaction parameters. In german we say "Man sieht sich immer zweimal im Leben", I really hope this is true for all of us.

I would like to thank all the people who accompanied my studies. In particular: **Hannes**, one of the first persons I luckily met; **Slawa**, who knows where this would have ended without your passion and patience, **Benji**, for introducing me to the best WG, **Nico**, **Sebastian**, **Johannes**, and **Jakob**. All of you made the studies of physics livable.

The first steps are often the hardest, thanks for the warm welcome in the Molspekkies to **Monika**, **Sabrina**, **Alex**, and **Lars**. You showed me how valuable team spirit is. In this sense I would also like to thank all **members and former members of the Molspekkies and Oskar and his friends**. **Sandra**, **Christoph K.**, **Stefan**, **Sven F.**, **Marius**, **Nadine**, **Bettina**, **Katharina**, **Elena**, **Phillip**, **Thomas**, **Christoph G. and many more**, thanks for bringing fun to every day over the last years. A big thank you goes to **Luis** you have been a great and helpful student. Furthermore big thanks go to the whole **I. Physikalisches Institut**, and with that also to both workshops and to the team behind the team, i.e. thanks to **Petra** and **Bettina**.

Vielen Dank auch an alle Leute die mich teilweise seit meiner Kindheit begleiten. Besonderen Dank an "der Elfte", die besten WGler **Julius**, **Fabian**, **Jakob** und **Benji**, an **Christopher** und **Johannes** und alle weiteren Freunde, insbesondere aus Delhoven. Das Bier für Revival Treffen wird uns nicht ausgehen.

Die Widmung dieser Arbeit an meine Nichte ist auch als Wertschätzung meiner ganzen Familie zu verstehen, allen Cousins und Cousinnen, (Paten-)Onkeln und (Paten-)Tanten und allen "Dazugestoßenen". Danken möchte ich **Opa Hubert** und **Oma Gerda**, es gibt wohl niemanden der dem Ende dieser Arbeit mehr entgegensehnt, sowie **Opa Jochen** und **Oma Büschi**. Oma Büschi, du hast mir als erstes beigebracht das sich Fleiß am Ende auszahlt, das werde ich nie vergessen. Großeltern müssen nicht erziehen, sie dürfen belohnen, das habt ihr gemacht!

Ein ganz besonderer Dank geht natürlich an meine Freundin, die gerade in den letzten Wochen ordentlich zurück stecken musste. Ich liebe dich, **Swenja**.

Mein allergrößter Dank gilt aber meinen **Eltern und meinem Bruder! Dani**, ich frage mich ständig, wer von uns beiden eigentlich der große Bruder ist. Danke für deine bedingungslose Unterstützung. Ich bin so unfassbar stolz auf dich, **Annika** und **Leonie**. **Mama** und **Papa**, euch danke ich aus tiefstem Herzen für ein sorgenfreies Studium, aber noch viel mehr für meine übergläckliche Kindheit, die wohl bis heute andauert. Danke für alles.

Thanks. Merci. Arigato. Und danke.

Eigenständigkeitserklärung

„Hiermit versichere ich an Eides statt, dass ich die vorliegende Dissertation selbstständig und ohne die Benutzung anderer als der angegebenen Hilfsmittel und Literatur angefertigt habe. Alle Stellen, die wörtlich oder sinngemäß aus veröffentlichten und nicht veröffentlichten Werken dem Wortlaut oder dem Sinn nach entnommen wurden, sind als solche kenntlich gemacht. Ich versichere an Eides statt, dass diese Dissertation noch keiner anderen Fakultät oder Universität zur Prüfung vorgelegen hat; dass sie - abgesehen von unten angegebenen Teilpublikationen und eingebundenen Artikeln und Manuskripten - noch nicht veröffentlicht worden ist sowie, dass ich eine Veröffentlichung der Dissertation vor Abschluss der Promotion nicht ohne Genehmigung des Promotionsausschusses vornehmen werde. Die Bestimmungen dieser Ordnung sind mir bekannt. Darüber hinaus erkläre ich hiermit, dass ich die Ordnung zur Sicherung guter wissenschaftlicher Praxis und zum Umgang mit wissenschaftlichem Fehlverhalten der Universität zu Köln gelesen und sie bei der Durchführung der Dissertation zugrundeliegenden Arbeiten und der schriftlich verfassten Dissertation beachtet habe und verpflichte mich hiermit, die dort genannten Vorgaben bei allen wissenschaftlichen Tätigkeiten zu beachten und umzusetzen. Ich versichere, dass die eingereichte elektronische Fassung der eingereichten Druckfassung vollständig entspricht.“

Teilpublikationen:

- M. Juanes, Journal of Molecular Structure 1211 (2020) 128080.
- M. H. Ordu, Astronomy & Astrophysics 629 (2019) A72.
- M. A. Martin-Drumel, Astronomy & Astrophysics 623 (2019) A167.
- O. Zingsheim et al., Journal of Physical Chemistry Letters 8, 16 (2017) 3776–3781.
- O. Zingsheim et al., Journal of Molecular Spectroscopy 342 (2017) 125 - 131.
- H. S. P. Müller, The Journal of Physical Chemistry A 121, 38 (2017) 7121 - 7129.
- S. Thorwirth, Journal of Molecular Spectroscopy 319 (2016) 47 - 49.
- M. A. Martin-Drumel, Journal of Molecular Spectroscopy 315 (2015) 72 - 79.
- M. A. Martin-Drumel, Journal of Molecular Spectroscopy 307 (2015) 33 - 39.



Köln, den 21.09.20 (Oliver Zingsheim)